ASSESSING COOPERATIVE BEHAVIOR IN DYNAMICAL NETWORKS WITH APPLICATIONS TO BRAIN DATA

THÈSE N^{O} 3651 (2006)

PRÉSENTÉE LE 3 NOVEMBRE 2006

À LA FACULTÉ INFORMATIQUE ET COMMUNICATIONS

Laboratoire de systèmes non linéaires

SECTION DES SYSTÈMES DE COMMUNICATION

ÉCOLE POLYTECHNIQUE FÉDÉRALE DE LAUSANNE

POUR L'OBTENTION DU GRADE DE DOCTEUR ÈS SCIENCES

PAR

Cristian CARMELI

laurea in ingegneria biomedica, Università degli Studi di Genova, Italie
et de nationalité italienne

acceptée sur proposition du jury:

Prof. E. Telatar, président du jury
Prof. M. Hasler, directeur de thèse
Prof. C. Fragouli, rapporteur
Prof. G. Innocenti, rapporteur
Prof. P. Tass, rapporteur

ÉCOLE POLYTECHNIQUE
FÉDÉRALE DE LAUSANNE

Lausanne, EPFL
2006

Abstract

Capturing the collective coherent spatiotemporal activity from measured data in large ensembles of coupled nonlinear sub-systems has revealed to be a key topic in many areas of applied sciences. Currently, this topic is addressed by considering multivariate time series analysis tools. They provide methods whose limiting factors are the amount and quality of data, or the restricted applicability to the class of narrow-band signals.

In this study, we propose three new methods to infer cooperativeness from broad-band multivariate signals that also cope with the constraints due to amount and quality of data. Successfully, we validated all the methods on prototypical models of dynamical networks. Also, we tested their sensitiveness upon amount of data, endogenous and exogenous noises intensity, and number of sub-systems.

The first two methods rely on statistical properties of the multivariate signals by using an entropy-like formula from the correlation matrix estimated from the data. They compute the amount of cooperativeness among the sub-systems by estimating the amount of shrinking of the network embedded space relative to the uncoupled case. The second method of them, based on the partial correlation matrix, may account for cooperation marginalizing third confounder systems. Furthermore, both methods may be applied to embedded and not embedded data, and may be used to estimate (partial) cooperativeness among communities of sub-systems.

The third method follows a deterministic dynamical modeling approach. By means of a suitably decomposed identification of dynamical systems, it can detect interactions among signals both in strength and direction. The method allows the adaptability of the algorithmic setup on the specific applications, and provides a model of local behavior.

In parallel to the methodological development, we applied the first method to two brain data sets in order to assess visual stimuli induced interhemispheric cooperativeness. According to the neuroscientist's interpretation, our results gave new insights about brain functioning.

We have been able to assay flexible stimulus-dependent modulation (*i.e.* behavior) of neuronal cooperativeness over two brain spatial scales: macroscopic by analyzing EEG recordings, and mesoscopic by analyzing LFP recordings.

The analysis on EEGs has extended previous results highlighting that the stimuli induced arrangement of cooperativeness goes beyond the one addressable by narrow-band analysis.

The analysis on LFPs allowed us to describe a new kind of inter-hemispheric integration. We assayed that inter-hemispheric connections modulate in a flexible, stimulus-dependent way, the cooperation in neuronal populations likely to be involved in stimulus detection and/or categorization.

Finally, contrary to current belief in neuroscience, our results showed that simple relations between frequencies and brain functions are unlikely to be true and that stimulus-driven cortical dynamics may change in a way still far from being fully understood.

Keywords: Networks of dynamical systems; Synchronization; Estimation of collective interactions; EEG and LFP; Cortical cooperative behavior.

Version Abrégée

Pour un grand nombre de sciences appliquées, la compréhension de l'activité collective et spatio-temporelle effectuée à partir de données mesurées au sein des réseaux dynamiques est devenue un sujet essentiel. Les spécialistes ont eu recours jusqu'à ce jour à des méthodes d'analyse qui considèrent des séries temporelles multivariées. Celles-ci présentent toutefois des facteurs de restriction, tels que la quantité et la qualité des données ou leur applicabilité qui se limite à la classe des signaux à bande étroite.

Dans cette étude, nous proposons trois nouvelles méthodes qui permettent d'inférer l'activité coopérative à partir de signaux multivariés à bande large. Chacune de ces méthodes a été validée avec succès auprès des modèles prototypiques de réseaux dynamiques. Parallèlement ont été testées leurs sensibilités à la quantité de données, à l'intensité du bruit endogène et exogène ainsi qu'au nombre de sous-systèmes. Nous avons également procédé à une comparaison avec d'autres méthodes existantes à ce jour.

Les deux premières méthodes calculent l'intensité de l'activité cooperative à partir de la réduction de l'espace d'tat reconstruit du réseau. Pour ce faire, elles se basent sur les proprietés statistiques des signaux multivariés en utilisant une formule en forme d'entropie que l'on calcule à partir de la matrice de corrélation. La deuxième méthode, qui est basée sur la matrice de corrélation partielle, peut calculer la coopération marginalisée par rapport à des sous-systèmes tiers connus. En outre, les deux méthodes peuvent être utilisées pour estimer de l'activité cooperative (partielle) parmi des communautés de sous-systèmes.

La troisième méthode se base sur l'identification d'un modèle. Elle permet d'inférer de l'intensité et de la direction des interactions entre sous-systèmes dynamiques faiblement couplés. Cette méthode permet d'adapter la réalisation algorithmique à l'application spécifique et fournit un modèle de comportement local.

Parallèlement au développement de la méthodologie, nous avons appliqué la première méthode à deux collections de données mesurant l'activité cérébrale lors d'une confrontation à des stimuli visuels, ceci dans le but d'évaluer la coopération entre les deux hémisphères.

Nous avons démontré la modulation (c'est à dire le comportement) flexible en fonction des stimuli de l'activité cooperative de neurones sur deux différentes échelles spatiales: une échelle macroscopique, où figure les analyses d' enregistrements EEGs, et une échelle mésoscopique, où figure les analyses d'enregistrements LFPs.

L'analyse des EEGs a complété les résultats précédents en soulignant que l'arrangement de l'acitivité cooperative induit par des stimuli va au-delà de celui qu'on pourrait inférer si on se limitait exclusivement à une analyse par bande étroite.

L'analyse des enregistrements LFPs a permis de décrire un nouveau type de communication entre les deux hémisphères. En effet, nous avons découvert que les connexions entre les deux hémisphères effectuent une modulation flexible et dépendante des stimuli de l'activité cooperative des populations de neurones qui sont probablement impliquées dans la perception et/ou la classification des stimulus.

Finalement, nos résultats ont infirmé l'hypothèse courante en neuroscience selon laquelle il existerait une relation simple entre fréquences et fonctions du cerveau et ont montré que les dynamiques corticales engendrées par les stimuli peuvent varier d'une façon que nous sommes encore loin de comprendre totalement.

Liste de mots-clés: Réseaux de systèmes dynamiques; Synchronization; Estimation d'interactions collectives; EEG et LFP; Comportement cooperatif du cortex.

Sinossi

In molte aree delle scienze applicate, l'acquisizione di dati spazio-temporali si è rivelata fruttuosa per comprendere la dinamica coerente di sistemi non lineari interagenti ed estesi. Ad oggi, questo problema è affrontato analizzando serie temporali multivariate. I metodi disponibili hanno fattori limitanti quali la quantità e qualità dei dati o l'applicabilità alla classe dei soli segnali a banda stretta.

In questo studio proponiamo tre nuovi metodi per inferire attività cooperativa da segnali multivariati a banda larga. Con successo abbiamo validato tutti i metodi su modelli di reti dinamiche. Inoltre, abbiamo testato la loro sensitività rispetto alla quantità dei dati, all'intensità del rumore endogeno ed esogeno, e al numero di sistemi.

I primi due metodi sfruttano la contrazione dello spazio di stato ricostruito della rete rispetto al caso di sistemi non interagenti. Essi si basano sulle proprietà statistiche dei segnali multivariati grazie a una formula entropica degli autovalori della matrice di correlazione stimata dai dati. Il secondo metodo, calcolato a partire dalla matrice di correlazione parziale, permette di calcolare cooperazione marginalizzando la conoscenza di sistemi terzi. Inoltre, tali stimatori possono essere usati per calcolare cooperatività (parziale) tra comunità di sistemi.

Il terzo metodo segue un approccio deterministico grazie a un'opportuna ricostruzione di un modello dinamico della rete. Il metodo permette di inferire sia l'intensità che la direzione delle interazioni fra i sistemi costituenti la rete. Il metodo fornisce un modello di comportamento locale e il suo setup algoritmico è adattabile alla specifica applicazione.

In parallelo allo sviluppo metodologico, abbiamo analizzato con i nostri metodi due insiemi di dati misurati dal cervello con lo scopo di valutare la cooperazione interemisferica indotta da stimoli visivi.

Abbiamo verificato la presenza di una modulazione della cooperatività neuronale indotta dallo stimolo su due scale spaziali: una macroscopica, analizzando elettroencefalogrammi di persone (EEG), e una mesoscopica, analizzando potenziali di campo locale (LFP).

L'analisi dei segnali EEG ha esteso risultati precedenti evidenziando che l'arrangiamento della cooperazione neuronale evocata dagli stimoli va ben oltre quella risolvibile da un'analisi a banda stretta.

L'analisi dei segnali LFP ha permesso di descrivere un nuovo tipo di integrazione interemisferica. Abbiamo scoperto che le connessioni interemisferiche modulano in una maniera flessibile e dipendente dallo stimolo la cooperatività di popolazioni neuronali coinvolte nel rivelamento e/o classificazione dello stimolo.

Infine, contrariamente al credo corrente in neuroscienza dell'esistenza di semplici relazioni fra frequenze e funzioni cerebrali, i nostri risultati ha mostrato che ciò è poco

probabile e che la dinamica corticale evocata dagli stimoli può cambiare in una maniera che ancora siamo lontani dal comprendere totalmente.

Parole chiave: Reti di sistemi dinamici; Sincronizzazione; Stima d'interazioni collettive; EEG e LFP; Comportamento cooperativo della corteccia.

Acknowledgments

Many people have contributed to this work and have enriched my soul in the last four years of unforgettable life in Lausanne.

I wish to thank my Ph.D. advisor, Martin Hasler. My gratitude for him is for his honesty and for having given me the opportunity of studying in his laboratory. Furthermore, I am grateful to him for having let me discover how important two daily coffee breaks can be in the life of a researcher.

Oscar De Feo has worked with me all along these years and has been an amazing and unique teacher and friend. I could share ideas and learn a bit of his scientific knowledge. My deepest gratitude is for his constant encouragement. I also remember with great pleasure the time spent together in various occasions, as at the school of neuroscience in Austria or the two weeks in Stockholm. Besides science, he has been a reference for cookery and wines.

Giorgio Innocenti has been an extraordinary neuroscientific tutor. He has prodded and stimulated me with wonderful questions. I also wish to thank Maria Knyazeva, who introduced me to the world of electroencephalographic recordings.

I wish to thank the members of my thesis committee: the president Emre Telatar and the experts Christina Fragouli, Giorgio Innocenti and Peter Tass. Thank you all for having read my manuscript and for the challenging questions asked during my exam.

During the last four year I have shared lunch times, coffee breaks and fondue evenings with my colleagues at LANOS. Especially, I wish to thank Enno for sharing opinions and Kumiko to have kindly accepted to work a while with myself.

In Lausanne I had also the unexpected chance to meet special people. Among all of them, my friend Roberto and my partner of dance Karine. Roberto has allowed me to know a bit of the culture of eastern part of Italy and has been a true friend at any time.

Finally, my deepest love goes to my parents and my brother, who have supported me and to whom I dedicate this thesis.

Contents

1

Introduction

Since its existence on earth, human kind bas been intrigued by all various phenomena present in nature. Philosophers and scientists have been observing nature processes to infer their governing laws and to verify modeling hypothesis about them [Galilei, 1638, Popper, 1934].

In the recent years, the study of networks, or ensembles of interacting units, has revolutioned human endeavor of taming real-world systems. The investigation of the properties of networks pervades all of science, from neurobiology to statistical physics. Empirical studies have shed light on the topology of food webs [Cohen et al., 1990, Williams and Martinez, 2000], cellular and metabolic networks [Bhalla and Iyengar, 1999, Hartwell et al., 1999], the World-Wide Web [Broder et al., 2000], co-authorship and citation networks of scientists [Redner, 1998, Newman, 2001].

Compared to previous fundamental human discoveries, networks propose new challenges. Indeed, network's components obey neither the extreme disorder of gases, in which a molecule can collide with any other molecule, nor the extreme order of magnets, where spins interact only with their immediate neighbors in a nicely periodic lattice. Rather, contrary to magnets spins for instance, network's units may be organized through various topologies, such as scale free or small-world graph, that theoretical studies have showed to greatly affect the whole network's properties [Watts and Strogatz, 1998, Barabási and Albert, 1999, Kurant and Thiran, 2006]. Furthermore, network anatomy is not the only ingredient affecting network's functions: network's units may possess nonlinear dynamics and the combination of this property with various interaction topologies may further enrich the catalogue of the whole network's properties [Strogatz, 2001].

From both theoretical and experimental sides, the greatest challenges is to capture the *properties* of the entire network ensemble [Wilson, 1998]. A significant example is given by the brain, where the interaction among relatively simple units, the neurons, allow living beings to face the earth unpredictable environment, *i.e.* to survive. In this case, an intriguing property could be brain behavior facing stimuli. Another example is again from systems biology: the collaboration among termites in termite colony produces the so-called termite "cathedral" mound. In this case, an intriguing property could be the topographical arrangement of the tunnel inside the cathedral. Often, such ensemble properties are labeled as "emergent". Emergent properties are characterized as those ones arising out of other properties and yet are novel or irreducible with respect to them. However, this concept of emergent property is controversial when the organizational principles or laws leading to it are known. We agree on the fact that the term emergence should be used only *in lieu* of a more meaningful explanation.

From the perspective of the nonlinear dynamics, dynamical networks may show interesting collective properties: they are able to synchronize in a flexible way, *i.e.* they can synchronize and de-synchronize in a threshold-like way [Pikovsky et al., 2001]. Furthermore, a whole network chaotic attractor may emerge from the interplay of simple, even linear, sub-systems [Popovich et al., 2005, Maistrenko et al., 2005, Zhang and Small, 2006].

In the field of dynamical system theory, the synchronization principles of coupled subsystems have been deeply studied. Different instances of synchronization, such as phase synchronization or general-like synchronization, have been discovered [Pikovsky et al., 2001].

On the other hand, theoretical studies have only started to unveil the network's synchronization mechanisms. They show, for instance, that network propensity for synchronization may strongly depend on coupling weight and coupling architecture [Barahona and Pecora, 2002, Chavez et al., 2005, Belykh et al., 2005]. Furthermore, synchronization may not happen at ensemble level, but only in some cluster or sub-collection of network units [Belykh et al., 2001].

Since the property of synchronization requires the interaction among the network's units to manifest itself, its exploration in real-world systems has been carried out by inferring cooperative activity from data. Historically, nonlinear time series analysis has been focused on inferring cooperativeness in bivariate measurements [Kantz and Schreiber, 2004]. Nevertheless, because multiple parallel recordings of the network under study are nowadays available, there is a concrete hope to use these multivariate information to unravel network's properties. Although techniques developed in the bivariate context are fundamental, they are difficult to apply on multivariate measurements for several practical problems. On the other hand, multivariate methods may potentially suffer for network's observability issues, as well for constraints due to the finite amount and quality of available data and computational complexity. These facts challenge the development of new multivariate techniques of data analysis and call for adequate validation studies.

This study deals with the problem of inferring cooperative behavior from the recorded activity of dynamical networks. By considering networks as open systems, we refer to behavior as the network coordinated activity related to exogenous causes. Our aim is especially addressed to the case when only minimal knowledge about cooperative properties is available. The hope is to gather new insights about those networks thanks to our study.

We have developed new methods to infer cooperativeness in the whole network or in sub-collections of network's units from real data. Methodically, we assessed their performances on toy models of dynamical systems. In particular, validation tests have been focused on assessing the methods sensitiveness upon data length, endogenous and exogenous noises, number of sub-systems and network's topologies. Also, a comparison with other existing methods has been considered.

In parallel to the methodological development, two applications to real data have been performed. In particular, thanks to the collaboration with neuroscientists, the analysis of cooperative behavior during perception in brain neuronal assemblies has been possible. These investigations were primarily motivated by current experimental evidence of the role of synchronization phenomena in the activity of neuronal assemblies involved in integrating or binding perceptual information [Gray et al., 1989, Singer, 1999].

From one side, this interdisciplinary study allowed the direct application of the developed methods to concrete situations. From another side, while the obtained results

were satisfactory and unexpected from current neuroscientific viewpoints, it unveiled the limitations of the current methodologies in data analysis to understand brain functioning mechanisms and, consequently, challenged further improvements and developments.

Part of this study has been published on one international journal and four international conference papers. Furthermore, one journal paper is under revision and one is under preparation.

The outline of this study is the following.

Chapter 2: an introduction to the *binding problem* in neuroscience is given and an overview of current approaches in time series analysis to infer cooperative behavior is presented.

Chapter 3: a new estimator of cooperativeness is described. Validation tests are illustrated by using prototypical models of networks and network topologies. Sensitiveness upon noise and amount of data and comparison with other methods are also given.

Chapter 4: two new estimators of cooperativeness marginalized upon third knowledge are described. They are validated on prototypical models of systems, and sensitiveness upon noise and amount of data is given. Furthermore, saliency upon the number of marginalized sub-systems and scalability upon the number of network's sub-systems are tested.

Chapter 5: Applications to brain data of the method introduced in Chapter 3 are described. The modulation of neuronal cooperative activity evoked by visual stimuli has been assayed from two different recording setups.

Chapter 6: Conclusions and outlooks for future investigations are given.

2

The Background: Bridging Neuroscience and Dynamical Systems Theory

Brief — This chapter gives an introduction to the *binding problem* in neuroscience and an overview of current approaches in time series analysis to infer cooperativeness. The presentation of these two topics is given in order to be understood by readers not necessarily familiar with both domains.

2.1 The binding problem in neuroscience

To explain how the brain interprets the world, the French philosopher Descartes postulated that we have a single center – the pineal gland – where all sensory signals converge and are evaluated jointly, where decisions are reached and future actions planned [Descartes, 1664]. Since the beginning of last century [Ramón y Cajal, 1904], progress in neurobiology has driven the neuroscientific community to adopt a different view: there are few, if any, places in the nervous system where all information necessary to carry out a particular task is localized [Kandel et al., 2000]. Furthermore, neuronal cells are believed to constitute the building block unities such that sensory, cognitive and motor processes result from parallel interactions among large populations of neurons distributed among multiple cortical and sub-cortical structures [Georgopulos et al., 1992, Young and Yamane, 1992, Wilson and McNaughton, 1993, Vaadia et al., 1995, Nicolelis et al., 1998]. As an example, evidence from neuroanatomy and neurophysiology suggests that processing streams in the visual system are segregated, so that features such as color, motion, location and object identity are processed in separate brain regions.

Binding, in a general sense, is the process responsible for functionally linking this distributed activity. To illustrate the richness of the binding processes, let us consider a simple example of a sensory-motor task. A reader may want to find this thesis manuscript on her[1] bookcase. She remembers that she left it on one shelf, but she is not sure which one, and there are many other objects on the shelves besides the one she is searching for. To find it, she has to visually scan the scene until you recognize the object. At each location of the gaze, her visual system must parse the scene into its component objects. This involves identifying which features in the scene belong to which objects. Once this is accomplished, or perhaps at the same time, the identity of a particular object can be evaluated. If it does not match what she is searching for, she must direct her gaze to a new location and repeat this process. This redirection of gaze may itself be guided by the prior parsing of the scene. Once she has identified the correct object, she can reach out, grasp it, and carry on with the task at hand.

[1] Let us imagine a female reader.

As it may be argued, binding is not a problem for the nervous systems, as evolution has sculpted their organization to solve the problem efficiently and effectively. However, it can be stated that the brain has difficulty in binding. For example, this can occur in normal brains when there are temporal or capacity limitations, which lead to errors such as "illusory conjunctions", *i.e.* the incorrect combinations of features belonging to different objects [Treisman and Schmidt, 1982]. Moreover, this can also occur in damaged brains, when deficits appear to inhibit normal cognitive operations. For example, a localized bilateral damage causes simultagnosia, the inability to perceive more than one object at a time [Damasio, 1985]. Furthermore, evidence for a dissociation between a vision-for-perception and a vision-for-action pathway has been reported in patients with lesions: they could discriminate objects according to shape, but could not properly grasp them in accordance with the visual percept [Goodale et al., 1991].

Finally, binding is a problem in that it requires an explanation for scientists. Indeed, if it is true that integration of distributed information is a phenomenon occurring in brains, then it is equally true that the mechanisms of how this is achieved are not yet completely known to the scientific community.

It is worthwhile to remember that something as complex as binding, writ large, may not have a single mechanistic solution. The potential mechanisms for binding suggested in literature are not mutually exclusive: there is ample room for temporal and combinatorial coding mechanisms to work together in the brain to process information, and there may well be other as yet undiscovered mechanisms at work as well.

In order to reduce difficulties and controversy in understanding the binding mechanisms, we do constrain the problem to the visual system, which since ever has been the object of great interest not only in neuroscience, but also in other disciplines such as computer vision, machine learning, or, more generally, computer science [Barlow, 1981, Schalkoff, 1989, Bishop, 1995]. Furthermore, it is the object of study in this thesis.

In the visual system, the binding problem corresponds to identifying the relationships among features in an image so that objects can be perceived as such. Within this context, the mechanisms enabling features to be grouped together are often labeled as *perceptual grouping*. Here, two models of perceptual grouping are considered in detail: binding by convergence and binding by dynamic formation of cells ensembles.

2.1.1 Binding through convergence

Binding through convergence is conceptually a simple model. It assumes that neurons detecting simple features of the input, such as color or orientation of the edges, converge on to neurons that are tuned to detect a specific constellation of features. Several iterations of this convergence produce binding neurons in the later stages of processing that respond only when a specific set of input neurons is activated. The responses of these individual binding neurons could signal the presence of particular aspects of the perceived object, or ultimately, could represent the whole object itself.

This model for feature integration relies on the well-established understanding that visual cortex is organized hierarchically into a collection of distinct areas [Hubel and Wiesel, 1962, De Yoe and Van Essen, 1988, Felleman and Van Essen, 1991, Sereno and Allman, 1991]. A mechanism of this type probably works for stereotypical, familiar patterns, allowing them to be processed very rapidly [Barlow, 1981, Riesenhuber and Poggio, 1999, Quian Quiroga et al., 2005]. However, it is difficult to see how it could deal with the large variety of changing, often unfamiliar, stimuli that living beings encounter in their everyday lives. There are just too many features to cover with appropriately tuned

neurons, and the possible combinations and different views would require an enormous number of binding units. Furthermore, the combination of all possible visual representations with all possible motor outputs constitutes another formidable problem.

Finally, this model also requires a large reservoir of unspecified neurons, available for specification when new patterns have to be learnt and recognized. However, there is not evidence for such a pool in the primate brain.

2.1.2 Binding through synchrony

It has been recognized by many investigators that the combinatorial problem of the previous model can be overcome by population coding, *i.e.* by representing complex features combinations with the activity of a population of neurons distributed within and across levels of the cortical hierarchy [Ballard et al., 1983, Van Essen and Anderson, 1990]. In this scheme, for example, each stimulus pattern could be represented by a distinct pattern of firing in a distributed population of cells. At first sight, population coding seems to make the numerical problem worse because large groups of neurons are required to represent a particular feature. However, because neurons are broadly tuned, populations representing different features overlap and an individual neuron can participate in the representation of many different features. This possibly reduces the number of representational units required and allows the formation of many, ephemerae clouds of simultaneously active neurons that code for this or that feature [Singer, 1999].

Nonetheless, the problem is how an ensemble of neurons is defined. Recently, the insight put forth to solve this problem has been to define cell assemblies on the basis of temporal correlation or synchronization of neuronal firing [Milner, 1974, von der Malsburg, 1981, 1985]. By retaining all the advantages inherent in population coding models, this temporal correlation model provides a physiologically plausible theoretical framework to account for the integration of distributed stimulus features into an emergent representation. Moreover, it allows a flexible dynamical processing of visual features.

A surge of interest in the correlation hypothesis took place when a series of experiments demonstrated that synchronous firing was stimulus-dependent in visual cortex [Eckhorn et al., 1988, Gray et al., 1989]. This first evidence unleashed a flurry of experimental studies corroborating the synchrony based model of the binding processes [Bressler et al., 1993, Munk et al., 1996, Kreiter and Singer, 1996, Roelfsema et al., 1997]. Nevertheless, a problem rests unsolved with the output side of the synchrony-defined binding hypothesis: the so called *read-out* problem. Indeed, how synchronous activity of neuronal populations is interpreted and transformed by other neurons to result in perception is unexplained.

The aforementioned neurophysiological studies represent a prominent example of concrete manifestation of synchronization, an interesting phenomenon that has been observed in several other domains since the seventeenth century [Huygens, 1673]. From its discovery, synchronization has attracted the interest of theoreticians and experimentalists, and nowadays represents a important matter of study within dynamical systems theory [Boccaletti et al., 2002a].

2.2 Synchronization in dynamical systems theory

One day in February 1655 the Dutch physicist Christiaan Huygens, inventor of the pendulum clock, was staring at two clocks he had recently built, which were hanging side by

side from a common support. Suddenly, he noticed perfect agreement between the oscillating motions of the two clocks, *i.e.* their synchronization. This fortuitous observation started theoretical and experimental investigations of this phenomenon in several various fields of science and engineering.

As reported in [Pikovsky et al., 2001], synchronization can be understood as an *adjustment of rhythms of oscillating deterministic sub-systems due to their weak interaction.* In more detail, the existence of self-sustained rhythms for each oscillating sub-system, even when autonomous, is the first main property which characterizes a synchronization phenomenon. An illustrative example of what is not synchronization may help to clarify this concept. The example comes from population dynamics: the hare-lynx cycle [Odum, 1953]. Synchronization between these two interacting populations does not formally exist because the hare-lynx ecological system cannot be separated into self-sustaining oscillating sub-systems. Indeed, either the lynxes will die without food or the hare population will explode. Another example is given when the rhythm of a sub-system is only induced by another one. This case is usually treated as a phenomenon of resonance and not of synchronization.

A second important aspect regarding synchronization processes is the existence of interactions or couplings among the considered sub-systems. The coupling can be either unidirectional or bidirectional. In the latter case, the sub-systems adjust their rhythms to each other and this is usually referred to mutual synchronization. In the former case, where the forcing sub-system is also called a drive system and the driven sub-system is called a response system, the rhythm of the response is adjusted to the rhythm of the driver.

Finally, a remarkable property of synchronization is its occurrence between deterministic systems showing irregular, not purely periodic behavior, *i.e.* chaos [Lorenz, 1963, Fujisaka and Yamada, 1983, Pecora and Carroll, 1990]. Deterministic chaos is characterized by sensitivity to initial conditions, *i.e.* trajectories starting from very close points in the state-space diverge exponentially. Therefore, in that sense synchronization between chaotic oscillators was not expected. However, experimental investigations in a variety of fields have proven its existence: electronics [Heagy et al., 1994, Parlitz et al., 1996], laser dynamics [Fabiny et al., 1993, Roy and Thornburg, 1994], plasma physics [Rosa et al., 2000], communication [Carroll and Pecora, 1993, Kocarev and Parlitz, 1995] and chaos control [Pyragas, 1992, Rulkov et al., 1994].

In literature, despite the fact that many types of synchronization have appeared, three main synchronization processes may be distinguished, namely identical synchronization, generalized synchronization, and phase synchronization. To easy their description, assume that a large stationary deterministic finite dimensional time continuous system is divided into two sub-systems,

$$\begin{cases} \dot{\theta}^{(1)}(t) = f^{(1)}\left(\theta^{(1)}(t), \theta^{(2)}(t)\right), \\ \dot{\theta}^{(2)}(t) = f^{(2)}\left(\theta^{(1)}(t), \theta^{(2)}(t)\right). \end{cases} \tag{2.1}$$

Here, $\theta^{(1)}(t) \in \mathbb{R}^{d^{(1)}}$ and $\theta^{(2)}(t) \in \mathbb{R}^{d^{(2)}}$ are the state-space vectors at time t of the two sub-systems of dimension $d^{(1)}$ and $d^{(2)}$ respectively; $f^{(1)}$ and $f^{(2)}$ are the vector fields which model the motion laws of the two sub-systems. To guarantee the condition of self-sustaining motion, these laws must contain nonlinear terms[2]. The phase-space

[2] In principle, a stable harmonic linear system can show self-sustaining motion. Nevertheless, synchronization phenomenons can appear only in interacting sub-systems containing some nonlinearity that, generally, can appear in the self-motion law or in the coupling term. When two undamped harmonic

and vector field of the large system is formed in a natural way from the product of the two smaller state-spaces and vector fields. Although we will introduce the three types of synchronization for two continuous dynamical sub-systems, the same description holds for $M \geq 2$ continuous/discrete time sub-systems.

2.2.1 Identical synchronization

This is the most frequently discussed and simplest form of synchronization within the nonlinear dynamics community. Here, the sub-systems are identical, *i.e.* $f^{(1)} \equiv f^{(2)}$ and $d^{(1)} \equiv d^{(2)}$. Identical or complete synchronization is observed if the trajectories of the coupled sub-systems coincide in the limit $t \to \infty$ [Fujisaka and Yamada, 1983], *i.e.*

$$\lim_{t\to\infty} \left\| \theta^{(1)}(t) - \theta^{(2)}(t) \right\| = 0. \tag{2.2}$$

where $\|\bullet\|$ is any norm in $\mathbb{R}^{d^{(1)}}$.

2.2.2 Generalized synchronization

Generalized synchronization involves synchronization between sub-systems whose vector fields are not identical because they have different functional form and/or different parameter values [Afraimovich et al., 1986, Rulkov et al., 1995]. It is also possible for the sub-systems to have different dimensions, *i.e.* $d^{(1)} \neq d^{(2)}$. In the literature, there is not a consistent unique definition about generalized synchronization. For convenience, as most papers indicate, we will say that the sub-systems are general-like synchronized if $\theta^{(1)}(t) = H\left(\theta^{(2)}(t)\right)$, where H is a smooth, invertible, time independent function [Kocarev and Parlitz, 1996]. Importantly, the equation $\theta^{(1)}(t) = H\left(\theta^{(2)}(t)\right)$ defines an invariant manifold (in the state-space of the large system) which can be used to determine the state of one sub-system given the state of the other sub-system. If the sub-systems are identical then $H\left(\theta^{(2)}(t)\right) = \theta^{(2)}(t)$.

2.2.3 Phase synchronization

Phase synchronization involves sub-system properties called "phases". Roughly speaking, the term "phase" carries many different meanings in physics. For instance, the word phase in the term phase-space has nothing to do with the phase in phase transition. The phenomena addressed within phase synchronization are based on the notion of the phase of an oscillation, which originates from the notion of phase in a harmonic motion. The phase is a specific variable of a motion as, for instance, the oscillation of a pendulum clock. A simple example is reported in Fig. 2.1.

Phase synchronization is a natural concept for the description of two nonlinearly coupled linear (harmonic) sub-systems, or of nonlinear sub-systems for which the definition

oscillatory systems are coupled in a linear way, the resulting motion is the linear composition of two harmonic modes. Even if the frequencies of the two oscillators are very similar, they do not synchronize, but instead show a phenomenon called beating: the energy slowly oscillates between the two systems, *i.e.* the amplitudes of their oscillations vary sinusoidally. Formally, this is the consequence of the existence of the superposition principle. Intuitively, this is a consequence of the particular property of harmonic motion that the oscillation period is independent of the amplitude oscillation. Hence, one oscillator can not adapt its period to the second one. The presence of nonlinearity makes such situation different. As observed by Huygens, two pendulum clocks mounted on a rack of finite stiffness, so that the rack starts to slightly rock itself, can synchronize due to this coupling.

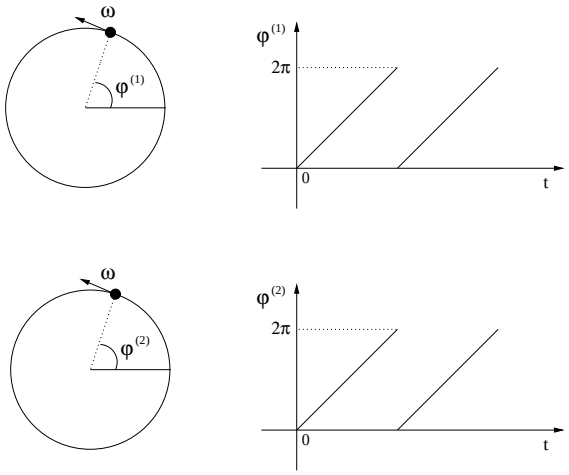

Fig. 2.1. Simple example of the phase as a variable of a motion. On the left, the motion of points on the unit circle is described by the variable $\varphi^{(1)}$, $\varphi^{(2)}$, *i.e.* the phases. On the right, the phases are plotted as a function of time. The phases are exactly the same because the points move with same speed ω (*i.e.* the slope of the straight lines in the right panel) and have started from the same initial points on the circle. Here, we plot the phases between the values 0 and 2π; however, they could be unwrapped and range from 0 to infinity.

and determination of a phase is straightforward. Recently, phase synchronization has been also extended to chaotic systems [Rosenblum et al., 1996] for which, however, the definition of a phase may not be unambiguous.

Phase synchronization between the two sub-systems in Eq. (2.1) can be defined as the entrainment of their phases, *i.e.*

$$\left| n\varphi^{(1)} - m\varphi^{(2)} \right| \leq const \tag{2.3}$$

where $\varphi^{(1)}$ and $\varphi^{(2)}$ are the unwrapped phases of the sub-system (1) and (2), respectively, and $n, m \in \mathbf{N}$. If Eq. (2.3) holds, the two sub-systems are said to be $n : m$ phase synchronized. A simple example of $1 : 1$ phase synchronization is given in Fig. 2.1.

Phase synchronization has fewer constraints than identical and generalized synchronization. Indeed, only the phases have to be locked whereas the amplitudes may be uncorrelated.

Commonly, identical synchronization is observed for sufficiently strong coupling of identical sub-systems. A relation between the weaker forms of synchronization, phase and generalized synchronization, cannot be defined in general. Indeed, while it has been first claimed [Parlitz et al., 1996] that generalized synchronization implies phase synchronization, *i.e.* the phase synchronization appears first with increasing of the interaction strength between the sub-systems, later it has been shown in several examples that the reverse order is also possible [Zheng and Hu, 2000].

2.2.4 Remarks

Up to now, we have presented different features of the phenomenon of synchronization, and we have roughly illustrated its theoretical concept. Although the presence or the absence of synchronization has been detected in many experimental conditions, it is not always an easy task to establish it. Difficulties arise, for instance, because synchronization is not a state, but a process (*e.g.* an adjustment of phases and frequencies within

phase synchronization) and its presence or absence cannot be established from a single observation. Furthermore, in experimental setups noise is unavoidable. Consequently, synchronization has to be detected in noisy systems for which synchronization transitions are smeared and there is not a distinct difference between synchronous and asynchronous states. Finally, and importantly, even if we reveal some inter-relations between the sub-systems under observation, a secondary analysis to determine the nonlinear nature of the sub-systems is necessary. By following the definition of synchronization given in Sec. 2.2, the self-sustaining character of those sub-systems has to be established. Indeed, when dealing with black-box experimental setups, inter-relations found in data analysis might also be due to another phenomenon such as resonance [Pikovsky et al., 2001].

Nevertheless, the analysis of signals aiming at the discovery of inter-relations between them may provide useful information about the interactions of the sub-systems that generated those signals. In the field of time series analysis this kind of investigations is usually referred to the term *interdependence analysis*. In the literature, the techniques devoted to this analysis are numerous: in the next section we will give an overview of them.

2.3 Interdependence analysis in time series

The analysis of interdependences within simultaneously recorded observables of interacting sub-systems deals with the determination of the degree of their inter-relation. More generally, data analyzers are interested not only in the strength of those interdependences, but also in their direction. The direction of an interaction is important, for instance, in drive-response relationships [Quian Quiroga et al., 2000]. In the following, for the sake of simplicity, we will focus only on tools to estimate interdependence strength, though most of the tools to determine a direction are derived from the concepts we will illustrate thereafter and review in Chapter 3.

In order to describe the methods available in literature to estimate interdependence strength, we introduce the model we assume throughout this thesis about the measurement process and about the sub-systems underlying the recordings.

Let us denote by $\Theta(t) \in \mathbb{R}^D$, where

$$\Theta(t) = \begin{bmatrix} \theta^{(1)}(t) \\ \vdots \\ \theta^{(i)}(t) \\ \vdots \\ \theta^{(M)}(t) \end{bmatrix},$$

the state-space vector at time t of M coupled heterogeneous dynamical sub-systems, that compose a generic large system, or network. The components $\theta^{(i)}(t) \in \mathbb{R}^{d^{(i)}}$ are the state variables of the generic $d^{(i)}$-dimensional sub-system (i) and $\sum_{i=1}^{M} d^{(i)} = D$. The model of the network is given by the noise-driven system

$$\dot{\Theta}(t) = \mathcal{F}(\Theta(t)) + \eta(t), \tag{2.4}$$

where the generic vector field $\mathcal{F} : \mathbb{R}^D \to \mathbb{R}^D$ models the network dynamics law. The vector $\eta(t) \in \mathbb{R}^D$ represents the unavoidable modeling noise[3], which we assume to be

[3] In literature, modeling noise is also referred to as dynamical noise. We prefer the word modeling instead of dynamical because with it we want to model the influences of the rest of the universe onto

independent from $\mathcal{F}(\Theta(t))$. We model the noise as a zero-mean Gaussian additive process with covariance function $\langle \eta(t), \eta(t') \rangle = R\delta(t-t')$ and diagonal covariance matrix R. With such a (nonlinear) stochastic dynamical system, we can still speak about synchronization, however, expectation values[4] of the considered properties (like phases in phase synchronization or state variables in generalized synchronization) should be taken into account [Brown and Kocarev, 2000]. Roughly speaking, if $\eta(t)$ has low intensity compared to that of $\mathcal{F}(\Theta(t))$, the hypothesis of determinism of the network dynamics is still tenable.

Generally, the recording process does not allow a direct access to the state $\Theta(t)$; however, an observable of it, $Y(t)$, is usually available. Here, covering a wide range of situations [Tass, 1999, Kantz and Schreiber, 2004], $Y(t)$ is assumed to be related to $\Theta(t)$ by a measurement function $\mathcal{G}: \mathbb{R}^D \to \mathbb{R}^P$, which we assume to be smooth and corrupted by some measurement (or observational) noise $\nu(t)$, that is additive, zero-mean, Gaussian-distributed, independent from $\mathcal{G}(\Theta(t))$. Moreover, we assume that $\nu(t)$ has covariance function $\langle \nu(t), \nu(t') \rangle = V\delta(t-t')$ and diagonal covariance matrix V.

Finally, accounting for the fact that measurements are usually performed with a fixed uniform sampling interval δt at times $t_0, t_0 + \delta t, \ldots, t_0 + (L-1)\delta t$, and by denoting discrete time values as subscripts, we can write the measurement equation of the network as

$$Y_t = \mathcal{G}(\Theta_t) + \nu_t, \tag{2.5}$$

yielding a P-variate time series Y_t, where $t = 0, \ldots, L-1$, $L < \infty$, and $\delta t = 1$, without loss of generality.

The model described by Eqs. (2.4) and (2.5) accounts for many concrete situations which are encountered in experimental investigations. For instance, setting apart current debates about the deterministic or stochastic nature of neuronal cells [Gerstner and Kistler, 2002, De Lange, 2006], Eq. (2.4) might model the dynamics of a network of M neurons or even populations of neurons. As further examples, it could model other biological systems of living beings, like pacemaker cells in the heart [Mirollo and Strogatz, 1990], insulin-secreting cells in the pancreas [Sturis et al., 1995] and fireflies swarms [Strogatz and Stewart, 1993] to cite a few. The list of examples could be extended to population dynamics in ecology [Murray, 2002] or social dynamics networks [Watts, 2003].

Let us now assume that $P \geq M$ measurements are available, and, as it is commonly assumed, with at least one measurement from each dynamical sub-system, *i.e.*

$$Y_t^{(i)} = \mathcal{G}^{(i)}\left(\Theta_t^{(i)}\right) + \nu_t^{(i)}, \tag{2.6}$$

$\forall i$. Without loss of generality[5] we can fix $P = M$, and, to facilitate the presentation of the tools for the interdependence analysis, we further fix $M = 2$. Some of the tools can be straightforwardly generalized to the case $M > 2$ or, traditionally, for the study of higher dimensional situations all possible pairs of bivariate data are considered. As we will illustrate in a later chapter, this procedure may lead to erroneous conclusions.

---

the system under study. Even with great care, experimentalists can only minimize but never exclude perturbations of their studied system by external influences.

[4] In other words, we stress the fact that that in this case the question "synchronous or not synchronous" cannot be answered unambiguously, but can be treated only in a statistical sense.

[5] A preprocessing technique of data reduction like Principal Component Analysis or Independent Component Analysis might be used.

2.3.1 Linear approach

The simplest and most common approach to measure interdependences between two sub-systems is given by linear tools [Brillinger, 2001]. There are measures defined both in time and frequency domain. In time domain, the most commonly used measure is the cross-correlation function. Its estimation from the data is usually given by

$$\rho^{(1,2)}(\tau) = \frac{1}{L-\tau} \sum_{t=0}^{L-\tau-1} \left(\frac{y_t^{(1)} - \overline{y^{(1)}}}{\sigma^{(1)}} \right) \left(\frac{y_{t+\tau}^{(2)} - \overline{y^{(2)}}}{\sigma^{(2)}} \right) \tag{2.7}$$

where $\overline{y^{(1)}}, \overline{y^{(2)}}$ denote sample mean values of the recorded time series[6] from sub-systems (1) and (2) respectively, similarly $\sigma^{(1)}, \sigma^{(2)}$ denote sample standard deviations and τ is a time lag (reasonably, $\tau \ll L$). In absolute value, the ranges of the cross-correlation function are 0 for the case of linearly independent sub-systems and 1 for the case of maximally linearly inter-related sub-systems. Furthermore, it is symmetric, *i.e.* $\rho^{(1,2)}(\tau) = \rho^{(2,1)}(\tau)$[7]. In applications, two common measures are $\rho^{(1,2)}(0)$, *i.e.* the cross-correlation at zero time lag, and $\max_{\tau} \left| \rho^{(1,2)}(\tau) \right|$.

At this point, it is relevant to underline the concept of *sample estimate*. A sample estimate is a number derived from a finite data set for the quantity we would like to measure. Due to the finite amount of recorded data usually available, for the same quantity we want to measure, such as a mean value, there can exist different estimates for different realization sets of such a quantity.

Regarding the linear interdependence measures in the frequency domain, the most common is the normalized cross-spectrum or coherence function, namely

$$Coh^{(1,2)}(f) = \frac{\left| s^{(1,2)}(f) \right|}{\sqrt{s^{(1,1)}(f)} \sqrt{s^{(2,2)}(f)}} \tag{2.8}$$

Here, $s^{(1,2)}(f)$ is the sample estimated cross-spectrum between the two sub-systems at the frequency f, $s^{(1,1)}(f), s^{(2,2)}(f)$ are the sample auto-spectrum at the frequency f for the sub-system (1) and (2) respectively. $Coh^{(1,2)}(f)$ ranges between 0 and 1 with similar meaning to the cross-correlation function, and it is as well symmetric. Being a function of f, this measure is useful when interdependence analysis is focused on a particular frequency band, as, for instance, it is usually the case for electroencephalographic (EEG) signals [Nunez, 1995]. In applications, a common measure is $\max_{f} \left| Coh^{(1,2)}(f) \right|$.

Finally, it has to be remarked that both cross-correlation and coherence functions, being based on second momentum properties, are possibly insensitive to nonlinear inter-relations eliciting higher momentums.

2.3.2 Information Theory inspired approach

To go beyond second order correlations, information-theoretic concepts are the most intriguing. Indeed, entropy-like quantities naturally depend on all higher moments of a probability distribution [Renyi, 1971].

[6] For the sake of clarity,

$$Y_t = \begin{bmatrix} y_t^{(1)} \\ y_t^{(2)} \end{bmatrix}.$$

[7] It is often supposed that a shift of the maximum of $\rho^{(2,1)}$ towards positive lags indicates that (1) couples into (2) with some delay. However, this can only partly be justified by causality [Kantz and Schreiber, 2004].

The most commonly used quantity is the so-called mutual information [Cover and Thomas, 1991]. Let us consider the time series available from the sub-systems as a realization of two stochastic processes with J possible outcomes, obtained, for instance, by partitioning $Y_t, t = 0, \ldots, L-1$, into J bins. Generally, for each outcome, a probability distribution $p_i, i = 0, \ldots, J-1$, with $p_i \geq 0, \forall i$, and $\sum p_i = 1$ has to be estimated. A first common estimate is to consider $p_i = m_i/L$, where m_i is the number of occurrences of the i-th outcome after L samples. From this set of probabilities, the mutual information of the two sub-systems is given by

$$MI^{(1,2)} = \sum_{i=0}^{J-1} \sum_{j=0}^{J-1} p_{i,j}^{(1,2)} \ln \frac{p_{i,j}^{(1,2)}}{p_i^{(1)} p_j^{(2)}} \tag{2.9}$$

Here, $p_{i,j}^{(1,2)}$ represents the estimated joint probability distribution of the generic outcomes i and j for the two sub-systems (1) and (2), respectively; $p_i^{(1)}$ and $p_j^{(2)}$ stands for the outcome-wise estimated probability distributions of the sub-systems (1) and (2), respectively. For independent sub-systems, $MI^{(1,2)}$ is zero. Indeed, in this case $p_{i,j}^{(1,2)} = p_i^{(1)} p_j^{(2)}, \forall i, j$. For identical signals, mutual information takes a positive maximum value, *i.e.* $MI^{(1,2)} = I^{(1)}$, where I the Shannon entropy. Indeed, in this case $p_{i,j}^{(1,2)} = p_i^{(1)}$ (or $p_i^{(2)}$) and the right hand side of Eq. (2.9) becomes $-\sum_{i=0}^{J-1} p_i^{(1)} \ln p_i^{(1)}$, that corresponds to the well-known Shannon entropy formula. Furthermore, mutual information is symmetric, *i.e.* $MI^{(1,2)} = MI^{(2,1)}$.

Being a particular case of a Kullback-Leibler divergence [Cover and Thomas, 1991], mutual information measures how the true joint probability distribution $p^{(1,2)}$ is different from the joint probability distribution of independent sub-systems.

To increase the saliency of interdependence detection, common approaches are the computation of mutual information on relatively time lagged time series [Kantz and Schreiber, 2004], or on an extended space, by delay embedding of the time series [Quian Quiroga et al., 2002]. The use of embedded data, whose meaning will be illustrated in the next section, leads to the difficult task of estimating higher dimensional probability distributions with fewer data. Generally, when the number of available samples L is relatively small, the naive definition $p_i = m_i/L, \forall i$ may indeed not be a good estimate of the true (unknown) probability distribution of the process under consideration[8]. In literature, some corrections terms have been introduced [Grassberger, 1988, Roulston, 1999], however, the probability estimation through correlation sum have been proved to give more accurate results [Prichard and Theiler, 1995]. Recently, a new *ad hoc* class of improved estimators for mutual information, based on k-nearest neighbor distances, has been introduced [Kraskov et al., 2004].

2.3.3 State-space approach

Another interesting approach going beyond second order correlation is an approach based on topological properties of the network state-space. For instance, the approximate repetition of a state, that is called *recurrence* [Eckmann et al., 1987], may be exploited. A

[8] The naive estimate converges to the true probability distribution when $L \to \infty$ and all bin sizes tend to zero. We mention that the bin size does not need to be the same for all bins. Optimized estimators using adaptive bin sizes exist.

recurrence is the return of the trajectory in state-space to a neighborhood of a point (a state) where it has been before[9]. Trivially, a purely deterministic system on a fixed point is recurrent for all times. In an analog system on a limit cycle, each point returns exactly to itself after one revolution.

This rather intuitive concept can be used to formalize an interdependence measure by considering a joint recurrent space of the two sub-systems [Romano et al., 2005]. This idea has been only recently formalized in an interdependence index [Romano et al., 2006].

However, the traditional rationale behind state-space based interdependence measures arises from generalized synchronization. As previously stated, two sub-systems are general-like synchronized if $\theta^{(1)}(t) = H\left(\theta^{(2)}(t)\right)$, where H is bijective. From the existence of H, it follows that close states of one sub-system will typically be mapped to close states of the other sub-system.

Several interdependences estimators based on this property are available in literature: method of mutual false nearest neighbors [Rulkov et al., 1995], index of mutual predictions [Schiff et al., 1996, Wiesenfeldt et al., 2001], index of similarity [Le Van Quyen et al., 1999], synchronization likelihood [Stam and van Dijk, 2002] "nonlinear interdependences" indices [Arnhold et al., 1999, Quian Quiroga et al., 2000].

However, we note that the first step to apply these methods is the reconstruction of the sub-systems state-space. Indeed, when dealing with real data, the first problem to face is the only indirect observation of the true state-space, as previously introduced in Eq. (2.5). Therefore, the measured time series have to be converted into state vectors. This is the important problem of *state-space reconstruction* or state-space embedding. Fortunately, a reconstruction of the original state-space is not really necessary for data analysis but it is sufficient to construct a new space such that the attractor in this space is topologically equivalent to the original one [Whitney, 1936, Sauer et al., 1991]. The way to find such a space is through the technique of time delay embedding [Takens, 1981, Sauer et al., 1991]. In practice, a delay reconstruction of a scalar measurement, *e.g.* $y_t^{(1)}, \forall t$, in $n^{(1)}$ dimensions is given by the vectors $x_t^{(1)} \in \mathbb{R}^{n^{(1)}}$

$$x_t^{(1)} = \left[y_{t-\left(n^{(1)}-1\right)\tau^{(1)}}^{(1)}, y_{t-\left(n^{(1)}-2\right)\tau^{(1)}}^{(1)}, \ldots, y_{t-\tau^{(1)}}^{(1)}, y_t^{(1)} \right].$$

We remark that, in general, $n^{(1)} \neq d^{(1)}$. The time difference $\tau^{(1)}$ between adjacent components of the delay vectors is referred to as the *lag* or *delay time*. When starting to analyze time series, these two parameters $\tau^{(1)}$ and $n^{(1)}$ are usually unknown. However, embedding theorems guarantee their existence (at least for ideal noise free data). In nonlinear time series analysis, for the case of purely deterministic systems, common and well-established approaches to estimate good embedding parameters are: first zero of autocorrelation function [Kantz and Schreiber, 2004] or first minimum for time delayed mutual information [Fraser and Swinney, 1986] for the time lag and the method of false nearest neighbors [Kennel et al., 1992, Hegger and Kantz, 1999, Boccaletti et al., 2002b] for the embedding dimension. For stochastic nonlinear systems these methods might not work, and other strategies may be advisable [Kantz and Schreiber, 2004].

Throughout this thesis, as representant of this approach, we have used the estimator H, that in [Quian Quiroga et al., 2000] has shown to be robust to observational noise intensity.

Let us suppose to have reconstructed the vectors $x_t^{(1)} \in \mathbb{R}^{n^{(1)}}$ and $x_t^{(2)} \in \mathbb{R}^{n^{(2)}}$, $t = 0, \ldots, l-1$, from time series measured in the two sub-systems (1) and (2), where $l =$

[9] Such recurrences exist in the state-space for all types of motion which are not transient.

$\min\left(l^{(1)}, l^{(2)}\right)$ and $l^{(i)}, i = 1, 2$ are the number of samples available for sub-system (i) after embedding. Furthermore, let us consider a neighborhood of $x_t^{(2)}$ containing the k closest[10] neighbors of $x_t^{(2)}$ and let us denote their generic time indices as $s_{t_j}, j = 1, \ldots, k$. If some relation exists between the two sub-systems, we can check whether delay vectors $x_{s_{t_j}}^{(1)}$ with the same indices $s_{t_j} \in \{s_{t_1}, \ldots, s_{t_k}\}$ are closer to $x_t^{(1)}$ than an average randomly chosen $x_{t'}^{(1)}, t' \notin \{t, s_{t_1}, \ldots, s_{t_k}\}$ vector. Along this line, the H estimator estimates the interdependence of sub-system (1) on sub-system (2) as

$$H^{(1,2)} = \frac{1}{l} \sum_{t=0}^{l-1} \log \frac{q_t^{(1)}}{q_t^{(1,2)}}. \tag{2.10}$$

This formula compares the average conditional distance

$$q_t^{(1,2)} = \frac{1}{k} \sum_{s_{t_j} \in \{s_{t_1}, \ldots, s_{t_k}\}} \left(x_t^{(1)} - x_{s_{t_j}}^{(1)}\right)^2, \tag{2.11}$$

to the mean squared distances to random points, *i.e.*

$$q_t^{(1)} = \frac{1}{l-1} \sum_{i \neq t} \left(x_t^{(1)} - x_i^{(1)}\right)^2, \tag{2.12}$$

and averages over all reconstructed state vectors.

Clearly, this quantity is asymmetric, *i.e.* $H^{(2,1)} \neq H^{(1,2)}$, and allows the quantification of the direction of an interaction. However, H might also reflect similar dynamical properties of each sub-system and not only their interaction [Arnhold et al., 1999]. If the sub-systems are independent, then $q_t^{(1,2)} \approx q_t^{(1)}$, so $H^{(1,2)} \simeq 0$. If the systems are inter-related, then $q_t^{(1,2)} < q_t^{(1)}$ and $H^{(1,2)}$ is positive but, *a priori*, a maximum value can not be defined.

2.3.4 Phase approach

An interesting approach to quantify interdependences between interacting sub-systems consists in the comparison of their phase angles. This is appealing because, as previously described in Sec. 2.2.3, phase synchronization phenomena may imply synchronized phases associated with uncorrelated amplitudes.

Obviously, the first step to study phase dynamics is to extract the phase from the observed time series [Pikovsky et al., 2001]. Several techniques are available to do the job. It can be done in a rather *ad hoc* geometric way, or it can be done by a transformation such as the Hilbert[11] or wavelet transform of the signals [Rosenblum et al., 1996, Lachaux et al., 1999], or it can be done by a suitable interpolation in between maxima of the signals [Pikovsky et al., 2001].

Let us suppose to have estimated the phases $\phi_t^{(1)}$, $\phi_t^{(2)}$, $t = 0, \ldots, L-1$, for the sub-systems (1) and (2), respectively. To detect generic $n : m$ phase lockings in noisy systems, we can look at the appearance of peaks in the distribution of the difference of the

[10] For exemplum, close in an Euclidean sense.

[11] Given a scalar time continuous signal $y(t)$, its estimated instantaneous phase $\phi(t)$ may be computed as $\phi(t) = \arctan\left(\frac{y_H(t)}{y(t)}\right)$, where $y_H(t)$ is the Hilbert transform of the signal. For discrete time signals, the Hilbert transform can be calculated from Fourier transform [Pikovsky et al., 2001].

unwrapped phases $\phi_t^{(1,2)} = n\phi_t^{(1)} - m\phi_t^{(2)}$, $\forall t$ [Tass et al., 1998]. Hence, an interdependence index can be defined [Mormann et al., 2000, Rosenblum et al., 2001] as

$$\gamma^{(1,2)} = \left| \frac{1}{L} \sum_{t=0}^{L-1} e^{\left(i\phi_t^{(1,2)}\right)} \right|^2 \tag{2.13}$$

In Fig. 2.2 we plot the phases on the unit circle, and not on the real line, to facilitate a geometric interpretation of this formula. The radius $r^{(1,2)}$ measures the (time) average phase coherence, and $\psi^{(1,2)}$ is the (time) average phase, *cf.* Fig. 2.2. For instance, if all the realizations of the relative phase $\phi^{(1,2)}$ move in a single tight clump, we have $r^{(1,2)} \approx 1$. On the other hand, if the realizations are scattered around the circle, then $r^{(1,2)} \approx 0$. Consequently, by construction, $\gamma^{(1,2)} = \left(r^{(1,2)}\right)^2$ is zero if the phases are independent ($\phi_t^{(1,2)}$ has an uniform distribution) and is one if the phase difference is constant (perfect phase synchronization). Furthermore, $\gamma^{(1,2)}$ is symmetric and, importantly, is parameter free. However, because $\gamma^{(1,2)}$ may underestimate interdependence strength[12], another more salient index may be defined from the Shannon entropy of the distribution of $\phi^{(1,2)}$ [Tass et al., 1998].

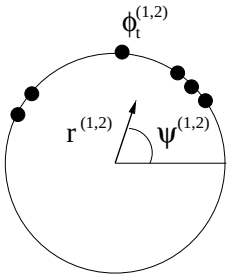

Fig. 2.2. Geometric interpretation of the order parameter Eq. (2.13). The phases $\phi_t^{(1,2)}$ are plotted on the unit circle. Their centroid is given by the complex number $r^{(1,2)}e^{\left(i\psi^{(1,2)}\right)}$, shown as an arrow.

Finally, it is common practice to check if the signals to be analyzed have a broadband or a multi-modal spectrum. In that case, the definition of a phase may be troublesome and some pre-filtering (not introducing phase distortions) of the signals might be necessary.

[12] When the distribution of $\phi^{(1,2)}$ is multi-modal, the phases, though locked, can cancel in the time average of Eq. (2.13) giving a low value of $\gamma^{(1,2)}$. This corresponds to the case where the phase difference remains fairly stable but occasionally jumps between different values [Zaks et al., 1999]. A multi-modal distribution of the phases can also appear if we look, *e.g.* , for a $1:1$ synchronization but the real relationship is $1:2$.

3

Assessing Cooperativeness in Dynamical Networks: the S Estimator

Brief — This chapter describes a new estimator of cooperativeness and validation tests by using prototypical models of networks and network topologies. Sensitiveness upon noise and amount of data and comparison with other methods are also given. The estimator has been firstly proposed by [Wackermann, 1996], We thank Dr. U. Feldmann for having introduced us to this estimator.
Personal Contribution — Our original ideas about the S estimator are: the interpretation of the S estimator in terms of a shrink in a embedded state-space; the extension of the S estimator to delay-embedded data; the normalization of the S estimator for delay-embedded data and the possibility to apply it to communities of sub-systems. The numerical validation of the S estimator is also a new piece of work.

3.1 Motivation

The last decade has witnessed the birth of a new movement of interest and research in the study of the behavior of *complex networks*[1]. Such networks can be characterized by an irregular structure as, *e.g.* , the small-world [Watts and Strogatz, 1998] and scale-free topologies [Barabási and Albert, 1999], or by a structure dynamically evolving in time [Dorogovtesev and Mendes, 2003], and by units that may exhibit nonlinear dynamics [Strogatz, 2001]. One important and peculiar characteristic of networks is the collective behavior of their units or some cluster of them, *i.e.* the phenomenon of cooperativeness among the constituent units due to their interactions.

In general, as introduced in the previous chapter, the inference of cooperativeness phenomena from experimental observations is related to the estimation of the interdependences among the measured signals. This means that to estimate the amount of cooperativeness within the network under consideration, we have to compute the amount of interdependences within the available set of recorded signals. By following the model composed of Eqs. (2.4), (2.5) and (2.6)[2], we have to estimate *multivariate*[3] interdependences, *i.e.* interdependences within a set of $P \geq 2$ measurements. To this purpose, as

[1] The word "complex" has been the subject of various epistemological debates [Goldenfeld and Kadanoff, 1999]: in one characterization, a complex system is one whose evolution is very sensitive to initial conditions or to small perturbations, one in which there are multiple pathways by which the system can evolve. A second characterization is more informal, *i.e.* the word complex quantifies the difficulties we have in describing or understanding the system.
[2] Again, we assume that $P = M$, and one time series from each observed sub-system, *cf.* Eq. (1.6).
[3] The word bivariate is used for $P = 2$.

illustrated in Chapter 2, four main approaches exist in time series analysis: the linear approach, the information theory based approach, the state-space approach and the phase dynamics approach.

Regarding the information theory based approach, mutual information naturally extends to a multivariate form. Indeed, once estimated a probability distribution $p_i, i = 1, \ldots, J$ for each sub-system, the estimated mutual information of the P sub-systems is given by

$$MI^{(1,2,\ldots,P)} = \sum_{i=0}^{J-1} \sum_{j=0}^{J-1} \cdots \sum_{q=0}^{J-1} p_{i,j,\ldots,q}^{(1,2,\ldots,P)} \ln \frac{p_{i,j,\ldots,q}^{(1,2,\ldots,P)}}{p_i^{(1)} p_j^{(2)} \cdots p_q^{(P)}} \tag{3.1}$$

Unfortunately, this quantity would be hard to estimate from experimental data that are, generally, of finite length. Indeed, a good estimate of high dimensional probability distribution would require incredibly long time series and heavy computational load. The situation would even worse in the case a delay embedding of the time series would be performed.

Regarding the state-space approach, most of the estimators introduced in literature are intrinsically bivariate and their extension to a multivariate setting is not straightforward. Recently, advances in recurrence plot analysis seem to be very promising [Romano et al., 2005].

Within the phase approach, a multivariate interdependence estimator can be defined via the complex order parameter, a quantity introduced in [Kuramoto, 1984] to visualize the dynamics of the phases in an ensemble of globally coupled nearly identical limit cycle oscillators. The estimated complex *order parameter* is given by

$$r_t^{(1,2,\ldots,P)} e^{\left(i\psi_t^{(1,2,\ldots,P)}\right)} = \frac{1}{P} \sum_{j=1}^{P} e^{\left(i\phi_t^{(j)}\right)} \tag{3.2}$$

and it is a macroscopic quantity that can be interpreted as the collective rhythm produced by the whole population of P sub-systems. It corresponds to the centroid of the phases. The radius $r_t^{(1,2,\ldots,P)}$ measures the phase coherence, and $\psi_t^{(1,2,\ldots,P)}$ is the average phase at time t, *cf.* Fig. 3.1. For instance, if all the sub-systems move in a single tight clump,

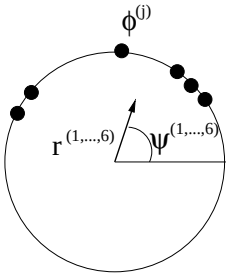

Fig. 3.1. Geometric interpretation of the order parameter in Eq. (3.2). The phases $\phi^{(j)}$ are plotted on the unit circle. Their centroid is given by the complex number $r^{(1,2,\ldots,6)} e^{\left(i\psi^{(1,2,\ldots,6)}\right)}$, shown as an arrow.

we have $r_t^{(1,2,\ldots,P)} \approx 1$ and the population acts like a giant oscillator. On the other hand, if the sub-systems are scattered around the circle, then $r_t^{(1,2,\ldots,P)} \approx 0$; the individual oscillations add incoherently and no macroscopic rhythm is produced.

A straightforward measure of the amount of interdependences within the P sub-systems is given by the time average of the radius, *i.e.* the modulus of the order parameter

$$Op^{(1,2,\ldots,P)} = \frac{1}{L}\sum_{t=0}^{L-1} r_t^{(1,2,\ldots,P)}. \tag{3.3}$$

Unfortunately, the difficulty of this approach relies on the definition of the phase. For a pure sine wave signal the notion of phase is obvious and trivial, provided the sampling rate is high enough. For a non-periodic signal a unique definition of phase is lacking [Boashash, 1992, Cohen et al., 1999, Cohen and Loughlin, 2003], although most researchers believe that it has a decent common sense definition. This can lead to ambiguous situations when trying to extract the phase for broad-band signals.

In this thesis, we propose a linear approach to *express* the amount of cooperativeness within M interacting sub-systems. This has the potential advantage of lower computational complexity and can be applied to a wide range of signals. The way we propose to *measure* the cooperativeness has been firstly proposed by [Wackermann, 1996, Stancak and Wackermann, 1998].

3.2 The *S* estimator

We start from the model composed of Eqs. (2.4), (2.5) and (2.6). We have available P time series, one from each dynamical sub-system under study, and we denote them by $\mathbf{Y} = \{Y_t\}$, $t = 0, \ldots, L-1$, where $Y_t \in \mathbb{R}^P$ is the t-th sample observation vector and L is the number of available samples. Without loss of generality, we can consider $\mathbf{Y}$ as de-trended to zero mean and normalized to unitary variance.

Let us consider the $P \times P$ estimated zero-lag correlation matrix[4] of the time-series

$$\mathbf{C} = \frac{1}{L-1}\sum_{t=0}^{L-1} Y_t^T Y_t \ , \tag{3.4}$$

with elements $\rho^{(i,i)} = 1$ and $\rho^{(i,j)} = \rho^{(j,i)}$, $i \neq j$, *i.e.* the correlation between the i-th and j-th time series. Let $\lambda^{(i)\prime} = \frac{\lambda^{(i)}}{P}$ be the normalized eigenvalues[5] of $\mathbf{C}$, the entropy-like quantity

$$I = -\sum_{i=1}^{P} \lambda^{(i)\prime} \log\left(\lambda^{(i)\prime}\right) \tag{3.5}$$

is a measure inversely proportional to the amount of interdependences between the P time series[6].

Indeed, it can be interpreted as a deviation from mutual orthogonality (lack of correlation) between the P signals. Let us suppose that all eigenvalues are equal. Then, it is to verify that $I = \log(P)$. Under this case, $\mathbf{YY}' = \mathbf{V}'\mathbf{IV}$, where $\mathbf{V}$ is a $P \times P$ unitary matrix of orthonormal eigenvectors of $\mathbf{YY}'$. Being $\mathbf{V}'\mathbf{IV} = \mathbf{V}'\mathbf{V} = \mathbf{I}$, $\mathbf{YY}' = \mathbf{I}$. This means that the rows of $\mathbf{Y}$ are orthonormal. Hence, we have shown that $I = \log(P)$ in the case of P uncorrelated signals. For the case of one eigenvalue equal to P and all the others zero and consequently $I = 0$, it can be similarly verified that the signals are perfectly correlated.

[4] In the field of statistics, this estimator is called the Pearson estimator of the correlation matrix.

[5] $\sum_{i=1}^{P} \lambda^{(i)} = trace(\mathbf{C}) = P$

[6] We will assume through this thesis that $0 \cdot \log(0) = 0$.

Furthermore, I may be seen as a measure of the difference in the distribution of the normalized eigenvalues. Indeed, in the case of P uncorrelated signals, $\mathbf{C} = \mathbf{I}$, the normalized eigenvalues are all equal (uniform distribution), *i.e.* $\lambda^{(i)'} = \frac{1}{P}, \forall i$, and I is equal to $\log(P)$. In the case of perfectly correlated identical signals, $\mathbf{C}$ has one unitary normalized eigenvalue and all the others zero (peaky distribution), and I is equal to 0. To have a measure proportional to the amount of interdependences, we can simply rearrange Eq. (3.5) as

$$S^{(1,2,\ldots,P)} = 1 - \frac{I}{\log(P)}, \tag{3.6}$$

which is 0 for uncorrelated signals and 1 for completely correlated ones.

Finally, we can outline an interesting and important property of the S estimator: the *rotational invariance*. This property is inherited from the eigenvalues of real symmetric matrices, as, for instance, correlation matrices are. Indeed, any symmetric matrix whose entries are real can be diagonalized by an orthogonal matrix. More explicitly: to every symmetric real matrix $\mathbf{C}$ there exists a real orthogonal matrix $\mathbf{Q}$ such that $\mathbf{D} = \mathbf{Q}^T\mathbf{A}\mathbf{Q}$ is a diagonal matrix. Every symmetric matrix is thus, up to choice of an orthonormal basis, a diagonal matrix.

3.2.1 The S estimator for embedded data

In the previous section, we have defined the S estimator directly from the measured time series. In principle, if we are measuring from a deterministic dynamical network, we may account for its state-space trajectory in the computation of the estimator. Indeed, we may reconstruct, through embedding, the trajectory of the dynamical phenomena under observation from the time series and then compute the S estimator by Eq. (3.6) in that extended space. However, in this case a normalizing step is necessary.

Given, for the sake of simplicity, two time series ($P = 2$), for which delay times ($\tau^{(1)}$ and $\tau^{(2)}$) and embedding dimensions ($n^{(1)}$ and $n^{(2)}$) have been estimated [Kantz and Schreiber, 2004], we can consider the embedded multivariate trajectory $\mathbf{X} = \{x_t\}_{t=0,\ldots,l}$[7], where $x_t \in \mathbb{R}^{\left(n^{(1)}+n^{(2)}\right)}$, l is the minimum number of samples available after the two reconstructions, and

$$x_t = \left[\underbrace{y^{(1)}_{t-\left(n^{(1)}-1\right)\tau^{(1)}}, \ldots, y^{(1)}_t}_{x^{(1)}_t} , \underbrace{y^{(2)}_{t-\left(n^{(2)}-1\right)\tau^{(2)}}, \ldots, y^{(2)}_t}_{x^{(2)}_t} \right].$$

The corresponding estimated correlation matrix can be block partitioned to highlight the contribution of the two systems, *i.e.*

$$\mathbf{C} = \begin{bmatrix} \mathbf{C}^{(1,1)} & \mathbf{C}^{(1,2)} \\ \mathbf{C}^{(1,2)^T} & \mathbf{C}^{(2,2)} \end{bmatrix}, \tag{3.7}$$

where the $n^{(i)} \times n^{(i)}$ matrices $\mathbf{C}^{(i,i)}$, $i = 1, 2$, collect the *intra-sub-system* correlation terms, *i.e.* the correlation between state-variables of the same sub-system, while the

[7] In literature, this state-space has been formally introduced with the term "*mixed state-space*" in [Wiesenfeldt et al., 2001]

$n^{(1)} \times n^{(2)}$ matrix $\mathbf{C}^{(1,2)}$ collects the *inter-sub-system* correlation terms, which are the interdependences in our interest.

To correctly estimate the *inter-dependence* between the two sub-systems, independently of the *intra-dependences*, we proceed through a suitable linear transformation of the reconstructed state space trajectory $\mathbf{X}$ which reduces the $\mathbf{C}^{(i,i)}$ to identity matrices; in other words, we intra-orthogonalize the state variables of the two sub-systems. As a result of the transformation, the estimated correlation matrix for the transformed trajectory will have non-zero off-diagonal elements only within the *inter-dependence* block $\mathbf{C}^{(1,2)}$.

The transformation is given by

$$\mathbf{Z} = \left[\mathbf{Z}^{(1)}\ \mathbf{Z}^{(2)}\right] = \left[\mathbf{X}^{(1)}\ \mathbf{X}^{(2)}\right] \begin{bmatrix} \mathbf{T}^{(1)} & \mathbf{0} \\ \mathbf{0} & \mathbf{T}^{(2)} \end{bmatrix} = \mathbf{X}\mathbf{T}, \tag{3.8}$$

with $\mathbf{T}^{(1)} = \mathbf{C}^{(1,1)^{-\frac{1}{2}}}$ and $\mathbf{T}^{(2)} = \mathbf{C}^{(2,2)^{-\frac{1}{2}}}$, *i.e.* the principal square root matrices of $\mathbf{C}^{(1,1)^{-1}}$ and $\mathbf{C}^{(2,2)^{-1}}$, respectively, where the inverses are guaranteed to exist if an appropriate embedding is performed[8]. Clearly, the estimated correlation matrix for the $\mathbf{Z}$ trajectory turns out to be

$$\mathbf{R} = \begin{bmatrix} \mathbf{I} & \mathbf{T}^{(1)^T}\mathbf{C}^{(1,2)}\mathbf{T}^{(2)} \\ \mathbf{T}^{(2)^T}\mathbf{C}^{(2,1)}\mathbf{T}^{(1)} & \mathbf{I} \end{bmatrix} = \begin{bmatrix} \mathbf{I} & \mathbf{R}^{(1,2)} \\ \mathbf{R}^{(1,2)^T} & \mathbf{I} \end{bmatrix}, \tag{3.9}$$

which can then be used, through Eq. (3.5), to correctly quantify the interdependence between the two sub-systems. If the two sub-systems are uncorrelated, $\mathbf{R}^{(1,2)} = \mathbf{0}$, $\mathbf{R}$ will be diagonal, and $I = log\left(n^{(1)} + n^{(2)}\right)$, while if the two sub-systems are "identical"[9], it can be verified that $\mathbf{R}^{(1,2)}$ will have ones on the main diagonal and zeros elsewhere. Under this case the entropy of the normalized eigenvalues will depend on the embedding dimensions ($n^{(1)}$ and $n^{(2)}$). We do not have a closed form formula to compute it; though, it can be easily computed numerically and we denote with I_{min} its value. Knowing the extremes, we can finally rearrange Eq. (3.5) as

$$S^{(1,2)} = \frac{log\left(n^{(1)} + n^{(2)}\right) - I}{log\left(n^{(1)} + n^{(2)}\right) - I_{min}}, \tag{3.10}$$

getting a measure proportional to the amount of interdependences and ranging from 0 to 1. Clearly, this procedure can be extended to estimate the whole cooperativeness within M interacting dynamical sub-systems.

3.2.2 The S estimator and synchronization

In this section, we propose a qualitative interpretation of the S estimator as a measure of synchronization. To do that, we need to introduce a general definition of synchronization, though, as stated in the previous chapter, a standard, unique, rigorous definition does not exist in literature and particular definitions are adopted according to the application or the investigations considered [Brown and Kocarev, 2000]. Following [Brown and Kocarev, 2000], we define as synchronization a process whereby two (or many) dynamical

[8] Furthermore, we remark that the square root of a matrix is unique for matrices whose eigenvalues have nonnegative real part. This is the case for our correlation matrices.

[9] In this case the matrix $\mathbf{C}$ has all the elements equal to one.

sub-systems adjust some of their time-varying properties to a common behavior due to coupling or external forcing. More precisely, considering a large stationary, deterministic, finite dimensional time continuous dynamical system, which can be divided into two $d^{(1)}$ and $d^{(2)}$ dimensional sub-systems, respectively

$$\begin{cases} \dot{\theta}^{(1)}(t) = f^{(1)}\left(\theta^{(1)}(t), \theta^{(2)}(t)\right), \\ \dot{\theta}^{(2)}(t) = f^{(2)}\left(\theta^{(1)}(t), \theta^{(2)}(t)\right). \end{cases} \tag{3.11}$$

we say that the two sub-trajectories $\theta^{(1)}(t) \in \mathbb{R}^{d^{(1)}}$ and $\theta^{(2)}(t) \in \mathbb{R}^{d^{(2)}}$ of the whole system are synchronized with respect to the properties (time dependent measures) $g^{(1)}$ and $g^{(2)}$

$$\begin{cases} g^{(1)} : \mathbb{R}^{d^{(1)}} \otimes \mathbb{R} \to \mathbb{R}^k, \\ g^{(2)} : \mathbb{R}^{d^{(2)}} \otimes \mathbb{R} \to \mathbb{R}^k \end{cases} \tag{3.12}$$

$k \leq min\left(d^{(1)}, d^{(2)}\right)$, if there is a time independent mapping $h : \mathbb{R}^k \otimes \mathbb{R}^k \to \mathbb{R}^k$ such that

$$\left\| h\left[g^{(1)}\left(\theta^{(1)}\right), g^{(2)}\left(\theta^{(2)}\right)\right] \right\| = 0 \tag{3.13}$$

where $\|\bullet\|$ is any norm in $\mathbb{R}^k$. As explained in [Brown and Kocarev, 2000], this unifying definition covers most kinds of usually considered synchronization, such as identical synchronization, phase synchronization, and generalized synchronization. In brief, condition in Eq. (3.13) requires a property $\left(g^{(1)}\right)$ of the trajectory $\theta^{(1)}(t)$ to be in a fixed relation (h) with another property $\left(g^{(2)}\right)$ of the trajectory $\left(\theta^{(2)}\right)$. As an example, let us consider two periodic trajectories (not necessarily equal) with the same frequency: they are synchronized according to condition in Eq. (3.13) if we assume $g^{(1)}$,$g^{(2)}$ to be the frequency and $h = g^{(1)} - g^{(2)}$. Actually, Eq. (3.13) implies that synchronized sub-trajectories lay on an r-dimensional manifold, where r depends on h and is $1 \leq r \leq k$. Consequently, the dimensionality of synchronized dynamics $\left(d^{(1)} + d^{(2)} - r\right)$ results to be smaller than that of the generic asynchronous dynamics $\left(d^{(1)} + d^{(2)}\right)$ in the whole system [Brown and Kocarev, 2000, Boccaletti et al., 2002a]. In other words, let us consider two independent dynamical sub-systems (1) and (2), whose state-spaces are of dimension $d^{(1)}$ and $d^{(2)}$, respectively. The compound system obtained considering the two systems together has dimension $d^{(1)} + d^{(2)}$. However, the embedding dimension of the dynamics of the compound system turns out to be smaller than $d^{(1)} + d^{(2)}$ when the two sub-systems are synchronized. For instance, two identically synchronized 2-dimensional periodic oscillators have dimension of the whole state-space 4, but the embedding dimension of the synchronized dynamics is only 2.

Exploiting what has just been discussed, we suggest that the S estimator quantifies the amount of synchronization within a data set by intrinsically comparing the actual dimensionality of the set with the expected full dimensionality of the asynchronous set.

To illustrate this in a easy to understand way, we start by assuming to have time series from the two sub-systems (1) and (2) and that we have reconstructed their trajectories $x_t^{(1)} \in \mathbb{R}^{n^{(1)}}$ and $x_t^{(2)} \in \mathbb{R}^{n^{(2)}}$, respectively. Being the correlation matrix $\mathbf{C}$ (of the compound trajectories) square and symmetric, its eigenvalues equal its singular values. Furthermore, we know that the singular values decomposition of $\mathbf{C}$ gives a set of orthonormal eigenbases of $\mathbf{C}$, which correspond to a transformed coordinate system[10] of

[10] In Principal Component Analysis (PCA) this new coordinate system is used to compute the so-called population of principal components. Indeed, when performing PCA, a given multivariate time series is

the original embedded coordinates $\left[x^{(1)}, x^{(2)}\right]$. In the linear sub-spaces spanned by these new bases, each normalized singular value plays the role of giving the relative importance of the corresponding sub-space[11]. This has an important consequence when evaluating the entropy of the eigenvalues of $\mathbf{C}$. Indeed, let us consider the two opposite cases, the case in which the two sub-systems are not synchronized and the case in which they are synchronized. As shown in Fig. 3.2, if the two sub-systems are not synchronized, all the sub-spaces of the embedded compound system will be important, giving an uniform distribution of the eigenvalues and, then, a high value of the entropy of the eigenspectrum. If the two sub-systems get synchronized, the compound system gets shrunk in the embedded state-space, so fewer sub-spaces will be important, the distribution of the eigenvalues will be peaky [12] and, then, the entropy of the eigenspectrum will have a low value.

This interpretation can be extended to the more general case of M interacting sub-systems.

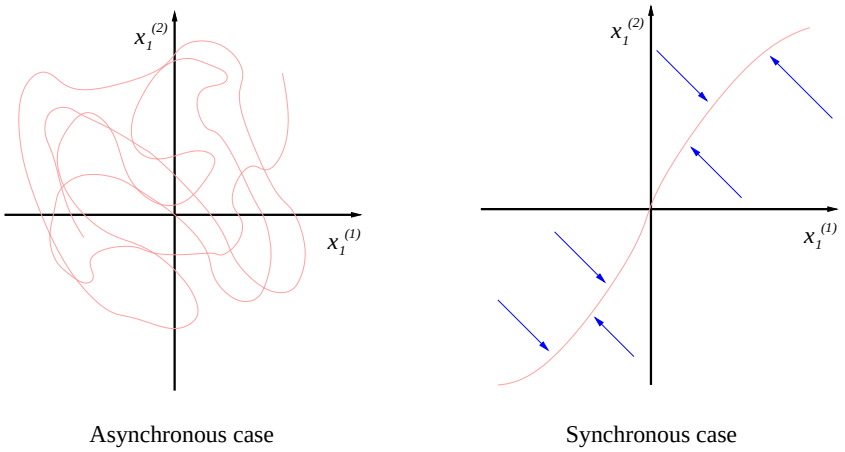

Fig. 3.2. Projection of the trajectory of the two sub-systems onto a bi-dimensional sub-space of the embedded compound state-space. $x_1^{(1)} \in \mathbb{R}$ and $x_1^{(2)} \in \mathbb{R}$ are the corresponding components. In the case the two sub-systems are independent, the trajectory fills or explores all the two-dimensional sub-space. In the case of synchrony, the trajectory gets confined in a shrunk sub-space.

3.3 Numerical Validation

In this section we proceed to the numerical assessment of the properties and performances of the S estimator. More precisely, we want to test its dependence upon the degree of cooperativeness in a measured dynamical network.

From a theoretical point of view, research has been done and is on the way to understand and unravel the principles underlying the propensity of a dynamical network to synchronize, the so-called synchronizability [Kuramoto, 1984, Barahona and Pecora, 2002, Chavez et al., 2005]. Most studies agree that the ability of a given network to

transformed into the principal components by a linear transformation that projects the original time series into the eigenbase of the correlation matrix of the time series itself [Joliffe, 2002]

[11] Here, importance is meant in terms of the justification of the variance of the projection of the original trajectory onto the corresponding sub-space component.

[12] For completely synchronized identical sub-systems, the line in Fig. 3.2 would be a straight line and all the eigenvalues would be zero except the one corresponding to the sub-space spanned by the straight line.

synchronize is strongly ruled by the structure of connections, *i.e.* topology and weight [Boccaletti et al., 2006]. Consequently, we proceed to the validation of S as following: 1) we test its dependence upon the coupling strength for two nonlinear noise-driven dynamical sub-systems; 2) we test its dependence upon the average connectivity degree in a network of 128 noise-driven nonlinear dynamical sub-systems. We have chosen this size of the network because it represents the state-of-art in modern experimental setups [Evans, 1996, Knyazeva et al., 2002, Santucci et al., 2005].

Moreover, we compare the performance of the S estimator with other measures of interdependences and we assess its sensitiveness to observational noise intensity, modeling noise intensity and amount of data.

3.3.1 Cooperativeness by coupling strength

In order to assess the dependence of S upon the coupling strength, we first have considered a classical synchronization paradigm [Boccaletti et al., 2002a, Quian Quiroga et al., 2002]: two different nonlinearly coupled noise-driven dynamical sub-systems, that is, a Rössler chaotic oscillator [Rössler, 1976], nonlinearly driving a chaotic Lorenz one [Lorenz, 1963], as given by

$$\begin{cases} \dot{\theta}_1^{(1)} = T\left[\theta_2^{(1)} + \theta_3^{(1)} + \eta_1^{(1)}\right], \\ \dot{\theta}_2^{(1)} = T\left[\theta_1^{(1)} + a\theta_2^{(1)} + \eta_2^{(1)}\right], \\ \dot{\theta}_3^{(1)} = T\left[b + \theta_3^{(1)}\left(\theta_1^{(1)} - c\right) + \eta_3^{(1)}\right], \\ \dot{\theta}_1^{(2)} = \sigma\left(\theta_2^{(2)} - \theta_1^{(2)}\right) + \eta_1^{(2)}, \\ \dot{\theta}_2^{(2)} = \rho\theta_1^{(2)} - \theta_2^{(2)} - \theta_1^{(2)}\theta_3^{(2)} + \mathcal{C}^{(2,1)}\left(\theta_2^{(2)} - \theta_2^{(1)}\right)^3 + \eta_2^{(2)}, \\ \dot{\theta}_3^{(2)} = \theta_1^{(2)}\theta_2^{(2)} - \beta\theta_3^{(2)} + \eta_3^{(2)}, \end{cases} \tag{3.14}$$

where $\theta_j^{(1)}$, $\theta_j^{(2)}$, $j = 1, 2, 3$, are the state variables of the Rössler and Lorenz sub-systems, respectively; a, b, c, σ, β, and r are parameters that are fixed at the standard values, *i.e.* $a = 0.4$, $b = 0.4$, $c = 5.7$, $\sigma = 10$, $\beta = 8/3$, and $r = 28$; the $\eta_j^{(i)}$, $i = 1, 2$, $j = 1, 2, 3$, are zero-mean uncorrelated Gaussian modeling noises; the time scale $T = 6$ adapts the speed of the Rössler to that of the Lorenz; and, finally, the parameter $\mathcal{C}^{(2,1)}$ represents the strength of the diffusive nonlinear coupling between the two sub-systems. $\mathcal{C}^{(2,1)}$ is varied in the range $[0, 0.9]$, which represents a condition of strong coupling between the two sub-systems.

For every considered value of $\mathcal{C}^{(2,1)}$, the differential equations were iterated, starting from random initial conditions, using the Heun algorithm [Quarteroni et al., 2004] with $\delta t = 0.005$, the initial 10000 points of each transient were dropped and, by means of a down-sampling ($\delta T = 0.02$), time series of 500 points each were collected. We collected a total of 80 trials from different initial conditions, measuring the coupled variables $\theta_2^{(1)}$ and $\theta_2^{(2)}$, *i.e.* $\mathcal{G}(\Theta) = \begin{bmatrix} \theta_2^{(1)} \\ \theta_2^{(2)} \end{bmatrix}$. Here, and through the numerical validations in this thesis, we consider ideal measurement conditions, *i.e.* a direct measure of the state-variables, though we are aware that this may not be the case in common experimental setups.

However, the aim here is to evaluate the dependence of our S estimator upon coupling strength and we refer the discussion of measurement issues later on. We studied the capability of estimating the cooperativeness of the network depending on the amount of data available for two cases: in the first simulation study, we fixed the modeling noise at a small value[13], *i.e.* 40 dB SNR, and we varied the observational noise intensity, *i.e.* 40, 20, 12 dB SNR; in the second simulation study, we fixed the observational noise at a small value (*i.e.* 40 dB SNR) and we varied the modeling noise intensity, *i.e.* 20, 12, 6 dB SNR.

Finally, we present also a simulation study in which we assess the capability of the S estimator to measure cooperativeness between two sub-systems which not only differ in their structure but even in their dimension.

Amount of data vs. *observational noise intensity*

Here, we show the result of the assessment of the robustness of the S estimator with respect to measurement noise and data length. For each of the values of $\mathcal{C}^{(2,1)}$ and observational noise intensities, we computed it trial-wise over 20, 40, and all the 80 trials. Furthermore, to have a comparison, we computed four other interdependence measures. The estimators we considered were: the maximum of spectral coherence $Coh^{(1,2)}$, the mutual information $MI^{(1,2)}$, the estimator $H^{(2,1)}$, our estimator with embedded and not embedded data (which we will call $S^{(1,2)}$ and $Sne^{(1,2)}$, respectively) and the phase synchronization estimator [14] $\gamma^{(1,2)}$. Consequently, all the approaches to estimate interdependences are considered.

The mutual information $MI^{(1,2)}$, the $H^{(1,2)}$ estimator and the $S^{(1,2)}$ estimator were computed considering delay-embedded time series. More precisely, we delay-embedded the time series in 4-dimensional spaces using embedding delay $\tau^{(1)} = 0.28$ for the Rössler sub-system and $\tau^{(1)} = 0.24$ for the Lorenz sub-system. These delays were obtained through the minima of the self-information [Kantz and Schreiber, 2004]. The embedding dimensions were estimated by the method of false nearest neighbor [Boccaletti et al., 2002b] applied to time series measured from weakly coupled sub-systems, 40 dB (SNR) of observational and modeling intensity. We verified the consistency of our results even with other choices of this parameter, *i.e.* 3 and 5, and we had similar results[15].

The mutual information was computed using the algorithm presented in [Kraskov et al., 2004] with 15 neighbors, the $H^{(1,2)}$ estimator was computed using 15 neighbors and a Theiler window of 0.1[16].

Regarding the estimator $\gamma^{(1,2)}$, we computed the phases by using the Hilbert transform of the time series and we considered the $1:1$ phase difference. To compute coherence, we used the Welch method with 64 points for the FFT, a Hamming window and with an overlapping of 32 points.

The results are summarized in Figs. 3.3, 3.4. To a fairer comparison, Fig. 3.3 compares

[13] We set it to a variance of 1% of the energy of the right hand side along the uncoupled attractors.

[14] The Rössler and Lorenz systems have a well-defined phase [Pikovsky et al., 2001].

[15] We remark that the best choice would be an adaptive choice of the embedding dimension upon the coupling strength. For instance, for synchronized sub-systems (strong coupling) we would probably estimate one of the (minimum) embedding dimension equal to 2. Instead, for uncoupled sub-systems, we would estimate both (minimum) embedding dimensions equal to 3.

[16] The Theiler window is an expedient to remove points that are in a neighborhood of each reference point because of closeness in time and not because of common properties of the sub-systems [Theiler, 1990].

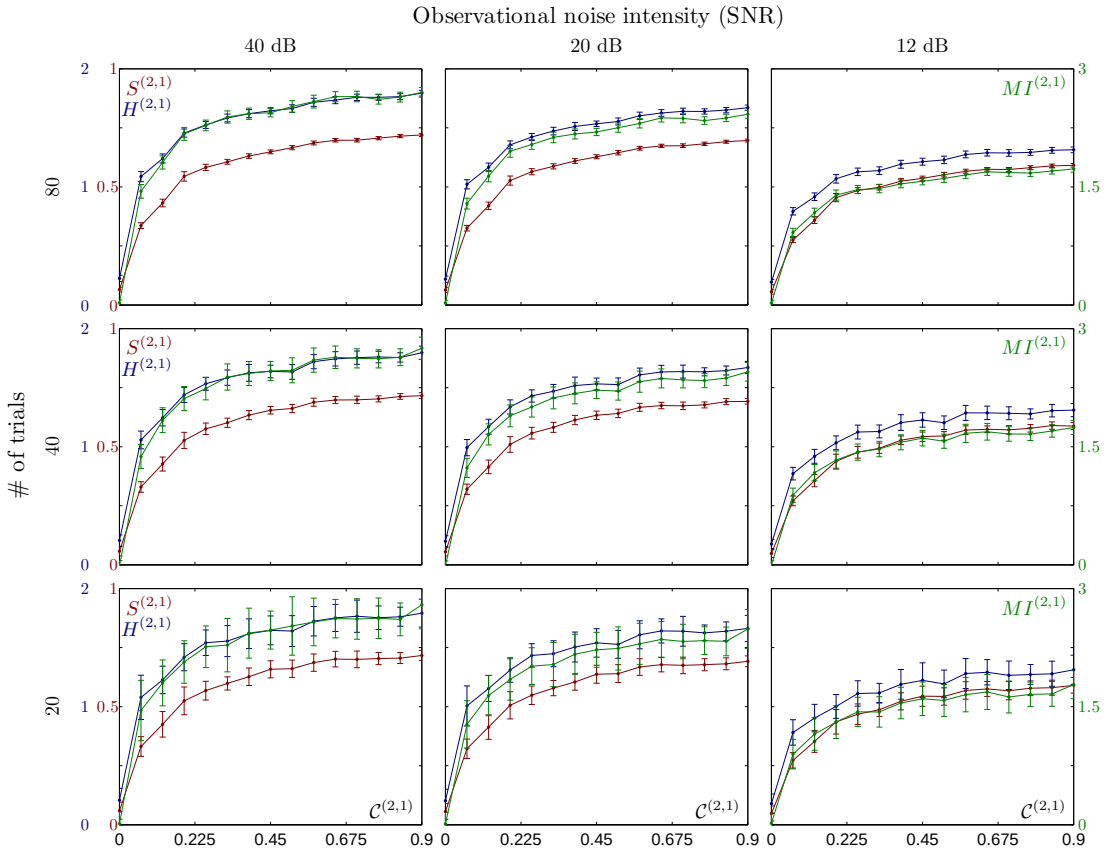

Fig. 3.3. Numerical assessment of the S estimator as a measure of cooperativeness given by coupling strength: sensitiveness upon observational noise intensity and data length; *case of embedded time series*. Dependence of the cooperativeness or synchronization between the sub-systems (1) and (2) of system Eq. (3.14), upon the coupling parameter $\mathcal{C}^{(2,1)}$, estimated with different techniques: $S^{(1,2)}$ (red); $MI^{(1,2)}$ (green); $H^{(2,1)}$ (blue). Robustness of the synchronization measures with respect to observational noise, considering 40, 20, and 12 dB Signal to Noise Ratio, and data lengths, considering 20, 40, and 80 trials of 500 samples each. The dots and errors bars illustrate the mean value and standard deviation, respectively.

the performance of the three cooperativeness estimators computed on the embedded state-space, whilst Fig. 3.4 compares the three estimator which do not require a state-space reconstruction.

The results in Fig. 3.3 show that $S^{(1,2)}$ scales similarly to the mutual information $MI^{(1,2)}$ and to the $H^{(2,1)}$ estimator upon the coupling parameter. For all the estimators, the computed values decrease when noise is increased; nevertheless, $S^{(1,2)}$ appears more robust since it decreases less than the others. Furthermore, as expected, the reliability of $S^{(1,2)}$ increases (*cf.* the error bars decrease) with data length, similarly to the other estimators. Finally, the reader should not be surprised by the fact that $S^{(1,2)}$ is not 1 for $\mathcal{C}^{(2,1)} = 0.9$ and that is not exactly zero for uncoupled sub-systems. Indeed, it would be one for synchronized structurally identical sub-systems, whilst in this case we have structurally different sub-systems. Furthermore, we are aware that in blind experimental setups it would be necessary a statistical determination of the condition of zero coupling, which is usually carried by surrogate techniques [Dolan and Neiman, 2002] when no explicit formulas are available [Dahlhaus, 2000]. However, this was not the aim of this numerical assessment.

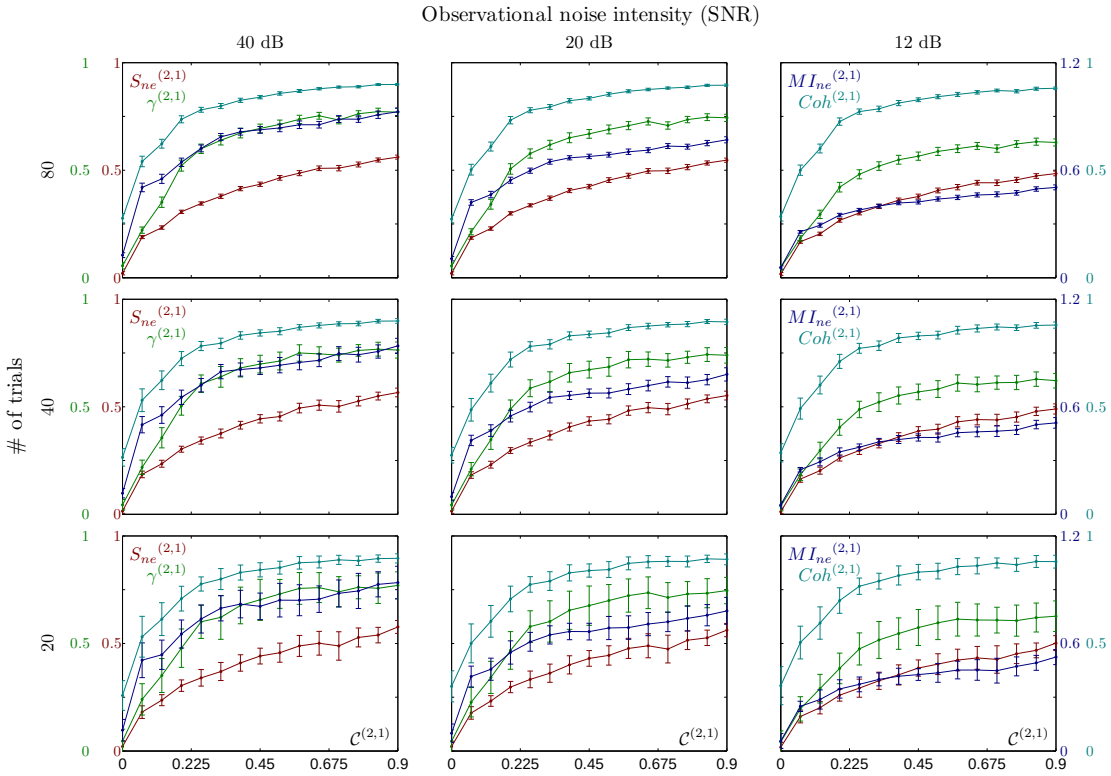

Fig. 3.4. Numerical assessment of the S estimator as a measure of cooperativeness given by coupling strength: sensitiveness upon observational noise intensity and data length; *case of not embedded time series*. Dependence of the cooperativeness or synchronization between the sub-systems (1) and (2) of system Eq. (3.14), upon the coupling parameter $\mathcal{C}^{(2,1)}$, estimated with different techniques: ${S_{ne}}^{(1,2)}$ (red); $\gamma^{(1,2)}$ (green); $Coh^{(1,2)}$ (cyan); ${MI_{ne}}^{(1,2)}$ (blue). Robustness of the synchronization measures with respect to observational noise, considering 40, 20, and 12 dB Signal to Noise Ratio, and data lengths, considering 20, 40, and 80 trials of 500 samples each. The dots and errors bars illustrate the mean value and standard deviation, respectively.

Concerning the case of not embedded time series, the results in Fig. 3.4 show that ${S_{ne}}^{(1,2)}$ scales similarly to the phase synchronization index $\gamma^{(1,2)}$, the mutual information ${MI_{ne}}^{(1,2)}$ and to the spectral coherence $Coh^{(1,2)}$ with respect to the coupling parameter. However, $\gamma^{(1,2)}$ scales in a wider range. For all the estimators, the computed values decrease when noise is increased; nevertheless, $Coh^{(1,2)}$ appears more robust since it decreases less than the others. However, as far as coherence is concerned, the high values at very low coupling suggest that coherence might reflect similar spectral properties of the two sub-systems rather than real coupling.

As expected, the reliability of ${S_{ne}}^{(1,2)}$ increases (*cf.* the error bars decrease) with data length, similarly to the other estimators. Finally, we remark that $\gamma^{(1,2)}$ appears to be slightly less sensitive than ${S_{ne}}^{(1,2)}$ to the different structure of the sub-systems: indeed, in case of strong couplings, its values are closer to 1.

Amount of data vs. *modeling noise intensity*

Here, we show the results of the assessement of the robustness of the S estimator with respect to modeling noise and data length. For each of the values of $\mathcal{C}^{(2,1)}$ and modeling noise intensities, we computed it trial-wise over 20, 40, and all the 80 trials. Furthermore,

to have a comparison, we computed other interdependence measures. The estimators we considered were: the mutual information $MI^{(1,2)}$ with delay embedded data and with not embedded data ${MI_{ne}}^{(1,2)}$, our estimator with embedded and not embedded data $S^{(1,2)}$ and ${S_{ne}}^{(1,2)}$, respectively, the phase synchronization estimator $\gamma^{(1,2)}$ and the interdependence estimator $H^{(2,1)}$. We did not consider spectral coherence because of the poor performance shown in the previous test.

We delay-embedded the time series using the same parameter values used for the previous simulation study. The mutual information were computed using the algorithm presented in [Kraskov et al., 2004] with 15 neighbors. The phases were computed by using the Hilbert transform of the time series and we considered the $1:1$ phase difference. The $H^{(1,2)}$ estimator was computed using 15 neighbors and a Theiler window of 0.1.

To a fairer comparison, Fig. 3.5 compares the performance of the three cooperativeness estimators computed on the embedded state-space, whilst Fig. 3.6 compares the three estimator which do not require a state-space reconstruction.

Concerning the case of embedded time series, the results in Fig. 3.5 show that for moderate intensity of the modeling noise, all the estimators scale with the coupling strength. For very strong intensity of the modeling noise, we remark a threshold effect for all the measures. At *i.e.* 6 dB (SNR), which corresponds to a noise variance of 50% of the energy of the right hand side along the uncoupled attractors, our S estimator scales very weakly upon the coupling parameter, similarly as $MI^{(1,2)}$, whilst $H^{(2,1)}$ appears to have high values without scaling upon the coupling. We remark that under this very noisy settings, the studied cooperativeness measures may give robust information about the presence or not of the coupling, while very poor information about scaling may be inferred.

By increasing modeling noise intensities, $S^{(1,2)}$ decreases weakly, while $MI^{(1,2)}$ appears to be stable. As expected, the reliability of the estimators increases with the amount of available data (*cf.* the error bars decrease), though, our $S^{(1,2)}$ appears to be more reliable than the others two.

Concerning the case of not embedded time series, the results in Fig. 3.6 show that for moderate intensity of the modeling noise, all the estimators scale with the coupling strength. For very strong intensity of the modeling noise, *i.e.* 6 dB (SNR), ${S_{ne}}^{(1,2)}$ scales very weakly upon the coupling parameter, whilst ${MI_{ne}}^{(1,2)}$ and $\gamma^{(2,1)}$ appear to have higher values than for lower modeling noise intensities and, further, do not scale upon the coupling.

By increasing modeling noise intensities, all the estimators increase their values for small coupling values, and among them, $\gamma^{(2,1)}$ appears to increase more.

As expected, the reliability of the estimators increases with the amount of available data (*cf.* the error bars decrease).

The poor performance of $\gamma^{(2,1)}$ can be due to the strong modeling noise or to fact that it is not sharp enough to detect differences in the distribution of the relative phase. Another estimator might be preferable in this context [Tass et al., 1998].

Finally, we stress the fact that under this very noisy settings, the studied cooperativeness measures may give robust information about the presence or not of the coupling, while very poor information about scaling may be inferred.

Cooperativeness between two completely different sub-systems

With the previous example we have shown the performance of our S estimator upon coupling strength within a synchronization paradigm covering a wide range of situations.

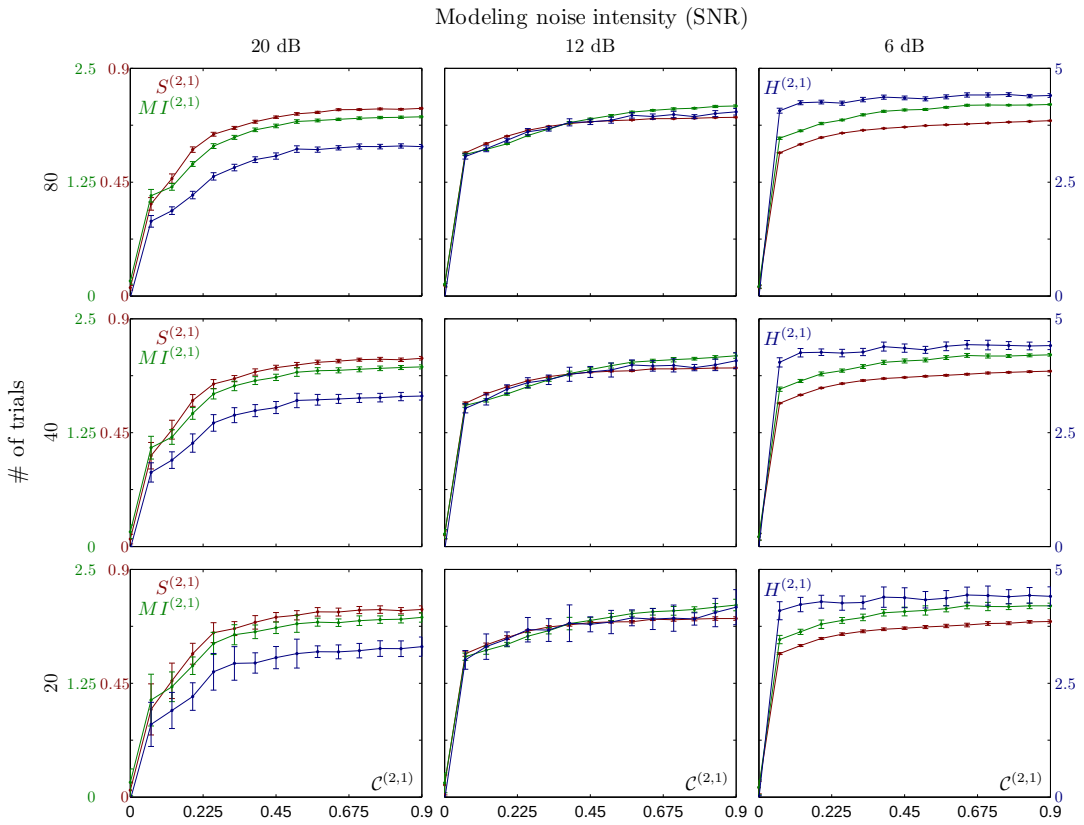

Fig. 3.5. Numerical assessment of the S estimator as a measure of cooperativeness given by coupling strength: sensitiveness upon modeling noise intensity and data length; *case of embedded time series*. Dependence of the cooperativeness or synchronization between the sub-systems (1) and (2) of system Eq. (3.14), upon the coupling parameter $\mathcal{C}^{(2,1)}$, estimated with different techniques: $S^{(1,2)}$ (red); $MI^{(1,2)}$ (green); $H^{(2,1)}$ (blue). Robustness of the synchronization measures with respect to modeling noise, considering 20, 12, and 6 dB Signal to Noise Ratio, and data lengths, considering 20, 40, and 80 trials of 500 samples each. The dots and errors bars illustrate the mean value and standard deviation, respectively.

However, it should be still checked how the S estimator behaves if not only the structure but also the dimension of the two sub-systems is different. To assess this, we consider the following synchronization paradigm: a noise-driven chaotic Lorenz sub-system linearly coupled with a noise-driven van der Pol sub-system [van der Pol, 1922], whose noise-free limit cycle attractor lays in a 2-dimensional space. The governing equations are

$$\begin{cases} \dot{\theta}_1^{(1)} = \sigma\left(\theta_2^{(1)} - \theta_1^{(1)}\right) + \eta_1^{(1)}, \\ \dot{\theta}_2^{(1)} = \rho\theta_1^{(1)} - \theta_2^{(1)} - \theta_1^{(1)}\theta_3^{(1)} + \mathcal{C}^{(1,2)}\left(\theta_2^{(2)} - \theta_2^{(1)}\right) + \eta_2^{(1)}, \\ \dot{\theta}_3^{(1)} = \theta_1^{(1)}\theta_2^{(1)} - \beta\theta_3^{(1)} + \eta_3^{(1)}, \\ \\ \dot{\theta}_1^{(2)} = \theta_2^{(2)} + \eta_1^{(2)}, \\ \dot{\theta}_2^{(2)} = \left(-\mu\left(\theta_1^{(2)}\right)^2 - 1\right)\theta_2^{(2)} - \theta_1^{(2)} + \mathcal{C}^{(2,1)}\left(\theta_2^{(1)} - \theta_2^{(2)}\right) + \eta_2^{(2)}, \end{cases} \tag{3.15}$$

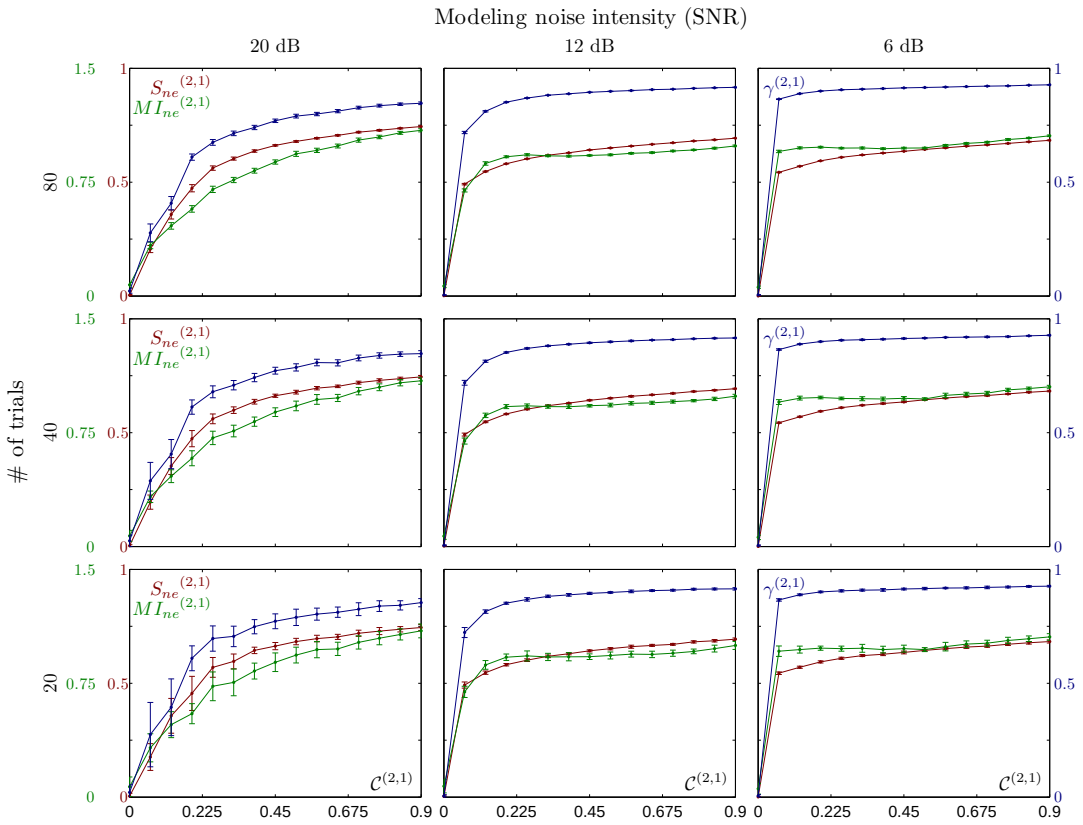

Fig. 3.6. Numerical assessment of the S estimator as a measure of cooperativeness given by coupling strength: sensitiveness upon modeling noise intensity and data length; *case of not embedded time series*. Dependence of the cooperativeness or synchronization between the sub-systems (1) and (2) of system Eq. (3.14), upon the coupling parameter $\mathcal{C}^{(2,1)}$, estimated with different techniques: ${S_{ne}}^{(1,2)}$ (red) (green); ${MI_{ne}}^{(1,2)}$ (green); $\gamma^{(1,2)}$ (blue). Robustness of the synchronization measures with respect to modeling noise, considering 20, 12, and 6 dB Signal to Noise Ratio, and data lengths, considering 20, 40, and 80 trials of 500 samples each. The dots and errors bars illustrate the mean value and standard deviation, respectively.

where $\theta_j^{(1)}$, $j = 1, 2, 3$, are the state variables of the Lorenz sub-system, while $\theta_j^{(2)}$, $j = 1, 2$, are the state variables of the van der Pol sub-system; σ, β, r, and μ are parameters that are fixed at the standard values, *i.e.* $\sigma = 10$, $\beta = 8/3$, $r = 28$, and $\mu = 1.5$; the $\eta_j^{(i)}$, are zero-mean uncorrelated Gaussian random noises (set in simulations to a variance of 1% of the energy of the right hand side along the uncoupled attractors); and, finally, the parameters $\mathcal{C}^{(1,2)}$, $\mathcal{C}^{(2,1)}$ represent the strength of the diffusive linear coupling between the two sub-systems.

For every considered value of $\mathcal{C}^{(2,1)}$ and $\mathcal{C}^{(1,2)}$, the differential equations were iterated, starting from random initial conditions, using the Heun algorithm with $\delta t = 0.005$, the initial 10000 points of each transient were dropped and, by means of a down-sampling ($\delta T = 0.02$), time series of 500 points each were collected. We collected a total of 30 trials from different initial conditions, measuring the coupled variables $\theta_2^{(1)}$ and $\theta_2^{(2)}$, corrupted by zero-mean white Gaussian observational noise leading to 40 dB SNR[17].

[17] Here, we do not consider the same robustness validation with respect to observational/modeling noise intensity and data length because this has already been done with the previous experimental setup.

Further to our S estimator with embedded and not-embedded data, we computed the phase synchronization index γ.

We considered two sub-experiments. In the first, we considered the situation in which the van der Pol sub-system drives the Lorenz sub-system, *i.e.* we set $\mathcal{C}^{(2,1)} = 0$ and we varied $\mathcal{C}^{(1,2)}$ in the interval $[0, 5]$, which represents a value of strong coupling. We reconstructed the state-space of the two sub-systems by delay-embedding. More precisely, we delay-embedded the time series from the Lorenz sub-system in a 4-dimensional space using embedding delay $\tau^{(1)} = 0.2$ and the time series from the van der Pol sub-system in a 3-dimensional space using embedding delay $\tau^{(1)} = 0.1$. These parameters were determined with the same strategy and tools used in the previous tests. The phase of the two sub-systems was computed by means of the Hilbert transform and the $1:1$ phase difference was computed. The left panel of Fig. 3.7 shows the results for the three estimators $S^{(1,2)}$, ${S_{ne}}^{(1,2)}$ and $\gamma^{(1,2)}$. Both versions of the S estimator scale similarly as the phase synchronization index with respect to the coupling parameter. Furthermore, we remark that for low coupling values the three measures are not sensitive to the coupling strength.

As second sub-experiments, we considered the situation in which the Lorenz sub-system drives the van der Pol sub-system, *i.e.* we set $\mathcal{C}^{(1,2)} = 0$ and we varied $\mathcal{C}^{(2,1)}$ in the interval $[0, 0.75]$, which represents a value of strong coupling. We reconstructed the state-space of the two sub-systems by delay-embedding the measured time series with the same parameters used in the first sub-experiment. The phase of the two sub-systems was computed by means of the Hilbert transform. The right panel of Fig. 3.7 shows the results for the three estimators $S^{(1,2)}$, ${S_{ne}}^{(1,2)}$ and $\gamma^{(1,2)}$. All the three estimators scale with respect to the coupling parameter, however, we remark that ${S_{ne}}^{(1,2)}$ varies within a range smaller than the other two estimators.

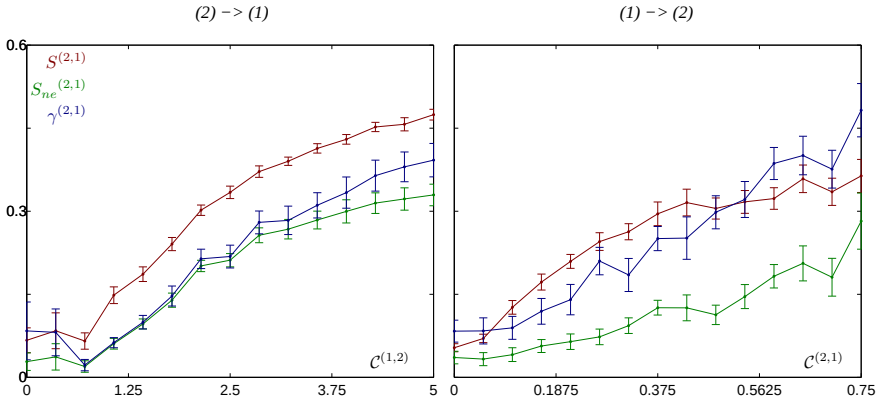

Fig. 3.7. Numerical assessment of the S estimator as a measure of cooperativeness given by coupling strength: case of sub-systems with different structure and dimension. Dependence of the cooperativeness or synchronization between the sub-systems (1) and (2) of system Eq. (4.16), upon the coupling parameter $\mathcal{C}^{(1,2)}$ for the left panel and $\mathcal{C}^{(2,1)}$ for the right panel and, estimated with different techniques: $S^{(1,2)}$ (red); ${S_{ne}}^{(1,2)}$ (green); $\gamma^{(1,2)}$ (blue). The dots and errors bars illustrate the mean value and standard deviation, respectively.

3.3.2 Cooperativeness by connectivity degree

In the previous section we have assessed the dependence of our S estimator with respect to the coupling strength. In this section, we proceed to the assessment of the S estimator

as a measure of cooperativeness in a network with respect to the average degree of connectivity. In order to assess this dependence, we considered a network of linearly coupled non-identical noise-driven Colpitts oscillators [De Feo et al., 2000], namely

$$\begin{cases} \dot{\theta}_1^{(i)} = \dfrac{g^{(i)}}{Q^{(i)}\,(1-k)} \left(\alpha \left(1 - e^{-\theta_2^{(3)}}\right) + \theta_3^{(i)}\right) + \eta_1^{(i)}, \\ \dot{\theta}_2^{(i)} = \dfrac{g^{(i)}}{Q^{(i)} k} \left((1-\alpha) \left(1 - e^{-\theta_2^{(3)}}\right) + \theta_3^{(i)}\right) + \displaystyle\sum_{j \neq i} \mathcal{C}^{(i,j)} \left(\theta_2^{(j)} - \theta_2^{(i)}\right) + \eta_2^{(i)}, \\ \dot{\theta}_3^{(i)} = -\dfrac{Q^{(i)} k\,(1-k)}{g^{(i)}} \left(\theta_1^{(i)} + \theta_2^{(i)}\right) - \dfrac{1}{Q^{(i)}} \theta_3^{(i)} + \eta_3^{(i)}, \end{cases} \tag{3.16}$$

where $\theta_j^{(i)}, j = 1, 2, 3$, are the state variables of each sub-system $i = 1, \ldots, 128$; α and k are parameters fixed at the standard values 0.996 and 0.5; $Q^{(i)}$ and $g^{(i)}$ are parameters whose values are chosen randomly in an interval ($\pm 10\%$) around the standard values $10^{0.15}$ and $10^{0.625}$, respectively; $\eta_j^{(i)}$ are zero-mean uncorrelated Gaussian random noises; and $\mathcal{C}^{(i,j)}$ are the strengths of diffusive couplings between the second state variables.

To assess cooperativeness phenomenons independently on the structure of the connections, we considered three network models, which cover some possible topology structures. In particular, we considered a random network, a regular network and a scale free network. The average connectivity degree of such networks was changed adding at each step 128 unidirectional interactions accordingly with the chosen structure model. Furthermore, we fixed the strength of each interaction at the value of 0.07, which represents a condition of weak interaction for *two* coupled oscillators.

We varied the average connectivity degree within the range $[0, 63]$ and for every considered value the differential equations were iterated, starting from random initial conditions, using the Heun algorithm with $\delta t = 0.005$, the initial 10000 points of each transient were dropped and, by means of a down-sampling ($\delta T = 0.063$), time series of 1000 points each were collected. We collected a total of 80 trials from different initial conditions, measuring the coupled variables $\theta_2^{(i)}\ \forall i$. We studied the capability of estimating the cooperativeness of the network depending on the amount of data available for two cases: in the first simulation study, we fixed the modeling noise intensity at a small value (*i.e.* 40 *dB* SNR) and we varied the observational noise intensity, *i.e.* 40, 20, 12 *dB* SNR; in the second simulation study, we fixed the observational noise intensity at a small value (*i.e.* 40 *dB* SNR) and we varied the modeling noise intensity, *i.e.* 20, 12, 6 *dB* SNR. The measures we used to estimate the network cooperativeness were: our S estimator, with embedded data $S^{(1,\ldots,128)}$ and not embedded data ${S_{ne}}^{(1,\ldots,128)}$ and the modulus of the order parameter[18] $Op^{(1,\ldots,128)}$. All the three measures were computed trial-wise. The delay-embedded data were obtained by delay embedding the observed time series with a (usually estimated) common value for the time lag and embedding dimension, *i.e.* $\tau^{(i)} = 1.634$ and $n^{(i)} = 4$, $\forall i$.

Random network

Here, we show the results of the assessment of the sensitiveness of our S estimator as measure of cooperativeness upon the average connectivity degree in a network with random topology.

[18] The phase is well defined for the Colpitts oscillator with the considered parameter values. We estimated them with the Hilbert transform based method.

In Fig. 3.8 are the results relative to the analysis of sensitiveness upon the amount of available data and observational noise intensity. For all the estimators, the computed values scale with the average connectivity degree. For all the estimators, the values decreased when noise was increased; nevertheless, $S^{(1,\dots,128)}$ appears less robust since it decreases more than the others. It would be interesting to study the behavior of $S^{(1,\dots,128)}$ for different choices of the embedding dimension, however, it was not the aim of this numerical validation. Furthermore, we remark that it should be also taken into account the fact that the measurement-wise network's state-space reconstruction is more and more jeopardized by the synchronization of more and more sub-systems.

As expected, the reliability of the estimators increases (*cf.* the error bars decrease) with data length, nevertheless, $Op^{(1,\dots,128)}$ appears less reliable than the others being the error bars wider. Finally, we remark that for the uncoupled network, both $S^{(1,\dots,128)}$ and ${S_{ne}}^{(1,\dots,128)}$ show a consistently non zero value higher than the corresponding $Op^{(1,\dots,128)}$, in particular ${S_{ne}}^{(1,\dots,128)}$[19]. This could be due to the fact that the S estimator is also affected by correlations on the amplitudes of the signals (although with slightly different parameters, the sub-systems have similar structure), and not only by those on their phases. However, we want to remark that this may also be due to the number of data available for each trial. Indeed, in this numerical validation we considered 128 sub-systems, almost two order of magnitude bigger than the previous numerical assessment given by Eq. (3.14). Consequently, 1000 data points might be not sufficient for a reliable estimation of the correlation matrix of such huge amount of variables. To verify that, we computed the S estimator for the uncoupled network, not trial-wise but appending the trials in a unique long trial[20]. By appending 10 trials, so that to have 10000 points, the S estimators values decreased, in particular the ${S_{ne}}^{(1,\dots,128)}$ value was comparable with the one of $Op^{(1,\dots,128)}$, *i.e.* ≈ 0.06.

Fig. 3.9 depicts the results relative to the analysis of sensitiveness upon the amount of available data and modeling noise intensity. For all the estimators, the computed values scale upon the average connectivity degree. Nevertheless, for strong modeling noise intensity, *i.e.* 6 dB, and for low values of the average connectivity degree, ${S_{ne}}^{(1,\dots,128)}$ appears slightly decreasing. For all the estimators, the values decreased when noise was increased; nevertheless, $S^{(1,\dots,128)}$ appears less robust since it decreases more than the others. As expected, the reliability of the estimators increases (*cf.* the error bars decrease) with data length. Finally, we remark that for the uncoupled network, both $S^{(1,\dots,128)}$ and ${S_{ne}}^{(1,\dots,128)}$ show a consistently non zero value higher than the corresponding $Op^{(1,\dots,128)}$, in particular ${S_{ne}}^{(1,\dots,128)}$. While $S^{(1,\dots,128)}$ decreases for stronger modeling noise intensity, ${S_{ne}}^{(1,\dots,128)}$ does not. However, as previously done, we computed ${S_{ne}}^{(1,\dots,128)}$ on more data, *i.e.* by appending 10 trials for a total of 10000 points. ${S_{ne}}^{(1,\dots,128)}$ shown a much lower value for uncoupled sub-systems and a correct scaling (monotonic increase) for low values of the average connectivity degree.

Regular network

Here, we show the results of the assessment of the sensitiveness of our S estimator as measure of cooperativeness upon the average connectivity degree in networks with regular topology. Certainly, many kinds of regular networks might be defined. We chose a regular

[19] The lower value of $S^{(1,\dots,128)}$ with respect to ${S_{ne}}^{(1,\dots,128)}$ may be due to the de-correlating effect of the delay embedding and of the normalization illustrated in Sec. 3.2.1.

[20] In an experimental setup, this strategy can be applied under the hypothesis that each trial is a measure of a network with same dynamics.

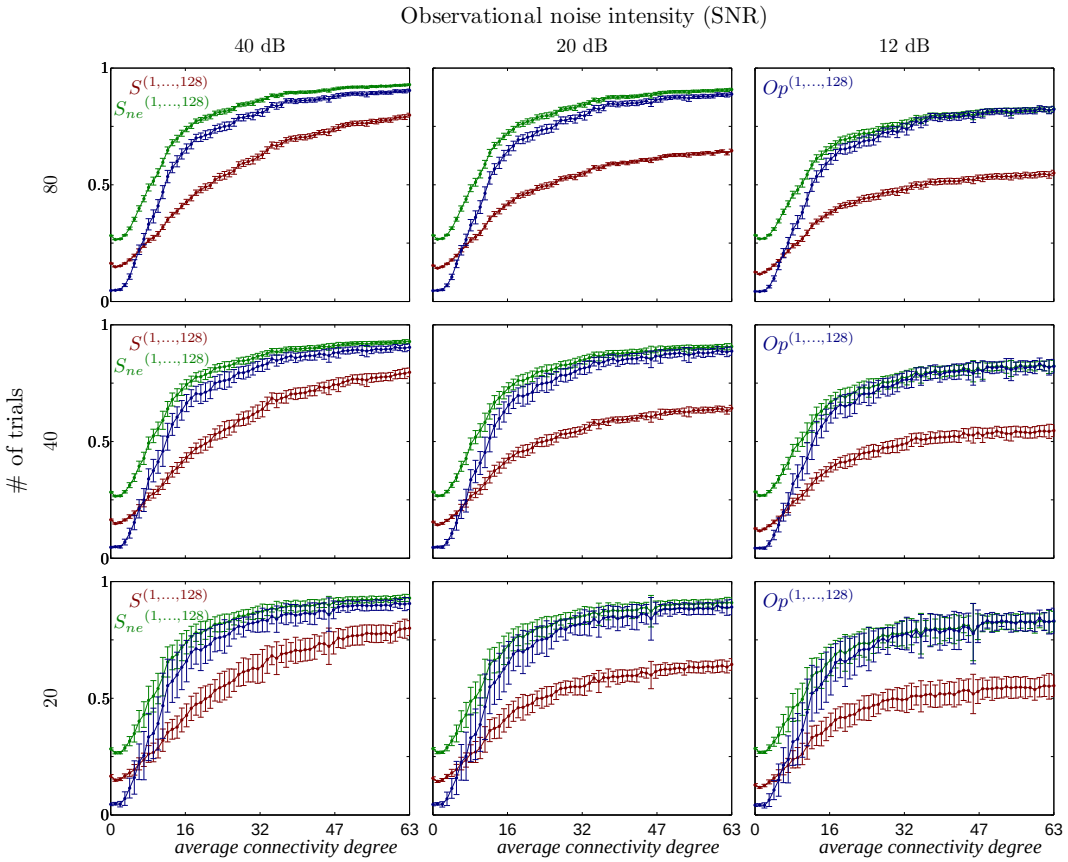

Fig. 3.8. Numerical assessment of the S estimator as a measure of cooperativeness given by connectivity degree: sensitiveness upon observational noise intensity and data length; *case of random network*. Dependence of the cooperativeness or synchronization among the sub-systems $(i)\,, \forall i, i = 1, \dots, 128$ of system in Eq. (3.16), upon the average connectivity degree. The cooperativeness was estimated with three different techniques: $S^{(1,\dots,128)}$ (red); $S_{ne}{}^{(1,\dots,128)}$ (green); $Op^{(1,\dots,128)}$ (blue). Robustness of the synchronization measures with respect to observational noise, considering 40, 20, and 12 dB Signal to Noise Ratio, and data lengths, considering 20, 40, and 80 trials of 1000 samples each. The dots and errors bars illustrate the mean value and standard deviation, respectively.

network as following. Imagine all the uncoupled 128 sub-systems (or nodes) shaped on a ring structure. For an observer placed in the center of the ring, as first step we added a directed edge from each node to its first left neighbor. As second step, we added a directed edge from each node to its second left neighbor. Finally, the n-th step was to add a directed edge from each node to its n-th left neighbor. We iterated this procedure 63 times until the undirected network graph was fully connected.

In Fig. 3.10 are the results relative to the analysis of sensitiveness upon the amount of available data and observational noise intensity. For all the estimators, the computed values scale with the average connectivity degree till a plateau (reached around 20 for $S_{ne}{}^{(1,\dots,128)}$ and $Op^{(1,\dots,128)}$). Instead, we remark that for low observational noise intensity (*i.e.* 40 dB SNR) $S^{(1,\dots,128)}$ is able to scale in a wider range (it shows a plateau around 40) than the other two estimators. For all the estimators, the values decreased when noise was increased; nevertheless, $S^{(1,\dots,128)}$ appears less robust since it decreases more than the others, *i.e.* it approximately halves its plateau value at 12 dB with respect to the value at 40 dB SNR. It would be interesting to study the behavior of $S^{(1,\dots,128)}$

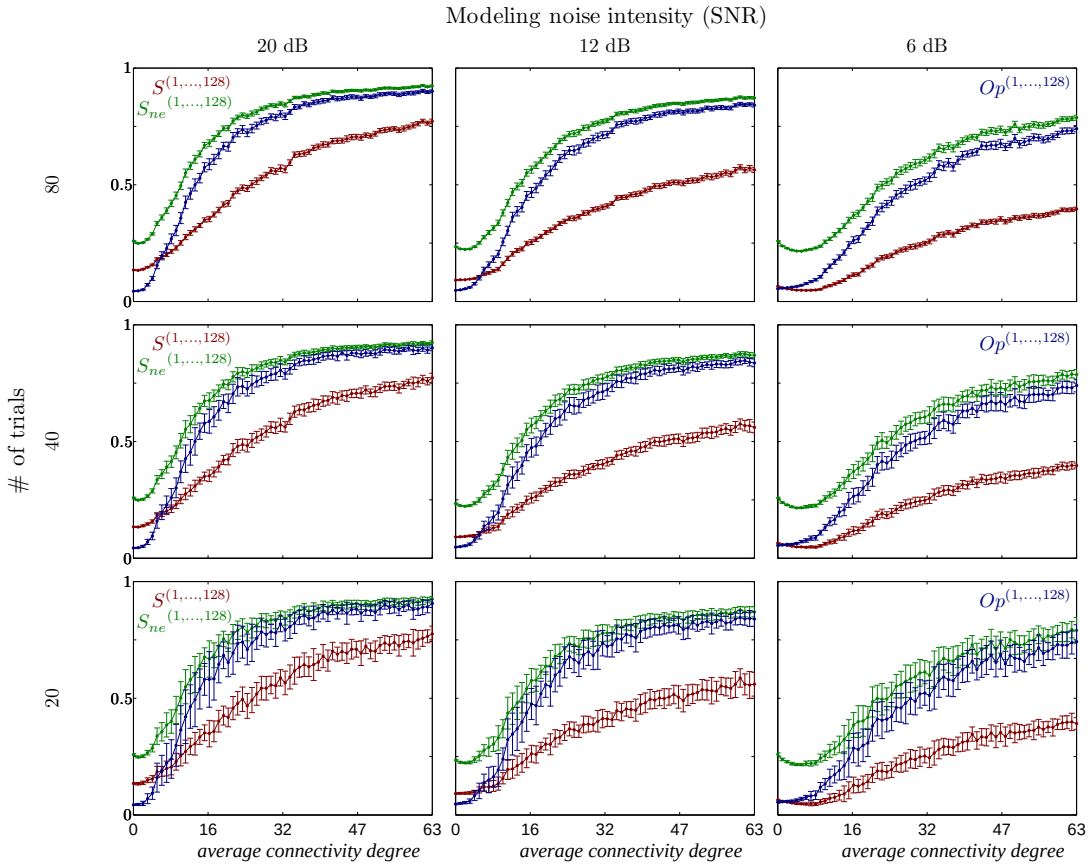

Fig. 3.9. Numerical assessment of the S estimator as a measure of cooperativeness given by connectivity degree: sensitiveness upon modeling noise intensity and data length; *case of random network*. Dependence of the cooperativeness or synchronization among the sub-systems $(i), \forall i, i = 1, \ldots, 128$ of system in Eq. (3.16), upon the average connectivity degree. The cooperativeness was estimated with three different techniques: $S^{(1,\ldots,128)}$ (red); $S_{ne}{}^{(1,\ldots,128)}$ (green); $Op^{(1,\ldots,128)}$ (blue). Robustness of the synchronization measures with respect to modeling noise, considering 20, 12, and 6 dB Signal to Noise Ratio, and data lengths, considering 20, 40, and 80 trials of 1000 samples each. The dots and errors bars illustrate the mean value and standard deviation, respectively.

for different choices of the embedding dimension, however, it was not the aim of this numerical validation.

As expected, the reliability of the estimators increases (*cf.* the error bars decrease) with data length, nevertheless, $Op^{(1,\ldots,128)}$ appears less reliable than the others being the error bars wider before reaching the plateau. Finally, we remark that for the uncoupled network, both $S^{(1,\ldots,128)}$ and $S_{ne}{}^{(1,\ldots,128)}$ show a consistent non zero value and higher than the corresponding $Op^{(1,\ldots,128)}$, in particular $S_{ne}{}^{(1,\ldots,128)}$. As previously done, we verified that with the availability of more data points either $S^{(1,\ldots,128)}$ and $S_{ne}{}^{(1,\ldots,128)}$ lowered their values.

In Fig. 3.11 are the results relative to the analysis of sensitiveness upon the amount of available data and modeling noise intensity. For all the estimators, the computed values scale upon the average connectivity degree. Nevertheless, for strong modeling noise intensity, *i.e.* $6dB$, and for low values of the average connectivity degree, $S_{ne}{}^{(1,\ldots,128)}$ appears slightly decreasing. For all the estimators, the values decreased when noise was increased; nevertheless, $S^{(1,\ldots,128)}$ appears less robust since it decreases more than the

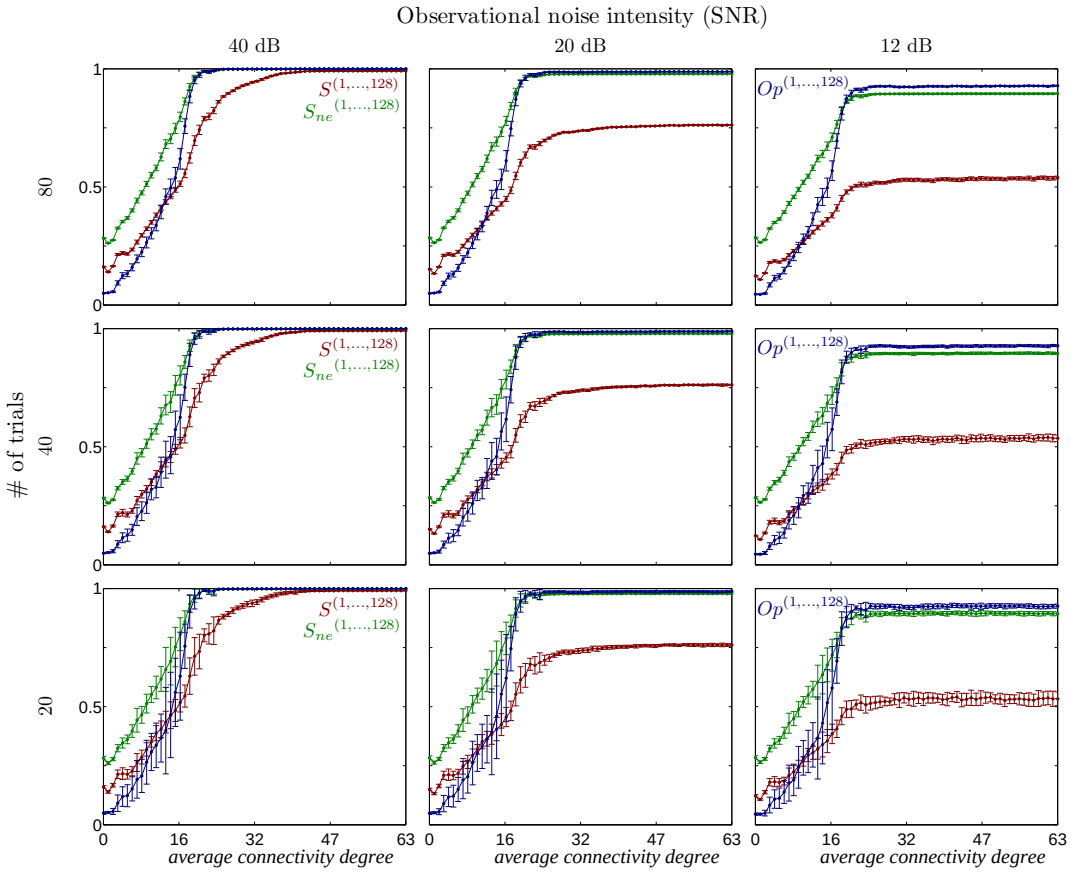

Fig. 3.10. Numerical assessment of the S estimator as a measure of cooperativeness given by connectivity degree: sensitiveness upon observational noise intensity and data length; *case of regular network*. Dependence of the cooperativeness or synchronization among the sub-systems $(i)\,, \forall i, i = 1, \ldots, 128$ of system in Eq. (3.16), upon the average connectivity degree. The cooperativeness was estimated with three different techniques: $S^{(1,\ldots,128)}$ (red); $S_{ne}{}^{(1,\ldots,128)}$ (green); $Op^{(1,\ldots,128)}$ (blue). Robustness of the synchronization measures with respect to observational noise, considering 40, 20, and 12 dB Signal to Noise Ratio, and data lengths, considering 20, 40, and 80 trials of 1000 samples each. The dots and errors bars illustrate the mean value and standard deviation, respectively.

others. As expected, the reliability of the estimators increases (*cf.* the error bars decrease) with data length. Finally, we remark that for the uncoupled network, both $S^{(1,\ldots,128)}$ and $S_{ne}{}^{(1,\ldots,128)}$ show a consistently non zero value higher than the corresponding $Op^{(1,\ldots,128)}$, in particular $S_{ne}{}^{(1,\ldots,128)}$. While $S^{(1,\ldots,128)}$ decreases for stronger modeling noise intensity, $S_{ne}{}^{(1,\ldots,128)}$ does not. However, as previously done, we computed $S_{ne}{}^{(1,\ldots,128)}$ on more data, *i.e.* by appending 10 trials for a total of 10000 points. $S_{ne}{}^{(1,\ldots,128)}$ shown a much lower value for uncoupled sub-systems and a correct scaling for low values of the average connectivity degree.

Scale Free network

The two kinds of networks we have previously described were the usual case in the network community until a few years ago. Roughly speaking, random or regular lattices in graph are characterized by the homogeneity in the interaction structure, in the sense that all nodes (or sub-systems) are topologically equivalent. The degree distribution of such network shows to be binomial or Poisson in the limit of large graph size. Lately, real-

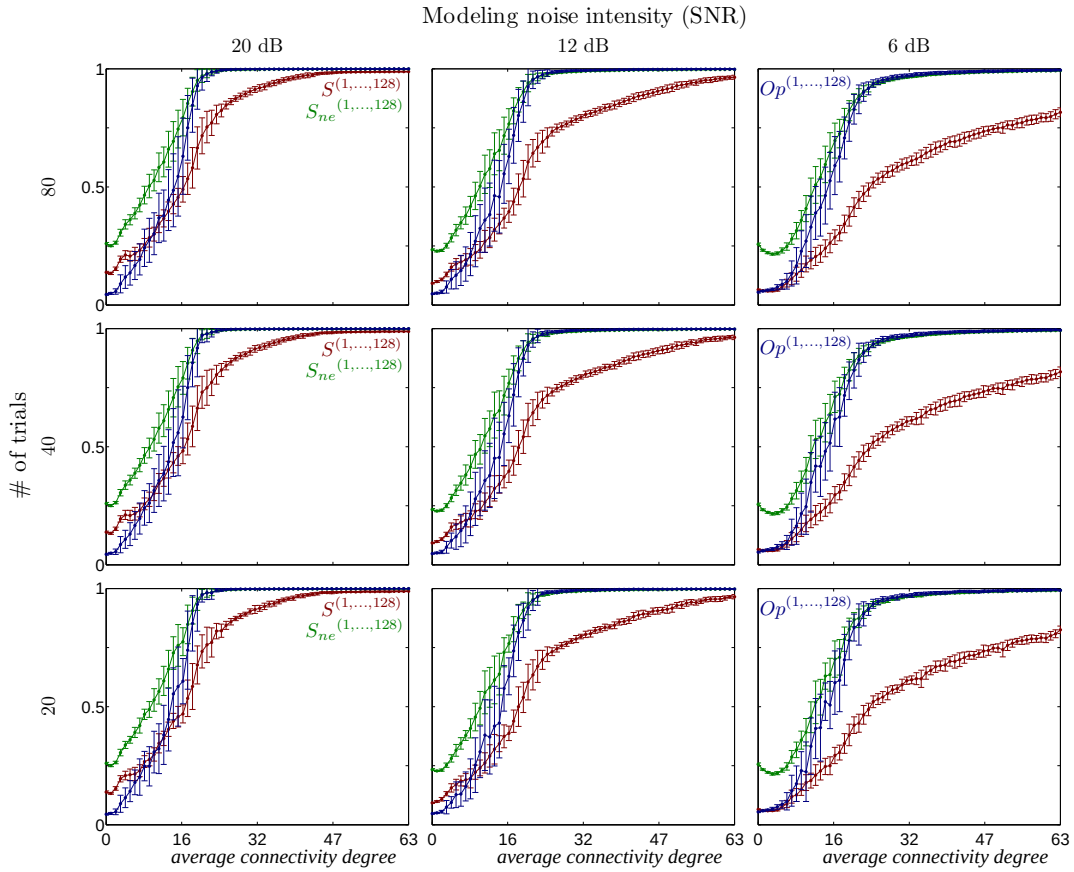

Fig. 3.11. Numerical assessment of the S estimator as a measure of cooperativeness given by connectivity degree: sensitiveness upon modeling noise intensity and data length; *case of regular network*. Dependence of the cooperativeness or synchronization among the sub-systems $(i), \forall i, i = 1, \dots, 128$ of system in Eq. (3.16), upon the average connectivity degree. The cooperativeness was estimated with three different techniques: $S^{(1,\dots,128)}$ (red); $S_{ne}{}^{(1,\dots,128)}$ (green); $Op^{(1,\dots,128)}$ (blue). Robustness of the synchronization measures with respect to modeling noise, considering 20, 12, and 6 *dB* Signal to Noise Ratio, and data lengths, considering 20, 40, and 80 trials of 1000 samples each. The dots and errors bars illustrate the mean value and standard deviation, respectively.

world networks were discovered to show a highly inhomogeneous interaction structure, the so-called scale free graphs [Barabási and Albert, 1999]. These networks present the simultaneous presence of a few nodes linked to many other nodes, and a large number of poorly connected elements. This feature is characterized by power laws in their degree distributions.

Several recipes to construct scale free networks have been proposed in literature, based on the assumption that a node has some weight [Boccaletti et al., 2006]. To build our scale free network, we followed the recipe proposed in [Goh et al., 2001]. To each node (i) we assigned a weight $w^{(i)} = i^{-\alpha}, i = 1, \dots, 128$, where α is a tunable parameter in $[0, 1)$. Two different nodes, (i) and (j), are selected with probabilities equal to the normalized weights $\frac{w^{(i)}}{\sum_l w^{(l)}}$ and $\frac{w^{(j)}}{\sum_l w^{(l)}}$, respectively, and are connected if there is not already a link between them. The process is iterated until 128 links are added in the system, so that the average connectivity degree has been increased of 1. When $\alpha = 0$ this procedures allows to obtain a random graphs. As shown in [Goh et al., 2001], when $\alpha \neq 0$ the graph obtained has a power law degree distribution with an exponent $1 + \frac{1}{\alpha}$. We chose $\alpha = 0.5$.

In Fig. 3.12 are the results relative to the analysis of sensitiveness upon the amount of available data and observational noise intensity. For all the estimators, the computed values scale upon the average connectivity degree. For all the estimators, the values decreased when noise was increased. Furthermore, as expected, the reliability of the estimators increases (*cf.* the error bars decrease) with data length; nevertheless, $Op^{(1,\ldots,128)}$ appears less reliable than the others being the error bars wider. Finally, we remark that for the uncoupled network, both $S^{(1,\ldots,128)}$ and ${S_{ne}}^{(1,\ldots,128)}$ show a consistent non zero value and higher than the corresponding $Op^{(1,\ldots,128)}$, in particular ${S_{ne}}^{(1,\ldots,128)}$. As previously said, this is due the amount of available data.

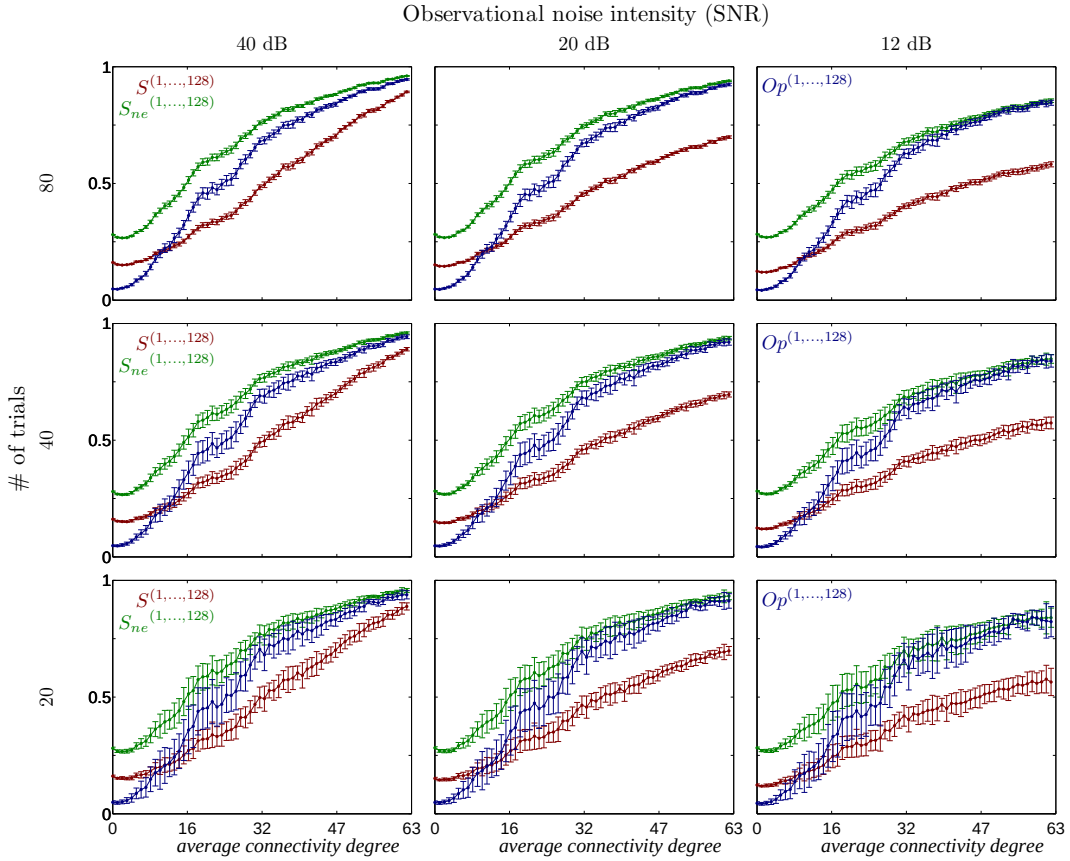

Fig. 3.12. Numerical assessment of the S estimator as a measure of cooperativeness given by connectivity degree: sensitiveness upon observational noise intensity and data length; *case of scale free network*. Dependence of the cooperativeness or synchronization among the sub-systems $(i)\,, \forall i, i = 1, \ldots, 128$ of system Eq. (3.16), upon the average connectivity degree. The cooperativeness was estimated with three different techniques: $S^{(1,\ldots,128)}$ (red); ${S_{ne}}^{(1,\ldots,128)}$ (green); $Op^{(1,\ldots,128)}$ (blue). Robustness of the synchronization measures with respect to observational noise, considering 40, 20, and 12 dB Signal to Noise Ratio, and data lengths, considering 20, 40, and 80 trials of 1000 samples each. The dots and errors bars illustrate the mean value and standard deviation, respectively.

In Fig. 3.13 are the results relative to the analysis of sensitiveness upon the amount of available data and modeling noise intensity. For all the estimators, the computed values scale upon the average connectivity degree. For all the estimators, the values decreased when noise was increased; nevertheless, $S^{(1,2,\ldots,128)}$ appears to decrease more than the others. Furthermore, as expected, the reliability of the estimators increases (*cf.* the error bars decrease) with data length; nevertheless, $Op^{(1,\ldots,128)}$ appears slightly

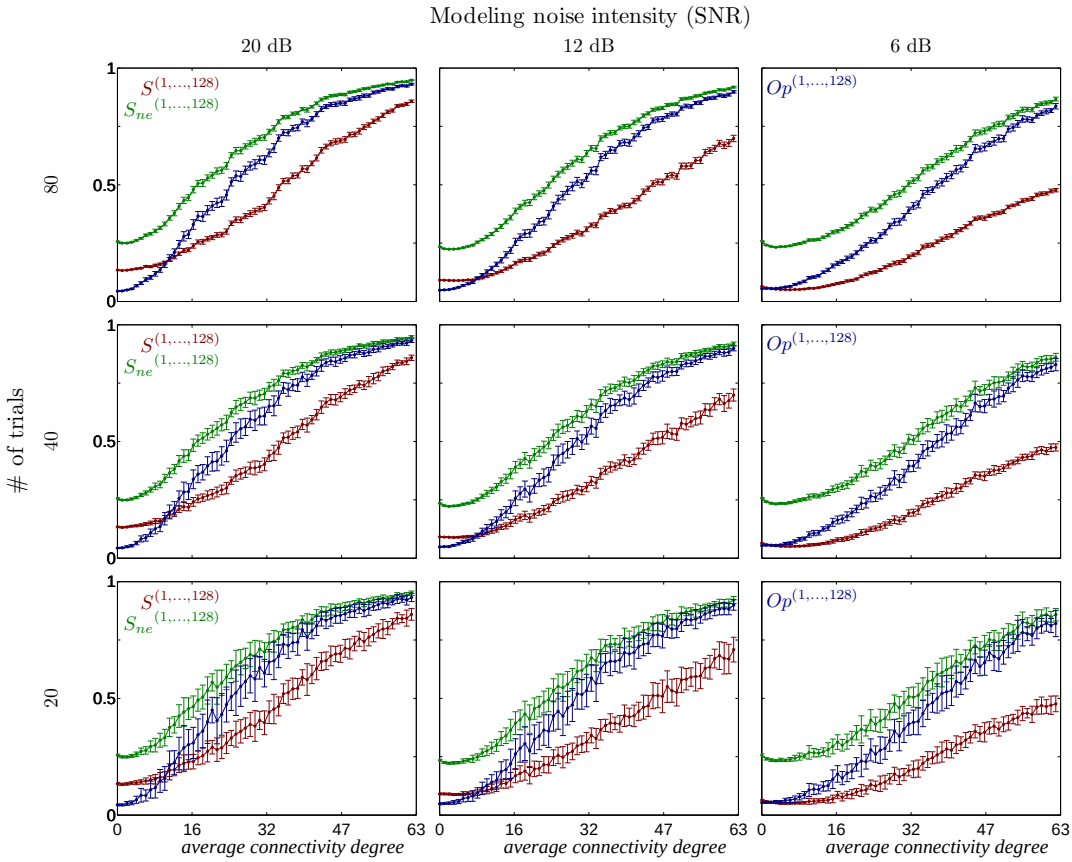

Fig. 3.13. Numerical assessment of the S estimator as a measure of cooperativeness given by connectivity degree: sensitiveness upon modeling noise intensity and data length; *case of random network*. Dependence of the cooperativeness or synchronization among the sub-systems $(i), \forall i, i = 1, \ldots, 128$ of system in Eq. (3.16), upon the average connectivity degree. The cooperativeness was estimated with three different techniques: $S^{(1,\ldots,128)}$ (red); $S_{ne}{}^{(1,\ldots,128)}$ (green); $Op^{(1,\ldots,128)}$ (blue). Robustness of the synchronization measures with respect to modeling noise, considering 20, 12, and 6 dB Signal to Noise Ratio, and data lengths, considering 20, 40, and 80 trials of 1000 samples each. The dots and errors bars illustrate the mean value and standard deviation, respectively.

less reliable than the others being the error bars wider. For uncoupled sub-systems, $S_{ne}{}^{(1,\ldots,128)}$ appears to have a consistently non-zero value for all noise intensities, while $S^{(1,\ldots,128)}$ lowers. As previously done, we verified that with the availability of more data points $S_{ne}{}^{(1,\ldots,128)}$ lowered its value.

3.3.3 Cooperativeness among meta-aggregations

In the previous two sections we have tested and shown the performance of our S estimator as a measure of cooperativeness in noise-driven dynamical networks. In this section, we want to show that our S estimator can naturally be extended to the analysis of interdependences among communities of dynamical networks, an issue commonly encountered in social sciences [Wasserman and Faust, 1994]. Communities can be defined as groups of dynamical sub-systems, such that there is a higher density of interactions within groups than between them. An example is given in Fig. 3.14. The S estimator can account for meta-structure because the normalization procedure we introduced in Sec. 3.2.1 can be chosen accordingly. Indeed, we can partition the estimated correlation matrix of the network in Eq. (3.7) in such a way as to highlight the community groups we want to

study. Finally, the transformation in Eq. (3.8) will allow to take into account only the intra-dependences among the so defined communities.

To show this feature of the S estimator, we proceed to a numerical example, that, we are aware, however does not validate exhaustively this feature. We consider a network

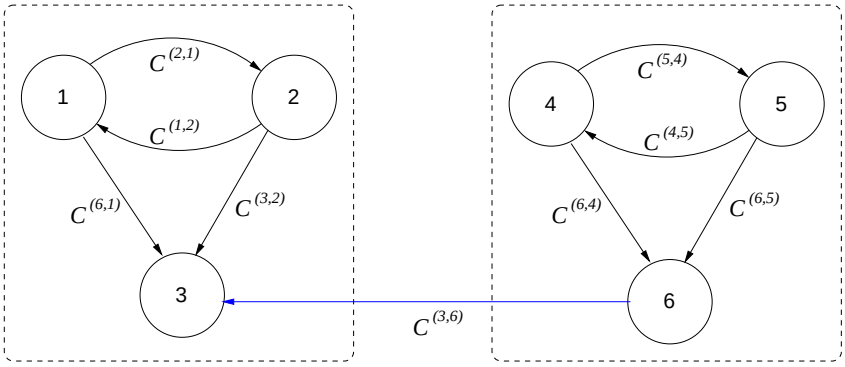

Fig. 3.14. Example of community like structure in a network of six sub-systems. Within the two groups marked by a dashed rectangular box are four interactions, whilst between the two groups only one interaction is present.

composed by six sub-systems arranged as reported in Fig. 3.14. In particular, each node is represented by noisy Lorenz like sub-systems, whose dynamics is given by

$$\begin{cases} \dot{\theta}_1^{(i)} = \sigma^{(i)} \left(\theta_2^{(1)} - \theta_1^{(1)} \right) + \eta_1^{(1)}, \\ \dot{\theta}_2^{(i)} = \rho^{(i)} \theta_1^{(1)} - \theta_2^{(1)} - \theta_1^{(1)} \theta_3^{(1)} + \sum_{j \neq i} \mathcal{C}^{(i,j)} \left(\theta_2^{(j)} - \theta_2^{(i)} \right) + \eta_2^{(i)}, \\ \dot{\theta}_3^{(i)} = \theta_1^{(1)} \theta_2^{(1)} - \beta^{(i)} \theta_3^{(1)} + \eta_3^{(1)}, \end{cases} \tag{3.17}$$

where $\theta_j^{(i)}, j = 1, 2, 3$, are the state variables of each sub-system $i = 1, \ldots, 6$; $\sigma^{(i)}$, $\rho^{(i)}$ and $\beta^{(i)}$ are parameters whose values are chosen randomly in an interval ($\pm 5\%$) around the standard values 10, 27, and 8/3, respectively; $\eta_j^{(i)}$ are zero-mean uncorrelated Gaussian random noises (set in simulations to a variance of 1% of the energy of the right hand side along the uncoupled attractors); and $\mathcal{C}^{(i,j)}$ are the strengths of diffusive couplings between the second state variables. We set $\mathcal{C}^{(2,1)}, \mathcal{C}^{(1,2)}, \mathcal{C}^{(3,1)}, \mathcal{C}^{(3,2)}, \mathcal{C}^{(5,4)}, \mathcal{C}^{(4,5)}, \mathcal{C}^{(6,4)}$ and $\mathcal{C}^{(6,5)}$ to the value 1, which guarantees a condition of weak coupling within the two communities[21], we set $\mathcal{C}^{(1,3)} = \mathcal{C}^{(2,3)} = \mathcal{C}^{(4,6)} = \mathcal{C}^{(5,6)} = \mathcal{C}^{(6,3)} = 0$ and we varied the inter-community coupling $\mathcal{C}^{(3,6)}$ within the range $[0, 10]$.

For every considered value of $\mathcal{C}^{(3,6)}$, the differential equations were iterated, starting from random initial conditions, using the Heun algorithm with $\delta t = 0.005$, the initial 10000 points of each transient were dropped and, by means of a down-sampling ($\delta T = 0.02$), time series of 1000 points each were collected. We collected a total of 30 trials from different initial conditions, measuring the coupled variables $\theta_2^{(j)}, \forall j$, corrupted by zero-mean white Gaussian observational noise leading to 40 dB (SNR).

[21] In principle, if the sub-systems composing a community are strongly synchronized, *i.e.* nearly or not distinguishable one from the other, pre-processing technique like PCA could allow data reduction and the standard version of S would suffice.

The intra-community cooperativeness was assessed with our S estimator in embedded form $S^{(1,2,3),(4,5,6)}$ and not embedded ${S_{ne}}^{(1,2,3),(4,5,6)}$. For comparison, we also assessed the global network cooperativeness ${S_{ne}}^{(1,\ldots,6)}$.

To reconstruct the state-space, we used delay-embedding with time delay $\tau^{(i)} = 0.2\ \forall i$, and embedding dimension $n^{(i)} = 4\ \forall i$.

The results are shown in Fig. 3.15. From the curves on the left panel, we observe that, correctly, both estimators scale similarly with the coupling parameter. Instead, as shown in the right panel, by taking just into account the all network, it would harder to infer changes in the cooperativeness and, importantly, the condition of no coupling between the two communities.

Finally, we remark that both $S^{(1,2,3),(4,5,6)}$ and ${S_{ne}}^{(1,2,3),(4,5,6)}$ are not exactly zero for the uncoupled community, *cf.* Fig. 3.15. It should be checked whether the estimated values decrease with increasing amount of data. This is planned as future investigation.

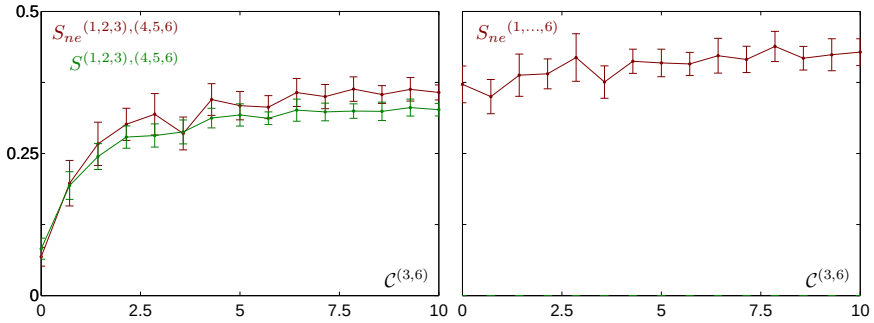

Fig. 3.15. Assessment of the S estimator as a measure of cooperativeness between communities. On the left panel, dependence of the cooperativeness between the two communities in Fig. 3.14 of the network in Eq. (3.17), upon the coupling parameter $\mathcal{C}^{(3,6)}$. The two curves represent: $S^{(1,2,3),(4,5,6)}$ (green); ${S_{ne}}^{(1,2,3),(4,5,6)}$ (red). On the right panel, dependence of the network cooperativeness upon the coupling parameter $\mathcal{C}^{(3,6)}$ estimated with ${S_{ne}}^{(1,\ldots,6)}$. The dots and errors bars illustrate the mean value and standard deviation, respectively. $S^{(1,\ldots,6)}$ is not reported here because gave similar results to ${S_{ne}}^{(1,\ldots,6)}$.

3.4 Remarks

In this chapter we have introduced and numerically validated a new method to estimate cooperativeness in noise-driven dynamical networks. Being defined on the time domain, it can be extended to the analysis of delay-embedded data.

Conceptually, the new estimator (for not embedded signals) is simpler than the existing ones, in the sense that unlike mutual information, H estimator and coherence is parameter free; unlike mutual information has lower computational cost, and unlike phase synchronization indices does not need any preprocessing stage as the phase extraction. Furthermore, this means that it may be applied to a wider class of systems. However, *a priori* this might have the disadvantage of being more prone to error in noise-driven nonlinear dynamical networks, because the method takes into account only second moments and also the amplitudes of the signals.

We validated the estimator on numerically generated data. The estimator has shown to be able to measure cooperativeness in noisy networks of chaotic dynamical sub-systems

independently on the network topology. In particular, the version of the estimator for not embedded data shown to be more robust to both observational and modeling noise intensity than the version on embedded data, especially for the case of large networks. Nevertheless, this should not be conclusive, because the sensitiveness of the estimators upon the observed variable should be considered. This is matter of ongoing research.

Concerning the numerical validation of large systems, we remark that reliable results need the availability of an adequate amount of data points and that a further validation is necessary. Indeed, we did not validate the statistical significance of the S estimator behavior with respect to several realizations of the network topologies under study. This will be matter of future investigations.

We would like to mention the possibility to test the S estimator when breaking the hypothesis of modeling and observational noises *white* and/or with uncorrelated components. For instance, it would be interesting to test whether the S estimator is sensitive to false correlations given by noises of common color in uncoupled sub-systems.

In Appendix A we will show some more numerical examples in order to illustrate the behavior of the S estimator. We will show that superimposed signals lead to a spurious detection of interdependence of the S estimator as well as a phase synchronization index. We will also show that the S estimator applied on not-embedded signals has poor performance in detecting purely phase synchronized systems. However, we will show that the S estimator applied to embedded signals performs well under this case. Finally, we will show that the S estimator does not measure complexity.

An important feature of the S estimator, that is conceptually shared with mutual information, is the possibility to study cooperativeness among communities of subsystems. We believe that the possibility to study the cooperative behavior between meta-aggregations of sub-systems may help in unraveling the emergence of phenomena not observable at single sub-system (aggregation) level.

Finally, we want to remark that even if the new estimator is based on linear correlations, the entropy-like statistics could be extracted from other linear similarity matrices. For instance, we could use a (spectral) coherence matrix. However, to go beyond second order correlations, it would be interesting to use a mutual information based similarity matrix. For instance, one based on the quantity $\frac{MI^{(i,j)}}{I^{(i,j)}}\ \forall i,j$ [Li et al., 2001]. Potentially, this would allow a further advantage: our entropy-like statistics would transform this powerful pair-wise similarity quantity, into a single (intensive) cooperativeness value. Mutual information allows itself a multivariate estimation, however, it would be difficult to obtain a reliable estimation from a finite amount of data. Therefore, an S estimator defined on bivariate mutual information would represent a good statistical compromise to assess cooperativeness in a mutual information sense. Despite all this, it should be theoretically checked and investigated the geometrical meaning of the so-defined S estimator.

To conclude this chapter, we mention that during the period of this thesis work, we have developed a Matlab toolbox. The "S Toolbox" contains various algorithms to compute the S estimator, to estimate parameters for the delay-embedding reconstruction and to define in a flexible way sub-network structures for the study of the topographical organization of cooperativeness in spatially (2D) extended networks. Special attention has been given to applications in the field of electroencephalographic (EEG) analysis with some *ad hoc* functions.

This toolbox is freely available through the World Wide Web. The current address is $http://aperest.epfl.ch/docs/software.htm$.

4

Assessing Partial Cooperativeness in Dynamical Networks

Brief — This chapter describes two new estimators of cooperativeness marginalized upon third knowledge. They are validated on prototypical models of systems, and sensitiveness upon noise and amount of data. Furthermore, their saliency upon the number of marginalized sub-systems and scalability upon the number of network's sub-systems are tested.
Personal Contribution — The first, non-parametric method is our original idea. The second, parametric method is an original idea of Dr. O. De Feo. Our contributions were in its development and validation.

4.1 Motivation

The study of the collective behavior of ensembles of interacting sub-systems is the most basic issue when exploring networks. In the previous chapter, we have derived and tested a new estimator of the amount of the cooperative activity within the recorded network. When exploring networks, however, other issues exist, in particular those concerning their structural properties. For instance, an important and bold task is represented by the process of unraveling the network wiring diagram. Networks may possess an intricate tangle of connections that greatly affect their behavior [Strogatz, 2001].

Conceptually, the estimators presented in the previous chapter apply to this task. Indeed, the graph of the interactions of the network under observation may be obtained by a pair-wise analysis on all the possible couple of sub-systems. Unfortunately, this strategy is not satisfactory in general. Indeed, we may incidentally infer a link between two sub-systems from the simple fact that these two sub-systems are commonly interacting with another one [Wittaker, 1990]. This case is usually referred to the "common source" problem. In graph jargon, the inferred not-existing interaction is labeled as "undirect", whilst the true ones are labeled as "direct" [Dahlhaus, 2000].

This difficulty can be overcome by methods that estimate the inter-relation between sub-systems conditionally upon the knowledge of third sub-systems. This procedure is often called marginalization or partialization [Stuart et al., 1999].

In literature, various methods have appeared to this concern. Within the linear approach, methods can be classified depending on the domain, *i.e.* frequency or time. In the former, the two major classes of estimators are from graphical models [Dahlhaus, 2000] and spectral coherence, such as partial and partial directed coherence [Kamiński and Blinowska, 1991, Baccalà and Sameshima, 2001]. These estimators are able to estimate the strength of the interaction and even its direction. In the latter, recently a nonlinear Granger causality index has appeared in [Chen et al., 2004]. The rationale behind

Granger causality [Granger, 1969] is to examine whether the prediction of one time series can be improved by incorporating information from the others. Specifically, once a linear model has been built, if the variance of the prediction error of a given time series at the present time is reduced by the inclusion of past measurements from the other time series, then the latter are said to have a causal influence on the former. Certainly, the roles can be inverted to address the question of causal influence in the opposite direction. In [Chen et al., 2004] this idea has been extended to the case of nonlinear time series by restricting its application to local linear models and then averaging the resulting statistical quantity over the entire data set. Although this estimator is conceptually interesting, a numerical validation of it is still missing to our knowledge.

Within the information theory inspired approach, a natural extension of mutual information to take into account thirds is the conditional mutual information. For the sake of clarity, it is based on conditional probability distributions. However, mutual information being a symmetric quantity, a directionality cannot be estimated from it. To this concern, recently the concept of transfer entropy has been introduced [Schreiber, 2000, Kaiser and Schreiber, 2002]. Transfer entropy is a modified version of the Kullback-Leibler entropy [Cover and Thomas, 1991].

Within the phase approach, very recently a partial phase synchronization index has been introduced [Schelter et al., 2006]. This method allows the estimation of the strength but not of the direction of interdependences. To this concern, an approach exists and it is based on the modeling of the phase dynamics [Rosenblum et al., 2001, Cimponeriu et al., 2003]. This latter estimator allows the estimation of strength and direction when the hypothesis of weak interactions among the sub-systems is plausible.

In this chapter, we describe two new estimators to extract partial cooperativeness within the network under study. The first estimator is a natural extension of the S estimator and is based on the partial correlation matrix instead of the correlation one. Partial correlations are a well established statistical tool to examine correlations between signals conditionally upon third signals [Stuart et al., 1999]. We call this estimator *partial S estimator*. The partial S estimator allows the inference of the strength of the interaction and not of its direction. We propose another new method, which allows to estimate strength and direction of weak interactions within multivariate time series when a deterministic hypothesis about the processes behind the recordings is plausible. This last method is parametric and consists of building a functional model from the multivariate data by identifying an autonomous multi-output system.

A detailed description of the partial S estimator is given in Sec. 4.2, whilst in Sec. 4.3 we test it with artificial data. In Sec. 4.5 we introduce the other (parametric) method, and in Sec. 4.6 we validate it on numerically generated data.

4.2 Partial S estimator

We start from the model composed of Eqs. (2.4), (2.5) and (2.6). We have available P time series, one from each dynamical sub-system under study, and we denote them by $\mathbf{Y} = \{Y_t\}$, $t = 0, \ldots, L-1$, where $Y_t \in \mathbb{R}^P$ is the t-th sample observation vector and L is the number of available samples. Without loss of generality, we can consider $\mathbf{Y}$ as de-trended to zero mean and normalized to unitary variance.

To illustrate the procedure, let us consider $P = 3$ and let us suppose that we want to estimate the interdependence between the first two sub-systems marginalizing the

knowledge of the third one. Furthermore, we consider delay-embedded signals in $n^{(i)}$-dimensional spaces, $\forall i$. For not-embedded signal, it is equivalent to fix $n^{(i)} = 1$, $\forall i$.

Let us compute the $N \times N$ (where $N = \sum_{j=1}^{3} n^{(j)}$) zero-lag correlation matrix $\mathbf{C}$ of the whole network embedded trajectory. $\mathbf{C}$ can be tri-partitioned as

$$\mathbf{C} = \begin{bmatrix} \mathbf{C}^{(1,1)} & \mathbf{C}^{(1,2)} & \mathbf{C}^{(1,3)} \\ \mathbf{C}^{(1,2)^T} & \mathbf{C}^{(2,2)} & \mathbf{C}^{(2,3)} \\ \mathbf{C}^{(1,3)^T} & \mathbf{C}^{(2,3)^T} & \mathbf{C}^{(3,3)} \end{bmatrix}, \tag{4.1}$$

where the $n^{(i)} \times n^{(i)}$ matrices $\mathbf{C}^{(i,i)}$, $i = 1, 2, 3$, collect the *intra-sub-system* correlation terms, *i.e.* the correlation between state-variables of the same sub-system, the $n^{(1)} \times n^{(2)}$ matrix $\mathbf{C}^{(1,2)}$ collects the *inter-sub-system* correlation terms, which are the interdependences in our interest. We would like to marginalize them with respect to the "rest of the world" correlation terms collected by the $n^{(1)} \times n^{(3)}$ matrix $\mathbf{C}^{(1,3)}$ along with the $n^{(2)} \times n^{(3)}$ matrix $\mathbf{C}^{(2,3)}$.

By following the procedure proposed in [Stuart et al., 1999], the correlation structure of sub-systems (1) and (2) conditionally upon sub-system (3) is given by the the following matrix transformation

$$\begin{aligned} \mathbf{H} &= \begin{bmatrix} \mathbf{H}^{(1,1)} & \mathbf{H}^{(1,2)} \\ \mathbf{H}^{(1,2)^T} & \mathbf{H}^{(2,2)} \end{bmatrix} = \\ &= \begin{bmatrix} \mathbf{C}^{(1,1)} & \mathbf{C}^{(1,2)} \\ \mathbf{C}^{(1,2)^T} & \mathbf{C}^{(2,2)} \end{bmatrix} - \begin{bmatrix} \mathbf{C}^{(1,3)} \\ \mathbf{C}^{(2,3)} \end{bmatrix} \mathbf{C}^{(3,3)^{-1}} \begin{bmatrix} \mathbf{C}^{(1,3)^T} & \mathbf{C}^{(2,3)^T} \end{bmatrix}. \end{aligned} \tag{4.2}$$

By construction, $\mathbf{H}$ is a $\left(n^{(1)} + n^{(2)}\right) \times \left(n^{(1)} + n^{(2)}\right)$ matrix. $\mathbf{H}$ accounts for the marginalized interdependences between the sub-systems (1) and (2). $\mathbf{H}$ is still not a proper correlation matrix, because usually a transformation to have ones on the diagonal is performed. In our case, a normalization step to transform $\mathbf{H}^{(1,1)}$ and $\mathbf{H}^{(2,2)}$ to identity matrices is possible. Indeed, we can proceed similarly as in Sec. 3.2.1 with the similarity transformation $\mathbf{H}' = \mathbf{T}^T \mathbf{H} \mathbf{T}$, where

$$\mathbf{T} = \begin{bmatrix} \mathbf{H}^{(1,1)^{-\frac{1}{2}}} & \mathbf{0} \\ \mathbf{0} & \mathbf{H}^{(2,2)^{-\frac{1}{2}}} \end{bmatrix}$$

This transformation holds if an appropriate embedding is performed. Once the partial correlation matrix has been computed, we can quantify the interdependence between the first two sub-systems marginalized upon the third one through the formula in Eq. (3.10). From here on, we shall denote as pS the estimates of partial interdependences.

Clearly, this strategy can be extended to the marginalization of more than one sub-system, and, moreover, can be extended to the study of partial interdependences between communities of sub-systems.

For the interested reader, the proof of Eq. (4.2) may be found in [Stuart et al., 1999].

4.3 Numerical validation of partial *S*

In this section we test the ability of the method to estimate correctly direct interdependences among interacting sub-systems. In particular, we address the issue of discerning between direct and indirect couplings among three interacting sub-systems. Moreover,

we test the robustness of the partial S estimator with respect to the amount of data, the observational noise intensity, and the modeling noise intensity. Finally, we test its ability to detect the interactions in a large network of interacting sub-systems.

4.3.1 Marginalization of third knowledge

Here, we test the capability of the partial S estimator to marginalize third knowledge. We considered a heterogenous network composed of three structurally different noise-driven dynamical sub-systems, namely Rössler (R), Lorenz (L) and Colpitts (C) chaotic systems. We coupled them correspondingly to the three situations reported in Figs. 4.1 (a), (b), and (c). The first two coupling schemes are representative of multivariate settings in which spurious relationships can arise when the analysis is limited to a subset of the interacting sub-systems [Hsiao, 1982, Dahlhaus et al., 1997]. In (a) an undirect connection between L and C may be inferred because of the common source R, also called a confounder. In the case of a chain-like interaction topology as reported in (b), a non existent (undirect) connection between R and C may be inferred when the analysis does not marginalize the knowledge about L.

While in the two former cases a marginalization procedure is useful and necessary, in the third case (c) it would lead to a wrong result. Indeed, in scheme (c), a non-existent interaction between R and L may be inferred when marginalizing with respect to their common destination C, or child[1]. Consequently, as we will show later, a combined approach of the partial S estimator and of the S estimator is necessary.

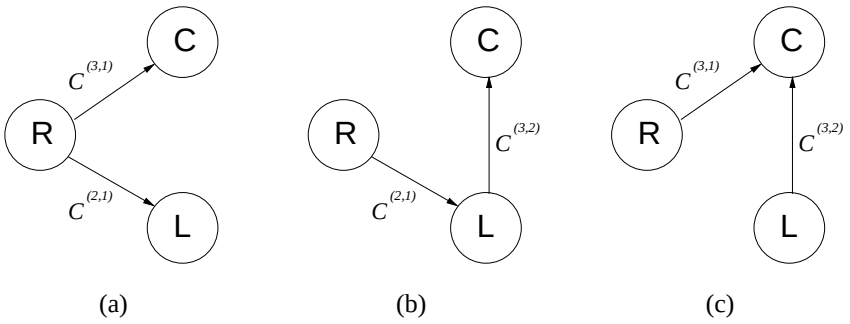

Fig. 4.1. Connection setups used for the validation of the method. (a, b, c) Setups for triangular interdependence assessments – coupled Rössler (R), Lorenz (L) and Colpitts (C) dynamical sub-systems, *cf.* Eq. (4.3): (a) case of common source; (b) case of chain connection; (c) case of common child.

Going back to our validation tests, the equations governing the dynamics of these three coupled sub-systems are

[1] This scheme is a particular instance of a more general setting which in jargon refers to the "marrying-parents" effect [Wittaker, 1990].

$$
\begin{cases}
\dot{\theta}_1^{(1)} = T\left[\theta_2^{(1)} + \theta_3^{(1)} + \mathcal{C}^{(1,2)}\left(\theta_1^{(2)} - \theta_1^{(1)}\right) + \mathcal{C}^{(1,3)}\left(\theta_1^{(3)} - \theta_1^{(1)}\right) + \eta_1^{(1)}\right], \\
\dot{\theta}_2^{(1)} = T\left[\theta_1^{(1)} + a\theta_2^{(1)} + \eta_2^{(1)}\right], \\
\dot{\theta}_3^{(1)} = T\left[b + \theta_3^{(1)}\left(\theta_1^{(1)} - c\right) + \eta_3^{(1)}\right], \\
\\
\dot{\theta}_1^{(2)} = \sigma\left(\theta_2^{(2)} - \theta_1^{(2)}\right) + \mathcal{C}^{(2,1)}\left(\theta_1^{(1)} - \theta_1^{(2)}\right) + \mathcal{C}^{(2,3)}\left(\theta_1^{(3)} - \theta_1^{(2)}\right) + \eta_1^{(2)}, \\
\dot{\theta}_2^{(2)} = r\theta_1^{(2)} - \theta_2^{(2)} - \theta_1^{(2)}\theta_3^{(2)} + \eta_2^{(2)}, \\
\dot{\theta}_3^{(2)} = \theta_1^{(2)}\theta_2^{(2)} - \beta\theta_3^{(2)} + \eta_3^{(2)}, \\
\\
\dot{\theta}_1^{(3)} = T\left[\frac{g}{Q\,(1-k)}\left(\alpha\left(1 - e^{-\theta_2^{(3)}}\right) + \theta_3^{(3)}\right) + \mathcal{C}^{(3,1)}\left(\theta_2^{(1)} - \theta_2^{(3)}\right) + \mathcal{C}^{(3,2)}\left(\theta_2^{(2)} - \theta_2^{(3)}\right) + \eta_1^{(3)}\right], \\
\dot{\theta}_2^{(3)} = T\left[\frac{g}{Qk}\left((1-\alpha)\left(1 - e^{-\theta_2^{(3)}}\right) + \theta_3^{(3)}\right) + \eta_2^{(3)}\right], \\
\dot{\theta}_3^{(3)} = -T\left[\frac{Qk\,(1-k)}{g}\left(\theta_1^{(3)} + \theta_2^{(3)}\right) + \frac{1}{Q}\theta_3^{(3)} + \eta_3^{(3)}\right],
\end{cases}
\tag{4.3}
$$

where $\theta_j^{(1)}, \theta_j^{(2)}, \theta_j^{(3)}$, $j = 1, 2, 3$ are the state variables of the Rössler, Lorenz and Colpitts dynamical sub-systems, respectively; $a = 0.4$, $b = 0.4$, $c = 5.7$, $\sigma = 10$, $\beta = 8/3$, $r = 28$, $g = 10^{0.625}$, $Q = 10^{0.15}$, $\alpha = 0.996$, $k = 0.5$ are standard valued parameters; $\eta_j^{(i)}$, $i, j = 1, 2, 3$, are zero-mean uncorrelated Gaussian random noises (set to the strength of 1% of the energy of the right hand side along the uncoupled attractors); and $\mathcal{C}^{(i,j)}$, $i \neq j$, $i, j = 1, 2, 3$, are the strengths of diffusive couplings between the first state variables $\theta_1^{(1)}$, $\theta_1^{(2)}$ and $\theta_1^{(3)}$. The parameter $T = 6$ is introduced in order to adapt the relative speed differences between the three sub-systems. To simulate the three schemes (a), (b), (c) in Fig. 4.1, we set the values of the coupling strengths as following: for (a), $\mathcal{C}^{(1,2)} = \mathcal{C}^{(1,3)} = \mathcal{C}^{(2,3)} = \mathcal{C}^{(3,2)} = 0$ and $\mathcal{C}^{(2,1)}$, $\mathcal{C}^{(3,1)}$ non zero and positive; for (b), $\mathcal{C}^{(1,2)} = \mathcal{C}^{(1,3)} = \mathcal{C}^{(2,3)} = \mathcal{C}^{(3,1)} = 0$ and $\mathcal{C}^{(2,1)}$, $\mathcal{C}^{(3,2)}$ non zero and positive; and for (c), $\mathcal{C}^{(1,2)} = \mathcal{C}^{(1,3)} = \mathcal{C}^{(2,3)} = \mathcal{C}^{(2,1)} = 0$ and $\mathcal{C}^{(3,1)}$, $\mathcal{C}^{(3,2)}$ non zero and positive.

These active parameters were varied as following: for (a), $\mathcal{C}^{(3,1)}$ within the interval $[0, 5]$ and $\mathcal{C}^{(2,1)}$ within the interval $[0, 15]$; for (b), $\mathcal{C}^{(3,2)}$ within the interval $[0, 10]$ and $\mathcal{C}^{(2,1)}$ within the interval $[0, 20]$; for (c), $\mathcal{C}^{(3,2)}$ and $\mathcal{C}^{(3,1)}$ within the interval $[0, 5]$. All of them represent a condition of strong coupling.

For every considered value of the couplings, the network was simulated starting from random initial conditions. The transients were discarded, and time series of length $L = 5000$ were collected by sampling ($\delta T = 0.02$) the coupled variables $\theta_1^{(1)}$, $\theta_1^{(2)}$ and $\theta_1^{(3)}$ corrupted by zero-mean white Gaussian observational noise leading to 40 dB SNR. From these measurements, we reconstructed 4-dimensional state spaces by delay embedding the time series with $\tau^{(1)} = 0.24$, $\tau^{(2)} = 0.18$, and $\tau^{(3)} = 0.3$. As usual, the delay times were estimated by the first minimum of the time delayed mutual information. For the sake of the simplicity, we fixed to 4 the dimension of the embedded state-spaces for all the sub-systems; however, we verified the consistency and the robustness of the results for other choices of this parameter, *i.e.* 3, 4 or 5.

Common source like connection

The results for the case of the common source (Fig. 4.1 (a)) are shown in Figs. 4.2 and 4.3. Figure 4.2 reports the dependence of $pS^{(2,3)}$ ($= pS^{(3,2)}$) and $S^{(2,3)}$ upon the coupling strengths $\mathcal{C}^{(2,1)}$ and $\mathcal{C}^{(3,1)}$ evaluated at 100 evenly spaced points. Correctly, $pS^{(2,3)}$ stays close to zero and do not scale with neither of the coupling strengths, whilst the $S^{(2,3)}$ does scale, showing that the marginalization upon the measurements from the third sub-system does improve the interdependence estimation. We remark that $pS^{(2,3)}$ scales weakly upon the couplings, however at very low values compared to $pS^{(1,2)}$ and $pS^{(1,3)}$. Indeed, we remark that $pS^{(2,3)}$ is almost always lower to $pS^{(1,2)}$ and $pS^{(1,3)}$, which, as shown in Fig. 4.3, scale correctly with the coupling strengths. Also, we remark that they decrease slowly with the increase of both coupling strengths. This phenomenon can be explained by the fact that the three sub-systems influence each other and, consequently, become more and more similar, jeopardizing the measurement-wise reconstruction.

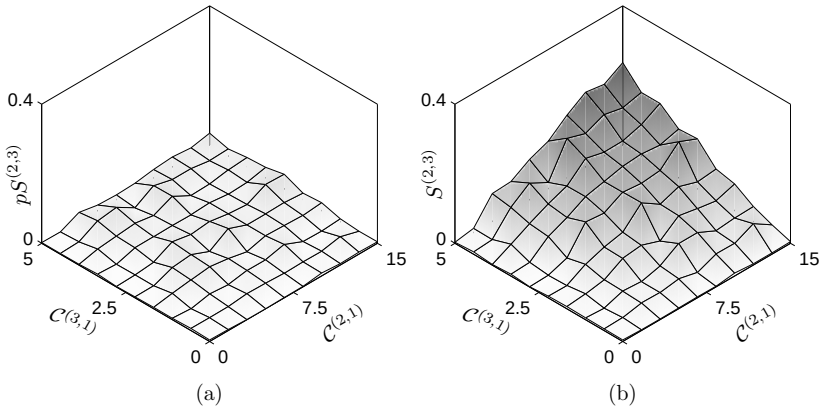

Fig. 4.2. Numerical assessment of the partial S estimator as a measure of direct interdependence: estimated C – L interdependence in the case of common source connection (*cf.* Fig. 4.1(a)). Dependence of (a) – $pS^{(2,3)}$ and (b) – $S^{(2,3)}$ upon the coupling strengths $\mathcal{C}^{(3,1)}$ and $\mathcal{C}^{(2,1)}$.

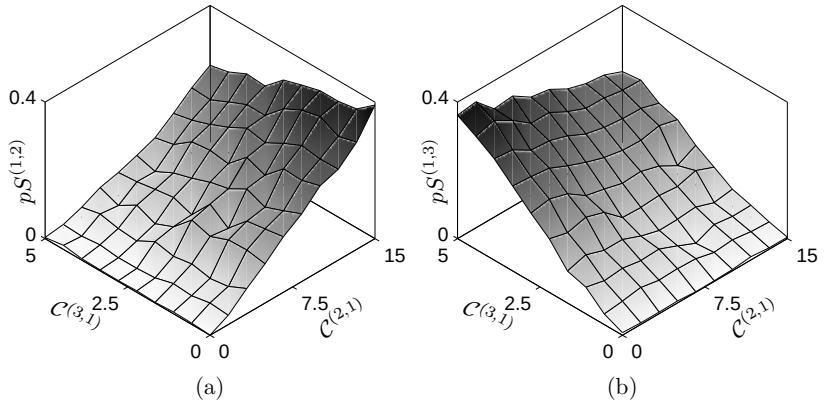

Fig. 4.3. Numerical assessment of the partial S estimator as a measure of direct interdependence: estimated R – C and R – L interdependences in the case of common source connection (*cf.* Fig. 4.1(b)). Dependence of (a) – $pS^{(1,2)}$ and (b) – $pS^{(1,3)}$ upon the coupling strengths $\mathcal{C}^{(3,1)}$ and $\mathcal{C}^{(2,1)}$.

Chain like connection

The results for the case of the chain connection (Fig. 4.1 (b)) are shown in Figs. 4.4 and 4.5. Figure 4.4 reports the dependence of $pS^{(1,3)}$ ($= pS^{(3,1)}$) and $S^{(1,3)}$ upon the coupling strengths $\mathcal{C}^{(3,2)}$ and $\mathcal{C}^{(2,1)}$ evaluated at 100 evenly spaced points. Correctly, $pS^{(1,3)}$ stays closer to zero than $S^{(1,3)}$, showing that the marginalization upon the measurements from the third sub-system does improve the interdependence estimation. We remark that $pS^{(1,3)}$ scales weakly upon the couplings, however at very low values compared to $pS^{(1,2)}$ and $pS^{(2,3)}$. Indeed, we remark that $pS^{(1,3)}$ is almost always lower to $pS^{(1,2)}$ and $pS^{(2,3)}$, which, as shown in Fig. 4.5, scale correctly with the coupling strengths. Also, we remark that they decrease slowly with the increase of both coupling strengths. This phenomenon can be explained by the fact that the three sub-systems influence each other and, consequently, become more and more similar, jeopardizing the measurement-wise reconstruction.

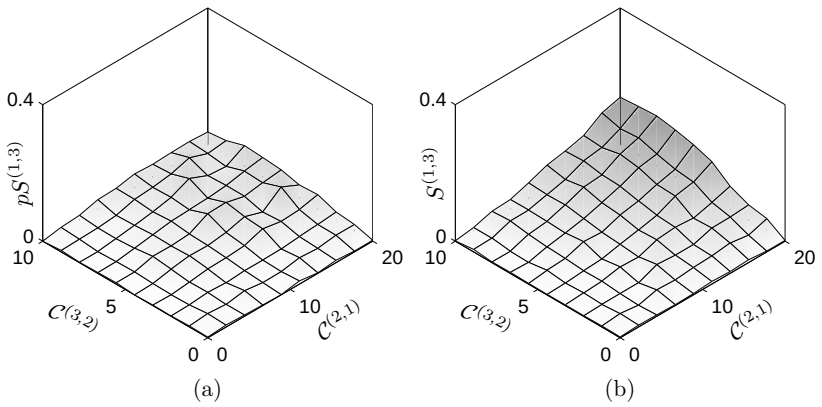

Fig. 4.4. Numerical assessment of the partial S estimator as a measure of direct interdependence: estimated R – C interdependence in the case of chain connection (*cf.* Fig. 4.1(b)). Dependence of (a) – $pS^{(1,3)}$ and (b) – $S^{(1,3)}$ upon the coupling strengths $\mathcal{C}^{(3,2)}$ and $\mathcal{C}^{(2,1)}$.

Common child like connection

As a consequence of the results showed in the previous two paragraphs, it might be thought to consider only partial S for estimating interdependences, disposing of S. However, this is not the case because of the so-called "marrying-parents" effect, commonly observable in the case, illustrated in Fig. 4.1(c), of a common child. For this case, as shown in Fig. 4.7, $pS^{(1,3)}$ and $pS^{(2,3)}$ scale correctly with the coupling strengths $\mathcal{C}^{(3,1)}$ and $\mathcal{C}^{(3,2)}$. However, as shown in Fig. 4.6(a), $pS^{(1,2)}$ does scale with the couplings, leading to the incorrect inference of a non-existent interdependence between R and L. However, the voidance of this coupling can be easily tested by means of the $S^{(1,2)}$ estimator which, as shown in Fig. 4.6(b), correctly stays close to zero.

From these three numerical experiments we can conclude that, by combining both S and pS estimators, we can correctly estimate the interdependences within a network of

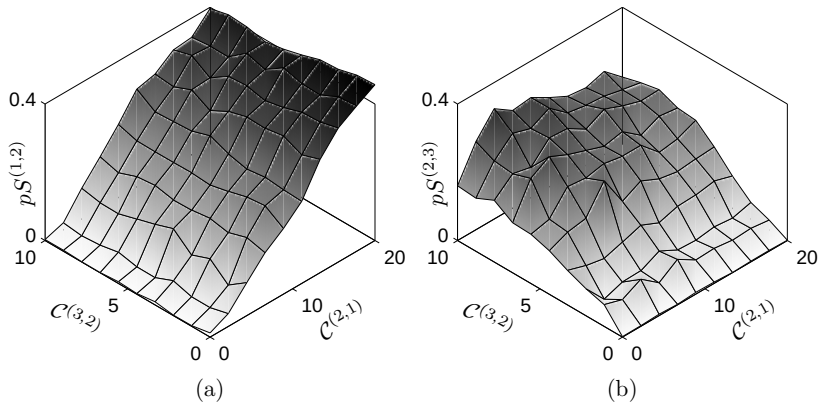

Fig. 4.5. Numerical assessment of the partial S estimator as a measure of direct interdependence: estimated R – L and L – C interdependences in the case of chain connection (*cf.* Fig. 4.1(a)). Dependence of (a) – $pS^{(1,2)}$ and (b) – $pS^{(2,3)}$ upon the coupling strengths $\mathcal{C}^{(3,2)}$ and $\mathcal{C}^{(2,1)}$.

coupled dynamical sub-systems. The strategy is to compute both estimators for each interaction of interest, and to consider as its strength the smaller value between the computed two.

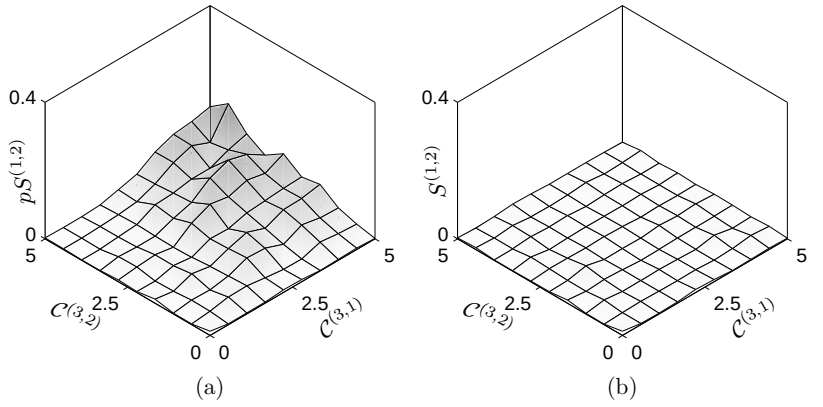

Fig. 4.6. Numerical assessment of the partial S estimator as a measure of direct interdependence: estimated R – L interdependence in the case of common child connection (*cf.* Fig. 4.1(c)). Dependence of (a) – $pS^{(1,2)}$ and (b) – $S^{(1,2)}$ upon the coupling strengths $\mathcal{C}^{(3,2)}$ and $\mathcal{C}^{(3,1)}$.

4.3.2 Robustness assessment

In this section we proceed to the numerical assessment of the sensitiveness of the partial S estimator to observational noise intensity, modeling noise intensity and amount of data. We considered a network of three noise-driven sub-systems, namely a chaotic Hindmarsh-Rose system [Hindmarsh and Rose, 1984] nonlinearly driving a chaotic Lorenz one, with a non-coupled chaotic Colpitts system as model of the rest of the world. The equations governing the dynamics were

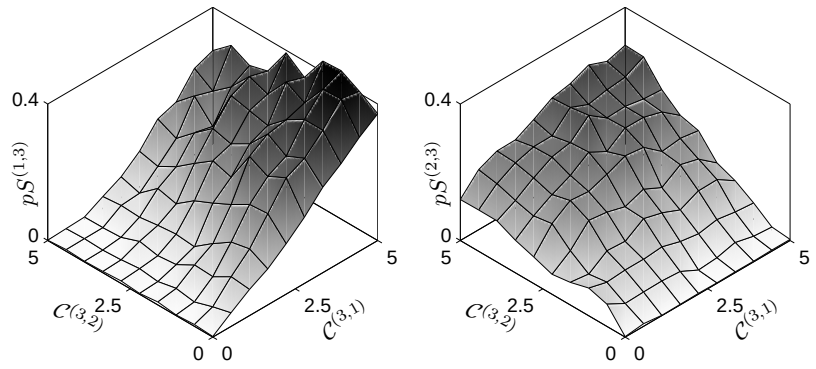

(a) (b)

Fig. 4.7. Numerical assessment of the partial S estimator as a measure of direct interdependence: estimated R – C and L – C interdependences in the case of common child connection (*cf.* Fig. 4.1(c)). Dependence of (a) – $pS^{(1,3)}$ and (b) – $pS^{(2,3)}$ upon the coupling strengths $\mathcal{C}^{(3,2)}$ and $\mathcal{C}^{(3,1)}$.

$$
\begin{cases}
\dot{\theta}_1^{(1)} = T^{(1)} \left[\theta_2^{(1)} - \left(\theta_1^{(1)}\right)^3 + b \left(\theta_1^{(1)}\right)^2 - \theta_3^{(1)} + I + \eta_1^{(1)} \right], \\
\dot{\theta}_2^{(1)} = T^{(1)} \left[1 - s \left(\theta_1^{(1)}\right)^2 + \eta_2^{(1)} \right], \\
\dot{\theta}_3^{(1)} = T^{(1)} \left[\mu \left(h \left(\theta_1^{(1)} + c\right) - \theta_3^{(1)} \right) + \eta_3^{(1)} \right], \\
\\
\dot{\theta}_1^{(2)} = \sigma \left(\theta_2^{(2)} - \theta_1^{(2)}\right) + \mathcal{C}^{(2,1)} \left(\theta_1^{(1)} - \theta_1^{(2)}\right)^3 + \eta_1^{(2)}, \\
\dot{\theta}_2^{(2)} = r\theta_1^{(2)} - \theta_2^{(2)} - \theta_1^{(2)}\theta_3^{(2)} + \eta_2^{(2)}, \\
\dot{\theta}_3^{(2)} = \theta_1^{(2)}\theta_2^{(2)} - \beta\theta_3^{(2)} + \eta_3^{(2)}, \\
\\
\dot{\theta}_1^{(3)} = T^{(3)} \left[\dfrac{g}{Q\,(1-k)} \left(\alpha \left(1 - e^{-\theta_2^{(3)}} \right) + \theta_3^{(3)} \right) + \eta_1^{(3)} \right], \\
\dot{\theta}_2^{(3)} = T^{(3)} \left[\dfrac{g}{Qk} \left((1-\alpha) \left(1 - e^{-\theta_2^{(3)}} \right) + \theta_3^{(3)} \right) + \eta_2^{(3)} \right], \\
\dot{\theta}_3^{(3)} = -T^{(3)} \left[\dfrac{Qk\,(1-k)}{g} \left(\theta_1^{(3)} + \theta_2^{(3)} \right) + \dfrac{1}{Q}\theta_3^{(3)} + \eta_3^{(3)} \right],
\end{cases}
\tag{4.4}
$$

where $\theta_j^{(1)}, \theta_j^{(2)}, \theta_j^{(3)}$, $j = 1, 2, 3$ are the state variables of the Hindmarsh-Rose, Lorenz and Colpitts dynamical sub-systems, respectively; $\mu = 0.01$, $c = 1.6$, $s = 5$, $h = 4$, $b = 2.83$, $I = 3.86$, $\sigma = 10$, $\beta = 8/3$, $r = 28$, $g = 10^{0.625}$, $Q = 10^{0.15}$, $\alpha = 0.996$, $k = 0.5$ are standard valued parameters; $\eta_j^{(i)}$, $i, j = 1, 2, 3$, are zero-mean uncorrelated Gaussian random noises and $\mathcal{C}^{(2,1)}$ is the strength of nonlinear coupling between the first state variables $\theta_1^{(1)}$, $\theta_1^{(2)}$. The parameters $T^{(1)} = 18$ and $T^{(3)} = 6$ are introduced in order to adapt the relative speed differences between the three sub-systems.

In the simulation, we varied $\mathcal{C}^{(2,1)}$ within the interval $[0, 0.5]$, which represents a condition of strong coupling. For every considered value of $\mathcal{C}^{(2,1)}$, the differential equations were iterated, starting from random initial conditions. The transients were discarded,

and time series of 500 points each were collected ($\delta T = 0.02$). We collected a total of 80 trials from different initial conditions, measuring the variables $\theta_1^{(1)}$, $\theta_1^{(2)}$ and $\theta_1^{(3)}$.

From these measurements, we reconstructed 4-dimensional state-spaces by delay embedding the time series with $\tau^{(1)} = 0.56$, $\tau^{(2)} = 0.2$ and $\tau^{(3)} = 0.3$. The time lag were computed as the first minimum of the time delayed mutual information. The embedding dimensions were estimated by applying the method of the false nearest neighbors [Boccaletti et al., 2002b] to time series corrupted with 40 dB SNR of observational noise and measured from the sub-systems under weak coupling and with 40 dB SNR of modeling noise.

Amount of data vs. *observational noise intensity*

Here, we show the result of the assessment of the robustness of the partial S estimator with respect to measurement noise and data length. In the simulation, we fixed the modeling noise intensity to 40 dB SNR and we varied the observational noise intensity, *i.e.* 40, 20, 12 dB SNR. We computed the partial S estimator on delay embedded data and not, that we indicate as pS and pS_{ne}, respectively. These two estimators were computed trial-wise on 20, 40 and 80 trials, respectively.

The results are showed in Fig. 4.8. $pS^{(1,2)}$ and ${pS_{ne}}^{(1,2)}$ scale similarly upon the coupling parameter; nevertheless, ${pS_{ne}}^{(1,2)}$ scales in a wider range. For the two estimators, the computed values decrease when noise is increased. Furthermore, as expected, their reliability increases (*cf.* the error bars decrease) with data length.

Finally, we remark that the better performance of ${pS_{ne}}^{(1,2)}$ with respect to $pS^{(1,2)}$ should not be illusive. Indeed, the choice of the embedding parameters may not be optimal for strongly interacting sub-systems, when synchronization manifolds arise and, consequently, the embedding dimension of the whole network decreases. Furthermore, we studied the sensitiveness of the two estimators upon the observed state variables. We found that in most cases $pS^{(1,2)}$ correctly detects the presence of coupling, while ${pS_{ne}}^{(1,2)}$ does it in a few number of cases.

Amount of data vs. *modeling noise intensity*

Here, we show the result of the assessment of the robustness of the partial S estimator with respect to modeling noise and data length. In the simulation, we fixed the observational noise intensity to 40 dB SNR and we varied the modeling noise intensity, *i.e.* 20, 12, 6 dB SNR. We computed the partial S estimator on delay embedded data and not trial-wise on 20, 40 and 80 trials, respectively.

The results are shown in Fig. 4.9. $pS^{(1,2)}$ and ${pS_{ne}}^{(1,2)}$ scale similarly upon the coupling parameter; nevertheless, ${pS_{ne}}^{(1,2)}$ scales in a wider range (the same considerations of the previous case hold). For the two estimators, the computed values decrease when noise is increased. Furthermore, as expected, their reliability increases (*cf.* the error bars decrease) with data length.

4.3.3 Saliency and scalability

In the previous sections, we have tested the capability of the method in standard problems arising in multivariate settings. Still, we shall discuss its feasibility when dealing with large systems in terms of saliency to infer the network wiring and scalability upon the number of sub-systems.

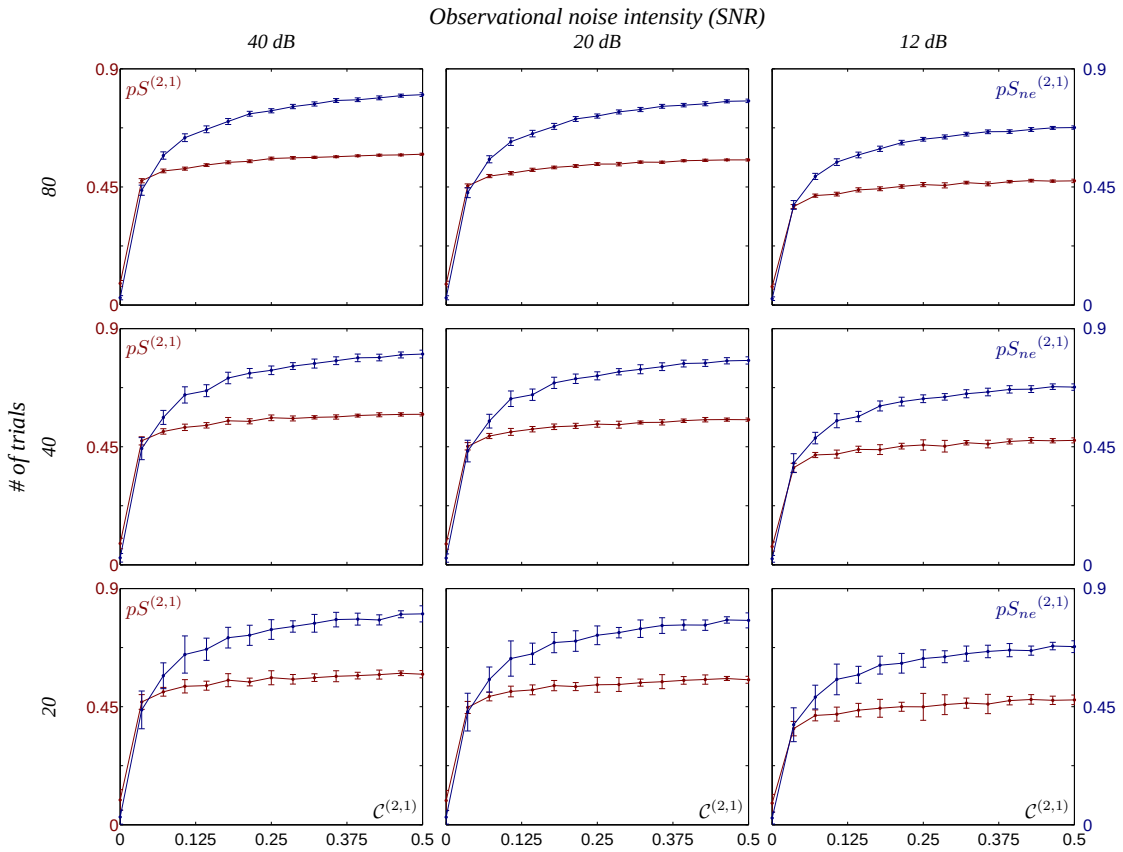

Fig. 4.8. Numerical assessment of the partial S estimator as a measure of direct interaction: sensitiveness upon observational noise intensity and data length. Dependence of the interdependence between the sub-systems (1) and (2) upon sub-system (3) of system Eq. (4.4), upon the coupling parameter $\mathcal{C}^{(2,1)}$, estimated with different techniques: $pS^{(2,1)}$ (red); $pS_{ne}{}^{(2,1)}$ (blue). Robustness of these measures with respect to observational noise, considering 40, 20, and 12 dB Signal to Noise Ratio, and data lengths, considering 20, 40, and 80 trials of 500 samples each. The dots and errors bars illustrate the mean value and standard deviation, respectively.

Saliency is the property related to the ability of infer the interdependence strength independently on the number of sub-systems composing the third knowledge. Ideally, the inferred strength should be (statistically) constant with respect to the number of marginalized sub-systems.

In this section, we describe two tests to assess these two aspects of the method within the same paradigm. We considered a large network composed of $M = 128$ sub-systems, a number that represents the state-of-art in modern experimental setups. Similarly to the test presented in the previous chapter, we considered noise-driven linearly coupled non-identical sub-systems, namely Colpitts systems. The equations governing their dynamics were

$$\begin{cases} \dot{\theta}_1^{(i)} = \dfrac{g^{(i)}}{Q^{(i)}\left(1-k\right)}\left(\alpha\left(1-e^{-\theta_2^{(3)}}\right)+\theta_3^{(i)}\right)+\displaystyle\sum_{j\neq i}\mathcal{C}^{(i,j)}\left(\theta_1^{(j)}-\theta_1^{(i)}\right)+\eta_1^{(i)}, \\ \dot{\theta}_2^{(i)} = \dfrac{g^{(i)}}{Q^{(i)}k}\left(\left(1-\alpha\right)\left(1-e^{-\theta_2^{(3)}}\right)+\theta_3^{(i)}\right)+\eta_2^{(i)}, \\ \dot{\theta}_3^{(i)} = -\dfrac{Q^{(i)}k\left(1-k\right)}{g^{(i)}}\left(\theta_1^{(i)}+\theta_2^{(i)}\right)-\dfrac{1}{Q^{(i)}}\theta_3^{(i)}+\eta_3^{(i)}, \end{cases} \tag{4.5}$$

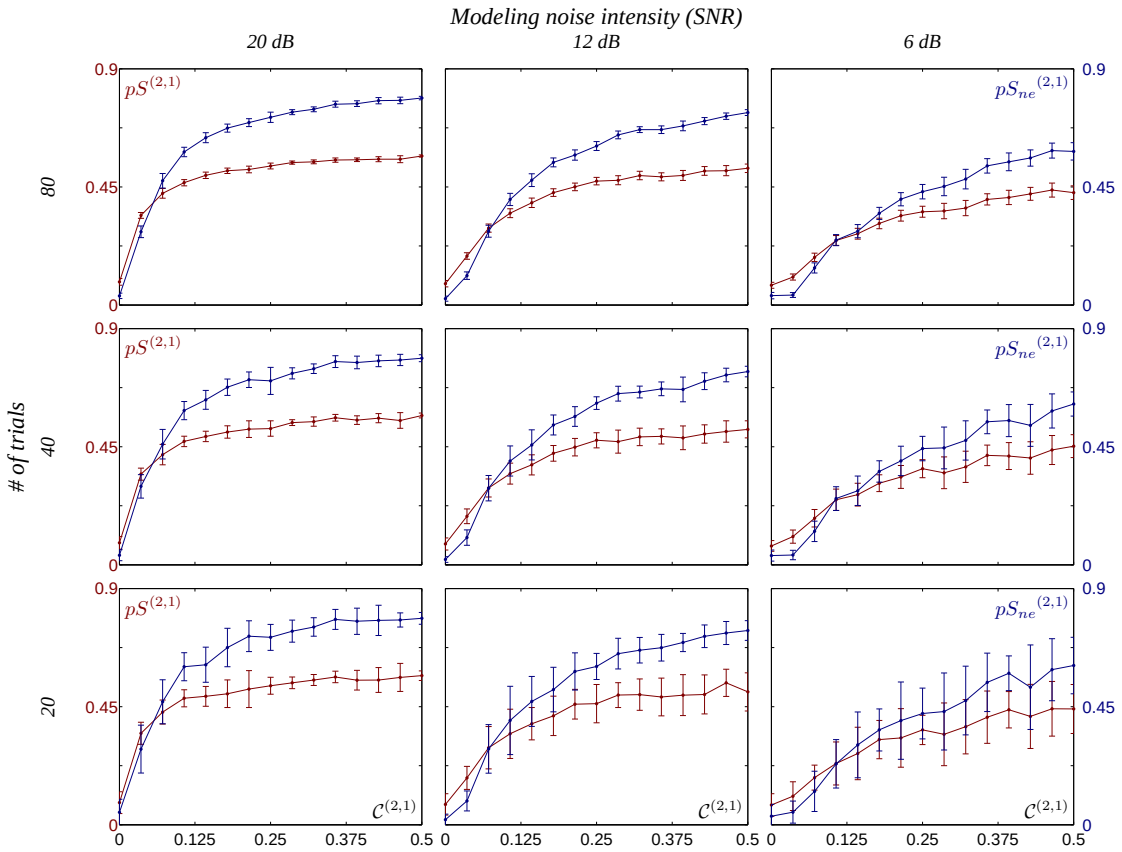

Fig. 4.9. Numerical assessment of the partial S estimator as a measure of direct interaction: sensitiveness upon modeling noise intensity and data length. Dependence of the interdependence between the sub-systems (1) and (2) upon sub-system (3) of system Eq. (4.4), upon the coupling parameter $\mathcal{C}^{(2,1)}$, estimated with different techniques: $pS^{(2,1)}$ (red); $pS_{ne}{}^{(2,1)}$ (blue). Robustness of these measures with respect to modeling noise, considering 20, 12, and 6 dB Signal to Noise Ratio, and data lengths, considering 20, 40, and 80 trials of 500 samples each. The dots and errors bars illustrate the mean value and standard deviation, respectively.

where $\theta_j^{(i)}, j = 1, 2, 3$, are the state variables of each sub-system $i = 1, \ldots, 128$; α and k are parameters fixed at the standard values 0.996 and 0.5; $Q^{(i)}$ and $g^{(i)}$ are parameters whose values are chosen randomly in an interval ($\pm 10\%$) around the standard values $10^{0.15}$ and $10^{0.625}$, respectively; $\eta_j^{(i)}$ are zero-mean uncorrelated Gaussian random noises (set in simulations to a variance of 1% of the energy of the right hand side along the uncoupled attractors); and $\mathcal{C}^{(i,j)}$ are the strengths of diffusive couplings between the first state variables. We proceeded to test saliency and scalability as following.

Saliency vs. *number of third sub-systems*

To test the property of saliency of the partial S estimator, we considered two cases: in the first, we set the coupling strength $\mathcal{C}^{(2,1)} = 0.21$ and all the others to zero, in the second all the couplings were zero. We iterated the differential equations, starting from random initial conditions, and we dropped the transients. We recorded a total of 30 trials of different length, namely of 1000, 5000 and 10000 points ($\delta T = 0.063$). We measured the second state variable of each sub-system, *i.e.* $\theta_2^{(i)}, i = 1, \ldots, 128$, to which we added

zero-mean white Gaussian observational noise leading to a signal to noise ratio of 40, dB. To reconstruct the state-space, we used delay-embedding with time delay $\tau^{(i)} = 0.2\ \forall i$, and embedding dimension $n^{(i)} = 4\ \forall i$, that were computed as usual. We computed trial-wise the partial S estimator on delay-embedded data ($pS^{(2,1)}$) and not ($pS_{ne}{}^{(2,1)}$) for the sub-systems (1) and (2) marginalizing at each step upon an increasing number of sub-systems.

For the first case, the results are shown in Fig. 4.10. We remark that for both estimators the estimated non-zero interdependence decreases with the number of marginalized sub-systems. However, the saliency increases when the amount of data points is increased. Furthermore, $pS_{ne}{}^{(2,1)}$ appears to be more salient than $pS^{(2,1)}$. We remark that this might be due to the fact that, because of the embedding, the partial interdependence $pS^{(2,1)}$ is estimated from a bigger number of variables than $pS^{(2,1)}$. This may result in a loss of precision for two reasons: number of available data and condition number of the inverse matrix necessary to compute the partial correlation matrix (*cf.* Eq. (4.2)). Future development of the partial S estimator may include the possibility of improving the computation of this inverse matrix, by, for instance, some regularization technique [Golub and von Matt, 1997].

Finally, we remark that, as expected, the reliability increases (*cf.* the error bars decrease) with the amount of data length.

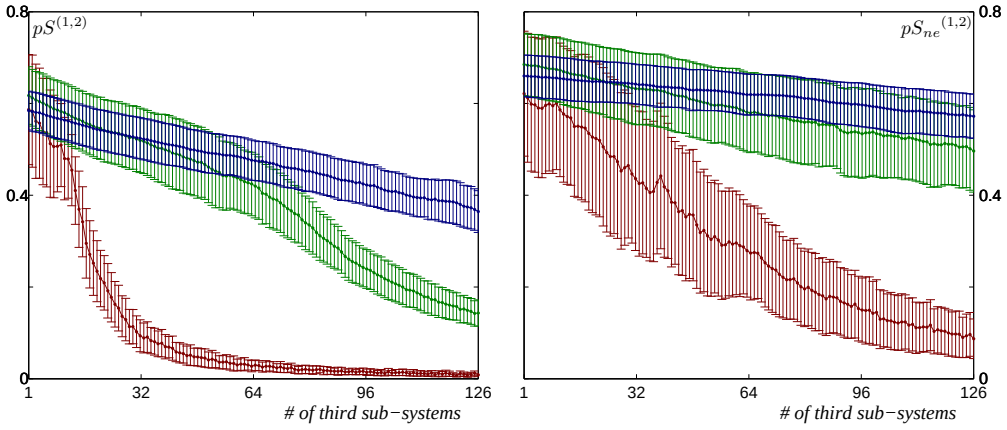

Fig. 4.10. Numerical assessment of the partial S estimator as a measure of direct interaction: saliency upon the number of marginalized dynamical sub-systems, *case of non-zero coupling*. Setup: 128 coupled non-identical Colpitts dynamical systems, *cf.* Eq. (4.5). Dependence of the non-zero interdependence between sub-systems (1) and (2) upon the number of marginalized sub-systems for different trial length: 1000 points (red), 5000 points (green); 10000 points (blue). $pS^{(2,1)}$ estimates are on the left panel, while $pS_{ne}{}^{(2,1)}$ estimates are on the right panel. The dots and errors bars illustrate the mean value and standard deviation, respectively.

For the second case, the results are shown in Fig. 4.11. We remark that zero-interdependence estimation may be troublesome for small numbers of third sub-systems. However, we remark that for both estimators the saliency increases when the amount of data points is increased, *i.e.* the partial S estimations stay closer to zero. Furthermore, as before, $pS_{ne}{}^{(2,1)}$ appears to be more salient than $pS^{(2,1)}$.

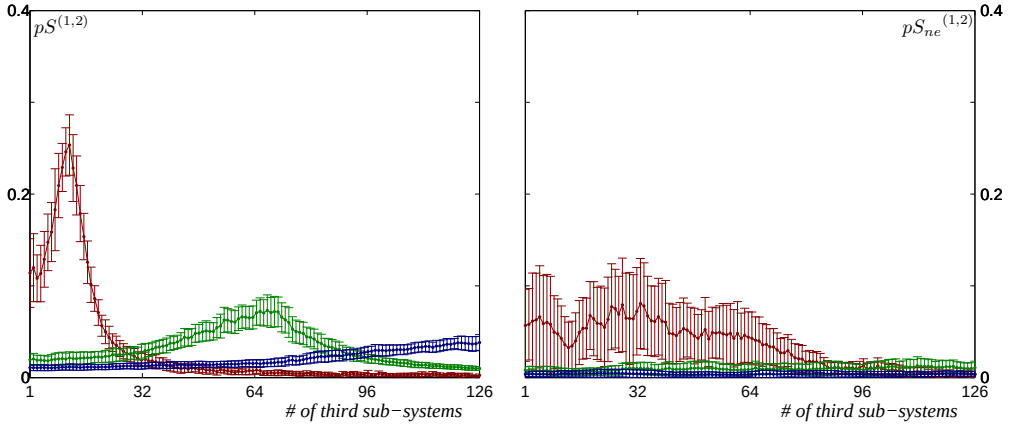

Fig. 4.11. Numerical assessment of the partial S estimator as a measure of direct interaction: saliency upon the number of marginalized dynamical sub-systems, *case of zero coupling*. Setup: 128 coupled non-identical Colpitts dynamical systems, *cf.* Eq. (4.5). Dependence of the zero interdependence between sub-systems (1) and (2) upon the number of marginalized sub-systems for different trial length: 1000 points (red), 5000 points (green); 10000 points (blue). $pS^{(2,1)}$ estimates are on the left panel, while $pS_{ne}{}^{(2,1)}$ estimates are on the right panel. The dots and errors bars illustrate the mean value and standard deviation, respectively.

Finally, we remark that, as expected, the reliability increases (*cf.* the error bars decrease) with the amount of data length.

Scalability vs. *number of sub-systems*

To test the scalability of the partial S estimator, we randomly set the connectivity within the network by choosing an average of two couplings for each sub-system, with a strength value of 0.21, which represents a value of mild coupling.

The differential equations were iterated, starting from random initial conditions, and the transients were dropped. We collected a total of 18 trials from different initial conditions of length $L = 1000$ ($\delta T = 0.063$), measuring the second state variable of each sub-system, *i.e.* $\theta_2^{(i)}, i = 1, \ldots, 128$, to which we added zero-mean white Gaussian observational noise of different intensities, *i.e.* 40, 20 and 12 dB (SNR). Afterwards, we assessed the sensitiveness of the method with respect to measurement noise and data length. This was done for the chosen connectivity matrix and observational noise intensities, over 3, 5, 8, 12 and all the 18 trials[2]. To reduce the computational load, we computed the S and partial S estimators on not embedded data.

The results are reported in Fig. 4.12, which shows the dependence of the percentage of correctly detected couplings upon the number of available data points at the different noise intensities considered. Namely, by partitioning all the estimated interdependences into clusters, we labeled the couplings as either present or absent. Figure 4.12 reports the percentage of the correctly detected non-zero and zero couplings (black and gray curves, respectively).

In general, we expect the percentage of the correctly detected absent couplings (the true negatives) to be higher than that of the present couplings (the true positives), simply

[2] Not trial-wise, but on the merged trials.

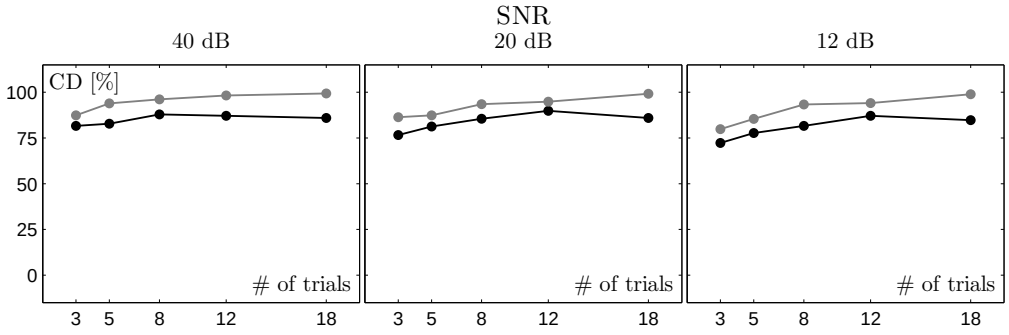

Fig. 4.12. Numerical assessment of the S estimator and partial S estimator as a measure of direct interaction: scalability *vs.* the number of sub-systems. Setup: 128 coupled non-identical Colpitts dynamical systems, *cf.* Eq. (4.5). Dependence of the percentage of correctly detected couplings upon data length (number of trials of 1000 samples each) and intensity of measurement noise (Signal to Noise Ratio, SNR): percentage of correctly detected present (black) and absent (gray) couplings.

because in the considered setup there are 16000 zero connections against 256 non-zero connections. However, for the same reason, we expect correspondingly a percentage of false negatives higher than that of false positives.

The result shows that the reliability of coupling detection is very high for all considered noise intensities and, generally, increases with the amount of data available. Nevertheless, we notice that the percentage of correctly detected non-zero couplings does not improve strongly with the amount of data and stays around 85%, whilst the percentage of false positives (the complement of the percentage of true negatives) does decrease and it falls below 5% with already as few as 8000 points.

Finally, we remark that the power of our method, *i.e.* the percentage of good detections, is remarkably much higher than a purely combinatorial guess, which would result in percentages of almost 2%.

4.4 Remarks

In the previous sections, we have presented a new method to estimate interdependences with respect to third knowledge. We validated the method on artificial data, and the method proved to work well and to be robust with respect to amount of data, observational and modeling noise intensity. Furthermore, the method proved to be satisfactorily salient and scalable upon the number of sub-systems. Apart from this, we remark that further studies about the method are needed: the method should be applied to networks with different topologies, as scale free or regular, to test its capability of extracting network topology; a study of the sensitiveness of the partial S estimator upon different choices of the embedding dimension would be useful. Finally, we think that, if possible, a level of significance for the no-coupling condition should be quantitatively worked out: this may be useful especially for passive experiments (*i.e.* experiment with only one system observation at hand).

Our method presents some limitations. First, it does not estimate a direction of the coupling. Second, it relies upon second order momentum properties of the sub-systems under consideration and, consequently, it might fail in the detection of interdependences weak or eliciting higher momentums.

However, as noticed for the S estimator in the previous chapter, the partial S estimator could be computed as well starting from other partial inter-relation matrices. For instance, we mention the possibility of building a matrix with conditional mutual information as elements [Cover and Thomas, 1991].

Moreover, this property would potentially allow the definition of a *directed* partial S estimator by using a pair-wise partial directed interdependence measure.

However, we stress that we need to estimate pair-wise interdependence quantities conditioned upon the rest of the world, that could be represented by a large amount of variables. Indeed, the mapping between pair-wise interdependences to multivariate partial interdependences is unfortunately valid only for linear correlations. Indeed, the transformation reported in Eq. (4.2) is valid for linear correlation coefficients. It would be interesting to explore the possibility of using such transformation with other interdependence measures.

In the next sections, we address the problem of estimating not only the strength, but also the direction of interdependences in multivariate time series.

4.5 Method

Here, we illustrate a method to estimate the connectivity matrix of several interacting dynamical sub-systems by assuming that such a network is composed of weakly coupled heterogeneous deterministic dynamical sub-systems. Our approach consists of building a functional model from the multivariate data by identifying an autonomous multi-output system. However, such a "black-box" modeling approach may quickly become computationally intractable, and simplifying assumptions have to be made. For the case of weakly interacting dynamical systems, we proceed as follows. For each measured signal, we reconstruct separately a nonlinear dynamical system. Then, by assuming weak (linear) interactions, we construct a linear model of the interactions by means of a classical linear multi-output system identification method.

This method presents some similarities with two other methods that have been proposed for a particular application in neuroscience [Paninski et al., 2004, Makarov et al., 2005] and with the one based on phase dynamics [Rosenblum et al., 2001].

Let us illustrate this method. For the sake of clarity, let us recall the network model introduced in Chapter 2, namely

$$\dot{\Theta}(t) = \mathcal{F}(\Theta(t)) + \eta(t), \tag{4.6}$$

Let us focus on a generic sub-system (i). Under the hypothesis of *weak coupling*, the equation governing the (i)-th dynamics can be written as

$$\dot{\theta}^{(i)}(t) = \mathcal{F}_S^{(i)}\left(\theta^{(i)}(t)\right) + \varepsilon \mathcal{F}_C^{(i)}(\Theta(t)) + \eta^{(i)}(t), \tag{4.7}$$

where $\mathcal{F}_S^{(i)} : \mathbb{R}^{d^{(i)}} \to \mathbb{R}^{d^{(i)}}$ describes the *self* dynamics of the sub-system (i) in the absence of interactions within the network; $\mathcal{F}_C^{(i)} : \mathbb{R}^D \to \mathbb{R}^{d^{(i)}}$, weighted by the small constant ε, describes the weak inter-sub-system interactions (couplings); and $\eta^{(i)} \in \mathbb{R}^{d^{(i)}}$ is the (i)-th sub-vector of η.

Under the assumption of Eq. (4.7), the average interdependences along a given trajectory $\tilde{\Theta}(t)$ between the sub-system (i) and any other sub-system (j) can be naturally quantified as

$$\mathcal{K}^{(i,j)} = \frac{1}{T}\int_0^T \varepsilon \frac{\partial \mathcal{F}_C^{(i)}}{\partial \theta^{(j)}}\bigg|_{\Theta=\tilde{\Theta}(\xi)} d\xi,\ \forall j \neq i, \tag{4.8}$$

where T is the time horizon of the trajectory $\tilde{\Theta}(t)$. Afterwards, by means of a suitable arrangement of all the $\mathcal{K}^{(i,j)}$, $i = 1, \ldots, M$, the matrix $\mathcal{K}$ describing the connectivity within the network can be given as

$$\mathcal{K} = \begin{bmatrix} \emptyset & \cdots & \mathcal{K}^{(1,i)} & \cdots & \mathcal{K}^{(1,j)} & \cdots & \mathcal{K}^{(1,M)} \\ \vdots & \ddots & \vdots & & \vdots & & \vdots \\ \mathcal{K}^{(i,1)} & \cdots & \emptyset & \cdots & \mathcal{K}^{(i,j)} & \cdots & \mathcal{K}^{(i,M)} \\ \vdots & & \vdots & \ddots & \vdots & & \vdots \\ \mathcal{K}^{(j,1)} & \cdots & \mathcal{K}^{(j,i)} & \cdots & \emptyset & \cdots & \mathcal{K}^{(j,M)} \\ \vdots & & \vdots & & \vdots & \ddots & \vdots \\ \mathcal{K}^{(M,1)} & \cdots & \mathcal{K}^{(M,i)} & \cdots & \mathcal{K}^{(M,j)} & \cdots & \emptyset \end{bmatrix},$$

where the generic sub-matrix $\mathcal{K}^{(i,j)}$ of dimension $d^{(i)} \times d^{(j)}$ models the coupling from the sub-system (j) to the sub-system (i), and the diagonals blocks, representing the self-couplings, are by assumption set to zero and consequently denoted by $\emptyset$.

The goal is to estimate $\mathcal{K}$ from measurements. This task is not straightforward because we do not have normally a direct access to the state $\Theta(t)$; however, an observable of it, $Y(t)$, is usually available. Let us recall the model introduced in Chapter 2 of the measurement equation, namely

$$Y_t = \mathcal{G}(\Theta_t) + \nu_t, \tag{4.9}$$

yielding a P-variate time series Y_t, $t = 0, \ldots, L-1$.

Let us now assume that we have available $P \geq M$ measurements, with at least one measurement from each dynamical sub-system. As will be shown later, without loss of generality for the case $P = M$, we may proceed to the estimation of the influences model $\mathcal{K}$ in three steps.

4.5.1 First Step — State-Space Reconstruction

The method exploits dynamical state-space properties of the data; hence, the first step is to reconstruct a state-space that is topologically equivalent to the original one [Sauer et al., 1991]. Denoted by $y_t^{(i)}$, $t = 0, \ldots, L-1$, the (i)-th scalar time series, we assume the (i)-th component of Eq. (4.9) to be only function of $\theta^{(i)}$, namely

$$y_t^{(i)} = \mathcal{G}^{(i)}\left(\theta_t^{(i)}\right) + \nu_t^{(i)}.$$

Hence, because of the weak interactions, by embedding the time series $y^{(i)}$ we can expect to obtain a state-space $x^{(i)} \in \mathbb{R}^{n^{(i)}}$ that is dynamically equivalent to the original $\theta^{(i)}$ and not to the whole Θ. This is done on all M measurements, getting the "*mixed state-space*"[3] $X \in \mathbb{R}^N$ of the network, where $N = \sum_{i=1}^M n^{(i)}$.

[3] Mixed state-space is a term that has been formally introduced in [Wiesenfeldt et al., 2001]

4.5.2 Second Step — Self Modeling

By following the assumption in Sec. 4.5.1 and naturally moving to discrete time equations, we use Eq. (4.7) to write the dynamics of the reconstructed sub-system (i) as

$$x_{t+1}^{(i)} = F_S^{(i)}\left(x_t^{(i)}\right) + \varepsilon F_C^{(i)}\left(X_t\right) + \xi_t^{(i)}, \tag{4.10}$$

where, again, the function $F_S^{(i)}: \mathbb{R}^{n^{(i)}} \to \mathbb{R}^{n^{(i)}}$ describes the dynamics of the sub-system (i) in the absence of interactions, *i.e.* the $(i)-th$ sub-system "self-dynamics"; $F_C^{(i)}: \mathbb{R}^N \to \mathbb{R}^{n^{(i)}}$, weighted by the small constant ε, describes the weak inter-sub-system interactions (couplings), and $\xi_t^{(i)} \in \mathbb{R}^{n^{(i)}}$ accounts for the modeling noise.

Let us consider a generic reconstructed trajectory $\tilde{X}_t$, and let us assume, without loss of generality, that it has zero mean and that $F_C^{(i)}(0) = 0$. Then, by Taylor expansion (up to the first order) about the average point of the trajectory (the origin) of the second term of Eq. (4.10), we obtain

$$x_{t+1}^{(i)} = F_S^{(i)}\left(x_t^{(i)}\right) + \sum_{i \neq j} \varepsilon \frac{\partial F_C^{(i)}(X)}{\partial x^{(j)}}\bigg|_{X=0} x_t^{(j)} + \varepsilon \mathcal{O}\left(\|X_t\|^2\right) + \xi_t^{(i)}, \tag{4.11}$$

where the $n^{(i)} \times n^{(j)}$ matrices $\varepsilon \frac{\partial F^{(i)}}{\partial x^{(j)}}\Big|_{X=0}$ describe the average couplings directed from the $n^{(j)}$ state variables of sub-system (j) to the $n^{(i)}$ state variables of sub-system (i).

According to the hypothesis of weak interactions within the network, the term $\omega_t^{(i)} = \sum_{i \neq j} \varepsilon \frac{\partial F_C^{(i)}(X)}{\partial x^{(j)}}\Big|_{X=0} x_t^{(j)} + \varepsilon \mathcal{O}\left(\|X_t\|^2\right) + \xi_t^{(i)}$ on the right hand side of Eq. (4.11) can be considered small with respect to the self-dynamic $F_S^{(i)}\left(x_t^{(i)}\right)$. Hence, given

$$x_{t+1}^{(i)} = F_S^{(i)}\left(x_t^{(i)}\right) + \omega_t^{(i)}, \tag{4.12}$$

where $\omega_t^{(i)}$ is considered as a small modeling noise, and neglecting its small dependence on $F_s^{(i)}\left(x_t^{(i)}\right)$, we proceed to identify $F_S^{(i)}$ by using a least squares (in predictive sense) algorithm. Namely, for each sub-system (i), we estimate a model $\hat{F}_S^{(i)}$ from data so as to minimize the total square prediction error, *i.e.*

$$\hat{F}_S^{(i)} = \arg\min_{F_S^{(i)}} \sum_{k=1}^{l^{(i)}-1} \left\| x_k^{(i)} - F_S^{(i)}\left(x_{k-1}^{(i)}\right) \right\|^2,$$

where $\|\cdot\|$ stands for the 2-norm and $l^{(i)}$ is the number of samples available for sub-system (i) after the embedding.

4.5.3 Third Step — Cross Modeling

Using the self-model $\hat{F}_S^{(i)}$ estimated at the previous step, we can introduce the modeling residuals $r^{(i)}$, *i.e.*

$$r_t^{(i)} = x_t^{(i)} - \hat{x}_t^{(i)}, \tag{4.13}$$

where $\hat{x}_t^{(i)} = \hat{F}_S^{(i)}\left(x_{t-1}^{(i)}\right)$ is the current state predicted on the basis of the only local past information $x_{t-1}^{(i)}$. These residuals represent the dynamics unjustified by the estimated

local self-models. As a next step, we justify these residual dynamics with the dynamical interactions within the network. In practice, according to Eq. (4.11) we can rewrite Eq. (4.13) as

$$r_{t+1}^{(i)} = \sum_{i \neq j} \varepsilon \frac{\partial F_C^{(i)}(X)}{\partial x^{(j)}} \bigg|_{X=0} x_t^{(j)} + \epsilon_t^{(i)}, \tag{4.14}$$

where $\epsilon_t^{(i)}$ accounts for the higher order terms of Eq. (4.11) and the modeling noise; hence, it is small under the hypothesis of deterministic dynamics and weak interactions, and with a small dependence with X_t, that we neglect. Finally, by means of a least squares linear regression (in predictive sense) over all the residuals time samples, we estimate the $\hat{K}^{(i,j)}$ $(n^{(i)} \times n^{(j)})$ matrices. Namely, for each sub-system (i), we estimate the $\hat{A}^{(i)}$ $(n^{(i)} \times \sum_{j \neq i} n^{(j)})$ matrix as

$$\hat{A}^{(i)} = \arg\min_{A^{(i)}} \sum_{k=1}^{\min\{l^{(i)}\}-1} \left\| r_k^{(i)} - A^{(i)} X_{k-1}^{(\neg i)} \right\|^2,$$

where $X^{(\neg i)}$ is the state vector without the (i)-th sub-system components. Consequently, the estimated matrix

$$\hat{A}^{(i)} = \left[\hat{K}^{(i,1)} \ \cdots \ \hat{K}^{(i,j \neq i)} \ \cdots \ \hat{K}^{(i,M)} \right]$$

is the concatenation of all the nonzero coupling matrices. Clearly, the estimate of the whole network connectivity matrix $\hat{K}$ follows straightforwardly as a suitable rearrangement of the estimated sub-blocks

$$\hat{K} = \begin{bmatrix} \emptyset & \cdots & \hat{K}^{(1,i)} & \cdots & \hat{K}^{(1,j)} & \cdots & \hat{K}^{(1,M)} \\ \vdots & \ddots & \vdots & & \vdots & & \vdots \\ \hat{K}^{(i,1)} & \cdots & \emptyset & \cdots & \hat{K}^{(i,j)} & \cdots & \hat{K}^{(i,M)} \\ \vdots & & \vdots & \ddots & \vdots & & \vdots \\ \hat{K}^{(j,1)} & \cdots & \hat{K}^{(j,i)} & \cdots & \emptyset & \cdots & \hat{K}^{(j,M)} \\ \vdots & & \vdots & & \vdots & \ddots & \vdots \\ \hat{K}^{(M,1)} & \cdots & \hat{K}^{(M,i)} & \cdots & \hat{K}^{(M,j)} & \cdots & \emptyset \end{bmatrix}.$$

4.5.4 Remarks

The use of least squares procedures is justified by the fact that, under our deterministic and weak coupling hypotheses, we want to minimize the random disturbances $\omega_t^{(i)}$ in Eq. (4.12), and $\epsilon_t^{(i)}$ in Eq. (4.14). However, the coupling estimated here, through the second least squares operation, is the average coupling with respect to the average point of the trajectory (center of the expansion). In general, this does not coincide with the ideal estimate of the coupling, *i.e.* the average value of the instantaneous couplings as given by Eq. (4.8). Though, this latter is generally not inferable in a completely blind setup as the one here considered.

As an advantage, the least squares technique also supplies a formula for computing the covariance matrix of the estimates. This further allows us to compute statistical hypotheses tests concerning the estimated coupling matrices $\hat{K}^{(i,j)}$ [Stuart et al., 1999], which will allow a rigorous statistical analysis in Sec. 4.6.2.

In conclusion, it should be noted that usually a single number quantifying the influence from $y^{(j)}$ to $y^{(i)}$ is more suitable than a matrix. Therefore, we propose to compute a norm of $\hat{K}^{(i,j)}$. For instance, the 1-norm would correspond to detecting the strongest influence under the assumption that each $y^{(i)}$ is a linear observation of the corresponding $x^{(i)}$.

4.6 Method Validation

In this section we test the method on artificial data. First, we test the ability of the method to estimate correctly couplings among interacting sub-systems under the hypotheses described in Sec. 4.5. In particular, we address two issues: i) the assessment of the directionality of the coupling in the case of two mutually coupled sub-systems; ii) the ability to discern between direct and indirect couplings among three interacting sub-systems.

Second, we test the sensitiveness of the method upon the amount of data, the observational noise and modeling noise intensity. We considered the case of two non-linearly coupled sub-systems.

Third, we test saliency and scalability in a large network of 128 dynamical sub-systems.

4.6.1 Numerical setup for coupling assessment

To test the ability of the method to estimate correctly the couplings among interacting sub-systems, we considered the following paradigms.

Directionality assessment

To test the ability of the method to assess the directionality of the coupling we considered two numerical examples. First, we considered two noise-driven non-identical Lorenz dynamical sub-systems, mutually coupled as in Fig. 4.13(a). The corresponding dynamical equations are

$$\begin{cases} \dot{\theta}_1^{(1)} = \sigma^{(1)} \left(\theta_2^{(1)} - \theta_1^{(1)} \right) + \eta_1^{(1)}, \\ \dot{\theta}_2^{(1)} = r^{(1)} \theta_1^{(1)} - \theta_2^{(1)} - \theta_1^{(1)} \theta_3^{(1)} + \mathcal{C}^{(1,2)} \left(\theta_2^{(1)} - \theta_2^{(2)} \right) + \eta_2^{(1)}, \\ \dot{\theta}_3^{(1)} = \theta_1^{(1)} \theta_2^{(1)} - \beta^{(1)} \theta_3^{(1)} + \eta_3^{(1)}, \\ \\ \dot{\theta}_1^{(2)} = \sigma^{(2)} \left(\theta_2^{(2)} - \theta_1^{(2)} \right) + \eta_1^{(2)}, \\ \dot{\theta}_2^{(2)} = r^{(2)} \theta_1^{(2)} - \theta_2^{(2)} - \theta_1^{(2)} \theta_3^{(2)} + \mathcal{C}^{(2,1)} \left(\theta_2^{(1)} - \theta_2^{(2)} \right) + \eta_2^{(2)}, \\ \dot{\theta}_3^{(2)} = \theta_1^{(2)} \theta_2^{(2)} - \beta^{(2)} \theta_3^{(2)} + \eta_3^{(2)}, \end{cases} \tag{4.15}$$

where $\theta_j^{(1)}, \theta_j^{(2)}$, $j = 1, 2, 3$ are the state variables of the first and second oscillator, respectively; $\sigma^{(i)}$, $r^{(i)}$, $\beta^{(i)}$, $i = 1, 2$, are parameters whose values are chosen randomly in a small interval ($\pm 5\%$) around the standard values 10, 27, and 8/3, respectively; $\eta_j^{(i)}$, $i = 1, 2$, $j = 1, 2, 3$, are zero-mean uncorrelated Gaussian random noises (set in simulations to a variance of 1% of the energy of the right hand side along the uncoupled attractors); and $\mathcal{C}^{(1,2)}$, $\mathcal{C}^{(2,1)}$ are the strengths of diffusive couplings between the second state variables

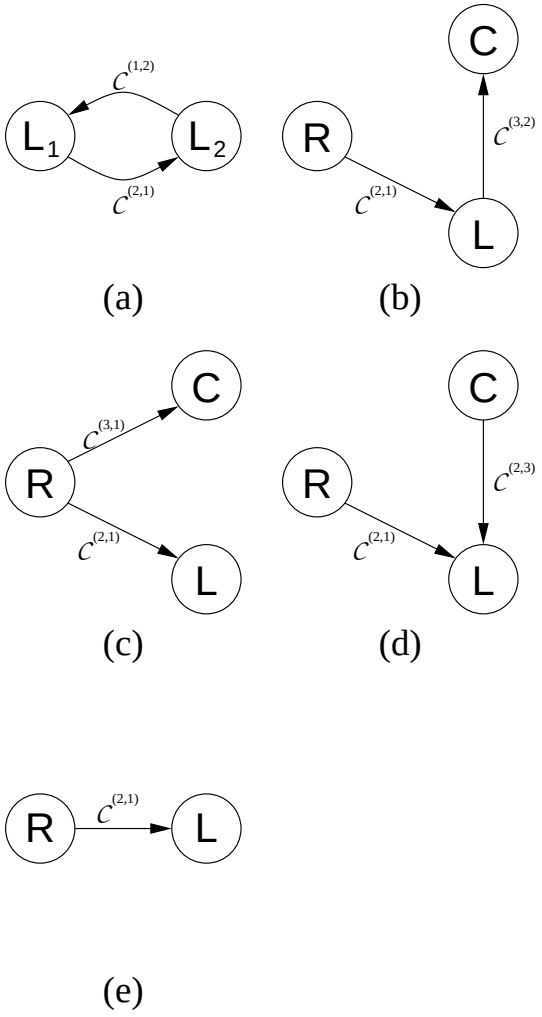

Fig. 4.13. Connection setups used for the validation of the method. (a) Setup for the directionality assessment – two Lorenz (L_1 and L_2) dynamical sub-systems mutually coupled, *cf.* Eq. (4.15). (b, c, d) Setups for triangular interdependence assessments – coupled Rössler (R), Lorenz (L) and Colpitts (C) dynamical sub-systems, *cf.* Eq. (4.3): (b) case of chain connection; (d) case of common source; (e) case of common child. (e) Setup for the robustness assessment, nonlinearly coupled Rössler (R) and Lorenz (L) dynamical sub-systems, *cf.* Eq. (4.18).

$\theta_2^{(1)}$ and $\theta_2^{(2)}$. Their values are varied within the interval $[0, 0.5]$, which guarantees the validity of the hypothesis of weakly interacting oscillators.

For every considered value of the couplings $\mathcal{C}^{(1,2)}$ and $\mathcal{C}^{(2,1)}$, the differential equations were iterated starting from random initial conditions, the transients were discarded. Then, time series of lengths $L = 500$ were collected ($\delta T = 0.02$). To ensure repeatability and statistical stability of the results, we collected a total of 25 trials from different initial conditions. We measured the variables $\theta_2^{(1)}$ and $\theta_2^{(2)}$, to which we added zero-mean white Gaussian observational noise at an intensity of 1% of the signal energy, *i.e.* 40 dB of Signal to Noise Ratio (SNR).

In the second example, we tested the ability of the method to estimate directionality in the general case of two structurally different sub-systems. Namely, we considered a noise-driven Lorenz sub-system bidirectionally coupled with a noise-driven Van der Pol one. The coupling scheme is identical to Fig. 4.13(a). The corresponding dynamical equations

are

$$\begin{cases} \dot{\theta}_1^{(1)} = \sigma\left(\theta_2^{(1)} - \theta_1^{(1)}\right) + \eta_1^{(1)}, \\ \dot{\theta}_2^{(1)} = \rho\theta_1^{(1)} - \theta_2^{(1)} - \theta_1^{(1)}\theta_3^{(1)} + \mathcal{C}^{(1,2)}\left(\theta_2^{(2)} - \theta_2^{(1)}\right) + \eta_2^{(1)}, \\ \dot{\theta}_3^{(1)} = \theta_1^{(1)}\theta_2^{(1)} - \beta\theta_3^{(1)} + \eta_3^{(1)}, \\ \\ \dot{\theta}_1^{(2)} = T\left(\theta_2^{(2)} + \eta_1^{(2)}\right), \\ \dot{\theta}_2^{(2)} = T\left(\left(-\mu\left(\theta_1^{(2)}\right)^2 - 1\right)\theta_2^{(2)} - \theta_1^{(2)} + \mathcal{C}^{(2,1)}\left(\theta_2^{(1)} - \theta_2^{(2)}\right) + \eta_2^{(2)}\right), \end{cases} \tag{4.16}$$

where $\theta_j^{(1)}$, $j = 1, 2, 3$, are the state variables of the Lorenz sub-system, while $\theta_j^{(2)}$, $j = 1, 2$, are the state variables of the van der Pol sub-system; σ, β, r, and μ are parameters that are fixed at the standard values, *i.e.* $\sigma = 10$, $\beta = 8/3$, $r = 28$, and $\mu = 1.5$; the $\eta_j^{(i)}$, are zero-mean uncorrelated Gaussian random noises (set in simulations to a variance of 1% of the energy of the right hand side along the uncoupled attractors); $T = 18$ adapts the speed of the Van der Pol sub-system to the one of the Lorenz sub-system; and, finally, the parameters $\mathcal{C}^{(1,2)}$, $\mathcal{C}^{(2,1)}$ represent the strength of the diffusive linear coupling between the two sub-systems. Their values are varied within the interval $[0, 0.35]$ for $\mathcal{C}^{(1,2)}$ and $[0, 0.035]$ for $\mathcal{C}^{(2,1)}$, which guarantees the validity of the hypothesis of weakly interacting oscillators.

For every considered value of $\mathcal{C}^{(2,1)}$ and $\mathcal{C}^{(1,2)}$, the differential equations were iterated, starting from random initial conditions, the transients were dropped and time series of 500 points each were collected ($\delta T = 0.02$). We collected a total of 25 trials from different initial conditions, measuring the coupled variables $\theta_2^{(1)}$ and $\theta_2^{(2)}$, corrupted by zero-mean white Gaussian observational noise leading to 40 dB SNR.

Marginalization assessment

To test the ability to discern between direct and indirect couplings among three interacting sub-systems, we considered a heterogenous network composed of three structurally different noise-driven dynamical sub-systems, namely Rössler (R), Lorenz (L) and Colpitts (C) dynamical systems. We coupled them corresponding to the three situations reported in Figs. 4.13(b), (c), and (d).

The equations governing the dynamics of these three coupled oscillators are the same of Eq. (4.3). Also, we considered them with the same parameter values. To simulate the three schemes (b), (c), (d) in Fig. 4.13, we set the values of the coupling strengths as following: for (b), $\mathcal{C}^{(1,2)} = \mathcal{C}^{(1,3)} = \mathcal{C}^{(2,3)} = \mathcal{C}^{(3,1)} = 0$ and $\mathcal{C}^{(2,1)}$, $\mathcal{C}^{(3,2)}$ non zero and positive; for (c), $\mathcal{C}^{(1,2)} = \mathcal{C}^{(1,3)} = \mathcal{C}^{(2,3)} = \mathcal{C}^{(3,2)} = 0$ and $\mathcal{C}^{(2,1)}$, $\mathcal{C}^{(3,1)}$ non zero and positive; and for (d), $\mathcal{C}^{(1,2)} = \mathcal{C}^{(1,3)} = \mathcal{C}^{(3,2)} = \mathcal{C}^{(3,1)} = 0$ and $\mathcal{C}^{(2,1)}$, $\mathcal{C}^{(2,3)}$ non zero and positive. To guarantee the validity of the hypothesis of weakly interacting oscillators (no strong synchronization), the active parameters were varied within the interval $[0, 0.1]$ or $[0, 0.3]$, depending on the case.

Similarly to the previous case, the network was simulated starting from random initial conditions, the transients were dropped, and 25 trials of 500 points each were collected ($\delta T = 0.02$). We measured the second state variables $\theta_2^{(i)}$ from all oscillators, adding

zero-mean white Gaussian observational noise at an intensity of 1% of the signal energy (40 dB SNR).

4.6.2 Data analysis setup

By referring to the three steps described in Sec. 4.5, the analysis of the generated data was performed with the following algorithm. As a first step, the state-space reconstruction from the observations was performed by means of a Principal Component Analysis (PCA) based embedding technique [Broomhead and King, 1986]. By following procedures similar to those described in [Kantz and Schreiber, 2004, Small and Tse, 2003], we performed the PCA on embedded vectors with unit time delay (*i.e.* $T_d = 0.02$) and 25 steps window length (*i.e.* $T_w = 0.5$). Finally, we projected the resulting over-embedded space onto the first four components, yielding 4-dimensional reconstructed state-spaces, for the Rössler, Lorenz and Colpitts sub-systems. Regarding the Van der Pol sub-system, we projected the over-embedded space onto the first three components, yielding 3-dimensional reconstructed state-spaces. This approach is suitable for its robustness to noise and for the orthogonality of the constructed state-space components; the latter is a useful property for the next two steps of (multivariate) identification. We remark that this is related to modern methods that combine features from linear regression and PCA, such as partial least squares [Hellan, 1990], total least squares [Crassidis and Junkins, 2004], and subspace identification techniques [Van Overschee and DeMoor, 1996].

As a second step, radial basis functions (RBF) were used to fit the self-models and, in order to improve the RBF modeling, we first identified a linear model by ordinary least squares. RBF provide a very flexible non-linear model class and, importantly, an efficient Matlab toolbox is available [Orr, 2001].

As a third step, a regularized ordinary least squares approach was used [Golub and von Matt, 1997] to identify the cross-dependences. We used regularization because of the high number of independent variables (*i.e.* state-space components) involved in this regression step.

As discussed in Sec. 4.5.3, at this point a single number quantifying the influence from $y^{(j)}$ to $y^{(i)}$ would be more suitable than the estimated connectivity matrix $\hat{K}^{(i,j)}$. Instead of applying a norm directly, it would be advisable to zero those elements of the connectivity matrices which may represent spurious dependences. To address this concern, we performed the statistical procedure described in the next paragraph.

Assessing statistical significant dependences

Here, we report the procedure used to estimate the influence of a sub-system (j) on a sub-system (i) starting from the connectivity matrix $\hat{K}^{(i,j)}$ identified in Sec. 4.5.3. For the sake of simplicity, let us focus on a generic element of $\hat{K}^{(i,j)}$, which, to simplify the notation, we denote simply as $\hat{k}$.

Thanks to the least squares procedure, we also have an estimate of its standard deviation, which we denote $\hat{\sigma}$. Under the assumption that $\hat{k}$ is normally distributed, with mean μ and variance σ^2, we wish to test the null hypothesis

$$H_0 : \mu = 0, \sigma = \hat{\sigma}$$

against the alternative hypothesis

$$H_1 : \mu = \hat{k}, \sigma = \hat{\sigma}$$

From F-statistics, we can easily compute the p-value; namely, the probability of a *Type I error*, which is the probability that we may wrongly reject the null hypothesis, H_0, when it is true. Then, the p-value can be used to compute the probability that we may wrongly accept H_0 when it is false, *i.e.* the probability β of a *Type II error*. Usually, its complementary probability, *i.e.* $1-\beta$, is called the *power* of the test of the hypothesis H_0 against the alternative hypothesis H_1 [Stuart et al., 1999]. Under normal distribution hypothesis, the power is given by

$$1-\beta = G\left\{\sqrt{L'}\hat{k}/\hat{\sigma} - z\right\}, \tag{4.17}$$

where L' is the number of samples used to get the estimate $\hat{k}$, G is the standardized normal distribution function and z is such that $G(-z) = p$ holds. We fixed the power of our hypothesis testing to $1-\beta = 0.95$, *i.e.* we allowed a 5% of *Type II errors*, and, consequently, we zeroed $\hat{k}$ if the power computed in Eq. (4.17) exceeded this value.

Finally, after repeating the same procedure for all the elements of $\hat{K}^{(i,j)}$, we applied a 2-norm to obtain an estimate of the influence of sub-system (j) on (i).

4.6.3 Results

Directionality assessment

The results for the directionality assessment are shown in Figs. 4.14 and 4.15.

Regarding the two mutually coupled Lorenz systems, in Figs. 4.14 the surfaces of the non trivial elements of the estimated connectivity matrix $\left\|\hat{K}^{(i,j)}\right\|$, $i \neq j,\ i,j = 1,2$ are evaluated at 100 evenly spaced points. Remarkably, the coupling estimates $\left\|\hat{K}^{(1,2)}\right\|$ and $\left\|\hat{K}^{(2,1)}\right\|$ scale with the mutual coupling strength $\mathcal{C}^{(1,2)}$ and $\mathcal{C}^{(2,1)}$ (*cf.* Eq. (4.15)), respectively, detecting the asymmetry of the mutual influence. We remark that this holds with a few exceptions. These exceptions, for instance at $\mathcal{C}^{(1,2)} \simeq 0.45$ and $\mathcal{C}^{(2,1)} \simeq 0.28$, occur at places where the network undergoes a bifurcation, leading to strong synchrony. Furthermore, we remark that the estimated couplings decrease slowly with the increase of both coupling strengths. This phenomenon can be explained by the fact that the two sub-systems influence each other and, consequently, become more and more similar jeopardizing the reconstruction. However, the directionality and relative strength of the coupling are still correctly estimated and, as testified by the uniform coloring of the surface (*cf.* figure caption) these estimates are uniformly precise.

Regarding the mutually coupled Lorenz and Van der Pol system, in Figs. 4.15 the surfaces of the non trivial elements of the estimated connectivity matrix $\left\|\hat{K}^{(i,j)}\right\|$, $i \neq j,\ i,j = 1,2$ are evaluated at 100 evenly spaced points. Remarkably, the coupling estimates $\left\|\hat{K}^{(1,2)}\right\|$ and $\left\|\hat{K}^{(2,1)}\right\|$ scale with the mutual coupling strength $\mathcal{C}^{(1,2)}$ and $\mathcal{C}^{(2,1)}$ (*cf.* Eq. (4.16)), respectively, detecting the asymmetry of the mutual influence. Furthermore, we remark that as testified by the uniform coloring of the surface (*cf.* figure caption) these estimates are uniformly precise.

Marginalization assessment

The results for the triangular dependency assessment are reported in Figs. 4.16, 4.17 and 4.18, where the surfaces of the non trivial elements of the estimated connectivity matrix $\left\|\hat{K}^{(i,j)}\right\|$, $i \neq j,\ i,j = 1,2,3$ are evaluated again at 100 evenly spaced points.

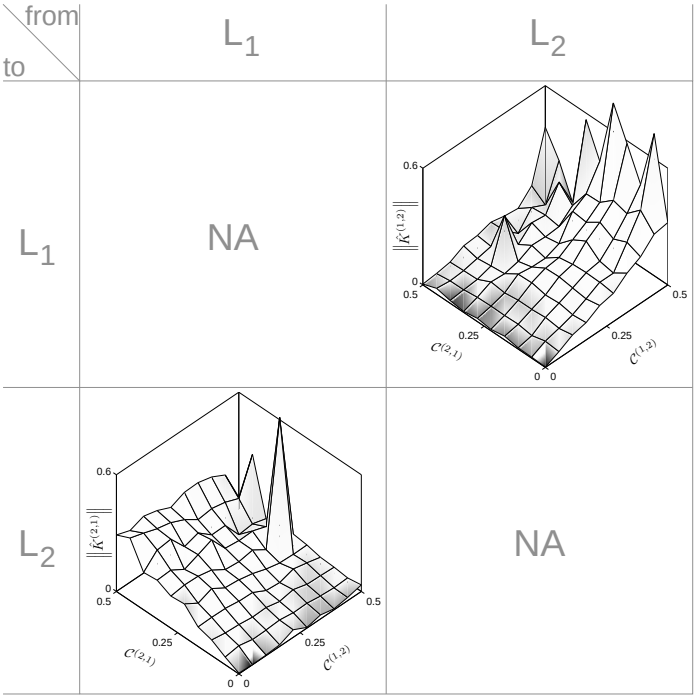

Fig. 4.14. Numerical assessment of the method as a measure of strength and direction of interaction: ability to discern mutual interdependences, *case of two non identical Lorenz systems*. Coupling setup as in Fig. 4.1(a). Dependence of the nontrivial elements of the estimated connectivity matrix, $\left\|\hat{K}^{(i,j)}\right\|$, $i \neq j$, $i,j = 1,2$, upon the mutual coupling parameters $\mathcal{C}^{(1,2)}$ and $\mathcal{C}^{(2,1)}$ of Eq. (4.15). The surface coloring represents the precision of the estimation, *i.e.* ratio of the standard deviation and the mean of the estimated couplings; the whiter the color the higher is the precision.

Figure 4.16 shows the results relative to the coupling setup of Fig. 4.13(b). It shows that $\left\|\hat{K}^{(2,1)}\right\|$ and $\left\|\hat{K}^{(3,2)}\right\|$ scale correctly with the coupling strengths $\mathcal{C}^{(2,1)}$, $\mathcal{C}^{(3,2)}$ of Eq. (4.3); moreover, the graph of the network can be correctly inferred, since the estimated active couplings $\left\|\hat{K}^{(2,1)}\right\|$, $\left\|\hat{K}^{(3,2)}\right\|$ are always bigger than the estimates of the zero couplings. In particular, this is remarkable for $\left\|\hat{K}^{(3,1)}\right\|$ and $\left\|\hat{K}^{(1,3)}\right\|$, which, in a bivariate inference approach, would scale with the couplings.

Figure 4.17 reports the results relative to the coupling setup of Fig. 4.13(c). The estimated interdependences $\left\|\hat{K}^{(2,1)}\right\|$ and $\left\|\hat{K}^{(3,1)}\right\|$ scale correctly with their corresponding coupling strengths $\mathcal{C}^{(2,1)}$ and $\mathcal{C}^{(3,1)}$, and the graph topology is correctly inferred, because the estimated couplings $\left\|\hat{K}^{(1,2)}\right\|$, $\left\|\hat{K}^{(1,3)}\right\|$, $\left\|\hat{K}^{(2,3)}\right\|$ and $\left\|\hat{K}^{(3,2)}\right\|$ are close to zero and almost always lower than $\left\|\hat{K}^{(2,1)}\right\|$ and $\left\|\hat{K}^{(3,1)}\right\|$. This is particularly true for $\left\|\hat{K}^{(3,2)}\right\|$ and $\left\|\hat{K}^{(2,3)}\right\|$ that would scale with the coupling in a bivariate inference approach.

Finally, Fig. 4.18 reports the results relative to the coupling scheme of Fig. 4.13(d). Once again, the estimated active couplings ($\left\|\hat{K}^{(2,1)}\right\|$ and $\left\|\hat{K}^{(2,3)}\right\|$) scale with their corresponding coupling strengths ($\mathcal{C}^{(2,1)}$ and $\mathcal{C}^{(2,3)}$), and values of the estimated inactive couplings ($\left\|\hat{K}^{(1,2)}\right\|$, $\left\|\hat{K}^{(1,3)}\right\|$, $\left\|\hat{K}^{(3,1)}\right\|$ and $\left\|\hat{K}^{(3,2)}\right\|$) close to zero allow us to infer the

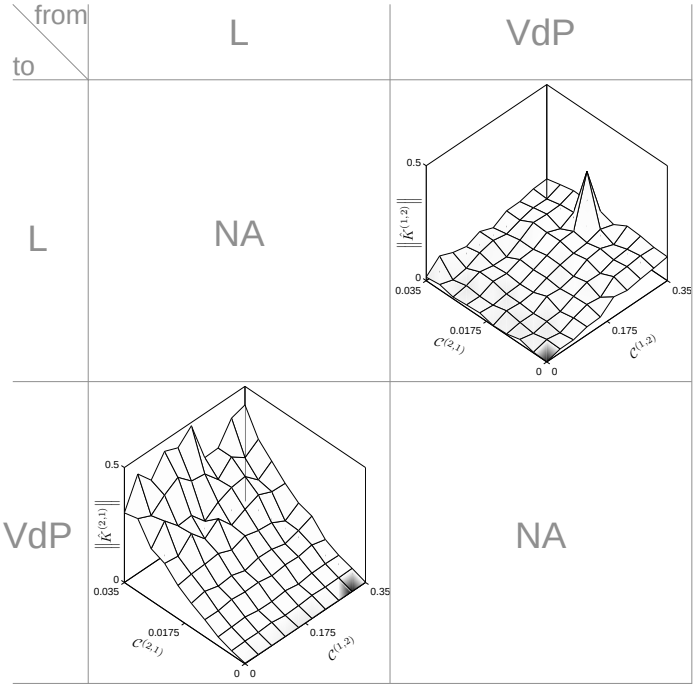

Fig. 4.15. Numerical assessment of the method as a measure of strength and direction of interaction: ability to discern mutual interdependences, *case of Lorenz and Van der Pol systems*. Coupling setup as in Fig. 4.1(a). Dependence of the nontrivial elements of the estimated connectivity matrix, $\left\|\hat{K}^{(i,j)}\right\|$, $i \neq j$, $i,j = 1,2$, upon the mutual coupling parameters $\mathcal{C}^{(1,2)}$ and $\mathcal{C}^{(2,1)}$ of Eq. (4.16). The surface coloring represents the precision of the estimation, *i.e.* ratio of the standard deviation and the mean of the estimated couplings; the whiter the color the higher is the precision.

graph topology correctly. In particular, this holds true for $\left\|\hat{K}^{(3,1)}\right\|$ and $\left\|\hat{K}^{(1,3)}\right\|$, which would turn out to be nonzero in a bivariate analysis setup.

Concerning the precision of the estimation, from the rather uniform coloring of the surface (*cf.* figure caption), we remark that the estimates are uniformly precise.

4.6.4 Robustness Assessment

The aim of this section is to assess the sensitivity of the method with respect to the amount of data available and to the level of noise. Moreover, we compare the performance of the proposed method with another one [Quian Quiroga et al., 2000]. To ensure a fair comparison, we selected from the techniques in the literature those exploiting dynamical state-space properties of the data. As a reference, we have chosen the bivariate estimator H, for which also a thorough robustness analysis has been published [Quian Quiroga et al., 2000].

Since the chosen reference method is bivariate, we considered a bivariate test bed, having already shown (*cf.* Sec. 4.6.3) the performance of our method in a multivariate setup. We considered a unidirectionally coupled network, where a noise-driven Rössler oscillator drives a noise-driven Lorenz oscillator, as shown in Fig. 4.13(e). Furthermore, in order to deny the most restricting consequence (*i.e.* linear coupling) of our modeling hypothesis, we considered non linearly coupled sub-systems. The governing equations are

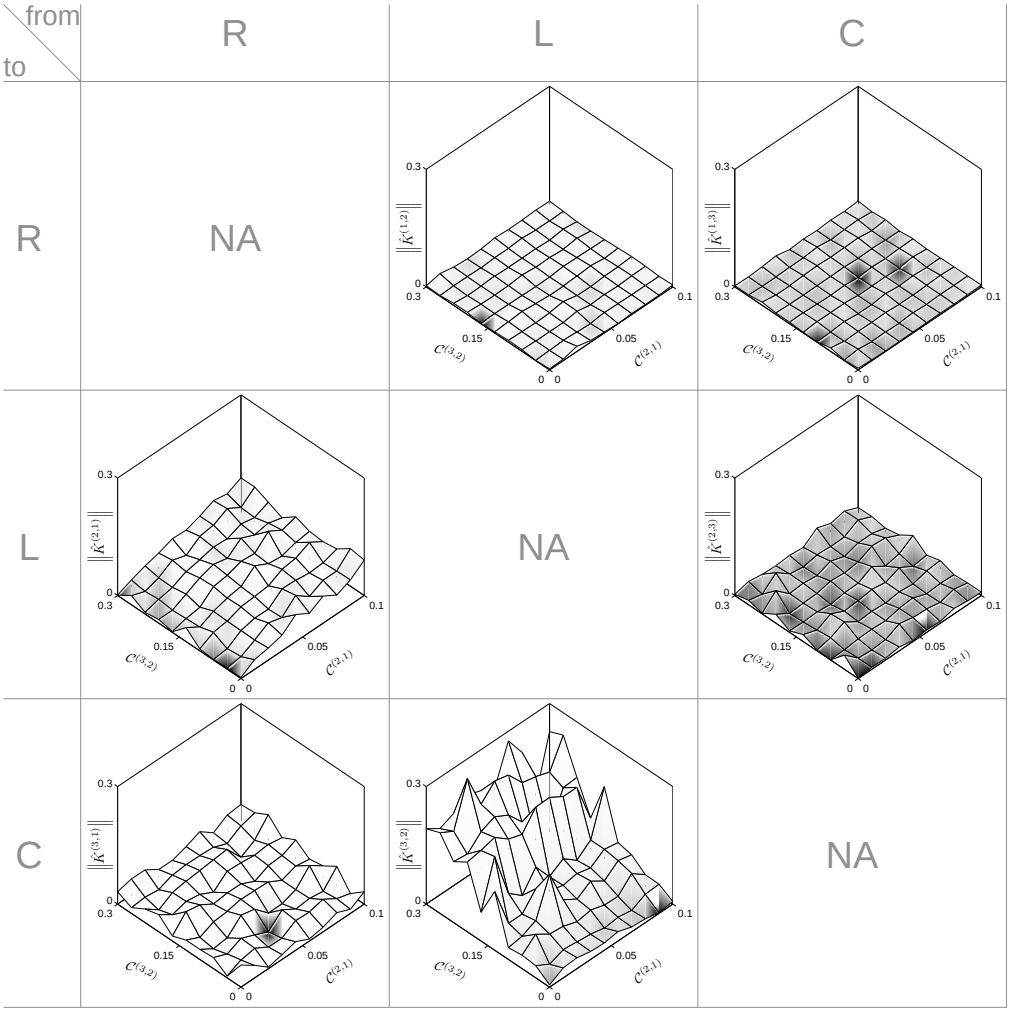

Fig. 4.16. Numerical assessment of the method as a measure of strength and direction of interaction: ability to discern triangular interdependences, *case of a chain connection*. Coupling setup as in Fig. 4.13(b). Dependence of the nontrivial elements of the estimated connectivity matrix, $\left\|\hat{K}^{(i,j)}\right\|$, $i \neq j$, $i, j = 1, 2, 3$, upon the nonzero mutual coupling parameters $\mathcal{C}^{(2,1)}$ and $\mathcal{C}^{(3,2)}$ of Eq. (4.3). Surface coloring as in Fig. 4.14.

$$
\begin{cases}
\dot{\theta}_1^{(1)} = T\left[\theta_2^{(1)} + \theta_3^{(1)} + \eta_1^{(1)}\right], \\
\dot{\theta}_2^{(1)} = T\left[\theta_1^{(1)} + a\theta_2^{(1)} + \eta_2^{(1)}\right], \\
\dot{\theta}_3^{(1)} = T\left[b + \theta_3^{(1)}\left(\theta_1^{(1)} - c\right) + \eta_3^{(1)}\right], \\
\\
\dot{\theta}_1^{(2)} = \sigma\left(\theta_2^{(2)} - \theta_1^{(2)}\right) + \mathcal{C}^{(2,1)}\left(\theta_1^{(1)}\right)^3 + \eta_1^{(2)}, \\
\dot{\theta}_2^{(2)} = \rho\theta_1^{(2)} - \theta_2^{(2)} - \theta_1^{(2)}\theta_3^{(2)} + \eta_2^{(2)}, \\
\dot{\theta}_3^{(2)} = \theta_1^{(2)}\theta_2^{(2)} - \beta\theta_3^{(2)} + \eta_3^{(2)},
\end{cases}
\tag{4.18}
$$

where $\theta_j^{(1)}$, $\theta_j^{(2)}$, $j = 1, 2, 3$, are the state variables of the Rössler and Lorenz sub-systems, respectively; a, b, c, σ, β, and r are parameters that are fixed at the standard values, *i.e.* $a = 0.4$, $b = 0.4$, $c = 5.7$, $\sigma = 10$, $\beta = 8/3$, and $r = 28$; the time scale $T = 6$ once again

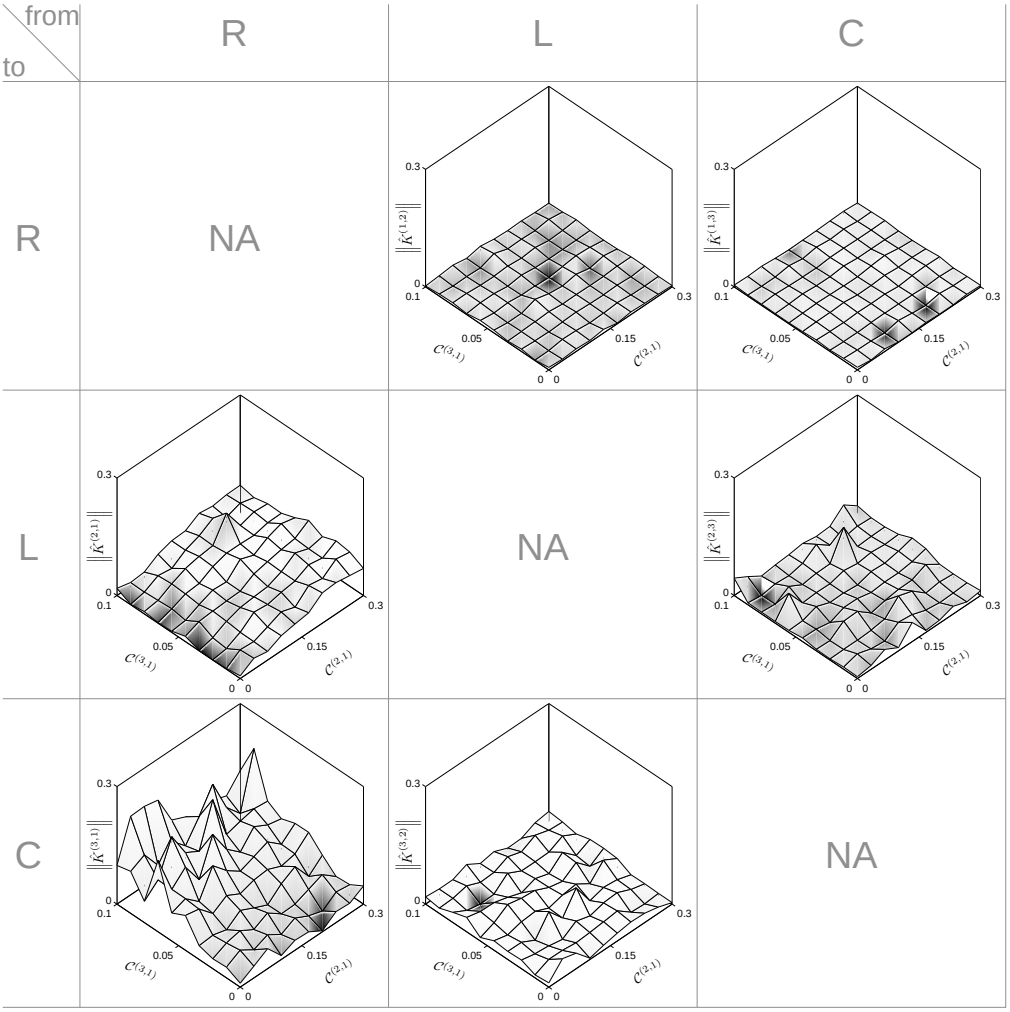

Fig. 4.17. Numerical assessment of the method as a measure of strength and direction of interaction: ability to discern triangular interdependences, *case of a common source*. Coupling setup as in Fig. 4.13(c). Dependence of the nontrivial elements of the estimated connectivity matrix, $\left\|\hat{K}^{(i,j)}\right\|$, $i \neq j$, $i, j = 1, 2, 3$, upon the nonzero mutual coupling parameters $\mathcal{C}^{(2,1)}$ and $\mathcal{C}^{(3,1)}$ of Eq. (4.3). Surface coloring as in Fig. 4.14.

adapts the speed of the Rössler to that of the Lorenz; and, finally, the parameter $\mathcal{C}^{(2,1)}$ is varied in the range $[0, 0.015]$ so that we have weak, though nonlinear, coupling between the two sub-systems.

For every considered value of $\mathcal{C}^{(2,1)}$, the differential equations were iterated, starting from random initial conditions, using the Heun algorithm with $\delta t = 0.005$, the initial 10000 points of each transient were dropped and, by means of a down-sampling ($\delta T = 0.02$), time series of 500 points each were collected. We collected a total of 90 trials from different initial conditions, measuring the coupled variables $\theta_1^{(1)}$ and $\theta_1^{(2)}$. For the method presented here, we used the same settings as described in Sec. 4.6.2. Regarding H, we used the same state-space reconstruction in order to have a fair comparison. Moreover, we used 15 nearest neighbors, a Theiler window of 0.2, and 30 bootstrapped sets of $\theta_1^{(1)}$ and $\theta_1^{(2)}$ for estimating its standard errors.

Finally, we proceeded as following: to assess the sensitiveness with respect to observational noise intensity, we fixed the modeling noise intensity to 40 dB (SNR) and we

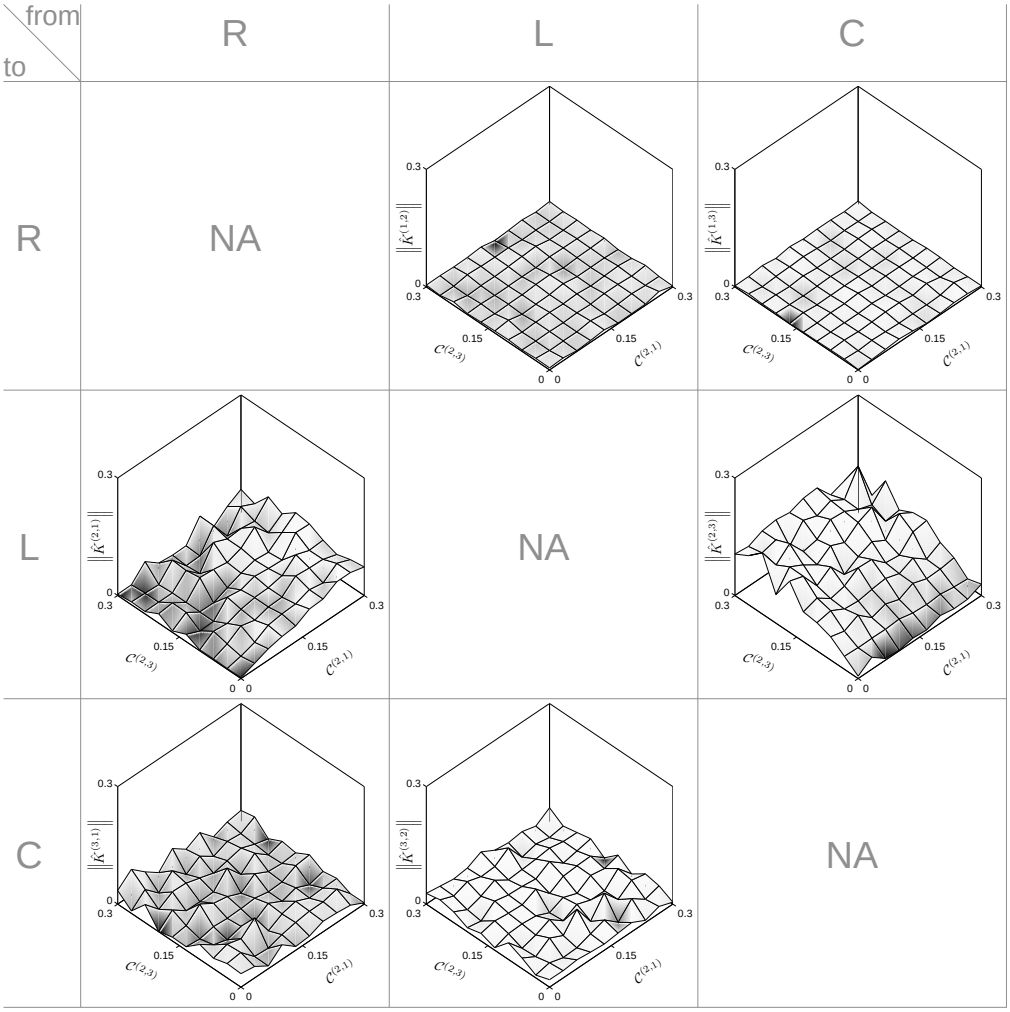

Fig. 4.18. Numerical assessment of the method as a measure of strength and direction of interaction: ability to discern triangular interdependences: *case of a common child*. Coupling setup as in Fig. 4.13(d). Dependence of the nontrivial elements of the estimated connectivity matrix, $\left\|\hat{K}^{(i,j)}\right\|$, $i \neq j$, $i, j = 1, 2, 3$, upon the nonzero mutual coupling parameters $\mathcal{C}^{(2,1)}$ and $\mathcal{C}^{(2,3)}$ of Eq. (4.3). Surface coloring as in Fig. 4.14.

considered zero-mean white Gaussian observational noise of different intensities, *i.e.* 40, 20 and 12 dB (SNR). Afterwards, to assess the sensitiveness upon modeling noise intensity, we fixed the observational noise intensity to 40 dB (SNR) and we considered white Gaussian modeling noise of different intensities, *i.e.* 36, 20 and 12 dB (SNR). This was done for each of the values of $\mathcal{C}^{(2,1)}$ and observational noise intensities, by comparing the two different measures of interdependence computed over 20, 55, and all the 90 trials.

4.6.5 Results

Observational noise vs. *data length*

The results are summarized in Fig. 4.19, which compares the dependence of the four estimated interdependences $\left\|\hat{K}^{(2,1)}\right\|$, $\left\|\hat{K}^{(1,2)}\right\|$, $H^{(2,1)}$ and $H^{(1,2)}$ on the coupling parameter $\mathcal{C}^{(2,1)}$ of Eq. (4.18) at the different noise intensities and number of trials considered. In

all panels, black curves denote $\left\|\hat{K}^{(i,j)}\right\|$ and gray curves are for $H^{(i,j)}$; the solid curves denote the estimated active coupling, *i.e.* from the Rössler to Lorenz sub-system, and the dotted curves denote the estimated inactive coupling, *i.e.* from the Lorenz to Rössler sub-system.

For most cases, the estimated interdependence $\left\|\hat{K}^{(2,1)}\right\|$ scales with the coupling strength $\mathcal{C}^{(2,1)}$, while $\left\|\hat{K}^{(1,2)}\right\|$ remains close to zero.

On the other hand, for the estimator H, neither $H^{(2,1)}$ nor $H^{(1,2)}$ scales with the coupling strength $\mathcal{C}^{(2,1)}$ and, keeping into account the variation of those estimates, it would be difficult to infer a coupling directionality. This can be due either to the limited number of bootstrapped samples used for estimating their standard deviation, or to the weak coupling setup we studied. Indeed, as reported in [Quian Quiroga et al., 2000, Carmeli et al., 2005], H should work well for stronger coupling, where the method presented here would be less effective.

Finally, as expected, the estimated interdependences worsen with higher noise intensity and/or small data length. Nevertheless, we remark that the method presented here already provides reliable estimates of interdependences in the presence of strong measurement noise (12 dB SNR) with as few as 55 trials.

Modeling noise vs. *data length*

Here, we test the sensitiveness of the method upon the amount of data and the modeling noise intensity. Consequently, we break one of the strongest hypothesis upon which the method is based. In this case, we do not compare the performance of our method to the H estimator because of the poor performance earlier shown. The results are summarized in Fig. 4.20, which compares the dependence of the estimated interdependences $\left\|\hat{K}^{(2,1)}\right\|$ and $\left\|\hat{K}^{(1,2)}\right\|$ on the coupling parameter $\mathcal{C}^{(2,1)}$ of Eq. (4.18) at the different noise intensities and number of trials considered. In all panels, the solid curves denote the estimated active coupling, *i.e.* from the Rössler to Lorenz sub-system, and the dotted curves denote the estimated inactive coupling, *i.e.* from the Lorenz to Rössler sub-system.

For all cases, the estimated interdependence $\left\|\hat{K}^{(1,2)}\right\|$ does not scale with the coupling strength $\mathcal{C}^{(2,1)}$ and stays close to zero. On the other hand, the estimated interdependence $\left\|\hat{K}^{(2,1)}\right\|$ does not scale with the coupling in most cases. This may be due to the fact that the coupling strength is very small and for higher modeling noise intensities is becomes hardly distinguishable from it. However, we remark that the condition of coupling/no coupling is already detectable in the case of strong modeling noise (20 dB SNR) with as few as 55 trials.

Finally, as expected, the estimated interdependences worsen with higher noise intensity and/or small data length.

4.6.6 Saliency and scalability

Hitherto, we have tested the capability of the method in standard problems arising in multivariate settings. Still, we shall discuss its feasibility when dealing with large systems in terms of saliency to infer the network wiring and scalability.

As said earlier, saliency is the property related to the ability of infer the interdependence strength independently on the number of sub-systems composing the rest of the

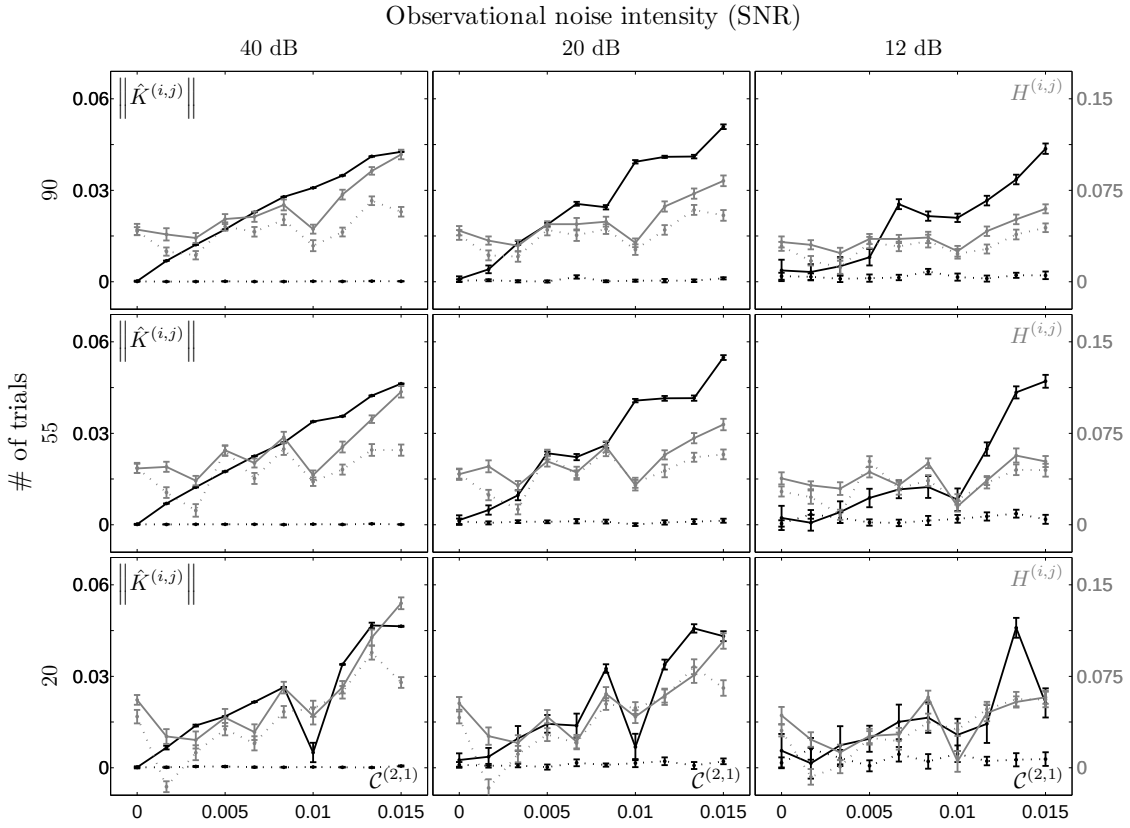

Fig. 4.19. Numerical assessment of the method as a measure of strength and direction of interaction: robustness with respect to data length (number of trials of 500 samples each) and intensity of measurement noise (Signal to Noise Ratio, SNR). Coupling setup as in Fig. 4.1(e). Dependence of the estimated coupling between the two sub-systems of Eq. (4.18), upon the nonlinear coupling strength $\mathcal{C}^{(2,1)}$ estimated with two different techniques: method proposed here (black); H estimator (gray); from sub-system (1) to (2) solid curves; from sub-system (2) to (1) dotted curves. The dots and errors bars illustrate the mean values and standard deviations of the estimations, respectively.

world. Ideally, the inferred strength should be (statistically) constant with the respect to the number of marginalized sub-systems.

Regarding the scalability of method upon the number of sub-systems, within our grey-box modeling framework, as reported in the procedure described in Sec. 4.5, we first estimate P "self-models", and then we estimate the cross-dependences by means of a multiple linear regression. Consequently, the costly non-linear identification part is done separately on each of the P sub-systems, potentially over a few variables at a time. Only the final linear regression is done over all the variables; for the linear regression we can take advantage of existing efficient software packages [Anderson et al., 1992] which can consider millions of variables in reasonable time.

In this section, we describe two tests performed to assess the effectiveness of the method when dealing with a large number of observed systems. We considered a network of 128 linearly coupled non-identical Colpitts oscillators, with the same governing equations as in Eq. (4.5).

We proceeded to test saliency and scalability as following.

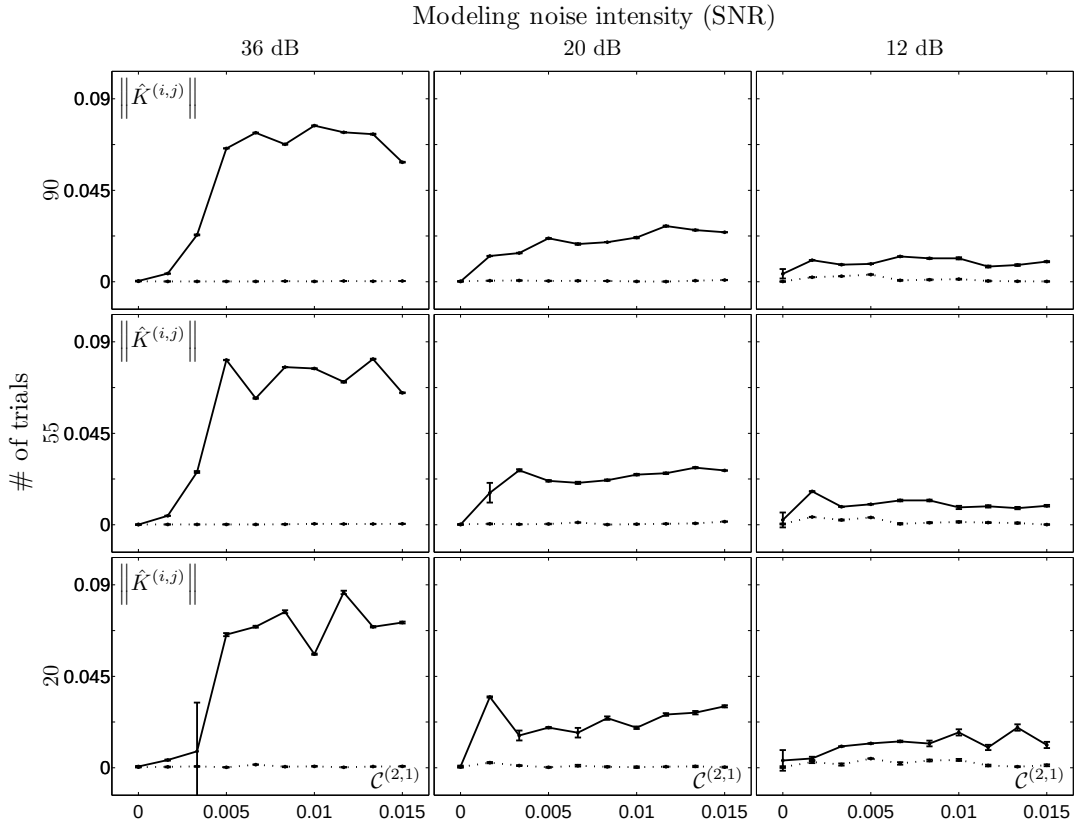

Fig. 4.20. Numerical assessment of the method as a measure of strength and direction of interaction: robustness with respect to data length (number of trials of 500 samples each) and intensity of modeling noise (Signal to Noise Ratio, SNR). Coupling setup as in Fig. 4.1(e). Dependence of the estimated coupling between the two sub-systems of Eq. (4.18), upon the nonlinear coupling strength $\mathcal{C}^{(2,1)}$ estimated with the method proposed here; from sub-system (1) to (2) solid curves; from sub-system (2) to (1) dotted curves. The dots and errors bars illustrate the mean values and standard deviations of the estimations, respectively.

Saliency vs. *number of third sub-systems*

To test the property of saliency of the method, we set the coupling strength $\mathcal{C}^{(2,1)} = 0.07$ and all the others to zero. We iterated the differential equations, starting from random initial conditions, the transients were discarded. We recorded a total of 15 trials of length of 1000 points ($\delta T = 0.063$). We measured the second state variable of each sub-system, *i.e.* $\theta_2^{(i)}, i = 1, \ldots, 128$, to which we added zero-mean white Gaussian observational noise leading to a signal to noise ratio of 40, dB. We performed the PCA on embedded vectors with unit time delay (*i.e.* $T_d = 0.02$) and 25 steps window length (*i.e.* $T_w = 0.5$). Finally, we projected the resulting over-embedded space onto the first four components, yielding 4-dimensional reconstructed state-spaces. We computed the connectivity values $\left\|\hat{K}^{(2,1)}\right\|$ and $\left\|\hat{K}^{(1,2)}\right\|$ considering at each step an increasing number of sub-systems. Finally, we repeated this for different amounts of data, namely 8, 10 and all 15 trials.

The results are shown in Fig. 4.21. We remark that the directionality is well detected for an increasing number of third sub-systems as the amount of data is increased. For instance, with 15 trials our method is able to correctly estimate the driver-driven relationship with at least 126 marginalized sub-systems. Furthermore, we remark that, generally,

the estimates do slightly increase with the number of third sub-systems. This could be due to the increasing number of spurious terms in the full (before the application of a norm) connectivity matrix. The dramatic decrease of $\left\|\hat{K}^{(2,1)}\right\|$ in the left panel may be due to the disadvantageous trade-off number of variables *vs.* data length under this case, which could not allow a consistent estimate of the regression coefficients (*cf.* third step of our method at Sec. 4.5.3).

Finally, we remark that, as expected, the reliability increases (*cf.* the error bars decrease) with the amount of data length.

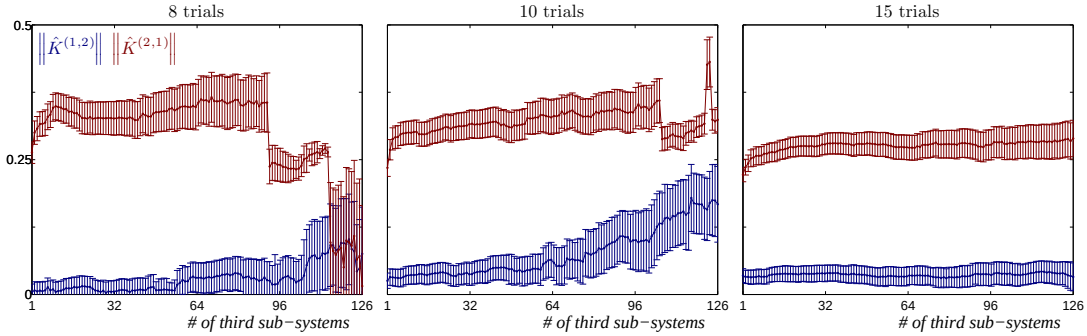

Fig. 4.21. Numerical assessment of the method as a measure of strength and direction of interaction: saliency upon the number of marginalized dynamical sub-systems. Setup: 128 coupled non-identical Colpitts dynamical systems, *cf.* Eq. (4.5). Dependence of the interdependence from sub-system (1) to sub-system (2) upon the number of marginalized sub-systems upon data length (number of trials of 1000 samples each): from left to right, 8 trials in the first, 10 trials in the second; 15 trials in the third. $\left\|\hat{K}^{(2,1)}\right\|$ estimates are in red, while $\left\|\hat{K}^{(1,2)}\right\|$ estimates are in blue. The dots and errors bars illustrate the mean value and standard deviation, respectively.

Scalability vs. *number of sub-systems*

To test the scalability of the method, we randomly set the connectivity within the network by choosing an average of two couplings for each sub-system, with a strength value of 0.07 to satisfy the hypothesis of weakly interacting oscillators.

The differential equations were iterated, starting from random initial conditions, the transients were discarded. We recorded time series of length $L = 1000$ points ($\delta T = 0.063$). We collected a total of 30 trials from different initial conditions, measuring the second state variable of each sub-system, *i.e.* $\theta_2^{(i)}, i = 1, \ldots, 128$, to which we added zero-mean white Gaussian observational noise of different intensities, *i.e.* 40, 20 and 12 *dB* (SNR). Afterwards, we assessed the robustness of the method with respect to measurement noise and data length. This was done for the chosen connectivity matrix and observational noise intensities, over 8, 11, 15, 21 and all the 30 trials.

The results are reported in Fig. 4.22, which shows the dependence of the percentage of correctly detected couplings upon the number of available data points at the different noise intensities considered. Namely, by partitioning all the estimated interdependences $\left\|\hat{K}^{(i,j)}\right\|$ into two clusters, we labeled the couplings as either present or absent. Figure 4.22 reports the percentage of the correctly detected non-zero and zero couplings (black and gray curves, respectively).

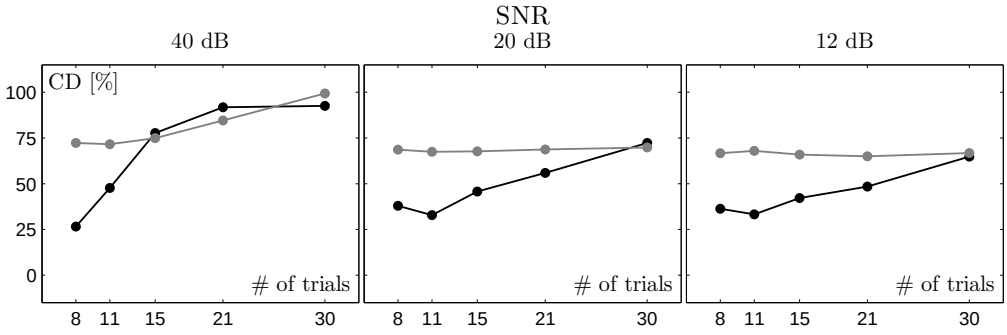

Fig. 4.22. Numerical assessment of the method as a measure of strength and direction of interaction: scalability to large numbers of dynamical sub-systems. Setup: 128 coupled non-identical Colpitts dynamical systems, *cf.* Eq. (4.5). Dependence of the percentage of correctly detected couplings upon data length (number of trials of 1000 samples each) and intensity of measurement noise (Signal to Noise Ratio, SNR): percentage of correctly detected present (black) and absent (gray) couplings.

In general, we expect the percentage of the correctly detected absent couplings (the true negatives) to be higher than that of the present couplings (the true positives), simply because in the considered setup there are 16000 zero connections against 256 non-zero connections. However, for the same reason, we expect correspondingly a percentage of false negatives (the complement of the true positives) higher than that of false positives (the complement of the true negatives).

The result shows that the reliability of coupling detection is very high for small noise intensities and, generally, increases with the amount of data available and decreases with the measurement noise intensity. However, in the case of strong noise intensity (*i.e.* 12 dB of SNR), the percentage of good detections does not fall below 60% when considering an adequate number of points.

Finally, we remark that the power of our method, *i.e.* the percentage of good detections, is remarkably much higher than a purely combinatorial guess, which would result in percentages of almost 2%.

4.7 Remarks

We have proposed a method to infer from multivariate time series the connectivity matrix of a network of weakly interacting dynamical systems, where we focused on the problem of inferring weak couplings because they are important in applications [Kuramoto, 1984, Likharev, 1991]. Furthermore, strong couplings are usually associated with synchronous regimes, in which case a direction of coupling is not unambiguously inferable.

The proposed method consists of a combination of well-established existing regression techniques, allowing the choice of an algorithmic setup that is suitably tuned to the specific application.

The estimation of the connectivity matrix is given by a least squares linear regression, which allows one to estimate parameters and their covariance matrix, making it easy to use F-tests for a statistical assessment of the results. This has the consequence that the statistical analysis of the (linear) connectivity model can be performed without time consuming techniques such as bootstrapping.

The method proved to be able to infer the asymmetry of coupling for two mutually coupled non-identical sub-systems, and proved to infer correctly the graph topology of

three coupled heterogenous sub-systems in three typical setups where bivariate methods would fail. Moreover, the method proved also to work in the case of nonlinearly coupled sub-systems. However, the reader should not be surprised by the poor performance of the bivariate method H compared to the proposed multivariate method because, for values of coupling larger than those considered in the numerical setup, the latter would suffer and H would behave better. Ongoing work is focused on the comparison of our method to the method based on the phase dynamics [Rosenblum et al., 2001, Smirnov and Bezruchko, 2003].

The method proved to be salient upon the number of marginalized third sub-systems and to scale quite well in a large network. Future work will be devoted to study the sensitiveness of the method upon the choice of the embedding dimension value, and to the study of its ability of extracting the graph topology of large systems with various topologies.

5

Assessing Cooperativeness in Brain Data

Brief — This chapter describes applications to brain data of the S estimator. The modulation of neuronal cooperative activity evoked by visual stimuli is shown to be assayed from two different recording setups. The interpretation and the neuroscientific impact of the results of our data analysis were possible thanks to the fertile collaboration with Prof. G. Innocenti and Dr. M. Knyazeva. This also allowed the acquaintance with neuroscientific notions. Part of the material presented here is a readaptation of a published journal article and of an article under preparation.
Personal Contribution — Design and execution of the data analysis.

5.1 Motivation

The operations performed by the cerebral cortex require the cooperative activity of neurons within distributed assemblies. To infer this cooperative phenomena from data, we have introduced the S estimator. Although in Chapter 2 we have already illustrated possible mechanisms underlying perceptual features *binding* performed by the brain in living beings, here we re-contextualize the issue to shed new light over the motivations of our study.

In human studies, neuronal assemblies have been identified with several non-invasive techniques: with functional magnetic resonance imaging (fMRI), which detects neuronal activity indirectly by measuring an increase of the blood oxygenation level [Logothetis, 2004]; with multichannel measurements of electric (electroencephalogram, EEG) or magnetic brain activity (magnetoencephalogram, MEG); and very recently, with synchronization tomography, which is a phase synchronization analysis applied to the cerebral current source density reconstructed with magnetic field tomography [Ioannides et al., 1990, Tass et al., 1998, 2003]. The fMRI technique provides a detailed static image but poor temporal resolution, whilst EEG and MEG techniques provide a dynamic image but poor spatial resolution. Recently, this trade-off has been overcome with a combination of fMRI and EEG or MEG [Goldman et al., 2000, Knyazeva et al., 2003], and by the synchronization tomography.

Traditionally, the use of EEG in the studies of neuronal assemblies has been guided by its relatively simple recording setup, a valuable feature especially in clinical applications. Furthermore, in principle EEG recordings allow the characterization of the organization of the cooperativeness within distantly distributed neuronal assemblies, *i.e.* at a macroscopic scale.

A deep investigation of the relation between EEG signals and different stimuli or tasks has been carried out [Eckhorn et al., 1988, Engel et al., 1991, Rodriguez et al.,

1999, Tallon-Baudry et al., 2001]. In particular, the association of particular frequencies or rhythms to specific perceptual, motor, cognitive states results deeply rooted in the tradition of the EEG community [Burgess and Gruzelier, 1997, Aoki et al., 1999, Keil et al., 1999, Miltner et al., 1999, Basar et al., 2001].

Consequently, the most common way of analyzing the cooperative cortical neuronal assemblies has been the study of the EEG spectral coherence. This method quantifies the cooperation of neuronal assemblies as a function of the correlation of EEG frequency components. Neurons in a assembly are supposed to be located in some proximity to the recording electrodes and to exhibit oscillatory activity with common spectral properties. The typical finding is that in a given perceptual, cognitive, or motor task, EEG coherence increases (or decreases) in a certain band of EEG frequency spectrum [Kiper et al., 1999, Knyazeva et al., 1999, Mima et al., 2001]. It is usually unclear if the functional cooperativeness revealed by the changed EEG coherence signifies anatomical cooperativeness between the neurons of the assembly [Horwitz, 2003], although this assumption has been verified in a very restricted number of experimental and/or clinical conditions [Kuks et al., 1987, Montplaisir et al., 1990, Pinkofsky et al., 1997].

The definition of cooperativeness used in the neurophysiological studies is narrower that that considered in system theory, especially the one referring to the concept of synchronization. Indeed, whilst the definition used in neurophysiology assumes two or many sub-systems sharing specific common frequencies, in system theory "synchronization" refers to a process whereby two or many sub-systems adjust some of their time-varying properties to a common behavior due to coupling or common external forcing. Hence, the general definition of synchronization does not imply a relationship between sub-systems at specific frequencies but at all of them. Clearly, the two above definitions coincide in the case of perfectly periodic sub-systems, though coherence at specific frequencies is not sufficient to fully define synchrony in a system theory sense. A figurative example will help in understanding the occurrence of non-periodically synchronized sub-systems. Let us consider a symphonic orchestra. During a performance, each player is continuously synchronized with the others by means of either the action of the Conductor (common forcing) or by listening to each other (mutual coupling). However, the symphony is neither strictly nor approximately periodic.

Although the methods focusing on the analysis of synchronization phenomena restricted to particular frequency bands have been the norm in EEG studies, work resorting to the approaches illustrated in Chapter 1 has begun to appear [Schiff et al., 1996, Tass et al., 1998, Arnhold et al., 1999, Mormann et al., 2000, Quian Quiroga et al., 2002, Tass et al., 2003].

Along this line, we have applied our new cooperativeness estimator, the S estimator, to quantify the visual stimuli induced manifestation of neuronal cooperativeness in the EEG activity. Our estimator holds some advantage being theoretically applicable to broadband signals and being parameter free (when applied to non embedded data), a property which may be crucial in multivariate contexts.

We applied the S estimator to analyze the stimuli-induced cooperativeness of activity between the brain hemispheres under the stimulation paradigm initially designed in [Knyazeva et al., 1999]. The results we obtained could be compared with those of the more traditional EEG coherence method, employed in that same study, and are in general consistent with the latter. However, the complexity of the changes induced by those simple stimuli seems to go well beyond what we had expected from previous work.

Furthermore, we applied our S estimator within the same context but with a different kind of recordings. Whilst with EEG recordings we could assess macroscopic arrangements of neuronal cooperativeness, with local field potentials (LFP) we could assess local neuronal cooperativeness phenomena. In particular, by local we mean the activity of a few hundred of neurons located in a small portion of the cerebral cortex, while with EEG measurements we can observe the activity of distant cortico-cortical neuronal interactions, probably resulting from several thousands of neurons.

Here, the investigation of stimulus-dependent modulation of neuronal cooperativeness has been assayed in a context where the presence of interactions among neuronal assemblies is physiologically motivated. We will discuss this in detail in next section. Hence, we will describe the results of the analysis of EEG and LFP recordings.

5.2 The visual pathway and Gestalt-like perceptions

The anatomical organization of the visual system in primate brains justify the study of cooperative activity among neuronal assemblies located in visual areas. In particular, as shown in Fig. 5.1, the visual pathway from the retina to the cerebral cortex of the occipital lobe[1] establishes a powerful example of binding. Indeed, information about the external world enters both eyes with a great deal of overlap as, for instance, one may experience closing one eye finding that the range of vision in the remaining eye is mainly limited by the nose. However, the structure of the visual pathway brings information about each visual hemifield only to the contralateral hemisphere. For instance, the processing of an image in the left part of the visual hemifield would take place in the right hemisphere. As a consequence of this anatomical organization, our perception of images centered in the visual field requires the interhemispheric interaction between visual areas. Most likely, this is achieved through the "wiring cables" which constitute the *Corpus Callosum*, a large white matter that interconnects the regions in the different halves of the brain.

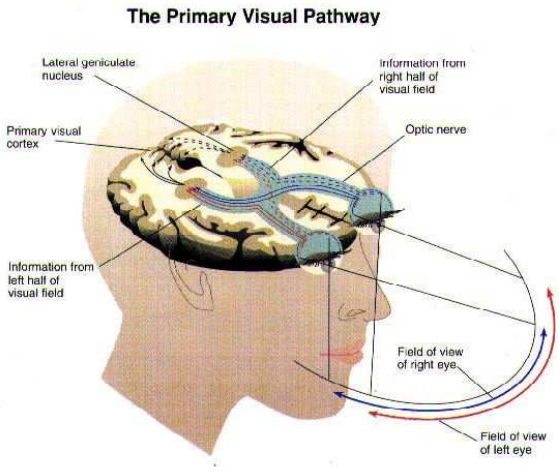

Fig. 5.1. A simple scheme of the visual pathway in primate brains.

[1] Traditionally, the cerebral cortex is made up of four lobes: the frontal, parietal, temporal and occipital lobes. It is believed that each of these areas has specific functions.

Finally, it follows that the study of the interhemispheric cooperative behavior of neuronal assemblies is justified when considering perceptual schemes given by bilateral stimulation, *i.e.* images having left and right halves fusible into a single percept.

The principles underlying perceptual grouping of spatial and temporal cues have been investigated by the so called Gestalt psychologists [Koffka, 1935]. The main laws they outlined are: proximity, similarity, symmetry, prägnanz and common fate. The principle of *proximity* can be demonstrated with the two figures reported in Fig. 5.2(a),(b). We are likely to notice fairly quickly that Fig. 5.2(a) is not just a pattern of dots but rather a series of rows of dots. The principle of proximity is that features which are close together are associated. In Fig. 5.2(b) is another example. Here, we are likely to group the dots together in columns.

Another major principle of perceptual organization is that of *similarity*. If we look at Fig. 5.2(c), the little circles and squares are evenly spaced both horizontally and vertically, so proximity does not come into play. However, we do tend to see alternating columns of circles and squares. Gestalt psychologists would argue that this is because of the principle of similarity, *i.e.* features which look similar are associated. Without the two different recurrent features we would see either rows or columns or both.

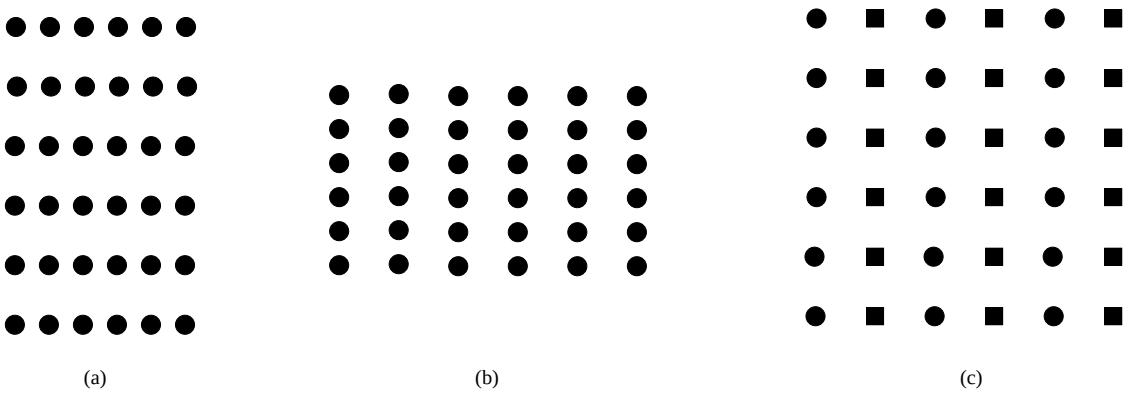

Fig. 5.2. Examples of two Gestalt principles for perceptual grouping: proximity in (a) and (b), similarity in (c).

We do not intend to explain all the principles postulated by the Gestalt psychology, however we stress the fact that these are laws to explain how brain *integrates* external information and not how brain *segregates* it.

5.3 Stimulus-dependent interhemispheric neuronal cooperativeness in EEG signals

In this section we describe the data analysis and results of EEG recordings under the stimulation paradigm used in [Knyazeva et al., 1999]. In that study the aim was to assess the stimulus-dependent modulation of interhemispheric interactions in humans. The experimental protocol was conceived and performed by the team of prof. G. Innocenti. For the sake of clarity, we illustrate the experimental protocol used to record the data in Sec. 5.3.1. Subsequently, in Sec. 5.3.2 we describe the strategy we used to analyze the EEG signals and that we first validated on numerically generated data as reported in Sec. 5.3.3. In Sec. 5.3.4 we describe the results of our analysis and we discuss them in Sec. 5.3.5.

5.3.1 Experimental Protocol

We have used the EEG recordings from nine normal right-handed adults (7 women, 2 men; mean age 30 *years*, range of 27-47 *years*), who participated in experiments aimed at mapping neural assemblies induced by visual stimulation [Knyazeva et al., 2002, 2003]. This had the advantage of testing our method with an experimental paradigm known to result in reproducible cooperative behavior, measured with spectral coherence analysis. All the subjects, *CD*, *EF*, *FG*, *KL*, *MR*, *NM*, *PH*, *UH* and *VO* signed written informed consent and all the procedures conformed to the Declaration of Helsinki (1964) by the World Medical Association concerning human experimentation and were approved by the local ethical committee of Lausanne University. During the EEG recording session, the subjects viewed the visual stimuli shown in Fig. 5.3.

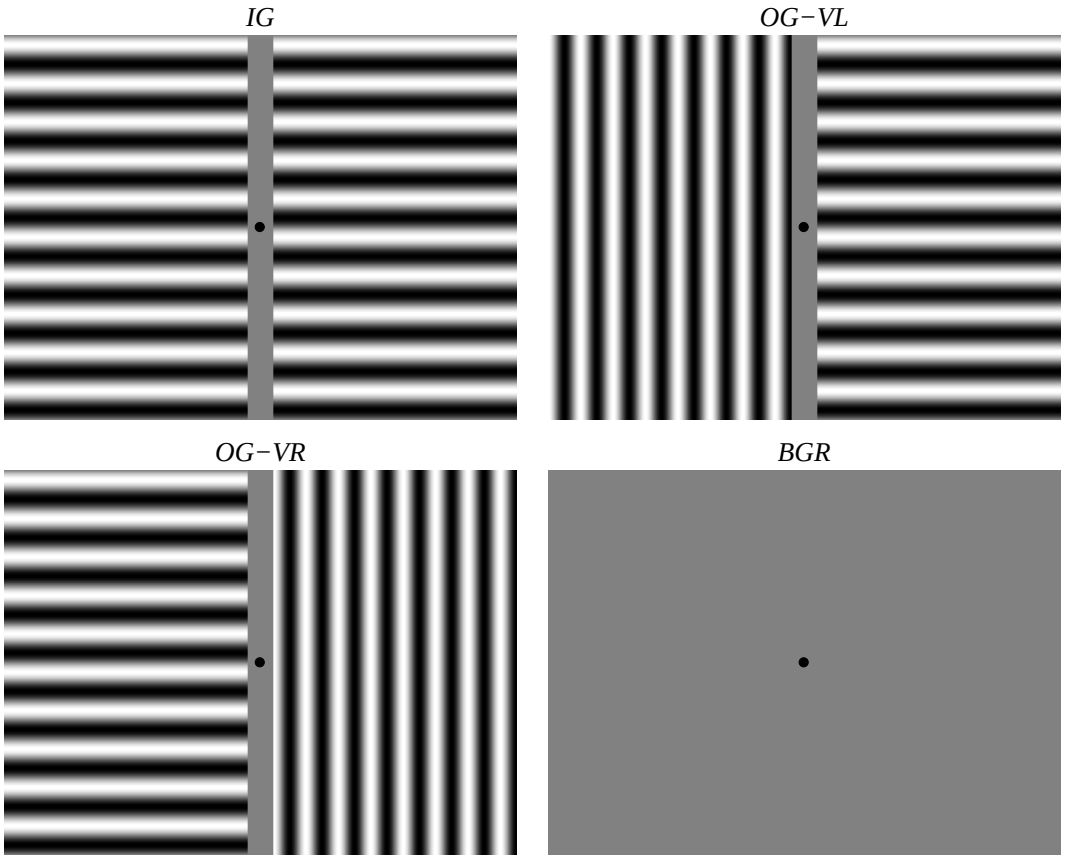

Fig. 5.3. The four different types of visual stimuli used for EEG recordings.

The stimuli were generated with a PC and presented on the computer display with a refresh rate of 75 Hz located at a distance of 57 cm. The subjects were instructed to fix a point in the center of the screen. The stimuli were black and white bilateral iso-oriented or orthogonally oriented sine-gratings centered on the fixation point. The iso-oriented gratings (IG) consisted of two identical patches of collinear, downwards-drifting horizontal gratings on both sides of the fixation point. Stimulus IG conforms to the Gestalt principle

of perceptual grouping by similarity or collinearity and common fate[2]. The orthogonally-oriented gratings (OG) consisted of a patch of horizontal downwards-drifting grating on one side and a patch of vertical rightwards-drifting grating on the other. Contrary to IG, stimulus OG presumably places the visual areas of the two hemispheres in a condition of perceptual rivalry, though this is not predicted by the Gestalt principles.

All the gratings had a spatial frequency of 0.5 $cycles/degree$, a contrast of 70%; the unilateral patches measured 13.5 deg (width) by 24 deg (height). They drifted with a temporal frequency of 2 Hz. A uniform gray screen of the same space-averaged luminance as the stimuli (32 cd/m^2) with a fixation point in the center served as a background stimulus. The vertical and horizontal gratings of the OG stimulus appeared in the left or right hemifield at random. The type of stimulus (OG, IG, and background), the stimulus exposure (2.2-2.6 s), and the inter-stimulus intervals (1.8-2.2 s) were also randomized.

The EEGs were recorded with a 128-channel Geodesics Sensor Net ©. All electrode impedances were kept under 50 $K\Omega$. The recordings were made with vertex reference using a low-pass filter set to 100 Hz. The signals were digitized with a 12-bit analog-to-digital converter at a rate of 500 $samples/s$. They were further filtered (FIR, band-pass of 3-70 Hz, notch of 50 Hz), and segmented into non-overlapping 1 s trials using NS2/NS3 (Electrical Geodesics, Inc.) software. Artifacts were edited off-line, first automatically, based on an absolute voltage threshold ($100\mu V$) and on a transition threshold ($50\mu V$), and then through visual inspection of Dr. M. Knyazeva, which allowed the identification of channels and/or trials with moderate muscle artifacts not reaching the threshold values. Finally, in order to assess only the steady-state, the first 200 ms following stimulus onset were removed, thus excluding stimulus-onset artifacts, response-onset transients, and stimulus-locked synchronization. We collected on average 85 artifact-free trials for each stimulation condition and for each individual, with a minimum of 78 and a maximum of 97.

5.3.2 Application to high surface sampling EEG

Previous studies based on coherence analyzes [Knyazeva et al., 1999, 2002] have shown that, for the stimuli used, an interhemispheric cooperativeness, probably implemented via callosal connections, can be detected at occipital electrodes close to the midline (*e.g.* electrode pairs $71-84$ and $70-90$ in Fig. 5.4).

In the present study the phenomenon of interhemispheric cooperativeness was also of interest and it was estimated that the adequate bi-hemispheric territory was covered within a distance of one or two electrodes across the midline. This corresponds to a distance of $6-9$ cm and is reasonably well spanned by the second order neighborhood of each electrode (*cf.* Fig. 5.4). On the contrary, the first order neighborhood would be too small to credibly span across the two hemispheres, as shown in Fig. 5.4, while the third order one would be too large, including about half of the electrodes at once. Therefore, we considered the second order neighborhood assuming that contiguous regions of cooperativeness crossing the midline could be interpreted as highlighting interhemispheric cooperativeness. However, it is clear that it would have been possible to assess distant cooperativeness phenomena by computing the S estimator for sets of far electrodes on the left and right hemispheres.

To summarize, the close interhemispheric cooperativeness was assessed by computing, for each of the nine subjects mentioned in Sec. 5.3.1, the topographical arrangement of

[2] The principle of similarity concerns static properties of the image, whilst the common fate or direction concerns its dynamic features.

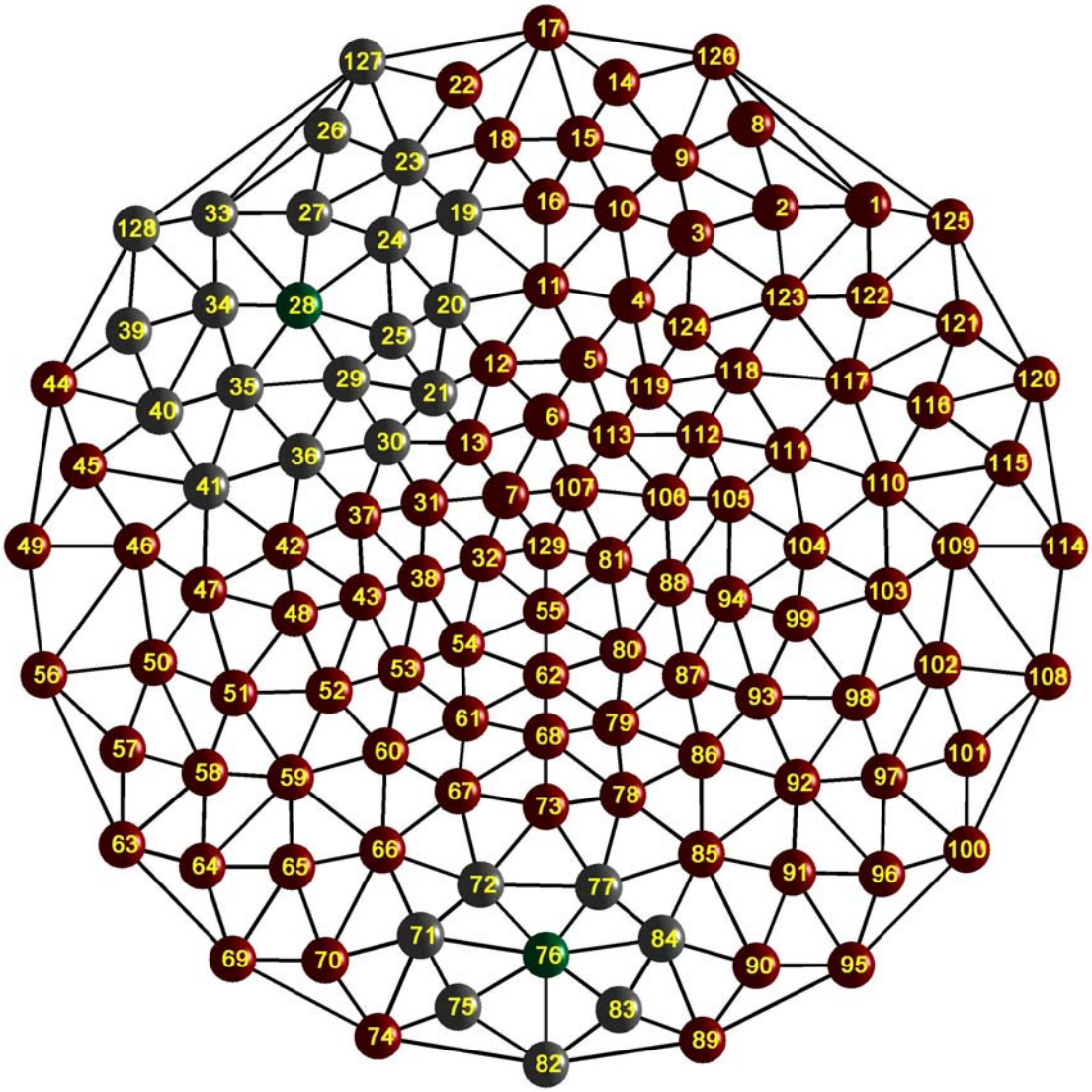

Fig. 5.4. Example of the spatial localization of the S estimator. As an example, first nearest neighbors (in gray) are shown for electrode 76 (in green), first and second neighbors (in gray) for electrode 28 (in green). The latter has been used in the computations reported here.

the cooperative activity as follows. First, for each electrode, the cooperativeness of the surrounding region was computed as the value of S over its second nearest topographical neighbors (Fig. 5.4) and an instantaneous topographical map of cooperativeness values (S) was obtained for each trial. The instantaneous values of trials corresponding to identical stimulus condition (BGR, IG, OG, and *cf.* Sec. 5.3.1) were averaged (over the available trials) obtaining the statistics, mean vector and covariance matrix, of the cooperativeness topography corresponding to each one of the three visual stimuli. Then, to highlight the reorganization of the topographical activity in the presence of different stimuli with respect to the background activity, we subtracted the average value of the estimator in the background from the average value in the two actively stimulated situations. In what follows, we refer to this difference as $\Delta S = S_{IG,OG} - S_{BG}$, where its positive values denote increased cooperativeness with respect to the background, and negative values indicate decreased cooperativeness. Therefore, extracting the regions corresponding to the

maxima of this differential cooperativeness estimator, we have highlighted the clusters of electrodes with cooperative behavior.

Statistical assessment of the results

As previously explained, in order to evaluate the topographical arrangement of stimulus-induced cooperativeness, we consider the variation ΔS of the mean values of the S estimator in the presence of the two grating conditions with respect to the values in the background. Hence, it is necessary to evaluate the statistical significance of ΔS.

The values of S over the electrode array constitute a multivariate population. Usually, for multivariate data the significance of the difference between the means of two populations is addressed with the one-way MANOVA (Hotelling's T^2) test [Johnson and Wichern, 2002]. However, when the hypothesis of a normal distribution of the data is not tenable, as in our case ($S \in [0, 1]$), one may resort to the *permutation version* of the Hotelling's T^2 [Higgins, 2004]. This version consists in a T^2 test, where the reference statistic distribution F is substituted by the empirical distribution of the randomly permuted data.

Accordingly, we have verified the statistical significance of ΔS, for individual cases as well as for the population, by considering the permutation version of the Hotelling's T^2 without the assumption that the two covariance matrices are equal [Krishnamoorthy and Jianqi, 2004]. For the individuals, the statistics were restricted to a group of artifact-free electrodes within a region of interest, and for the population, to the electrodes that were artifact-free for all the subjects (*cf.* Sec. 5.3.4).

5.3.3 Assessment of the topographical sensitivity of S estimator

The strategy described in the previous section relative to the assessment of the spatial localization of the S estimator was first validated on numerically generated data. We assessed the topographical sensitivity of the S estimator resorting to simulated data caricaturing the experimental EEG conditions. We considered the simulation of a network of coupled 128 noise-driven chaotic Colpitts sub-systems. The noise-free Colpitts system is a chaotic non-symmetrical oscillator which generates irregular sine-like signals such as the EEG [De Feo et al., 2000]; hence, we preferred it among the chaotic systems earlier considered. The dynamics of the network is given by Eq. (4.5).

We considered three different coupling schemes assuming a very simplified hypothesis about the three stimuli situations *BGR*, *OG* and *IG*. Respectively: (1) all oscillators being isolated (*BGR*), *i.e.* $\mathcal{C}^{(i,j)} = 0, \forall i, j$; (2) two isolated ring-clusters (*OG*) of three coupled sub-systems each: a cluster of electrodes 65, 66 and 71, and another (symmetric) one of electrodes 84, 85, and 91, *i.e.* $\mathcal{C}^{(i,j)} = 0, \forall i, j$ except $\mathcal{C}^{(66,65)}$, $\mathcal{C}^{(71,66)}$, $\mathcal{C}^{(65,71)}$, $\mathcal{C}^{(85,91)}$, $\mathcal{C}^{(84,85)}$ and $\mathcal{C}^{(91,84)}$ which are nonzero and positive; and, (3) the two clusters mentioned above unidirectionally coupled (*IG*) setting $\mathcal{C}^{(84,71)}$ to nonzero and positive. In the simulations, the nonzero $\mathcal{C}^{(i,j)}$ were randomly chosen (once for all) in the range $[1, 3]$, which guarantees strong coupling but not perfect synchronization.

The three networks were simulated with the Heun method ($\delta t = 0.025$) starting every time from random initial conditions. Then, the transients were dropped out and the data down-sampled ($\delta T = 0.075$) collecting 80 trials (the average number of available trials in our EEG data) of 500 points each (the length of one trial in our EEG data).

We measured the coupled variables $\theta_2^{(i)}$ from all sites, and we added zero mean white Gaussian observation noise of different intensities, *i.e.* 10, 4 and 0 dB SNR[3]. Afterwards, we assessed the topographical sensitivity and the robustness of the S estimator[4] with respect to measurement noise and data length. This was done for each of the values of the observation noise intensities analyzing the data as if they were real EEG according to the procedure described in Sec. 5.3.2, considering at once only 20, 40 or all the 80 epochs.

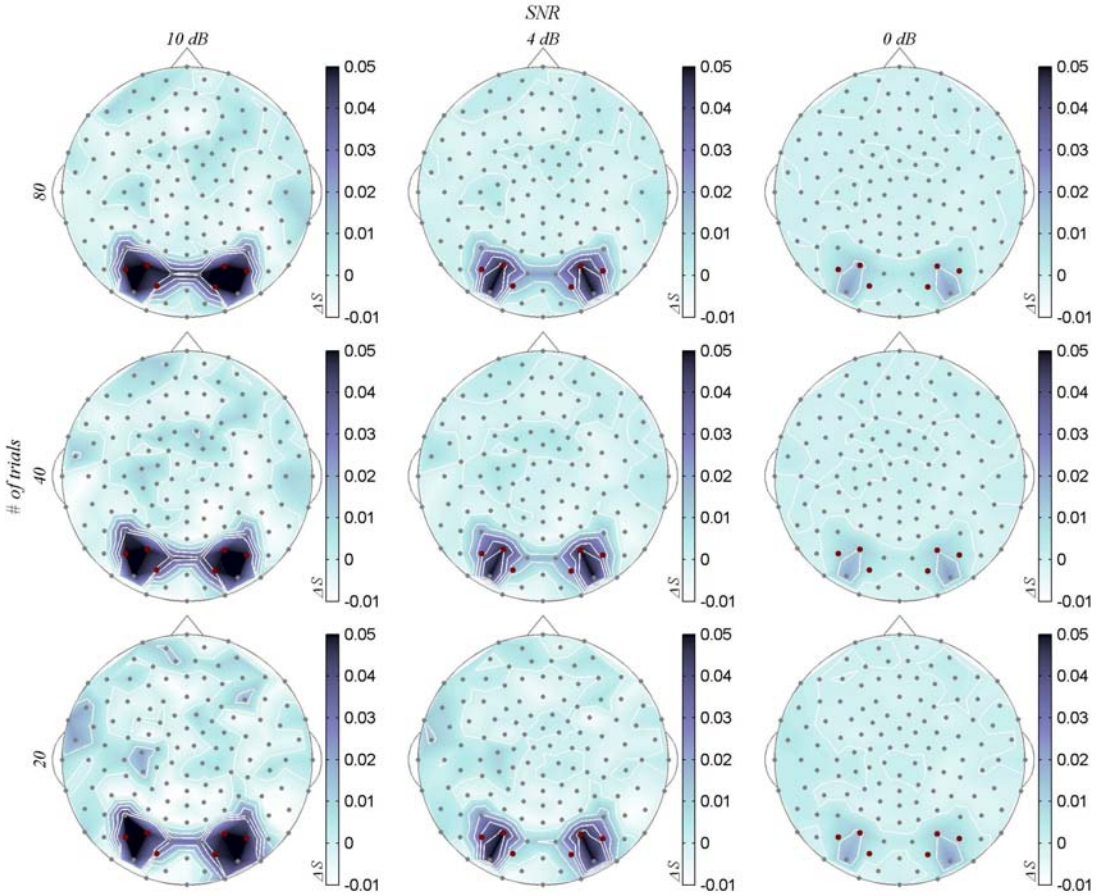

Fig. 5.5. Numerical assessment of the topographical sensitivity of the S estimator. Topographical maps of the variations of the mean synchronization (ΔS, see text) of the simulated EEG activities *OG vs. BGR*. Robustness of the synchronization topography with respect to observational noise intensity, considering 10, 4, and 0 dB Signal to Noise Ratio, and data lengths, considering 20, 40, and 80 trials of 500 samples each. White-bordered dark regions highlight the clusters of electrodes with the highest values. Five white contour lines emphasize the rate of transition from synchronized to unsynchronized clusters. The contour values are equally spaced between $\Delta S = 0$ (no augmentation of synchronous activity with respect to the background) and the maximal value of ΔS. The shade of colors is obtained by a tri-linear interpolation from the three nearest electrodes. Gray and red spots are the electrodes positions; the red spots show the position of the two synchronized clusters considered in the simulation (see text).

[3] We did not consider here an analysis of sensitiveness with respect to modeling noise intensity, however, in Chapter 3 our S estimator has shown to be robust in inferring the condition we are testing here of present/not present coupling.

[4] We applied it to non embedded data.

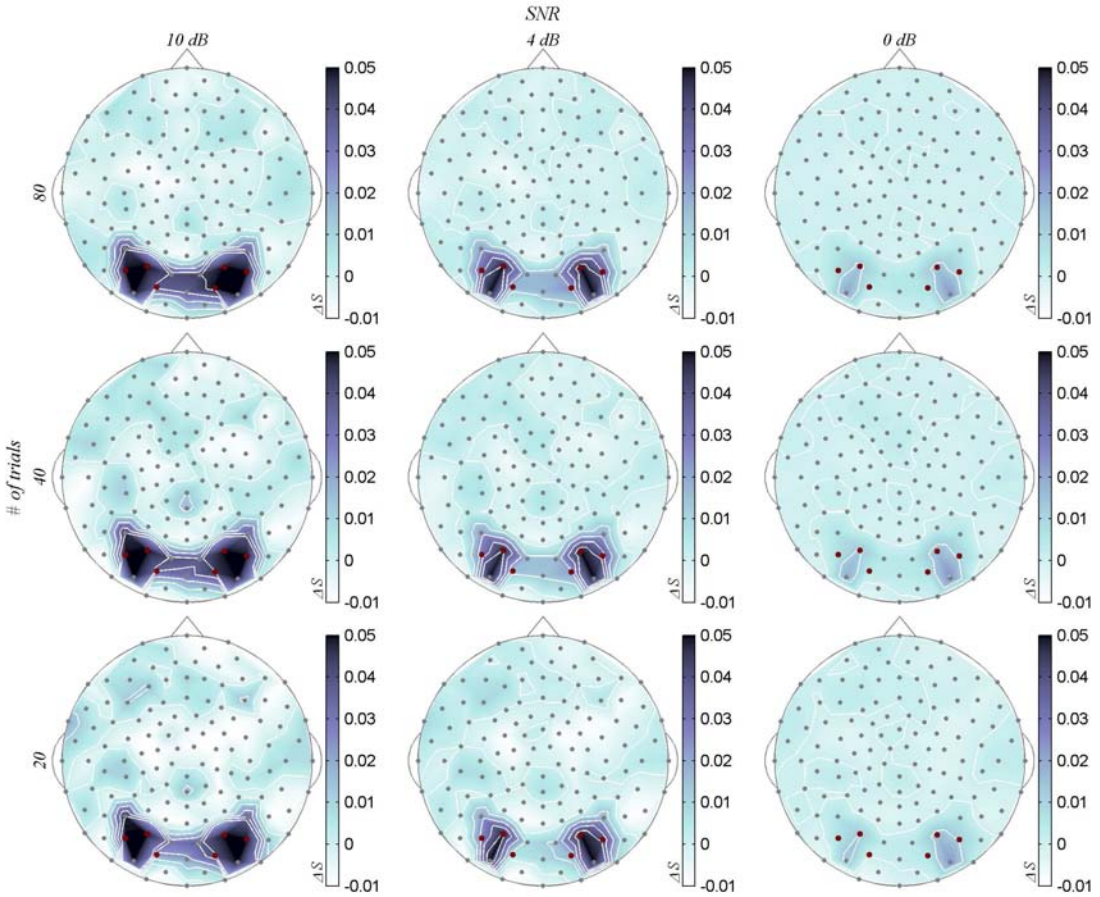

Fig. 5.6. Numerical assessment of the topographical sensitivity of the estimator. Topographical maps of the variations of the mean synchronization (ΔS, see text) of the simulated EEG activities *IG vs. BGR*. Robustness of the synchronization topography with respect to observational noise intensity, considering 10, 4, and 0 *dB* Signal to Noise Ratio, and data lengths, considering 20, 40, and 80 trials of 500 samples each. Other conventions as in Fig. 5.5.

The results are summarized in Figs. 5.5 and 5.6, which show the topography of ΔS values for the *IG vs. BGR* and *OG vs. BGR* arrangements, respectively, at the different noise intensities and number of trials. In both figures, the white-bordered dark regions highlight the territory with the highest ΔS values. In order to emphasize the steepness of the transition from synchronized to unsynchronized clusters, five white contour lines are drawn. The contour values are equally spaced between $\Delta S = 0$ and the maximal value of ΔS. Referring to the best case (80 trials and 10 *dB* SNR), it can be noticed that the synchronized clusters are correctly identified by the topography of ΔS without delay-embedding, even if in this complex case each signal comes from a different sub-system.

Furthermore, the second order neighborhood cluster analysis, as suggested in Sec. 5.3.2, is indeed adequate to observe close interhemispheric synchronizations, possibly caused by the *IG* stimuli, as shown by the wide cross-hemispheric synchronized regions in Fig. 5.6. On the contrary, when the clusters are uncoupled, the topography of ΔS also shows isolated regions of synchronization, *cf.* Fig. 5.5. As the SNR decreases, the synchronized clusters visually smear out at the chosen equal plotting scales. Nevertheless, the synchronized clusters, as well as the difference between the two topographical arrangements, can be verified to be statistically significant down to 4 *dB* with 40 trials and to 0 *dB* with 80 trials, as it was the case for the real EEG.

5.3.4 Results on EEG signals

The EEG data from nine subjects have been analyzed with the cooperativeness estimator S. This estimator highlighted regions whose cooperative activity was modulated by the visual stimuli. Furthermore, we broke down the analysis of the estimator to three of the traditional frequency bands of EEG analysis, the α $(7 - 13\ Hz)$, β $(13 - 30\ Hz)$, and γ $(30 - 70\ Hz)$ bands.

Cooperativeness topography

The visual stimuli used in this study were chosen primarily because it was previously found that they could reliably modify interhemispheric spectral coherence in animals and men [Kiper et al., 1999, Knyazeva et al., 1999]. Stimulus *IG* conforms to the Gestalt principle of perceptual grouping by collinearity and common fate and is likely to generate cooperative activity in the two hemispheres. Stimulus *OG*, instead, presumably places the visual area of the two hemispheres in a condition of perceptual rivalry. Consequently, according to the synchronization-based solution to the binding problem [Gray, 1999], high S values are predicted in areas of the brain involved in processing the *IG* stimulus, whilst the rest of the activity, remaining unorganized, should result in low S values. Indeed, as explained in an earlier chapter, a high value of S reflects a low amount of uncorrelated activity sources in the region processing the coherent stimulus.

The average topographical arrangement of ΔS values with the *IG* and *OG* stimuli are shown in Figs. 5.7 and 5.8. In both figures the white-bordered dark regions denote the clusters of electrodes (and indirectly the underlying cortical territory) with the highest ΔS values.

As for the simulations (*cf.* Sec. 5.3.3), in order to render the steepness of transition from more cooperative to less cooperative clusters, five white contour lines are superimposed to the figures. The contour values are equally spaced between $\Delta S = 0$ (no augmentation of cooperative activity with respect to the background) and the maximal value of ΔS. Among the nine subjects, the region of modulated cooperativeness induced by the *OG* stimulus (Fig. 5.7) is more often lateralized, whilst the one induced by the *IG* stimulus (Fig. 5.8) is more often centered at or near the electrodes close to the occipital lobes and spans the two hemispheres.

This is further highlighted in Fig. 5.10, which shows the response to the *IG vs.* the *OG* stimulus. Nevertheless, in this and in previous studies using the same stimuli and EEG coherence assessments [Knyazeva et al., 1999], individual differences were noticed in the degree of interhemispheric cooperativeness. Their origin is at present unexplained. The two most likely possibilities are: differences in the morphology of callosal connections or individual variability in attention to the stimuli. Both possibilities could be tested in future experiments. The stimulus-induced differences emerge even more clearly from the population analysis shown in Fig. 5.10. The *IG* stimulus evokes cooperative activity over a cluster of electrodes overlying the occipital poles and spanning both hemispheres. On the other hand, the *OG* stimuli induce a modulation of the cooperative activity in two symmetrical clusters of electrodes overlying the parieto-temporal regions of the two hemispheres. Statistical comparisons (permuted Hotelling T^2 test) returned highly significant differences (Bonferroni corrected for multiple comparisons; all electrodes included) for the *OG* and *IG* stimuli *vs.* background ($p < 0.001$) and for *IG vs. OG* ($p < 0.005$). At individual level, significant differences ($p < 0.01$) were obtained in all subjects in case the comparisons were restricted to the occipital electrodes with $\Delta S > 0$.

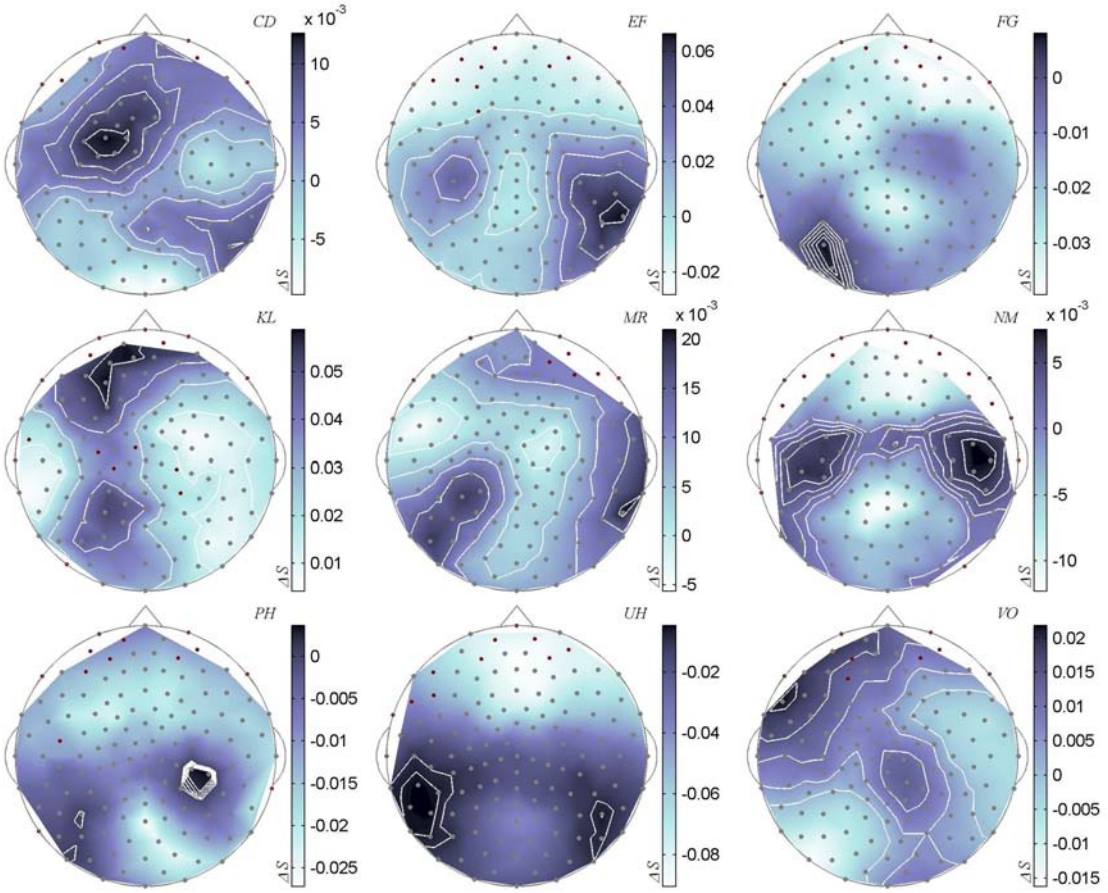

Fig. 5.7. Topographical maps of the variations of the mean synchronization (ΔS, see text) of EEG activity induced by the orthogonally oriented grating (OG) with respect to the background. White-bordered dark regions highlight the clusters of electrodes (and indirectly the underlying cortical territory) with the highest ΔS values. Gray and red spots are the electrodes positions, the red ones being excluded from the computation due to artifacts. *CD*, *EF*, *FG*, *KL*, *MR*, *NM*, *PH*, *UH* and *VO* denote the subjects. Other conventions as in Fig. 5.5.

Frequency bands arrangement

Although the above analysis might be satisfactory within the more general frame of system theory, the prevailing trend in studies of oscillatory cortical activity is to analyze separate frequency bands. Hence, we broke down the analysis of the S estimator into the three traditional bands of EEG frequencies: the α $(7-13\ Hz)$, β $(13-30\ Hz)$, and γ $(30-70\ Hz)$ frequency bands[5]. This was also done to compare the results of the present method for detecting cooperativeness with those of coherence analysis (of the same EEG recordings) reported in [Knyazeva et al., 2002, 2003] and summarized in the next section.

The results of such analysis at the population level are reported in Fig. 5.11. The bi-hemispheric, occipital modulation of cooperativeness induced specifically by the IG stimulus *vs.* background involves mainly the β band. The γ band is also involved by the stimuli, but no differences are observed between the OG and the IG stimuli. Interestingly,

[5] The signals in the different frequency bands were obtained by band pass filtering.

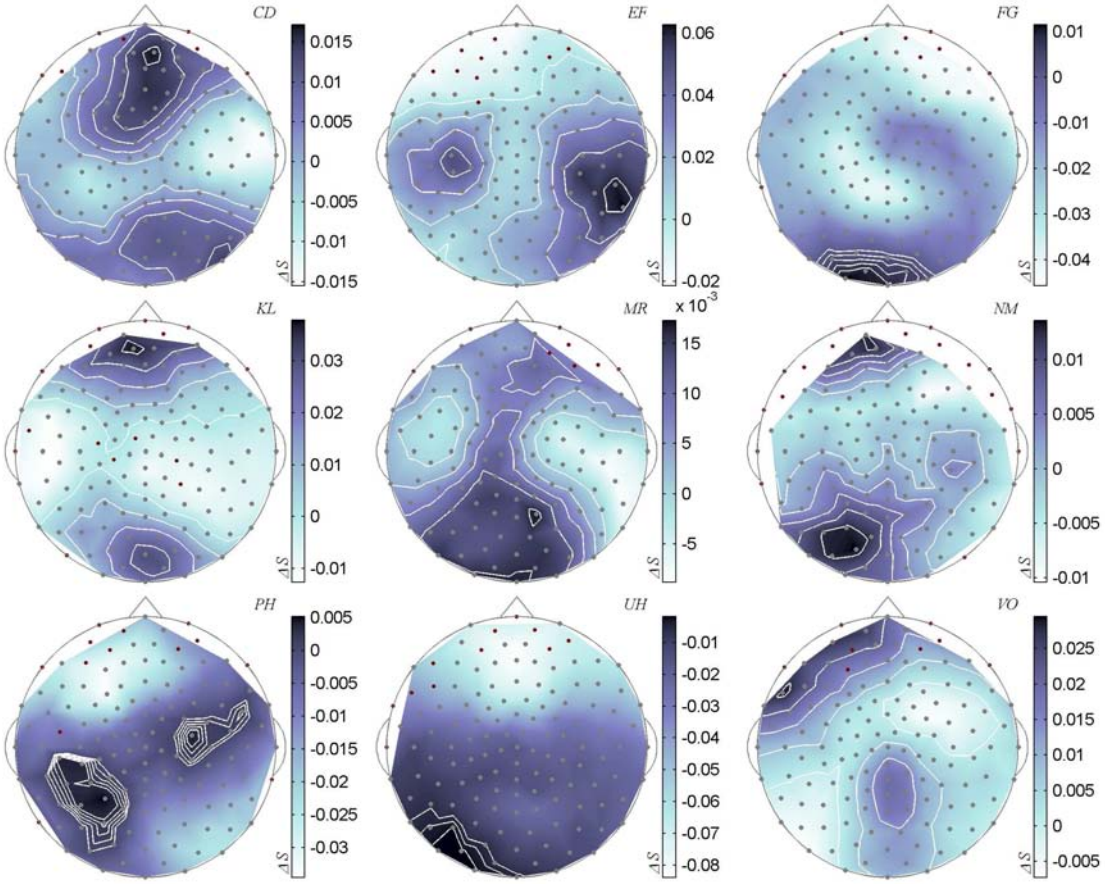

Fig. 5.8. Topographical maps of the variations of the mean synchronization (ΔS, see text) of EEG activity induced by the iso-oriented grating (IG) with respect to the background. Other conventions as in Fig. 5.7.

the topography of cooperativeness in the β and γ bands is also different. The selective activation in the β band is in agreement with the changes induced by the same stimuli in interhemispheric coherence [Knyazeva et al., 1999, 2002, 2003]. However, surprisingly, the OG stimuli evoked two symmetrical clusters of cooperativeness in the parieto-temporal electrodes in the α band, and a weaker cluster of trans-hemispheric cooperativeness in the occipital lobe in the β band. They also evoked a cluster of trans-hemispheric occipito-parietal cooperativeness in the γ band, similar to that induced by the IG stimulus.

5.3.5 Discussions

Techniques for assessing cooperative EEG activity, derived from system theory, have been mainly employed on three fronts. Firstly, at the brain modeling level, for verifying the hypothesis that synchronization exists between brain regions [Tononi et al., 1994, Breakspear, 2002, Stam et al., 2003]; secondly, for investigating the functional role of synchronization within the neuronal populations involved in a task [Lachaux et al., 1999, Tass et al., 2003, Micheloyannis et al., 2003]; and, thirdly, in clinical environment, for assessing the effects of lesions or diseases in the brain [Tass et al., 1998, Mormann et al., 2000, Quian Quiroga et al., 2002].

Along the second methodological line, we have applied our S estimator in order to investigate the functional role of a stimulus-induced modulation of cooperativeness in

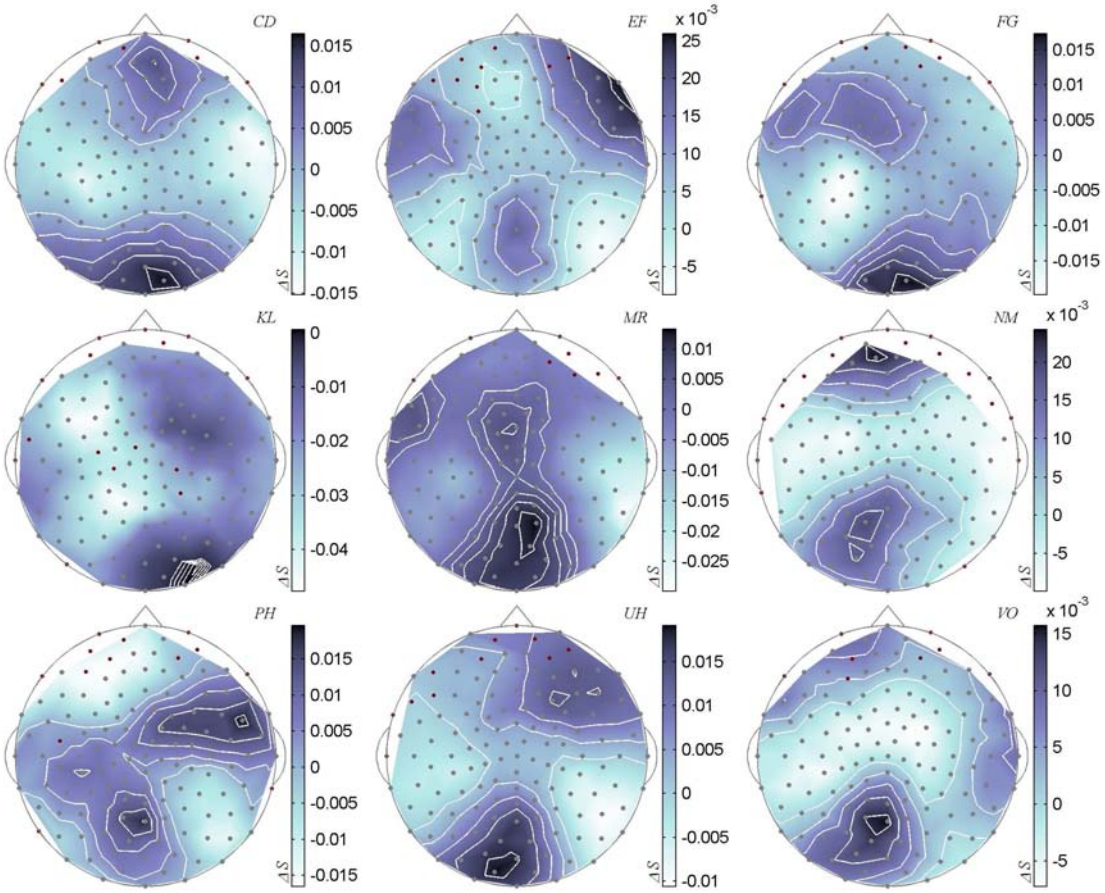

Fig. 5.9. Topographical maps of the variations of the mean synchronization (ΔS, see text) of EEG activity induced by the *IG* grating with respect to the *OG* grating. Other conventions as in Fig. 5.7.

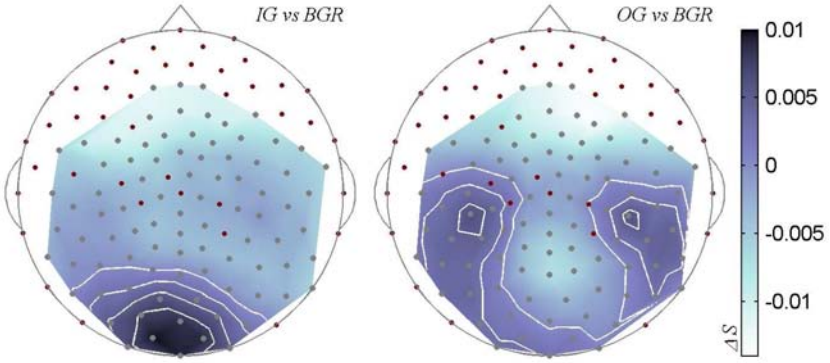

Fig. 5.10. Average topographical maps, for the entire population of subjects, of the variations, with respect to the background, of the mean synchronization (ΔS, see text) of EEG activity induced either by the iso-oriented grating (*IG vs. BGR*) or by the orthogonally oriented grating (*OG vs. BGR*). Other conventions as in Fig. 5.7.

EEG signals. We have used our measure for studying cooperativeness phenomena in conditions where frequency-specific linear methods, *i.e.* spectral coherence, were already applied. This has allowed comparisons between the two methodologies.

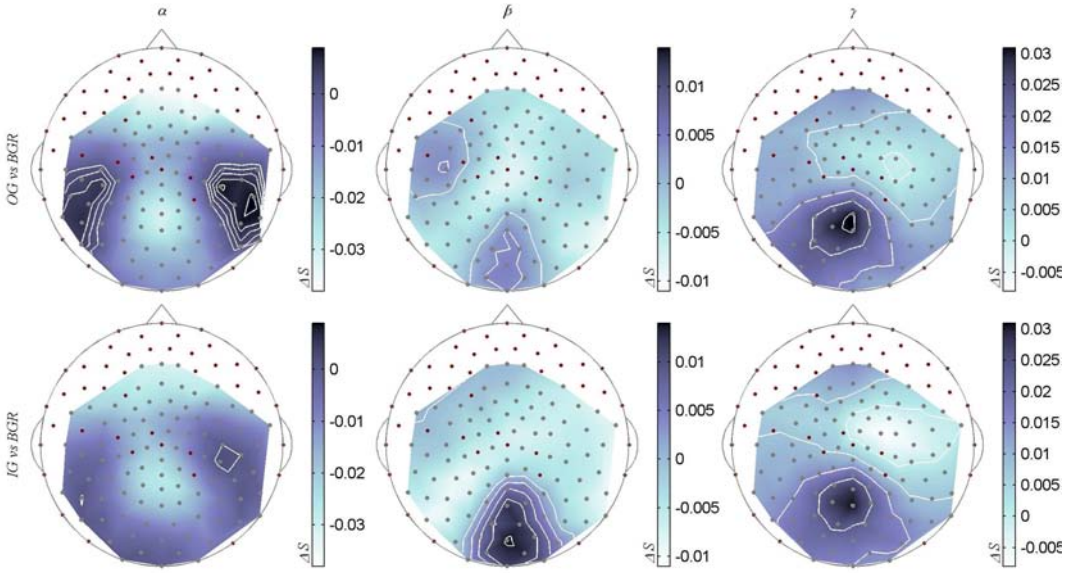

Fig. 5.11. Average topographical maps, for the entire population of subjects, of the variations, with respect to the background, of the mean synchronization (ΔS, see text) of EEG activity, within the α, β, and γ frequency bands, induced either by the iso-oriented grating (*IG vs. BGR*) or by the orthogonally oriented grating (*OG vs. BGR*). Other conventions as in Fig. 5.7.

The S estimator allowed demonstrating stimulus-specific changes in the overall cooperativeness of brain activity, in the population analysis and partially at the level of the examined single subjects.

We have applied S to simulated networks of coupled sub-systems, in situations caricaturing the hypothetical coupling generated between the hemispheres by *IG* and *OG* visual stimuli. In this test, the coupling scheme caricaturing the *OG* condition returned two adjacent, but separate clusters of increased S. The scheme caricaturing the *IG* condition returned a wide continuous cluster extending across the hemispheres, comparable to the findings in the human EEG recordings. It is to be noticed though, that the displacement of the clusters driven by the different stimuli in the spatial and frequency domains was not grasped by the simulation. This has potentially interesting consequences for the interpretation of the EEG data, beyond the aims of the present study.

The results obtained with the S estimator on EEG recordings can also be compared with those obtained with coherence analysis[6] on the same material [Knyazeva et al., 2002, 2003]. Because of its intrinsic multivariate nature addressing the whole skull topography, the S estimator turns out to be a complement to coherence analysis; the most commonly used linear method for the assessment of EEG cooperativeness. Indeed, when considering cooperativeness between more than a single pair of electrodes, the S estimator is more natural, being intrinsically multivariate, than coherence, and allows the analysis of cooperativeness phenomena spanning a wide territory. Finally, the S estimator addresses the investigations of broad-band cooperativeness phenomena.

For the data considered in this study, the following differences between the results obtained with the S estimator and the EEG coherence analysis are noteworthy. The S estimator highlighted changes over a broader set of electrodes than the coherence analysis. The latter, applied to regions of interest, demonstrated changes mainly restricted to a

[6] Coherence analysis is meant the study of the spectral coherence as a function of the difference frequencies.

single couple of electrodes in the occipital region, the electrodes 70 and 90 of Fig. 5.4, [Knyazeva et al., 2002, 2003]. Significant coherence changes were restricted to a narrow band of frequencies between 20 and 30 Hz. Finally, the formation of lateralized clusters of synchronous activity in the temporal region in the α band was not seen with the coherence analysis, nor was the fact that synchronization in the γ band did not differentiate between the two types of gratings.

The results obtained with the S estimator emphasize the complexity of the changes induced even by very simple stimuli, and appear to provide an easy to use and robust tool for the analysis of these changes.

Although the S-based analysis might be satisfactory within the frame of system theory, from other viewpoints it is not. The prevailing concept of cortical functioning suggests that frequency-specific oscillations are directly related to specific cortical functions, particularly in the visual domain [Eckhorn et al., 1988, Gray et al., 1989, Rodriguez et al., 1999]. It would also be expected that the function-and-frequency specific oscillators are also localized at specific sites, whose identification is a challenging task for contemporary research. Therefore, in the second part of the study we broke down the analysis of the S estimator to the α, β, and γ frequency bands. This analysis demonstrated that, compared to the background, the identical gratings induced a coherent activation of the two hemispheres in the β band, focused on the occipital electrodes. Similar but weaker effects were obtained with the orthogonal stimulus. These results are in line with those obtained by coherence analysis. Unexpectedly, however, the orthogonal stimulus gave raise to two symmetrical clusters of activation in the α frequency range in the occipito-temporal region. The two clusters dissolved with the identical gratings. The γ range was insensitive to stimulus diversity in the sense that both the orthogonal and collinear stimuli increased the values of the estimator mostly in the parietal region.

From the neurobiological point of view, the results summarized above raise two distinct sets of questions. The first one is related to the morpho-functional substrate of the observed phenomena. The response here is, to some extent, of an inferential kind. As one would have predicted by elementary notions of brain functional anatomy, the changes were concentrated in the occipital-temporal part of the brain. Indeed, the changes were induced by visual stimuli, which are known to powerfully activate the primary and secondary visual areas [Law et al., 1988, Kiper et al., 1999, Knyazeva et al., 1999]. When the two hemispheres viewed identical gratings, a field of cooperative activity was formed, spanning across the hemispheres. Instead, when they viewed orthogonally oriented and moving gratings, two separate fields of cooperative activity were formed in the two hemispheres. Presumably, the recorded activities inform on events occurring in relative close proximity to the electrodes involved, *i.e.* in the occipital temporal region. More precision on the topographical location of the recorded signal can be derived only from techniques of dipole localization [Sidman et al., 1991, Gevins et al., 1995], or possibly by correlation with the fMRI activation [Knyazeva et al., 2003]. Concerning the substrate of the interhemispheric cooperativeness, the similarity of some of our findings with those obtained by coherence responses to the same stimuli in animals and in man [Kiper et al., 1999, Knyazeva et al., 1999], suggests that, as in the latter, the cortico-cortical connections mediated through the Corpus Callosum, might be crucially involved.

The second question is of a more general, theoretical and methodological nature. The observed phenomena could be explained as the result of the interaction between different classes of cortical oscillators, each class being characterized by a different oscillatory frequency [Frank et al., 2000, Corchs and Deco, 2001]. Different stimuli could differently

bind/unbind the oscillators. Alternatively, the stimuli themselves could be involved in the generation of oscillations at different frequencies as well as in their binding. Possibly, some of the uncertainties discussed here could be resolved by the systematic analysis of periodic visual stimuli of different frequencies, and/or of non periodic visual stimuli.

Irrespectively of the answers to the questions above, another consideration seems to emerge from the results we described. The response of the visual areas to the extremely simple stimuli used is neither simple nor localized in either the frequency or in the spatial domain. Hence, as already suspected [Bressler et al., 1993, Basar et al., 2001], it is unlikely that the response might be satisfactorily characterized by assuming the existence of simple relations between EEG frequencies and functions. Instead, the complexity of cortical dynamics might be better characterized by approaches considering that brain activity continuously varies with time within a complex state-space [Bruns et al., 2000, Freeman, 2003]. Within this approach, several research lines seem to suggest a chaos-based hypothesis of brain functioning [Wright and Liley, 1996, Dafilis et al., 2001, Kaneko and Tsuda, 2003, Kay, 2003].

It has been suggested that the systems underlying some perceptual representations are chaotic and that learning creates modified attractors within or among parts of the system. Within this view, the sensing system of living beings would be definitely more than a simple transducer converting external stimuli into electric or magnetic fields. Sensorial cells could transform the external stimuli in a symbolic internal representation that might be intrinsically interpretable by the brain. As a possible mechanism, in [De Feo, 2004a,b] the phenomenon of *qualitative resonance* has been proposed. Roughly speaking and without entering into the details, it deals with the property of chaotic systems to "lock" (or synchronize) approximately to an input signal that is related to their internal chaotic dynamic, and consequently regularizing its dynamics. In contrast to this, their chaotic behavior is reinforced when the input signal has nothing to do with their internal dynamics[7].

Two important consequences can be sketched: first, synchronization or regularization of network behavior could be viewed as the side-phenomenon of the formation of a network's state corresponding to a given stimulus; second, importantly, the read-out problem would not be a problem anymore, because within this computational scheme the coding of external stimuli would be intrinsic. In this view, synchronization would play only a partial role in the perception of a stimulus, and the brain perceptual semantic would be obtained by the formation of an internal state.

To face this suggestive hypothesis of brain functioning, we approached the issue of unraveling nonlinear features from the recorded EEG signals. Indeed, the first step to state that we are observing a system with chaotic behavior is the inference of nonlinear properties from the measurements.

5.3.6 Identification of a model from the EEG signals

In this section we present the work done to identify a nonlinear model from the EEG signals. Because the results were not satisfactory, we do not enter into the details of this investigations.

[7] It may be argued that chaotic behavior is not necessary to realize such learning/perceptual scheme. Indeed, a state of a linear system and resonance phenomena would suffice. However, the potential role of chaos would be to make perception and learning more robust and flexible and would represent the evolutionary solution of cognitive systems to face unpredictable events [De Feo, 2001].

Starting from the hypothesis of a non entirely stochastic brain functioning, a host of investigations about the presence of nonlinearities in EEG recordings have been carried out. Contrasting results have risen: they range from evidence for chaotic attractors underlying the α rhythm [Soong and Stuart, 1989] to the conclusion that EEG data of healthy volunteers may be more appropriately modeled by linearly filtered noise [Theiler and Rapp, 1996]. Traditionally, such an investigation is performed by testing the null hypothesis that the data might be generated by a linear system. Some nonlinear observable from the data is computed, as, *e.g.* a Lyapunov exponent, a correlation dimension or a prediction error [Kantz and Schreiber, 2004]. Subsequently, it is tested if this value is consistent with the distribution of the same observable computed on linear stochastic processes, estimated by the method of *surrogate* data [Theiler et al., 1992], which mimick the linear properties of the original data.

Alternatively to this approach, it is possible to make a statistical comparison of the prediction error estimated with a linear and nonlinear model. In this case, we may say that a nonlinear system has generated the recorded data if a nonlinear model of them gives better prediction (in a statistical sense) than a linear model. We chose to use this approach to investigate about the nonlinear nature of the EEG signals recorded from humans under visual stimulation and described earlier. An example of them is shown in Fig. 5.12.

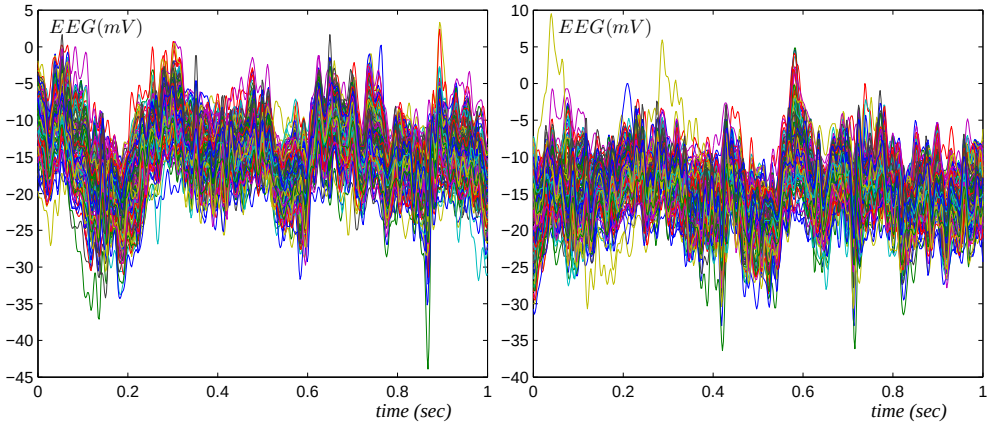

Fig. 5.12. Two examples of EEG recordings during the period of one trial. The time courses are from all the electrodes.

To build a linear model from the data, we used the System Identification Toolbox available with Matlab [Ljung, 1999]. To identify a nonlinear model, we used two kinds of fitting: a locally constant one (the so called zero-th order predictor[8] in [Kantz and Schreiber, 2004]), and a global model given by radial basis functions. We remind that regarding the latter, a powerful Matlab package exists [Orr, 2001].

For each trial, we computed the mean squared prediction error as

$$e^{(i)} = \sqrt{\frac{1}{L-h}\sum_{t=1}^{L-h}\left(y_{t+h}^{(i)} - \hat{y}_{t+h}^{(i)}\right)^2} \tag{5.1}$$

[8] A locally (in state-space) constant prediction.

where $e_j^{(i)}$ represents the error for sub-system (i) for a given trial, h is the time horizon of the prediction and $\hat{y}_{t+h}^{(i)} = \hat{F}(X_t, h)$ the predicted value h-step ahead from the whole-system reconstructed state X_t. We used half of the available trials to identify the model and the other half to compute the error prediction. Consequently, we obtained time series for the error prediction from the linear model and another from the nonlinear model. We compared them with a Wilcoxon rank-sum test. To reduce the computational effort, we computed a nonlinear model only for the self-model, while for the interaction we identified only a linear model (*cf.* Chapter 4).

Independently from the location on the skull (*i.e.* electrode position), from stimulus condition and from the subject, we found no difference in the error population of the linear model *vs.* nonlinear model. This result was robust with respect to the variation of h, which we varied from 1 to 20. Furthermore, in many cases the residual errors of the linear model even passed a test of whiteness.

For the sake of completeness, we also tested the time series after the application of the Laplace operator, to remove the spreading effects due to neighboring electrodes, and we obtained similar results.

The whole result is not really surprising. Indeed, as we pointed out above, in the literature convergent and unifying interpretations of EEG analysis results do not exist. Nevertheless, it is questionable whether EEG time series from different settings can carry enough information to reveal the dynamical properties of the underlying system. To investigate further this question, we analyzed different EEG data-sets. First, EEG signals recorded from patients during sleep have been analyzed (data available from "The Siesta Group Schlafanalyse GmbH" [group schlafanalyse gmbh, 2001]). We found an indication of nonlinear deterministic structure depending on the recording region and on the sleep state, particularly for non-REM states.

Second, EEG recordings from healthy subjects and from patients affected by pathological conditions, for instance epilepsy, has been studied (for a detailed description of this data-set, please see [Department of Epileptology, 2001]). Our analysis of surface EEG recordings from healthy volunteers with eyes closed and eyes open confirmed the conclusion, reported in [Andrzejak et al., 2001], of a not strong indication of nonlinear deterministic dynamics. Still being in agreement with the results shown in [Andrzejak et al., 2001], our analysis emphasizes the presence of nonlinear deterministic structures for the intracranially recorded time series from epileptic patients during seizures.

5.3.7 Discussion

In many studies, nonlinear time series techniques have been applied to different kinds of EEGs from humans, such as recordings from healthy volunteers at rest, sleep, during periods of cognitive activity, or from patients with diseases. The interpretations of the results range between two extremes, from evidences for chaos to conclusion that EEG data are linearly filtered noise. Here, as described in the previous section, we have analyzed our EEG data-set (ten subjects, three different visual stimuli). Independently from the subject and from the recording electrode, our analysis suggests that all the measures are from linear stochastic processes. Next, we have analyzed EEG data freely available on the web. The results comply with those obtained using different techniques and shown in [Andrzejak et al., 2001]. Strongest indications of nonlinear deterministic dynamics are only for intracranial recordings in regions where epileptic seizure activity appears, while for extra-cranial EEG recordings from healthy subjects with closed/open eyes, there is no significant indication of nonlinearity.

Three are the possible conclusions: first, the methodological investigation we used is not sharp enough to grasp nonlinear dynamical features in the data. Very recent advances in nonlinear time series analysis may result successful [Zhang et al., 2006, Zhang and Small, 2006].

Second, the system underlying that perceptual process has a merely linear dynamics; second, our observation is not rich enough, *i.e.* our time series are measures of signals that have lost their nonlinear dynamical properties because of spreading phenomena in the brain cortex and/or filtering through the skull. Third, it is also possible that those perceptual phenomena involve such huge number of brain sources that we observe gaussian processes according to the central limit theorem. Indeed, in an analysis of sleep EEG data, we found suggestion of nonlinearity in some regions during not-REM sleep (these status are usually considered as a brain state of moderate or minimal activity).

All these considerations seem to suggest a different recording strategy to successfully observe salient properties of the brain activity generated by visual stimuli: macroscopic intracranial recordings or measures at a mesoscopic spatial scale.

We had available a new set of measurements realized on a small region of the cerebral cortex with low impedance electrodes. This experiment was carried out on ferrets in order to assess the role of interhemispheric interactions in modulating the activity of the visual cortex within an hemisphere while the contralateral hemisphere was inactivated. We will discuss the results of the analysis of these data in next sections.

5.4 Stimulus-dependent interhemispheric neuronal cooperativeness in LFP signals

In the previous sections, we have described the analysis of stimulus-dependent interhemispheric interactions in human brains observed at a macroscopic scale, *i.e.* by EEG measurements. Here, we describe an experiment designed to allow the study of interhemispheric interactions at a mesoscopic scale, *i.e.* by local field potential (LFP) measurements. A LFP is a particular class of electrophysiological signal. A signal is recorded using a low impedance extracellular micro-electrode, placed sufficiently far from individual local neurons to prevent any particular cell dominating the electrophysiological signal. This signal is then low-pass filtered to obtain the LFP[9]. The low impedance and positioning of the electrode allows the activity of a large number of neurons to contribute to the signal, approximately a few hundred of them, while EEG signals are probably due to the superposition of the activity of thousands of neurons.

This new experiment was designed by the team of prof. G. Innocenti in order to study peculiarly the role of the Corpus Callosum (CC) in integrating the functions of the two hemispheres. CC is composed of fibers that establish the largest pathway interconnecting cortical areas of the two brain hemispheres. The role of CC and the presence of two hemispheres in primate brains has been the object of deep investigations since, at least, forty years [Sperry, 1982, Gazzaniga, 2005]. Surgical section of the CC, in man, divides the functions of the two hemispheres, a condition usually described as "two persons sharing the same body". How the intact CC integrates the function of the two hemispheres is generally unknown. Cues come from studies in the visual system of both animals and man showing that callosal connections i) enhance or depress responses to a visual stimulus [Berlucchi et al., 1967, Marzi et al., 1982, Payne et al., 1991, Ptito, 2003] and

[9] The low-pass filter removes the spike component of the signal.

ii) synchronize the activity of the two hemispheres [Engel et al., 1991, Munk et al., 1995, Kiper et al., 1999, Knyazeva et al., 1999, Carmeli et al., 2005].

The study presented in the previous sections belongs to the latter findings. However, those results may only suggest the involvement of CC fibers in the interhemispheric interactions because the same stimuli conditions were not studied without CC or after transection of it. Here, we describe a different experiment in which we could study peculiarly the role of CC by inactivating one hemisphere with a cooling. In particular, while in the EEG study we recorded brain activity spanning over both hemispheres, here we recorded the activity of neuronal assemblies within a hemisphere. We studied how inter-hemispheric interactions control the dynamics of intra-hemispheric as following: we measured how cooling the visual areas of one hemisphere affects cooperative behavior of stimulus-driven responses in the visual areas of the other hemisphere. With such a setting, we were able to unveil a new further kind of interhemispheric integration. By using our S estimator, we found that stimulus-driven cooperativeness of local neural activity in the visual areas of one hemisphere is modulated by input from the other hemisphere. Furthermore, this modulation is true only if the visual areas in the two hemispheres view identical stimuli which can be easily bound into a coherent percept. Therefore, inter-hemispheric connections contribute to *unifying* brain function by modulating in a flexible, stimulus-dependent way temporal parameters of neuronal population activities likely to be involved in stimulus *detection* and/or *categorization* [Gray et al., 1989, Engel et al., 2001, Romo et al., 2003, Womelsdorf et al., 2006].

In the next section we illustrate the experimental setup performed by the team of prof. G. Innocenti and the data analysis strategy. Finally, we describe the results of the latter.

5.4.1 Materials and methods

Ferrets bought from a Swedish authorized breeder were prepared for the experiment and maintained under anaesthesia according to protocols conform to Swedish and European Community guidelines for the care and use of animals in scientific experiments and approved by the ethic committee of Stockholm District (as in [Manger et al., 2002]). As shown in Fig. 5.13, during the experiment they viewed two types of gratings: identical stimuli (IS) consisted of 4 full-field gratings oriented around the clock in 45 deg steps and identical in the two hemifields; different stimuli (DS) were gratings as above but whose orientation and/or direction of motion differed by 90 deg in the two hemifields.

The stimuli remained static for 0.5 sec and then moved in one of the two directions perpendicular to their orientation for 3 sec followed by 3 sec of exposure to an equiluminant gray screen, the BKG stimulus. The gratings had a spatial frequency of 0.1 $cycle/deg$ and moved at 14 deg/sec. Local field potentials (LFPs) were recorded with an array of 15 tungsten microelectrodes aimed at areas $17-19$. The position of the microelectrodes was controlled histologically after the experiment. Hand mapped receptive fields confirmed by computerized mapping indicated that the electrodes recorded activity within 20 deg from the visual field midline, *i.e.* in parts of the visual field representations which are connected by axons of the Corpus Callosum [Gray et al., 1989]. Recordings were carried out from the right hemisphere using a matrix of 3×5 tungsten microelectrodes spaced at 410 μm from each other and conventional amplifiers. A custom made cryoloop as in [Lomber et al., 1999] was placed on the areas $17 - 19$ of the left hemisphere. The cryoloop was cooled to 20 $C \pm 1.5$ C as in [Payne et al., 1991, Lomber et al., 1999] over 20 min. This procedure is known to deactivate all cortical layers under the probe. After

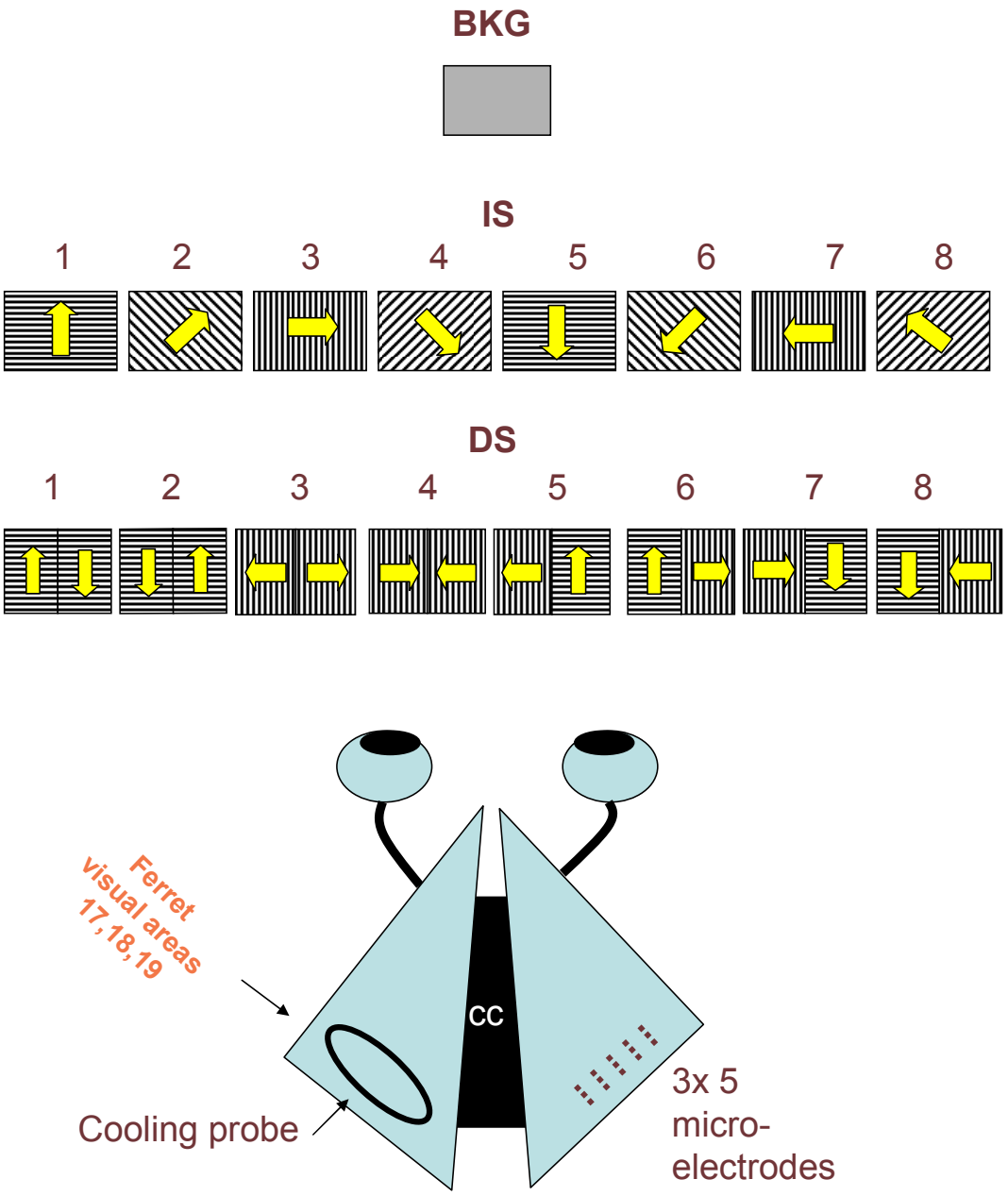

Fig. 5.13. Experimental setup. Anesthetized ferrets viewed either a uniform gray screen (BKG) or gratings moving in the direction shown by the arrows. IS stimuli activated identically and DS differently the hemifields (hence the hemispheres). Local field potentials were recorded with a 3×5 microelectrode array aimed at the visual areas 17,18 of the right hemisphere. The contra-lateral areas 17 to 19 were reversibly inactivated by cooling.

5 *min* waiting meant to stabilize the temperature, one stimulation cycle was performed, followed by 30 *min* recovery to normal temperature after which a new stimulation cycle was performed. All data were pre-processed in the following way: the 50 Hz power line was removed with a notch filter and the frequency range $0 - 70$ Hz was kept by low-pass filtering. The filtering procedure ensured that no phase lags were introduced. The standard structure of local field potentials recordings over 13 electrodes (two electrodes were inactivated) was the following: 0.5 *sec* during the presentation of the static IS or DS gratings), 3 *sec* during the presentation of the moving gratings, 3 *sec* when the BKG

stimulus was presented. The periods of moving and BKG stimuli were analyzed but the first second of each period was considered a transient, and discarded such that only the last 2 *sec* of these stimulation periods were taken for the further processing. Generally, 30 trials were collected for each of the two stimulus conditions mentioned above, either during Control, Cooling and Recovering after cooling. Noisy or unresponsive electrodes were discarded; on average, 10 electrodes were selected for the further processing. All data were de-trended to zero mean and normalized to unitary variance. To assess changes in the degree of cooperativeness among the recorded neuronal populations due to the presence of the structured stimulus with or without inter-hemispheric influence, we used the S estimator.

We computed the difference (trial-wise because of the known temporal order) $\Delta S = S_{BKG} - S_{Gratings}$, where its positive values denote increased cooperativeness with respect to the background, and negative values indicate decreased cooperativeness. To assess statistical changes in the degree of cooperativeness, we used non-parametric tests because S values are restricted between 0 and 1 and, consequently, the hypothesis of Gaussian distribution is not tenable. We used Wilcoxon signed rank test to test the null hypothesis of zero median for the $\Delta S = S_{BKG} - S_{Gratings}$; we used Wilcoxon rank sum test to assess the null hypothesis of equal medians for ΔS computed in two different conditions (Control and Cooling).

Finally, to assess global variations in the spectral distribution of energy due to the stimuli and/or cooling, we merged the trials of all the electrodes for a particular condition and on those we computed the power spectral density. We used the Welch's method with a Hamming window and with a resolution of 1 Hz.

5.4.2 Results of the data analysis

Seven different microelectrode positions were analyzed for a total of 14 presentations of the background and of 56 presentations of either IS or DS gratings, to a total of 112 presentations.

Exposure to BKG provided values of S of 0.58, on average (range $0.36 - 0.71$). In 109 of 112 cases both IS and DS significantly decreased the cooperativeness elicited by BKG (by 18% on average; range 4% to 34%), irrespective of the kind of stimulus used. In particular, we failed to demonstrate differences in cooperativeness depending on the orientation or direction of the IS gratings.

As reported below, cooling the contra-lateral visual areas modified S elicited by the stimuli. This indicates that the stimulus-induced cooperativeness had two components: a direct one presumably mediated through the retino-geniculo-cortical pathway and intra-hemispheric connections, and an indirect, inter-hemispheric component, presumably mediated via the CC. The second component is flexible, in that it depends on stimulus configuration and it can either enhance or decrease the local cooperativeness.

In most cases (10 of 14) cooling the contra-lateral visual areas significantly increased the cooperative activity elicited by BKG (by 10% on average; range 2% to 14%). In two cases, cooling decreased the cooperativeness and in two cases it was ineffective (*cf.* Fig. 5.14). Cooling modified the decrease of cooperativeness induced by the gratings relative to BKG ($\Delta S = S_{BKG} - S_{Grating}$) in the majority of IS cases (41 of 56; 71.5%), but only in 12 of 56 cases (21.4%) it affected that induced by DS (*cf.* Fig. 5.14). Furthermore, cooling affected more consistently the decrease of cooperativeness elicited by the vertical and horizontal gratings (24 of 28 cases; 85.7%) than elicited by the diagonal gratings (of IS; 16 of 28 cases; 57%) (*cf.* Fig. 5.14). Cooling either strengthened or weakened

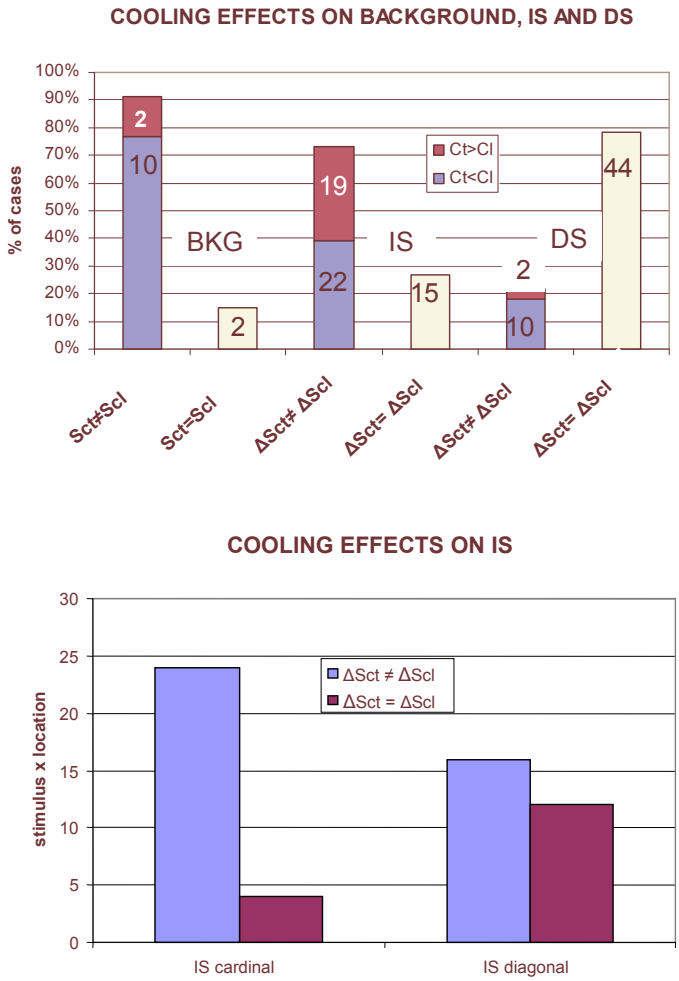

Fig. 5.14. Summary of cooling effects on stimulus-evoked cooperativeness. Top: Effect of cooling the contra-lateral hemisphere on the value of S during exposure to the background stimulus (BKG) and on that of ΔS ($\Delta S = S_{BKG} - S_{Grating}$) during the presentation of the IS and DS gratings. The data are normalized with the number of observations marked on each column segment. Notice that cooling less frequently modified the ΔS elicited by DS than by IS stimuli. The cooperativeness measured during exposure to background appears to be even more frequently affected by cooling. Bottom: Effects of cooling on the ΔS responses to cardinal and oblique gratings. The responses to the cardinal gratings are more often affected by cooling than those to the obliques. $Sct = S$ during control; $Scl = S$ during cooling; similarly $\Delta Sct = \Delta S$ during control and $\Delta Scl = \Delta S$ during cooling.

the decrease of cooperativeness elicited by IS in almost identical proportions (weakened in 19 of 41, *i.e.* 46.3% of cases and strengthened in 22 of 41, *i.e.* 53.6% of cases) (*cf.* Figs. 5.14 and 5.15). The magnitude of the changes in the two directions was almost symmetrical with an average attenuation of cooperativeness decrease of 46% (range 30% to 63%) and an enhancement of 50% on average (range 8% to 132%). In more than 70% of cases interrupting cooling returned cooperativeness towards control levels.

To test if the cooperative effects were specific for a given frequency component of the LFP we computed S separately for the conventional EEG bands, *i.e.* γ ($30 - 70\ Hz$), β ($13 - 30\ Hz$), α ($7 - 13\ Hz$) and lower bands ($< 7\ Hz$), as in [Carmeli et al., 2005]. We found that the effects of blocking inter-hemispheric cross-talk were stimulus dependent in all frequency bands. S was more frequently affected by the presentation of BKG than of IS and by the presentation of IS than of DS, (*cf.* Figs. 5.16 and 5.17 and Fig. 5.18).

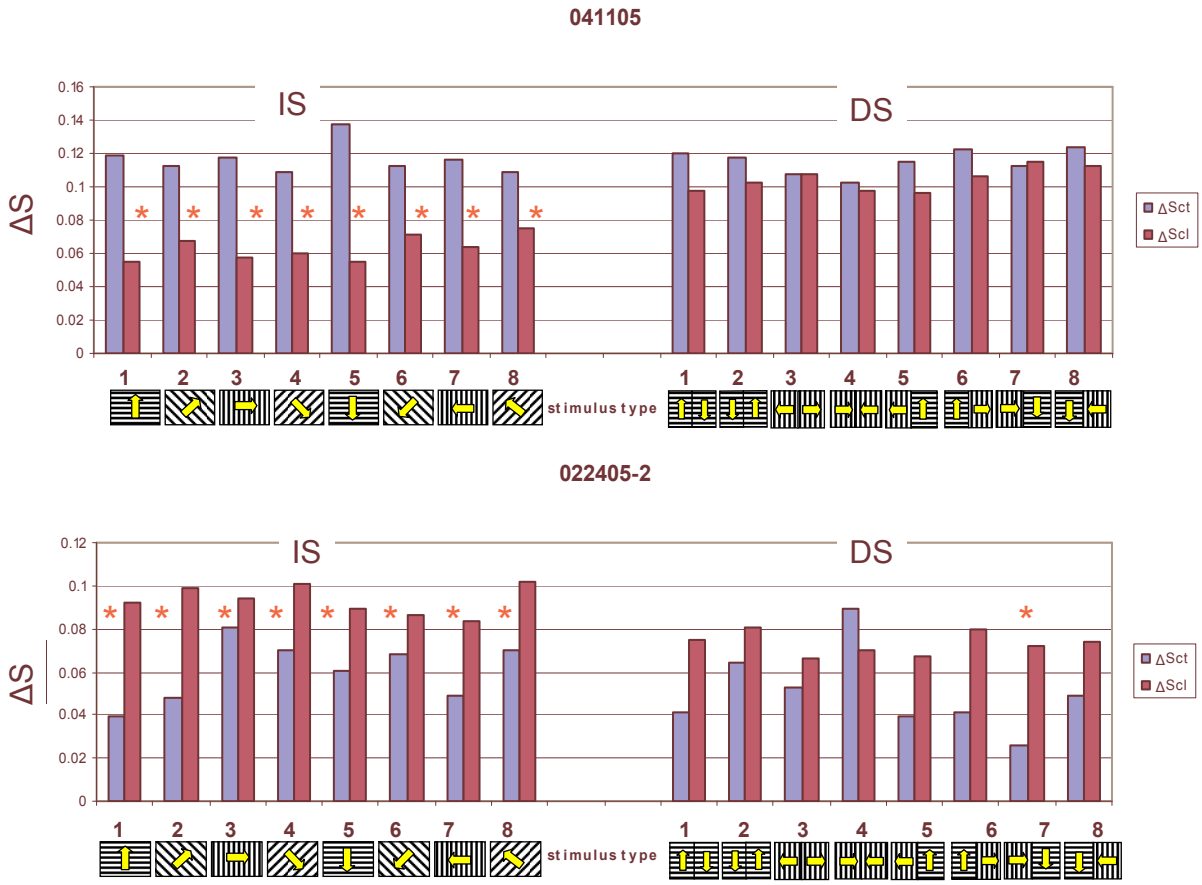

Fig. 5.15. Two examples of stimulus-evoked changes in cooperativeness (ΔS) in control condition (ΔSct) and during cooling (ΔScl). Statistically significantly different pairs are marked by stars. Notice that cooling affects the responses to IS stimuli, not to DS stimuli. In the experiment 041105 cooling decreases ΔS, *i.e.* stimulus decreases cooperativeness less (or, other hemisphere has a role of weakening cooperativeness) and in $022405-2$ cooling increases ΔS, *i.e.* stimulus decreases cooperativeness more, (or, other hemisphere has a role of strengthening cooperativeness). Other conventions as in Figs. 5.13 and 5.14. Although one might expect that in the cooling condition IS and DS should elicit identical ΔS for stimuli in which the left hemifield viewed identical gratings (*e.g.* $IS-1$ and $DS-1$ or 6) this was not always the case, probably due to residual inter-hemispheric interactions, in particular via extra-striate areas not inactivate by cooling.

The effects seemed slightly more robust in the γ and β bands, although the significance of changes in the different bands varied across experiments.

Since it is conceivable that the cooperativeness of neuronal pools recorded at one electrode as LFP might be reflected by power spectra, we computed the pooled spectra of all responsive electrodes in an exploratory sample of three experiments. This showed that compared to BKG, IS and DS caused power changes below 10 Hz, *cf.* Fig. 5.19. These changes were affected by cooling. Both the stimulus and the cooling related changes differed across experiments in ways unrelated to those of S.

5.4.3 Discussion

By computing the changes in the values of S between the hemispheres, we have previously shown (*cf.* Sec. 5.3) that identical horizontal stimuli in the two hemifields (a subset of IS stimuli) and orthogonal stimuli (a subset of the DS stimuli) differently modulate EEG cooperative activity between the two hemispheres. Therefore, here we used the same tool

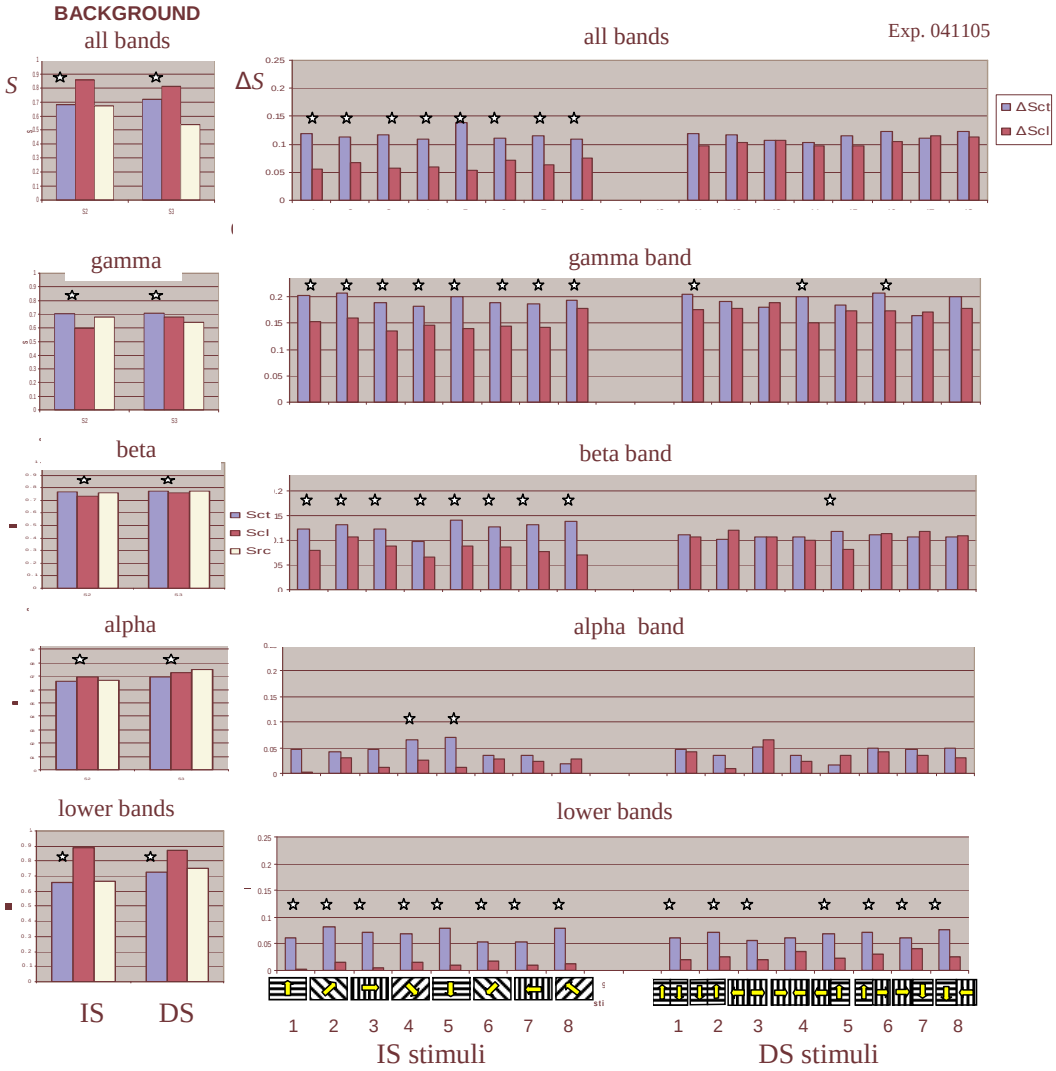

Fig. 5.16. Examples of the effects of cooling on S computed over all frequency bands and on S calculated for the different frequency bands. Same experiments and conventions as in Fig. 5.15. In this figure the effects of cooling on S computed during BKG stimulus are also indicated (Sct=control before cooling; Scl=cooling; Src=recovery after cooling). Notice that the effects tend to be consistent across the different frequency bands but do not reach statistical significance in the same bands.

for assessing the cooperativeness of the compound neuronal activity (local field potentials) recorded with multiple microelectrodes over the visual areas. The obtained results shed new light on how the hemispheres integrate visual input at the earliest stages of cortical processing.

First, different from what might have been expected, IS and DS gratings decreased overall local synchrony, compared with the homogeneous BKG stimulus. Though, this is not surprising because IS and DS, by preferentially activating subsets of neurons which specifically respond to the orientation and direction of the gratings, probably decrease the overall cooperativeness generated by the homogeneous BKG stimulus over the territory sampled by the microelectrodes.

Second, long-distance connections originating in the contra-lateral hemisphere modulate the stimulus-elicited decrease of cooperativeness. The modulation depends on stimulus configuration since it was more frequently seen with the BKG stimulus and with IS,

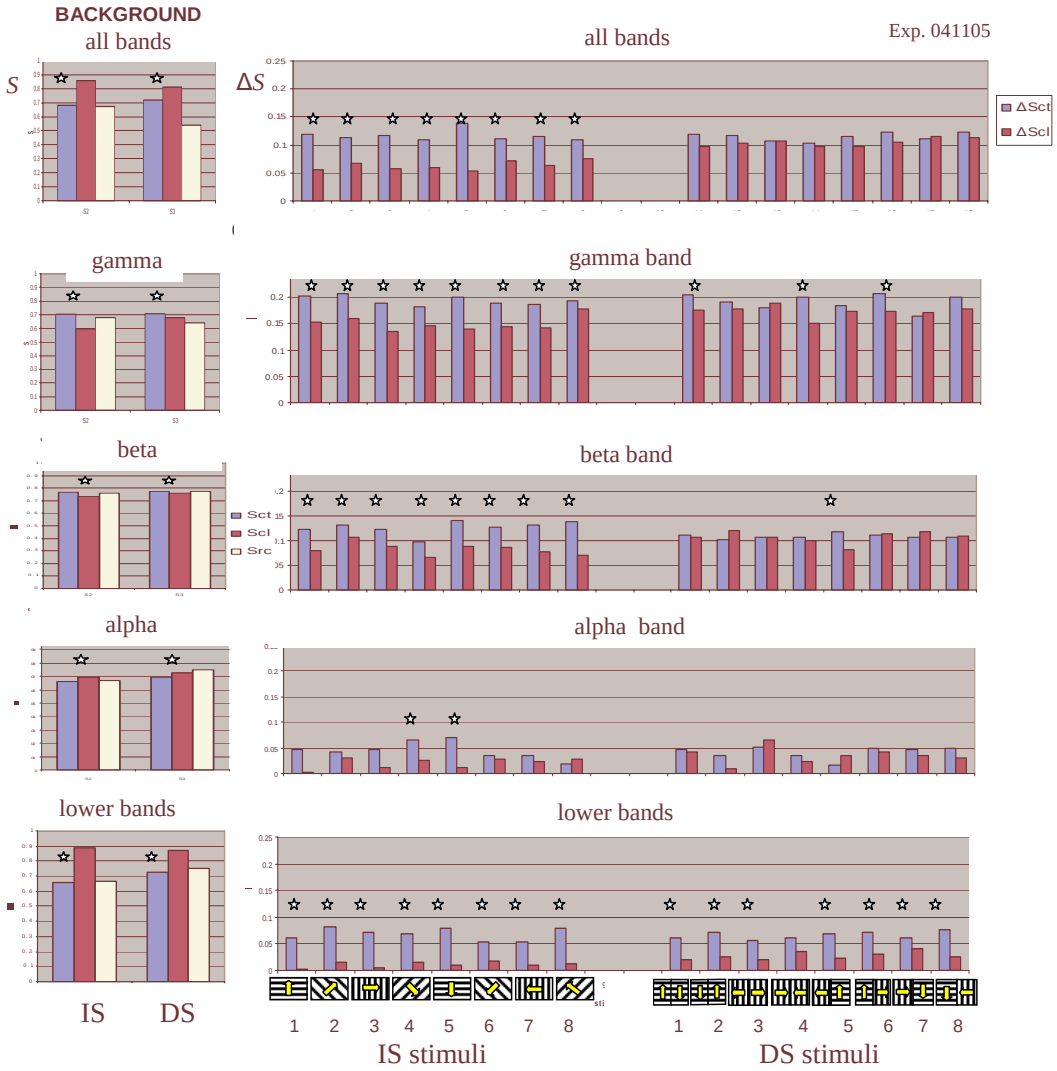

Fig. 5.17. Examples of the effects of cooling on S computed over all frequency bands and on S calculated for the different frequency bands. Same experiments and conventions as in Fig. 5.15. In this figure the effects of cooling on S computed during BKG stimulus are also indicated (Sct=control before cooling; Scl=cooling; Src=recovery after cooling). Notice that the effects tend to be consistent across the different frequency bands but do not reach statistical significance in the same bands.

but not with DS. Moreover, it was more consistently seen with the cardinal, than with the diagonal gratings of the IS stimuli. Finally, the contralateral hemisphere can either enhance or attenuate the stimulus-induced decrease of cooperativeness, which further stresses the flexible nature of inter-hemispheric cross-talk.

The interhemispheric interactions we described are strikingly consistent with the structure of callosal connections. In particular, they agree with the anticipated modulatory, rather than strongly excitatory role of visual callosal axons in the primary visual areas [Tettoni et al., 1998]. The fact that interhemispheric modulation of cortical cooperativeness was more robust with the IS than with the DS gratings is consistent with the proposal that callosal axons preferentially interconnect neurons with the same selectivity for stimulus orientation [Berlucchi et al., 1967, Schmidt et al., 1997], and, among those, particularly neurons responding to cardinal orientations of the stimulus.

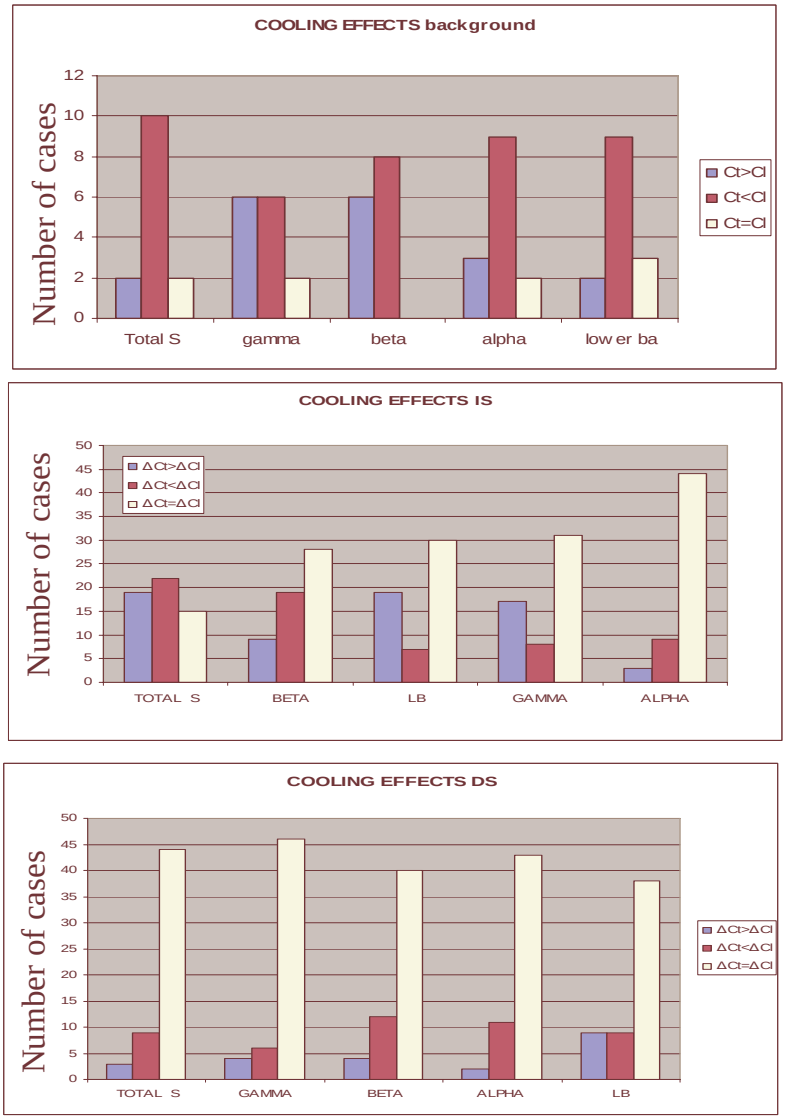

Fig. 5.18. Summary of effects on the different frequency bands. Conventions as in Fig. 5.15. The bands are ordered according to effects. Notice that in all bands the most robust effects are obtained during exposure to BKG, followed by the IS stimuli, while there is almost no effect on the responses to DS stimuli.

These findings suggest that callosal connections contribute to stimulus detection and/or categorizations through temporal population coding at the early stages of visual cortical processing. They also stress the flexible nature of inter-hemispheric interactions, which in humans, seems to be further enhanced in a task-dependent manner, probably by top-down cortico-cortical inputs [Stephan et al., 2005].

These findings have also other important implications. Indeed, while current trends in neuroscience focus on the role of frequency specific cooperativeness phenomena, in this study we were able to unveil significant cooperativeness phenomena only by considering all the frequency domains, *i.e.* the signals in the time domain. Furthermore, in this study our S estimator revealed to be a more effective and suitable cooperativeness estimator than the power spectra, widely used in neuroscientific studies. These results obtained with our S estimator are potentially fertile for investigations in systems neuroscience.

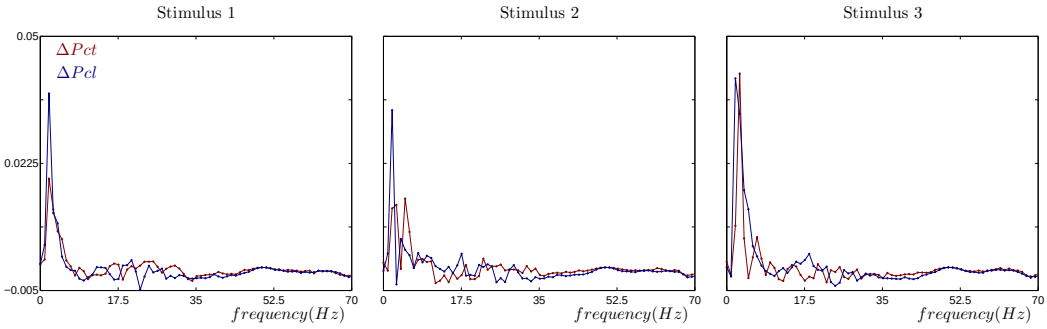

Fig. 5.19. Examples of power variation for IS stimuli. Notation: $\Delta Pct = P_{BKG} - P_{Grating}$ during Control (red); $\Delta Pcl = P_{BKG} - P_{Grating}$ during Cooling (blue). The variations are almost zero except for the low frequency band. The dots illustrate the mean value.

5.4.4 Addendum

Similarly to the EEG investigation, we identified a model from the LFP signals in order to look for nonlinear properties of such data. Indeed, *a priori* LFP signals should not suffer of blurring phenomena due to diffusion through the skull, as, on the contrary, EEG signals do suffer. We used the same strategy described in Sec. 5.3.6. The results of this analysis do not suggest any presence of nonlinear dynamics in such LFP recordings.

Starting from the evidence of nonlinear functioning of the brain building block, *i.e.* the neuron, our finding poses critical questions about the organization of the information at different levels in the brain. Probably, still at this mesoscopic level the number of sources elicited by the stimuli is very huge. Indeed, brain is an intricate system and highly excitable: even the simple stimuli we used might unleash the activity of many neurons or population of neurons. Furthermore, we have observed brain activity only over a very small portion of the cerebral cortex and, in particular, that assumed to be the most strongly modulated by the visual stimuli. Contrary to the current neuroscientific belief of specific spatial localization of brain functions, if we postulate that all brain is involved in perception, then it may be limiting the recording over the region most involved and then most easily observable. To comfort this hypothesis, some recent nonlinear analysis of (apparently) permanently spiking neurons, which are neglected in current neuroscientific investigations, may be non trivially modulated by stimuli and, therefore, may be involved in the nonlinear brain dynamics [De Feo, 2006]. This calls for the need of measurement setups which allow a holistic recording of brain activity, and, probably, to define stimuli/task experience aiming at unveiling dynamical features of the brain.

5.5 Final remarks

In this chapter, we have described the application of a new method to measure cooperative behavior in real data. Two classes of signals have been analyzed: signals recorded from the skull of humans, *i.e.* EEG, and signals recorded from a small region of the cortex in ferrets. In both cases the analysis gave new insights about brain functioning according to neuroscientists.

We applied in both cases our S estimator to data non delay embedded. We preferred this solution in order to reduce the computational load of the data analysis and because of the difficulty arising in estimating embedding dimensions for large interacting

sub-systems and, furthermore, when the recorded time series result from superimposed signals. We did not investigate this aspect in our simulation studies, however, given its importance, it is planned for future research.

Finally, we mention that lately our S estimator has also been applied to the study of cooperative phenomena among the sub-systems generating heartbeat, respiration and brain waves. We investigated the possibility to detect changes from depth to light anaesthesia by looking at changes in cooperative activity between those three sub-systems [Oshima et al., 2006].

To conclude, we mention that the S estimator have recently been used by an Australian group of researchers in another application [Celka and Kilner, 2006]. This stresses the applicability of our S estimator to other fields.

6

Conclusions

In this study, we have approached the problem of inferring cooperative behavior from measurements of networks of interacting dynamical sub-systems. This issue arises in many field of applied sciences, such as ecology, neuroscience and physiology, where is crucial the process of unraveling the principles governing the functional interactions within the network of interest.

Three new methods have been developed and tested on numerically generated data. One method, called S estimator, allows to assess cooperative activity within a collection of observed sub-systems, or time series. The other two methods allow to assess partial cooperative phenomena, or, in other words, the cooperativeness in sub-collections of network's units. Besides, an overview of earlier introduced techniques has been given.

Two applications to real data have been presented. We applied the S estimator to recordings from brains in order to study the modulation of neuronal cooperative activity evoked by visual stimuli. Our results were satisfactory from two viewpoints: first, they allowed a better understanding of the mechanisms which contribute to unifying brain functions; second, they showed to give new unexpected insights that other techniques commonly used in the neuroscientific community would have failed to assay.

6.1 Methodological development

In the field of time series analysis, four approaches aiming at estimating cooperativeness within simultaneously recorded time series may be outlined. We sketched them in Chapter 2. Most of them are bivariate, *i.e.* they allow the determination of inter-relations between two time series.

To assess the cooperativeness strength in multivariate time series, mutual information and the phase order parameter have been the natural candidate. Unfortunately, this two methods may have some disadvantages: the former requires the estimation of high-dimensional probability distributions with a finite amount of data, a constraint that may be prohibitive in a multivariate context. The latter requires the computation of the instantaneous phases, which may not be unambiguously extracted especially from broad-band signals.

Here, we have proposed a new cooperativeness estimator, composed of the so called S and partial S estimators. We validated it on numerically generated data. In particular, we assessed its sensitiveness upon amount of data, endogenous and exogenous noises, number of sub-systems and network's topologies. Furthermore, we assessed its ability to infer direct coupling strengths. The trade-off amount of data *vs.* noises intensity and

amount of data *vs.* number of sub-systems have been showed. A comparison with other known methods showed the our estimator has similar performances to them.

Conceptually, our estimator has higher estimation feasibility from multivariate data than mutual information, because we do not need to estimate probability distributions, and unlike phase synchronization indices does not need the extraction of the phase of the signals, which implies its applicability to a wider class of systems. However, we are aware that unlike phase synchronization indices, our estimator is also sensitive to amplitudes, eventually leading to pitfalls.

Unlike frequency-based methods, our estimator may be flexibly applied to both embedded and not embedded data.

Thanks to its construction, our estimator may be applied to the study of cooperativeness among communities of sub-systems or meta-clusters. This property, conceptually shared with mutual information, may further help in unraveling the emergence of phenomena not observable at single sub-system (aggregation) level.

A priori, our estimator is only sensitive on second-order inter-relations among the signals. To this reason, our estimator may not be sensitive to weak or nonlinear cooperativeness manifesting in higher orders inter-relations. We remark that even if the new estimator is based on linear correlations, the entropy-like statistics could be extracted from other similarity matrices. For instance, to go beyond second order correlations, it would be interesting to use a mutual information based similarity matrix. Potentially, this would further allow a "Divide et Impera" advantage: our entropy-like statistics would transform this powerful pair-wise similarity quantity, into a single (intensive) cooperativeness value. Mutual information allows itself a multivariate estimation, however, it would be difficult to obtain a reliable estimation from a finite amount of data. Therefore, an S estimator defined on bivariate mutual information would represent a good statistical compromise to assess cooperativeness in a mutual information sense. Despite all this, it should be theoretically checked and investigated the geometrical meaning of the so-defined S estimator.

To assess also a direction of cooperativeness, in Chapter 4 we have presented a new method to infer direction and strength of weak interactions within multivariate time series. The strong assumption we made is the determinism of the network. However, the method proved to give coupling information even in the case of strong modeling noise intensity.

The method proved to be able to infer asymmetry of coupling and direct couplings. Its sensitiveness upon amount of data, observational noise and number of sub-systems has been considered and the results were satisfactory. Moreover, the trade-off of data *vs.* noises intensity and the trade off of data *vs.* number of sub-systems have been explored. Finally, the results of comparison with another technique suggested that the method works very well for rather weak coupling, while it should still be verified its performance to stronger couplings, that, however, do not lead to synchronization.

The strength of the method is mainly given by its three steps: state-space reconstruction, self-modeling and cross-modeling. Several well-established regression techniques exist to this purpose. An implementation of this scheme has been used in our validation tests, however, the choice of an algorithmic setup may be suitably tuned to the specific application. For instance, we mention that such scheme could be applied to derive interactions from instantaneous phases dynamics.

A further consequence of this scheme is on the scalability properties of the method. The costly non-linear identification part is done separately on each of the sub-systems,

potentially over a few variables at a time. Only the final linear regression is done over all the variables; for the linear regression we can take advantage of existing efficient software packages which can consider millions of variables in reasonable time.

6.2 Applications to real data

Cooperative behavior has one of the most intriguing manifestation in the functioning of the brain. Thanks to the collaboration with Prof. G. Innocenti, we had the possibility to apply our methods to real data within a grounded context. Indeed, we investigated the phenomenon of stimulus-dependent modulation of neuronal cooperativeness between the two hemispheres, because inter-hemispheric interactions are physiologically motivated by the structure of the visual pathway and by the presence of fibers connecting the two hemispheres. In particular, we have applied the S estimator to two classes of signals: signals recorded from the skull of humans, *i.e.* electroencephalograms (EEGs), and signals recorded from a small region of the cortex in ferrets, *i.e.* local field potentials (LFPs).

In both signal classes, in agreement with the synchronization-based solution of the visual feature binding in perception [Gray, 1999], our cooperativeness estimator allowed to assay stimulus-dependent modulation of neuronal cooperativeness. While on EEGs similar results may be obtained with spectral (coherence) techniques, in LFPs this was not the case.

To test if the stimulus-dependent modulation of neuronal cooperativeness were specific for a given frequency range, we made separate calculations of the S estimator for different EEG/LFP frequencies. Indeed, the current belief in neuroscience is that specific brain functions are implemented via specific frequency band. In EEG signals, we found that different stimulus configurations caused a complex rearrangement of the cooperative neuronal assemblies distributed over the cortex not reducible to a simple localization in the frequency domain. Furthermore, the complexity of these changes went well beyond what we had expected from previous work, *i.e.* EEG coherence, that were already employed in that same study.

In LFP signals, the results showed no particular frequency-specific effect. As already suspected in [Bressler et al., 1993, Basar et al., 2001], all these findings suggest that the complex changes in the dynamics of cortical activity evoked by even very simple stimuli may not be adequately characterized by simple effects in specific frequency bands. Instead, approaches (to which the S estimator belongs) considering that brain activity continuously varies with time within a state-space might better characterize it.

The application of the S estimator to LFP signals allowed to extract a further new result. In that experiment, we were able to describe a new kind of inter-hemispheric integration. We found that stimulus-evoked cooperativeness of neuronal activity in one hemisphere is modulated by input from the other hemisphere. This were true only if the visual areas in two hemispheres viewed identical stimuli which can be easily bound into a coherent percept. Therefore, inter-hemispheric connections contribute to unifying brain function by modulating in a flexible, stimulus-dependent way, the cooperation in neuronal population likely to be involved in stimulus detection and/or categorization.

Although the synchronization-based mechanism of the perceptual features binding is appealing, it does not satisfactorily explain the complete mechanisms underlying brain perception. Indeed, the read-out problem rests unsolved. To this concern, a chaos-based paradigm of brain perception has been recently proposed [De Feo, 2001]. Within it,

synchronization phenomena are the manifestation of perceptual semantics produced by stimuli impinging upon a neuronal assembly state-space.

To approach this appealing paradigm, we investigated the presence of nonlinearities in our data. Unfortunately, we failed in finding them. Despite the possible reasons, this suggests that in brain data nonlinearities are hard to unveil and the verification of that perceptual paradigm is a very tough task. Hopefully, advances in nonlinear time series analysis and possibly the use of other recording techniques will make it possible.

Finally, we remark that the domain of applicability of the S estimator is not restricted to the neuroscience. Lately, we applied the S estimator to study cooperative phenomena among the sub-systems generating heartbeat, respiration and brain waves. Successfully, we detected different cooperative activity among those three sub-systems in depth anaesthesia with respect to light anaesthesia. Hopefully, this will help in assessing awareness during surgery.

6.3 Perspectives

The work described in the previous chapters has potential perspectives from two viewpoints: methodological and experimental.

Some further developments of the proposed methods may be possible. Regarding the S and partial S estimators, the use of similarity features other than linear correlation should be explored. Also, the possibility to use the transformation in Eq. (4.2) to other inter-relation quantities should be investigated. At the same time, we mention the possibility to fully exploit linear correlation-based inter-relations. Indeed, we used Pearson-like correlation coefficients, however, in literature, a more general class of correlation coefficient exist, that were introduced by Daniels [Daniels, 1944]. Rather than base the correlation coefficients on the actual observations, we could use measures based on the *ranks*, which might allow to improve the robustness of the estimator. However, in this case it should be investigated whether dynamical information is lost.

Furthermore, it would be useful to derive a significance level of the S and partial S estimator, so as to facilitate its interpretation especially for passive experiments.

Regarding the method based on model identification presented in Chapter 4, improvements might be obtained by considering more advanced estimation techniques, as the maximum likelihood approach [McSharry and Smith, 1999] or recent developments in identification theory [Ljung, 1999]. Also, the method might be extended to identify nonlinear couplings [Voss et al., 2003].

We believe that crucial improvements might also be possible by breaking the wall of the modeling assumptions made at the beginning of this manuscript (*cf.* Eqs. (2.4), (2.5) and (2.6)). In particular, future investigations should be focused on relaxing Eq. (2.6). In completely blind setup, this assumption is probably far from being satisfied, as, for instance, is the case of superimposed signals. Probably, one site measurement records the activity from several sub-systems or several measurements (and, of course, we do not know which among all of them) record the same sub-systems. Current approaches are the application of decomposition techniques like independent component analysis to de-mix the recordings. However, this approach is not satisfactory from our viewpoint, because we want to infer cooperative activity. We suggest that possible solutions might hopefully arise by considering *N-way* decomposition techniques that do not require independence constraints, as parallel factor-like decompositions [Harshman, 1970, Bro, 1998]. Other consequences of this development would be the removal of spurious cooperative values

and the improvement of state-space reconstruction. To this end, we also believe that, for the case of mild and strongly cooperative sub-systems, the used strategy of simply merging the sub-systems state-spaces to reconstruct network's state-space may not be satisfactory when analyzing interdependences (*cf.* Chapter 3 and 4). This poses the non trivial theoretical problem of network state-space reconstruction.

Besides these methodological developments, some further validation tests are needed. It should be tested, for instance, the behavior of our methods when breaking the assumptions made about modeling and observation noises. Moreover, more tests with large systems are needed: for instance, investigations about how estimators like partial S bias the true values of fundamental network properties (*e.g.* the characteristic path length), or evaluation of the ability of partialization methods to marginalize unobserved inputs. While the partial S estimator needs third knowledge, the method based on modeling may possess this capability.

Finally, we plan to complete the Matlab S toolbox with the partial S estimator. Freely available software is very important for reproducible research.

For the experimental point of view, further applications of the S estimator besides system neuroscience may be possible. In clinical neuroscience, ongoing work is exploring the applicability of S to study abnormal cooperativeness skull topography in patients suffering from Schizophrenia and Alzheimer diseases. We hope further applications in other domains like ecology, to study, for instance, cooperative behavior of species distributed over a territory.

In this study, we did not apply the two other methods, however, future applications of these are planned. The partial S estimator could be applied to investigate stimuli-induced arrangements of graph topology in LFP recordings. Nevertheless, we believe that this appealing investigation will be meaningful once advances in the identification of the real sub-systems activities from the recordings will be made.

Concerning the method based on modeling identification, we plan to apply it to the study of the interactions among three physiological sub-systems, *i.e.* brain, heart and respiratory sub-system. Indeed, in this case a weak coupling assumption is tenable and it is of interest the study of how they interact with one another, eventually providing a crucial insight into the changes taking place in the human body during anaesthesia [Musizza and Stefanovska, 2005].

Overall, we feel prone to work in contact with neuroscientists. The interdisciplinary team we worked with allowed fertile discussions and the birth of many fruitful ideas. Further, we believe that a long route is still ahead to unravel the functional mechanisms underlying brain perception. We think that this might be accomplished by closing the loop between two viewpoints: advances in the theoretical development of the features of dynamical networks, ranging from their observability properties to their meta properties (*e.g.* how network evolution affects topology, nodal dynamics affect connection strength), and advances in measurement techniques. Indeed, theoretical developments will help in the interpretation of data analysis results and, more importantly, in the establishment of experimental protocols able to untangle dynamical brain behavior, possibly nonlinear. Probably, this will be further corroborated by the use of recording techniques allowing the study of the brain as a whole.

A

Some further tests on the *S* estimator

In this Appendix, we present some other tests to validate the cooperativeness estimator described in Chapter 3, the so called S estimator. The aim is not to complete exhaustively these tests, but to show some other properties and limitations of such method.

Phase synchronization

In Chapter 3 we showed the performance of the S estimator with noisy chaotic nonlinearly coupled sub-systems. However, we did not test its performance under a classical phase synchronization paradigm, where amplitudes remain chaotic while phases are synchronized. The question arises naturally because our S estimator, by construction, is also sensitive to correlations in the amplitudes.

We considered the paradigm described in [Rosenblum et al., 1996], where two chaotic Rössler sub-systems are mutually linearly coupled. The equations governing their dynamics are

$$\begin{cases} \dot{\theta}_1^{(1)} = -\omega^{(1)}\theta_2^{(1)} - \theta_3^{(1)} + \mathcal{C}^{(1,2)}\left(\theta_1^{(1)} - \theta_1^{(2)}\right), \\ \dot{\theta}_2^{(1)} = \omega^{(1)}\theta_1^{(1)} + 0.15\theta_2^{(1)}, \\ \dot{\theta}_3^{(1)} = 0.2 + \theta_3^{(1)}\left(\theta_1^{(1)} - 10\right), \\ \\ \dot{\theta}_1^{(2)} = -\omega^{(2)}\theta_2^{(2)} - \theta_3^{(2)} + \mathcal{C}^{(2,1)}\left(\theta_1^{(2)} - \theta_1^{(1)}\right), \\ \dot{\theta}_2^{(2)} = \omega^{(2)}\theta_1^{(2)} + 0.15\theta_2^{(2)}, \\ \dot{\theta}_3^{(2)} = 0.2 + \theta_3^{(2)}\left(\theta_1^{(2)} - 10\right), \end{cases} \tag{A.1}$$

where $\omega^{(1)}$ and $\omega^{(2)}$ represents the average velocity of the two Rössler attractors, fixed at the values 1.015 and 0.985, respectively. The parameters $\mathcal{C}^{(2,1)}$, $\mathcal{C}^{(1,2)}$ represent the strength of the diffusive linear coupling between the two sub-systems. We fixed $\mathcal{C}^{(2,1)} = \mathcal{C}^{(2,1)}$ and we varied them in the range $[0, 0.05]$. At the strength value of 0.02 the two sub-systems are nearly phase synchronous and at 0.035 phase synchronization is observed [Rosenblum et al., 1996], *i.e.* their $1:1$ phase difference stays constant while their amplitudes are uncorrelated.

For every considered value of the coupling, the differential equations were iterated, starting from random initial conditions, using the *ode*45 Matlab function, the initial 10000 points of each transient were dropped and, by means of a down-sampling ($\delta T = 0.02$),

time series of 10000 points were collected. We collected 30 trials by measuring the coupled variables $\theta_1^{(1)}$, $\theta_1^{(2)}$, to which we added gaussian noise leading to 40 dB (SNR).

We computed our S estimator to embedded and not embedded data, and, as reference, the phase synchronization estimator γ. The data were delay embedded by using a delay time $\tau^{(1)} = \tau^{(2)} = 0.2$ and embedding dimension $n^{(1)} = n^{(2)} = 3$, which were chosen with the already previously mentioned methods [Kantz and Schreiber, 2004]. Phases were estimated by Hilbert transform and the $1:1$ phase difference were computed.

The results are showed in Fig. A.1. All three estimators scale upon the coupling

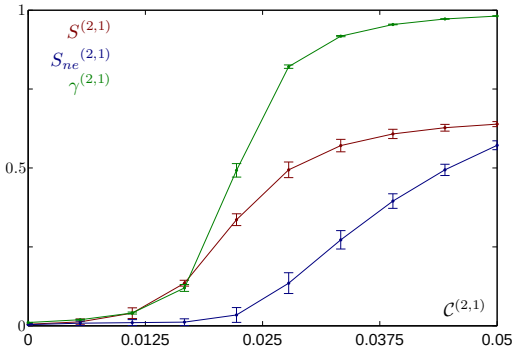

Fig. A.1. Numerical assessment of the S estimator as a measure of phase synchronization. Dependence of the cooperativeness or synchronization between the sub-systems (1) and (2) of system Eq. (A.1), upon the coupling parameter $\mathcal{C}^{(2,1)} = \mathcal{C}^{(1,2)}$, estimated with different techniques: $S^{(1,2)}$ (red); $S_{ne}{}^{(2,1)}$ (blue); $\gamma^{(1,2)}$ (green). The dots and errors bars illustrate the mean value and standard deviation, respectively.

strength, however $S_{ne}{}^{(2,1)}$ does not scale for lower coupling values. As showed by $\gamma^{(1,2)}$, the two sub-systems are nearly phase synchronous around 0.02 ($\gamma^{(1,2)} \approx 0.5$), while the amplitudes stays uncorrelated ($S_{ne}{}^{(2,1)}$ is close to zero). $S^{(2,1)}$ shows better performance than $S_{ne}{}^{(2,1)}$: indeed, it has higher values for nearly phase synchronous sub-systems (≈ 0.3). For phase synchronous sub-systems, correctly $\gamma^{(1,2)} \approx 0.9$, while $S_{ne}{}^{(2,1)}$ has lower value, *i.e.* ≈ 0.2, and $S^{(2,1)}$ is placed somehow in the middle, *i.e.* ≈ 0.55. We remark that, by its construction, the S estimator would be ≈ 1 for almost completely synchronous sub-systems (achieved with larger coupling strength values), while $\gamma^{(2,1)}$ is already ≈ 1 for phase synchronous sub-systems ($\mathcal{C}^{(2,1)} \approx 0.035$).

As last remark, we notice that in this setting the S estimator appears less reliable than $\gamma^{(2,1)}$ (*cf.* the error bars), which is probably due to the fluctuations in the amplitudes.

Superimposed signals

In Chapter 3, we introduced a model of dynamical network. In the part of the model regarding the observation of network activity, we made the strong hypothesis of associating at each measurement site the recording of the activity of one sub-system (*cf.* Eq. (2.6)). This is a common assumption in literature, however, real data may be far from this hypothesis. Indeed, as in the case of EEG recordings, the signal recorded at each electrode is probably given by the superposition of an unknown number of other signals, the so-called *sources*. Measuring superimposed signals has the consequence of jeopardiz-

ing the state-space reconstruction of the network sub-systems, and of altering the true value of cooperativeness within the network.

In this paragraph, we present a test to show how the S estimator is affected in a simple case of superimposed signals. We considered the paradigm introduced in Chapter 3 to assess the robustness of the S estimator. In that setting, a Rössler sub-systems were nonlinearly driving a Lorenz one. We considered the following observation process

$$\begin{cases} Y_t^{(1)} = (1-\mu)\,\Theta_t^{(1)} + \mu\Theta_t^{(2)} + \nu_t^{(1)}, \\ Y_t^{(2)} = \mu\Theta_t^{(1)} + (1-\mu)\,\Theta_t^{(2)} + \nu_t^{(2)}, \end{cases} \tag{A.2}$$

where the parameter μ controls the mixing process [Tass et al., 1998]. We collected 30 time series from different initial conditions and of 500 points each. We considered a modeling and observational noise intensity of 40 dB (SNR). To test the sensitiveness of the S estimator upon the degree of the mixing process, we considered mixing processes of different intensity, namely 1%, 10% and 25% (corresponding to $\mu = 0.01, 0.1, 0.25$, respectively).

We computed our S estimator to embedded and not embedded data, and the phase synchronization estimator γ for comparison. Parameters were the same as the ones used in Chapter 3.

The results are showed in Fig. A.2. As expected, for the three estimators the increase

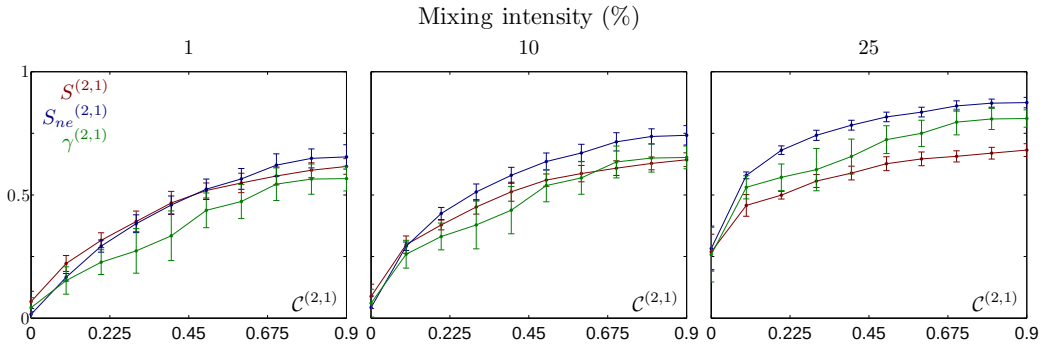

Fig. A.2. Numerical assessment of the S estimator as a measure of cooperativeness: *case of superimposed signals*. Dependence of the cooperativeness or synchronization between the sub-systems (1) and (2) of system Eq. (3.14), upon the coupling parameter $\mathcal{C}^{(2,1)}$, estimated with different techniques: $S^{(1,2)}$ (red); $S_{ne}{}^{(2,1)}$ (blue); $\gamma^{(1,2)}$ (green). Sensitivity upon the intensity of the mixing process, *i.e.* 1%, 10% and 25%. The dots and errors bars illustrate the mean value and standard deviation, respectively.

of the mixing of the signals leads to higher cooperativeness values. In particular, for uncoupled sub-systems and strong mixing intensity (*i.e.* 25%), spurious synchronization values arise.

Observed variables

In the previous paragraph we showed the performance of the S estimator under the condition of superimposed signals, a case which breaks one of our assumptions. Here, we consider the case of ideal recording processes, *i.e.* one signal from each sub-system, and we test the dependence of our S estimator upon the observed variable. Indeed, in

blind recording setup, we do not know which projection of the attractor we are observing. Clearly, this is tightly connected with the observability issue of the network activity.

To test this, we considered the same paradigm used in previous paragraph. We considered the same parameter setup, number and length of trials, modeling and observational noise intensity. We computed our S estimator to embedded and not embedded data, and the phase synchronization estimator γ for comparison.

The results are showed in Fig. A.3, which shows the dependence of these three estimators for all possible combinations of the recorded state-space variables. We remark that the dependence upon the observed variable is strong for all three estimators. The feature generally inferable is the presence or not of the coupling, while the scaling upon coupling strength results detectable in a restricted number of cases. Finally, we remark that the S estimator applied to embedded data allows more numerous correct inference of coupling than ${S_{ne}}^{(2,1)}$.

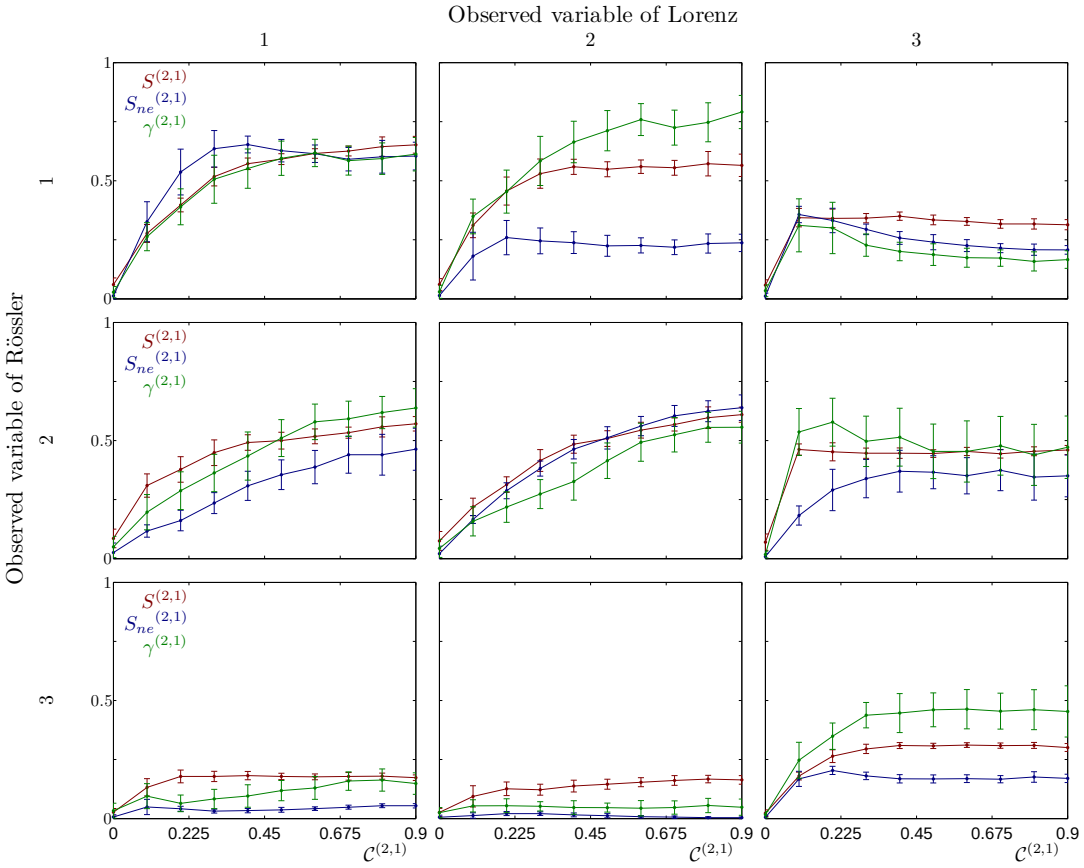

Fig. A.3. Numerical assessment of the S estimator as a measure of cooperativeness: sensitiveness upon the observed variable. Dependence of the cooperativeness or synchronization between the sub-systems (1) and (2) of system Eq. (3.14), upon the coupling parameter $\mathcal{C}^{(2,1)}$, estimated with different techniques: $S^{(1,2)}$ (red); ${S_{ne}}^{(2,1)}$ (blue); $\gamma^{(1,2)}$ (green). Sensitivity upon the observed variable of the two sub-systems. The dots and errors bars illustrate the mean value and standard deviation, respectively.

Complexity

In Chapter 3, we have introduced the S estimator as a measure of cooperativeness within a network of interacting sub-systems. Here, we want to show a test to corroborate this claiming. We considered a paradigm in which two sub-systems are uncoupled and we tested if a change of the complexity of one the two sub-systems causes a change in the inferred cooperativeness. By complexity we mean the limit set of one sub-system attractor, namely a limit cycle or a strange attractor.

We considered the two uncoupled sub-systems composed of a Rössler and Lorenz system (*cf.* Eq. (3.16)). In the first sub-experiment, both were chaotic. In the second sub-experiment, we modified the complexity of the Rössler sub-systems, *i.e.* from chaos to limit cycle. This were obtained by changing the parameter c from 5 to 2.5 [Strogatz, 1994].

To easy the comparison between the two sub-experiments, we did not consider any modeling or observational noise. We measured the second variable of each sub-system, and we collected 30 trials (from different initial conditions) of 500 samples each. We computed the S estimator to both embedded and not embedded data. To compare the estimated values of S we used a Wilcoxon rank sum test. This procedure was repeated 100 times, so to get a time series of p-values. The data were embedded using parameters obtained with the same method mentioned in Chapter 3 [Kantz and Schreiber, 2004].

For not embedded data we obtained 1 p-values less than 0.05. For embedded data, we considered the case of a 3 dimensional and 4 dimensional embedded space. In the first case, we obtained 5 p-values less than 0.05, in the second we obtained 13 p-values less than 0.05.

This result shows that the S estimator applied to not embedded data is a measure of cooperativeness not sensitive to change of complexity in the sub-systems (the error of type I is less than 5%). When applied to embedded data, this depends upon the dimension of the embedded state-spaces. For larger dimensions, which are plausible choices, the S estimator is affected by changes in the complexity (the error of type I is more than 5%). The choice of the embedding dimension appears here a crucial step when applying the S estimator on embedded data.

References

V. S. Afraimovich, N. N. Verichev, and M. I. Rabinovich. Stochastic synchronization of oscillations in dissipative systems. *Radiophysics Quantum Electronics*, 29:795, 1986.

E. Anderson, Z. Bai, C. Bischof, J. Demmel, J. Dongarra, J. Du Croz, A. Greenbaum, S. Hammarling, A. McKenney, S. Ostrouchov, and D. Sorenson. *LAPACK Users' Guide*. Society for Industrial and Applied Mathematics, Philadelphia, PA, USA, 1992.

R. G. Andrzejak, K. Lehnertz, F. Mormann, C. Rieke, P. David, and C. E. Elger. Indications of nonlinear deterministic and finite-dimensional structures in time series of brain electrical activity: Dependence on recording region and brain state. *Physical Review E*, 64:061907, 2001.

F. Aoki, E. E. Fetz, L. Shupe, E. Lettich, and G. A. Ojemann. Increased gamma-range activity in human sensorimotor cortex during performance of visuomotor tasks. *Clinical Electorencephalography*, 110:524–537, 1999.

J. Arnhold, P. Grassberger, K. Lehnertz, and C. E. Elger. A robust method for detecting interdependences: application to intracranially recorded EEG. *Physica D*, 134:419–430, 1999.

L. A. Baccalà and K. Sameshima. Partially directed coherence: a new concept in neural structure determination. *Biological Cybernetics*, 84:463–474, 2001.

D. H. Ballard, G. E. Hinton, and T. J. Sejnowski. Parallel visual computation. *Nature*, 306:21–26, 1983.

A. L. Barabási and R. Albert. Emergence of scaling in random matrices. *Science*, 286: 509–512, 1999.

M. Barahona and L. M. Pecora. Synchronization in small-world systems. *Physical Review Letters*, 89:054101, 2002.

H. B. Barlow. Critical limiting factors in the design of the eye and visual cortex. *Proceedings of the Royal Society of London. Series B, Biological Sciences*, 212:1–34, 1981.

E. Basar, C. Basar-Eroglu, S. Karakas, and M. Schurmann. Gamma, alpha, delta and theta oscillations govern cognitive processes. *International Journal of Psychophysiology*, 39:241–248, 2001.

I. Belykh, E. De Lange, and M. Hasler. Synchronization of bursting neurons: What matters in the network topology. *Physical Review Letters*, 94:8101, 2005.

V. N. Belykh, I. V. Belykh, and E. Mosekilde. Cluster synchronization modes in an ensemble of coupled chaotic oscillators. *Physical Review E*, 63:036216, 2001.

G. Berlucchi, M. S. Gazzaniga, and G. Rizzolatti. Microelectrode analysis of transfer of visual information by the corpus callosum. *Archives Italiennes de Biologie*, 105: 583–596, 1967.

U. S. Bhalla and R. Iyengar. Emergent properties of networks of biological signalling pathways. *Science*, 283:381–387, 1999.

C. M. Bishop. *Neural Networks for Pattern Recognition*. Oxford University Press, Oxford, 1995.

B. Boashash. Estimating and interpreting the instantaneous frequency of a signal. i. fundamentals. *Proceedings of the IEEE*, 80:520–538, 1992.

S. Boccaletti, J. Kurths, G. Osipov, D. L. Valladares, and C. S. Zhou. The synchronization of chaotic systems. *Physics Reports*, 366:1–101, 2002a.

S. Boccaletti, D. L. Valladares, L. M. Pecora, H. P. Geffert, and T. Carroll. Reconstructing embedding spaces of coupled dynamical systems from multivariate data. *Physical Review E*, 65:035204, 2002b.

S. Boccaletti, V. Latora, Y. Morenoy, M. Chavez, and D.-U. Hwan. Complex networks: Dynamics and structure. *Physics Report*, 424:175–308, 2006.

M. Breakspear. Nonlinear phase desynchronization in human electroencephalographic data. *Human Brain Mapping*, 15:175–198, 2002.

S. L. Bressler, R. Coppola, and R. Nakamura. Episodic multiregional cortical coherence at multiple frequencies during visual task performance. *Nature*, 366:153–156, 1993.

D. R. Brillinger. *Time Series: Data Analysis and Theory*. SIAM, 2001.

R. Bro. Multi-way analysis in the food industry, models algorithms, and applications. *University of Amsterdam*, 1998. Ph.D. Thesis.

A. Broder, R. Kumar, F. Maghoul, P. Raghavan, S. Rajagopalan, R. Stata, A. Tomkins, and J. Wiener. Graph structures in the web. *Computer Networks*, 33:309–320, 2000.

D. S. Broomhead and G. P. King. Extracting qualitative dynamics from experimental data. *Physica D*, 20:217–236, 1986.

R. Brown and L. Kocarev. A unifying definition of synchronization for dynamical systems. *Chaos*, 10:344–349, 2000.

A. Bruns, R. Eckhorn, H. Jokeit, and A. Ebner. Amplitude envelope correlation detects coupling among incoherent brain signals. *NeuroReport*, 11:1509–1514, 2000.

A. P. Burgess and J. H. Gruzelier. Short duration synchronization of human theta rhythm during recognition memory. *NeuroReport*, 8:1039–1042, 1997.

C. Carmeli, M. G. Knyazeva, G. M. Innocenti, and O. De Feo. Assessment of EEG synchronization based on state-space analysis. *NeuroImage*, 25:339–354, 2005.

T. L. Carroll and L. M. Pecora. Cascading synchronized chaotic systems. *Physica D*, 67: 126–140, 1993.

P. Celka and B. Kilner. Carmeli's S index assesses motion and muscle artefact reduction in rowers' electrocardiograms. *Physiological Measurement*, 27:737–755, 2006.

M. Chavez, D.-U. Hwang, A. Amann, and H. G. E. Hentschel. Synchronization is enhanced in weighted complex networks. *Physical Review Letters*, 94:218701, 2005.

Y. Chen, G. Rangarajan, J. Feng, and M. Ding. Analyzing multiple nonlinear time series with extended granger causality. *Physics Letters A*, 324:26–35, 2004.

L. Cimponeriu, M. G. Rosenblum, T. Fieseler, J. Dammers, M. Schiek, M. Majtanik, P. Morosan, A. Bezerianos, and P. A. Tass. Inferring asymmetric relations between interacting neuronal oscillators. *Progress of Theoretical Physics*, 150:22–36, 2003.

J. E. Cohen, F. Briand, and C. M. Newman. *Community Food Webs: Data and Theory*. Springer, Berlin, 1990.

L. Cohen and P. Loughlin. Author's reply. *Signal Processing*, 83:1821–1822, 2003.

L. Cohen, P. Loughlin, and D. Vakman. On an ambiguity in the definition of the amplitude and phase of a signal. *Signal Processing*, 79:301–307, 1999.

S. Corchs and G. Deco. A neurodynamical model for selective visual attention using oscillators. *Neural Networks*, 14:981–990, 2001.

T. M. Cover and J. A. Thomas. *Elements of Information Theory*. Jhon Wiley and Sons, Inc., 1991.

J. L. Crassidis and J. L. Junkins. *Optimal Estimation of Dynamical Systems*. Chapman & Hall/CRC, New York, 2004.

M. P. Dafilis, D. T. J. Liley, and P. J. Cadusch. Robust chaos in a model of the electroencephalogram: Implications for brain dynamics. *Chaos*, 11:474–478, 2001.

R. Dahlhaus. Graphical interactions models for multivariate time series. *Metrika*, 51: 157–172, 2000.

R. Dahlhaus, M. Eichler, and J. Sandkühler. Identification of synaptic connections in neural ensembles by graphical models. *Journal of Neuroscience Methods*, 77:93–107, 1997.

A. R. Damasio. *Disorders of complex visual processing: agnosia, achromatopsia, Balint's syndrome, and related difficulties of orientation and construction*. Philadelphia, 1985.

H. E. Daniels. The relation between measures of correlation in the universe of sample permutations. *Biometrika*, 33:129, 1944.

O. De Feo. Modeling diversity by strange attractors with application to temporal pattern recognition. *Swiss Federal Institute of Technology Lausanne, Lausanne, Switzerland*, 2001. Ph.D. Thesis.

O. De Feo. Qualitative resonance of shil'nikov-like strange attractors, part i: Experimental evidence. *International Journal of Bifurcation and Chaos*, 14 (3):873–891, 2004a.

O. De Feo. Qualitative resonance of shil'nikov-like strange attractors, part ii: Mathematical analysis. *International Journal of Bifurcation and Chaos*, 14 (3):893–912, 2004b.

O. De Feo. Inferring on the dynamical nature of spike trains. In *International Conference on Nonlinear Theory and its Applications NOLTA*, Bologna, Italy, September 2006.

O. De Feo, G. M. Maggio, and M. P. Kennedy. The Colpitts oscillator: Families of periodic solutions and their bifurcations. *International Journal of Bifurcation and Chaos*, 10: 935–958, 2000.

E. K. De Lange. Neuron models of the generic bifurcation type: Network analysis and data modelling. *Swiss Federal Institute of Technology Lausanne, Lausanne, Switzerland*, 2006. Ph.D. Thesis.

E. A. De Yoe and D. C. Van Essen. Concurrent processing streams in monkey visual cortex. *Trends in Neurosciences*, 11:219–226, 1988.

Bonn University Department of Epileptology. Epilectic eeg database. http://www.meb.uni-bonn.de/epileptologie/science/physik/eegdata.html, 2001.

R. Descartes. *Treatise of man*. 1664.

K. T. Dolan and A. Neiman. Surrogate analysis of coherent multichannel data. *Physical Review E*, 65:026108, 2002.

S.N. Dorogovtesev and J.F.F. Mendes. *Evolution of networks*. Oxford University Press, 2003.

R. Eckhorn, R. Bauer, W. Jordan, M. Brosch, W. Kruse, M. Munk, and H. J. Reitboeck. Coherent oscillations: a mechanism for feature linking in the visual cortex? *Biological Cybernetics*, 60:121–130, 1988.

J. P. Eckmann, S. Oliffson Kamphorst, and D. Ruelle. Recurrence plots of dynamical systems. *Europhysics Letters*, 4:973–977, 1987.

A. K. Engel, P. König, A. K. Kreiter, and W. Singer. Interhemispheric synchronization of oscillatory neuronal responses in cat visual cortex. *Nature*, 89:1177–1179, 1991.

A. K. Engel, P. Fries, and W. Singer. Dynamic predictions: oscillations and synchrony in top-down processing. *Nature Review Neuroscience*, 2:704–716, 2001.

J. N. S. Evans. *Biomolecular NMR Spectroscopy*. Oxford University Press, 1996.

L. Fabiny, P. Colet, and R. Roy. Coherence and phase dynamics of spatially coupled solid-state lasers. *Physical Review A*, 47:4287–4296, 1993.

D. J. Felleman and D. C. Van Essen. Distributed hierarchical in the primate cerebral cortex. *Cerebral Cortex*, 1:1–47, 1991.

T. D. Frank, A. Daffertshofer, C. E. Peper, P. J. Beek, and H. Haken. Towards a comprehensive theory of brain activity: coupled oscillator systems under external forces. *Physica D*, 144:62–86, 2000.

A. M. Fraser and H. L. Swinney. Independent coordinates for strange attractors from mutual information. *Physical Review A*, 33:11–34, 1986.

W. J. Freeman. Evidence from human scalp electroencephalograms of global chaotic itinerancy. *Chaos*, 13:1067–1077, 2003.

H. Fujisaka and T. Yamada. Stability theory of synchronized motion in coupled dynamical systems. *Progress in Theoretical Physics*, 69:32–47, 1983.

G. Galilei. *Discorsi e Dimostrazioni Matematiche, intorno a due nuove scienze*. Lowys Elzevir, Leiden, 1638.

M. S. Gazzaniga. Forty years of split-brain research and still going strong. *Nature Review Neuroscience*, 6:653–659, 2005.

A. P. Georgopulos, J. Ashe, N. Smyrnis, and M. Taira. The motor cortex and the coding of force. *Science*, 256:1692–1695, 1992.

W. Gerstner and W. M. Kistler. *Spiking Neuron Models: Single Neurons, Populations, Plasticity*. Cambridge University Press, 2002.

A. Gevins, H. Leong, M. E. Smith, J. Le, and R. Du. Mapping cognitive brain function with modern high-resolution electroencephalography. *Trends in Neuroscience*, 18:429–436, 1995.

K.-I. Goh, B. Kahng, and D. Kim. Universal behavior of load distribution in scale-free networks. *Physical Review Letters*, 87:278701, 2001.

N. Goldenfeld and L. P. Kadanoff. Simple lessons from complexity. *Science*, 284:87–89, 1999.

R. I. Goldman, J. M. Stern, J. J. Engel, and M. S. Cohen. Acquiring simultaneous EEG and functional MRI. *Clinical Neurophysiology*, 111:1974–1980, 2000.

G. H. Golub and U. von Matt. Tikhonov regularization for large scale problems. Technical report, Stanford University, 1997.

M. A. Goodale, A. D. Milner, L. S. Jakobson, and D. P. Carey. A neurological dissociation between perceiving objects and grasping them. *Nature*, 349:154–156, 1991.

C. W. J. Granger. *Econometrica*, 37:424, 1969.

P. Grassberger. Finite sample corrections to entropy and dimension estimates. *Physics Letters A*, 128:369–373, 1988.

C. M. Gray. The temporal correlation hypothesis of visual feature integration: still alive and well. *Neuron*, 24:31–47, 1999.

C. M. Gray, P. König, A. K. Engel, and W. Singer. Oscillatory responses in cat visual cortex exhibit inter-columnar synchronization which reflects global stimulus properties. *Nature*, 338:334–337, 1989.

The SIESTA group schlafanalyse gmbh. http://www.oefai.at/siesta/, 2001.

R. A. Harshman. Foundations of the parafac procedure: Models and conditions for an explanatory multimodal factor analysis. Technical report, UCLA Working Papers in Phonetics, 1970.

L. H. Hartwell, J. J. Hopfield, S. Leibler, and A. W. Murray. From molecular to modular cell biology. *Nature*, 402:C47–C52, 1999.

J. F. Heagy, T. L. Caroll, and L. M. Pecora. Synchronous chaos in coupled oscillator systems. *Physical Review E*, 50:1874–1885, 1994.

R. Hegger and H. Kantz. Improved false nearest neighbour method to detect determinism in time series data. *Physical Review E*, 60:4970–4973, 1999.

I. S. Hellan. Pls regression and statistical models. *Scandivian Journal of Statistics*, 17: 97–114, 1990.

J. J. Higgins. *Introduction to Modern Nonparametric Statistics*. Brooks/Cole-Thomson Learning, USA, 2004.

J. L. Hindmarsh and R. M. Rose. A model of neuronal bursting using three coupled first-order differential equations. *Proceedings of the Royal Society of London. Series B, Biological Sciences*, 221:87–102, 1984.

B. Horwitz. The elusive concept of brain connectivity. *NeuroImage*, 19:466–470, 2003.

C. Hsiao. Autoregressive modeling and causal ordering of econometric variables. *Journal of Economic Dynamics and Control*, 4:243–259, 1982.

D. Hubel and T. Wiesel. Receptive fields, binocular interaction and functional architecture in the cat's visual cortex. *Journal of Physiology*, 160:106–154, 1962.

C. Huygens. Horoloquium oscilatorium. 1673.

A. A. Ioannides, J. P. R. Bolton, and C. J. S. Clarke. Continuous probabilistic solutions to the biomagnetic inverse problem. *Inverse Problems*, 6:523–542, 1990.

R. Johnson and D. Wichern. *Applied Multivariate Statistical Analysis*. Prentice Hall, Englewood Cliffs, NJ, USA, 2002.

I. Joliffe. *Principal Component Analysis*. Springer Verlag, New York, 2 edition, 2002.

A. Kaiser and T. Schreiber. Information transfer in continuous processes. *Physica D*, 166:43–62, 2002.

M. Kamiński and K. J. Blinowska. A new method for the description of the information flow in the brain structures. *Biological Cybernetics*, 65:203–210, 1991.

E. R. Kandel, J. H. Schwartz, and T. M. Jessell. *Principles of Neural Science*. McGraw-Hill, 4th edition, 2000.

K. Kaneko and I. Tsuda. Chaotic itinerancy. *Chaos*, 13:926–936, 2003.

H. Kantz and T. Schreiber. *Nonlinear Time Series Analysis*. Cambridge University Press, Cambridge, 2nd edition, 2004.

L. M. Kay. A challenge to chaotic itinerancy for brain dynamics. *Chaos*, 13:1057–1066, 2003.

A. Keil, M. M. Muller, W. J. Ray, T. Gruber, and T. Elbert. Human gamma band activity and perception of a gestalt. *Journal of Neuroscience*, 19:7152–7161, 1999.

M. B. Kennel, R. Brown, and H. D. I. Abarbanel. Determining embedding dimension for phase-space reconstruction using a geometrical construction. *Physical Review A*, 45: 3403–3411, 1992.

D. Kiper, M. Knyazeva, L. Tettoni, and G. M. Innocenti. Visual stimulus-dependent changes in interhemispheric EEG coherence in ferrets. *Journal of Neurophysiology*, 82: 3082–3094, 1999.

M. G. Knyazeva, D. Kiper, V. Vidavsky, P. Despland, P. Maeder-Ingvar, and G. M. Innocenti. Visual stimulus-dependent changes in interhemispheric EEG coherence in humans. *Journal of Neurophysiology*, 82:3095–3107, 1999.

M. G. Knyazeva, P. Maeder, E. Fornari, R. Meuli, and G. M. Innocenti. Interhemispheric synchronization under visual stimulation: the evidence from dense array eeg. *Clinical Neurophysiology*, 113 (Suppl. 1):S68, 2002.

M. G. Knyazeva, E. Fornari, R. Meuli, G. M. Innocenti, and P. Maeder. Interhemispheric eeg synchronization correlates with fMRI BOLD response. *NeuroImage*, 19:N2, 2003.

L. Kocarev and U. Parlitz. General approach for chaotic synchronization with applications to communication. *Physical Review Letters*, 74:5028–5031, 1995.

L. Kocarev and U. Parlitz. Generalized synchronization, predictability, and equivalence of unidirectionally coupled dynamical systems. *Physical Review Letters*, 76:1816–1819, 1996.

K. Koffka. *Principles of Gestalt psychology*. Harcourt, Brace, and World, New York, 1935.

A. Kraskov, H. Stögbauer, and P. Grassberger. Estimating mutual information. *Physical Review E*, 69:066138, 2004.

A. K. Kreiter and W. Singer. Stimulus-dependent synchronization of neuronal responses in the visual cortex of the awake macaque monkey. *Journal of Neuroscience*, 16:2381–2396, 1996.

K. Krishnamoorthy and Y. Jianqi. Modified nel and van der merwe test for the multivariate beherens-fisher problem. *Statistics and Probability Letters*, 66:161–169, 2004.

J. B. Kuks, J. E. Vos, and M. J. O'Brien. Coherence patterns of the infant sleep EEG in absence of the corpus callosum. *Electroencephalography and Clinical Neurophysiology*, 66:8–14, 1987.

Y. Kuramoto. *Chemical Oscillations, Waves and Turbulence*. Springer, Berlin, 1984.

M. Kurant and P. Thiran. Layered complex networks. *Physical Review Letters*, 96: 138701, 2006.

J. Lachaux, E. Rodriguez, J. Martinerie, and F. Varela. Measuring phase synchrony in brain signals. *Human Brain Mapping*, 8:194–208, 1999.

M. I. Law, K. R. Zahs, and M. P. Stryker. Organization of primary visual cortex (area 17) in the ferret. *Journal of Computation Neurology*, 278:157–180, 1988.

M. Le Van Quyen, J. Martinerie, M. Baulac, and F. Varela. Anticipating epileptic seizure in real time by a nonlinear analysis of similarity between EEG recordings. *NeuroReport*, 10:2149–2155, 1999.

M. Li, J. H. Badger, X. Chen, S. Kwong, P. Kearney, and H. Zhang. An information-based sequence distance and its application to whole mitochondrial genome phylogeny. *Bioinformatics*, 17:149–154, 2001.

K. K. Likharev. *Dynamics of Josephson Junctions and Circuits*. Gordon and Breach, Philadelphia, 1991.

L. Ljung. *System Identification - Theory for the User*. PTR Prentice Hall, Upper Saddle River, N.J., 2nd edition, 1999.

N. K. Logothetis. *Functional Magnetic Resonance Imaging in Cognitive Sciences: Principles, Advanced Techniques and Applications*. MIT Press, Cambridge, MA, USA, 2004.

S. G. Lomber, B. R. Payne, and J. A. Horel. The cryoloop: an adaptable reversible cooling deactivation method for behavioural or electrophysiological assessment of neuronal function. *Journal of Neuroscience Methods*, 86:179–194, 1999.

E. N. Lorenz. Deterministic nonperiodic flow. *Journal of Atmospheric Science*, 20:130–141, 1963.

Y. L. Maistrenko, O. V. Popovich, and P. A. Tass. Chaotic attractor in the kuramoto model. *International Journal of Bifurcation and Chaos*, 15:3457–3466, 2005.

V. A. Makarov, F. Panetsos, and O. De Feo. A method for determining neural connectivity and inferring the underlying network dynamics using extracellular spike recordings. *Journal of Neuroscience Methods*, 144 (2):265–279, 2005.

P. R. Manger, D. Kiper, I. Masiello, L. Murillo, L. Tettoni, Z. Hunyadi, and G. M. Innocenti. The representaion of the visual field in three extrastriate areas of the ferret (*Mustela putorius*) and the relationship of retinotopy and field boundaries to callosal connectivity. *Cerebral Cortex*, 12:423–437, 2002.

C. A. Marzi, A. Antonini, M. Di Stefano, and C. R. Legg. The contribution of the corpus callosum to receptive fields in the lateral suprasylvian visual areas of the cat. *Behavioural Brain Research*, 4:155–176, 1982.

P. McSharry and L. A. Smith. Better nonlinear models from noisy data: Attractors with maximum likelihood. *Physical Review Letters*, 83:4285–4288, 1999.

S. Micheloyannis, M. Vourkas, M. Bizas, P. Simos, and C. J. Stam. Changes in linear and nonlinear eeg measures as a function of task complexity: evidence for local and distant signal synchronization. *Brain Topography*, 15:238–247, 2003.

P. Milner. A model for visual shape recognition. *Psychological Revie*, 81:521–535, 1974.

W. H. R. Miltner, C. Braun, M. Arnold, M. Witte, and E. Taub. Coherence of gamma-band EEG activity as a basis for associative learning. *Nature*, 397:434–436, 1999.

T. Mima, O. Oluwatimilehin, T. Hiraoka, and M. Hallet. Transient interhemispheric neuronal synchrony correlates with object recognition. *Journal of Neuroscience*, 21: 3942–3948, 2001.

R. E. Mirollo and S. H. Strogatz. Synchronization of pulse-coupled biological oscillators. *Siam journal on applied mathematics*, 50:1645–1662, 1990.

J. Montplaisir, T. Nielsen, J. Cote, D. Boinvin, I. Rouleau, and G. Lapierre. Interhemispheric eeg coherence before and after partial callosotomy. *Clinical Electroencephalography*, 21:42–47, 1990.

F. Mormann, K. Lehnertz, P. David, and C. E. Elger. Mean phase coherence as a measure for phase synchronization and its application to the EEG of epilepsy patients. *Physica D*, 144:358–369, 2000.

M. H. J. Munk, L. G. Nowak, J. I. Nelson, and J. Bullier. Structural basis of cortical synchronization. ii. effects of cortical lesions. *Journal of Neurophysiology*, 74:2401–2414, 1995.

M. H. J. Munk, P. R. Roelfsema, P. König, A. K. Engel, and W. Singer. Role of reticular activation in the modulation of intracortical synchronization. *Science*, 272:271–274, 1996.

J. D. Murray. *Mathematical Biology*. Springer-Verlag, 2nd edition, 2002.

B. Musizza and A. Stefanovska. Interactions between cardiac, respiratory, and brain activity in humans. In *Proceedings of SPIE*, 5841, 2005. 139-149.

M. E. J. Newman. The structure of scientific collaboration networks. *Proceedings of National Academy of Sciences*, 98:404–409, 2001.

M. A. Nicolelis, A. A. Ghazanfar, C. R. Stambaugh, L. M. Oliveira, M. Laubach, J. K. Chapin, R. J. Nelson, and J. H. Kaas. Simultaneous encoding of tactile information by three primate cortical areas. *Nature Neuroscience*, 1:621–630, 1998.

P. L. Nunez. *Neocortical Dynamics and Human EEG Rhythms*. Oxford University Press, New York, 1995.

E. P. Odum. *Fundamentals of Ecology*. Saunders, Philadelphia, 1953.

M. J. L. Orr. Matlab functions for radial basis function networks. http://www.anc.ed.ac.uk/∼mjo/software/rbf2.zip, 2001.

K. Oshima, C. Carmeli, and M. Hasler. State change detection using multivariate synchronization measure from physiological signals. In *International Workshop on Nonlinear Circuits and Signal Processing (NCSP)*, Hawaii, USA, March 2006.

L. Paninski, J. W. Pillow, and E. P. Simoncelli. Maximum likelihood estimation of a stochastic integrate-and-fire neural encoding model. *Neural Computation*, 16:2533–2561, 2004.

U. Parlitz, L. Junge, W. Lauterborn, and L. Kocarev. Experimental observation of phase synchronization. *Physical Review E*, 54:2115–2117, 1996.

B. R. Payne, D. F. Siwek, and S. G. Lomber. Complex transcallosal interactions in visual cortex. *Visual Neuroscience*, 6:283–289, 1991.

L. M. Pecora and T. L. Carroll. Synchronization in chaotic systems. *Physical Review Letters*, 64:821–824, 1990.

A. Pikovsky, M. Rosenblum, and J. Kurths. *Synchronization, A Universal Concept in Nonlinear Sciences*. Cambridge University Press, Cambridge, 2001.

H. B. Pinkofsky, F. A. Struve, M. A. Meyer, G. Patrick, and R. R. Reeves. Decreased multi-band posterior interhemispheric coherence with a lipoma on the corpus callosum: a case report of a possible association. *Clinical Electroencephalography*, 28:155–159, 1997.

O. V. Popovich, Y. L. Maistrenko, and P. A. Tass. Phase chaos in coupled oscillators. *Physical Review E*, 71:065201, 2005.

K. Popper. *Logic der Forschung*. Springer, Vienna, 1934.

D. Prichard and J. Theiler. Generalized redundancies for time series anaylsis. *Physica D*, 84:476–493, 1995.

M. Ptito. *Functions of the Corpus Callosum as derived from split-chiasm studies in cats*. Cambridge, Mass: MIT Press, 2003. 139-153.

K. Pyragas. Continuous control of chaos by self-controlling feedback. *Physics Letters A*, 170:421–428, 1992.

A. Quarteroni, R. Sacco, and F. Saleri. *Numerical Mathematics*. Springer-Verlag, 2004.

R. Quian Quiroga, J. Arnhold, and P. Grassberger. Learning driver-response relationships from synchronization patterns. *Physical Review E*, 61:5142–5148, 2000.

R. Quian Quiroga, A. Kraskov, T. Kreuz, and P. Grassberger. Performance of different synchronization measures in real data: A case study on electroencephalographic signals. *Physical Review E*, 65:041903, 2002.

R. Quian Quiroga, L. Reddy, G. Kreiman, C. Koch, and I. Fried. Invariant visual representation by single-neurons in the human brain. *Nature*, 435:1102–1107, 2005.

S. Ramón y Cajal. *Textura del sistema nervioso del hombre y de los vertebrados*. 1904.

S. Redner. How popular is your paper? an empirical study of the citation distribution. *European Journal of Physics B*, 4:131–134, 1998.

A. Renyi. *Probability Theory*. North Holland, Amsterdam, 1971.

M. Riesenhuber and T. Poggio. Hierarchical models of object recognition in cortex. *Nature Neuroscience*, 2:1019–1025, 1999.

E. Rodriguez, N. George, J. Lachaux, J. Martinerie, B. Renault, and F. Varela. Perception's shadow: long-distance synchronization of human brain activity. *Nature*, 397: 430–433, 1999.

P. R. Roelfsema, A. K. Engel, P. König, and W. Singer. Visuomotor integration is associated with zero time-lag synchronization among cortical areas. *Nature*, 385:157–161, 1997.

M. Romano, M. Thiel, J. Kurths, and W. von Bloh. Multivariate recurrence plots. *Physics Letters A*, 330:214–223, 2005.

M. C. Romano, M. Thiel, and J. Kurths. Detection and quantification of directional coupling using recurrences. In *International Conference on Nonlinear Theory and its Applications (NOLTA)*, Bologna, Italy, September 2006.

R. Romo, A. Hernandez, A. Zainos, and E. Salinas. Correlated neuronal discharges that increase coding efficiency during perceptual discrimination. *Neuron*, 38:649–657, 2003.

E. Jr. Rosa, W. B. Pardo, C. M. Ticos, J. A. Walkenstein, and M. Monti. Phase synchronization of chaos in a plasma discharge tube. *International Journal of Bifurcation and Chaos*, 10:2551–2563, 2000.

M. G. Rosenblum, A. S. Pikovsky, and J. Kurths. Phase synchronization of chaotic oscillators. *Physical Review Letters*, 76:1804–1807, 1996.

M. G. Rosenblum, A. S. Pikovsky, J. Kurths, C. Schäfer, and P. Tass. *Phase Synchronization: From Theory to Data Analysis*. Elsevier Science, New York, 2001. Neuroinformatics and Neural Modeling, Handbook of Biological Physics Vol. 4, pp. 279-321.

O. E. Rössler. Chaotic behavior in simple reaction systems. *Zeitschrift für Naturforschung*, 31A:259–264, 1976.

M. S. Roulston. Estimating the errors on measured entropy and mutual information. *Physica D*, 125:285–294, 1999.

R. Roy and K. S. Thornburg. Experimental synchronization on chaotic lasers. *Physical Review Letters*, 72:2009–2012, 1994.

N. F. Rulkov, L.S. Tsimring, and H. D. I. Abarbanel. Tracking unstable orbits in chaos using dissipative feedback control. *Physical Review E*, 50:314–324, 1994.

N. F. Rulkov, M. M. Sushchik L.S. Tsimring, and H. D. I. Abarbanel. Generalized synchronization of chaos in directionally coupled chaotic systems. *Physical Review E*, 51:980–994, 1995.

D. M. Santucci, J. D. Kralik, M. A. Lebedev, and M. A. L. Nicolelis. Frontal and parietal cortical ensembles predict single-trial muscle activity during reaching movements in primates. *European Journal of Neuroscience*, 22 (6):1529–1540, 2005.

T. Sauer, J. A. Yorke, and M. Casdagli. Embedology. *Journal of Statistical Physics*, 65: 579–616, 1991.

R. J Schalkoff. *Digital Image Processing and Computer Vision*. John Wiley, New York, 1989.

B. Schelter, M. Winterhalder, R. Dahlhaus, J. Kurths, and J. Timmer. Partial phase synchronization for multivariate synchronizing systems. *Physical Review Letters*, 96: 208103, 2006.

S. J. Schiff, P. So, T. Chang, R. E. Burke, and T. Sauer. Detecting dynamical interdependence and generalized synchrony through mutual prediction in a neural ensemble. *Physical Review E*, 54:6708–6724, 1996.

K. E. Schmidt, D. S. Kim, W. Singer, T. Bonhoeffer, and S. Löwel. Functional specificity of long-range intrinsic and interhemispheric connections in the visual cortex of strabismic cats. *Journal of Neuroscience*, 17:5480–5492, 1997.

T. Schreiber. Measuring information transfer. *Physical Review Letters*, 85:461–464, 2000.

M. I Sereno and J. M. Allman. *Cortical visual areas in mammals*. McMillan, New York, 1991. In The Neural Basis of Visual Function.

R. D. Sidman, D. J. Major, M. R. Ford, G. G. Ramsey, and C. Schlichting. Age-related features of the resting pattern-reversal visual evoked-response using the dipole localization method and cortical imaging technique. *Journal of Neuroscience Methods*, 37: 27–36, 1991.

W. Singer. Neuronal synchrony: a versatile code for the definition of relations? *Neuron*, 24:49–65, 1999.

M. Small and C. K. Tse. Optimal embedding parameters: a modelling paradigm. *Physica D*, 194:283–296, 2003.

D. A. Smirnov and B. P. Bezruchko. Estimation of interaction strength and direction from short and noisy time series. *Physical Review E*, 68:046209, 2003.

A. C. K. Soong and C. I. J. M. Stuart. Evidence of chaotic dynamics underlying the human alpha rhythm electroencephalogram. *Biological Cybernetics*, 62:58–62, 1989.

R. Sperry. Some effects of disconnecting the cerebral hemispheres. *Science*, 217:1223–1226, 1982.

C. J. Stam and B. W. van Dijk. Synchronization likelihood: an unbiased measure of generalized synchronization in multivariate data sets. *Physica D*, 163:236–251, 2002.

C. J. Stam, M. Breakspear, A. M. V. van Walsum, and B. W. van Dijk. Nonlinear synchronization in EEG and whole-head MEG recordings of healthy subjects. *Human Brain Mapping*, 19:63–78, 2003.

A. Stancak and J. Wackermann. Spatial EEG synchronization over sensorimotor hand areas in brisk and slow self-paced index finger movements. *Brain Topography*, 11:23–31, 1998.

K. E. Stephan, W. D. Penny, J. C. Marshall, G. R. Fink, and K. Friston. Investigating the functional role of callosal connections with dynamic causal models. *Annals of the New York Academy of Sciences*, 1064:16–36, 2005.

S. H. Strogatz. *Nonlinear dynamics and chaos: With applications to physics, biology, chemistry, and engineering*. Perseus Books, Cambridge MA, 1994.

S. H. Strogatz. Exploring complex networks. *Nature*, 410:268–276, 2001.

S. H. Strogatz and I. Stewart. Coupled oscillators and biological synchronization. *Scientific American*, 12:68–75, 1993.

A. Stuart, J. K. Ord, and S. Arnold. *Kendall's Advanced Theory of Statistics, Volume 2A: Classical Inference and the Linear Model*. Arnold, London, 6 edition, 1999.

J. Sturis, C. Knudsen, J. S. Thomsen, E. Mosekilde, E. Van Cauter, and K. S. Polonsky. Phase-locking regions in a forced model of slow insulin and glucose oscillations. *Chaos*, 5:193–199, 1995.

F. Takens. *Detecting Strange Attractors in Turbulence*. Springer, New York, 1981. Lecture Notes in Mathematics Vol. 898.

C. Tallon-Baudry, O. Bertrand, P. Bouchet, and C. Fischer. Oscillatory synchrony between human extrastriate areas during visual short-term memory maintenance. *Journal of Neuroscience*, 21:RC177, 2001.

P. A. Tass. *Phase resetting in Medicine and Biology: Stochastic Modelling and Data Analysis*. Springer-Verlag, New York, 1999.

P. A. Tass, M. Rosenblum, J. Weule, J. Kurths, A. Pikovsky, J. Volkmann, A. Schitzler, and H. Freund. Detection of n:m phase locking from noisy data: application to magnetoencephalography. *Physical Review Letters*, 81:3291–3294, 1998.

P. A. Tass, T. Fieseler, J. Dammers, K. Dolan, P. Morosan, M. Majtanik, F. Boers, A. Muren, K. Zilles, and G. R. Fink. Synchronization tomography: A method for three-dimensional localization of phase synchronized neuronal populations in the human brain using magnetoencephalography. *Physical Review Letters*, 90:088101, 2003.

L. Tettoni, F. Gheorghita-Baechler, R. Bressoud, E. Welker, and G. M. Innocenti. Constant and variable of axonal phenotype in cerebral cortex. *Cerebral Cortex*, 8:543–552, 1998.

J. Theiler. Estimating fractal dimension. *Journal of the Optical Society of America A-Optics Image Science and Vision*, 7 (6):1055–1073, 1990.

J. Theiler and P. Rapp. Re-examination of the evidence for low-dimensional, nonlinear structure in the human electroencephalogram. *Electroencephalography and Clinical Neurophysiology*, 98:213–222, 1996.

J. Theiler, S. Eubank, A. Longtin, B. Galdrikian, and J. D. Farmer. Testing for nonlinearity in time series: The method of surrogate data. *Physica D*, 58:77–94, 1992.

G. Tononi, O. Sporns, and G. M. Edelman. A measure for brain complexity: relating functional segregation and integration in the nervous system. *Proceedings of the National Academy of Sciences of the United States of America*, 91:5033–5037, 1994.

A. Treisman and H. Schmidt. Illusory conjunctions in the perception of objects. *Cognitive Psychology*, 14:107–141, 1982.

E. Vaadia, I. Haalman, M. Abeles, H. Bergman, Y. Prut, H. Slovin, and A. Aertsen. Dynamics of neuronal interactions in monkey cortex in relation to behavioral events. *Nature*, 373:515–518, 1995.

B. van der Pol. On oscillation hysteresis in a triode generator with two degrees of freedom. *Philos. Mag.*, 43:700–719, 1922.

D. C. Van Essen and C. H. Anderson. *Information processing strategies and pathways in the primate retina and visual cortex*. Academic Press, New York, 1990. In An Introduction to Neural and Electronic Networks.

P. Van Overschee and B. DeMoor. *Subspace Identification of Linear Systems: Theory, Implementation, Applications*. Kluwer Academic Publishers, 1996.

C. von der Malsburg. The correlation theory of brain function. Technical report, Max Planck Institut Biophysical Chemistry, Gottingen, Freiburg, 1981.

C. von der Malsburg. Nervous structures with dynamical links. *Ber. Bunsenges. Phys. Chem.*, 89:703–710, 1985.

H. U. Voss, H. Rust, W. Horbelt, and J. Timmer. A combined approach for the identification of continuous nonlinear systems. *International Journal of Adaptive Control and Signal Processing*, 17:335–352, 2003.

J. Wackermann. Beyond mapping: estimating complexity of multi-channel EEG recordings. *Acta Neurobiologiae Experimentalis*, 56:197–208, 1996.

S. Wasserman and K. Faust. *Social Network Analysis*. Cambridge University Press, Cambridge, 1994.

D. J. Watts. *Small Worlds: The Dynamics of Networks between Order and Randomness*. Princeton University Press, 2003.

D. J. Watts and S. H. Strogatz. Collective dynamics of "small-world" networks. *Nature*, 393:440–442, 1998.

H. Whitney. Differentiable manifolds. *Annals of Mathematics*, 37:645–680, 1936.

M. Wiesenfeldt, U. Parlitz, and W. Lauterborn. Mixed state analysis of multivariate time series. *International Journal of Bifurcation and Chaos*, 11 (8):2217–2226, 2001.

R. J. Williams and N. D. Martinez. Simple rules yield complex food webs. *Nature*, 404: 180–183, 2000.

E. O. Wilson. *Consilience*. Knopf, New York, 1998.

M. A. Wilson and B. L. McNaughton. Dynamics of the hippocampal ensemble code for space. *Science*, 261:1055–1058, 1993.

J. Wittaker. *Graphical Models in Applied Multivariate Statistics*. John Wiley, Chichester, 1990.

T. Womelsdorf, P. Fries, P. P. Mitra, and R. Desimone. Gamma-band synchronization in visual cortex predicts speed of change detection. *Nature*, 439:733–736, 2006.

J. J. Wright and D. T. J. Liley. Dynamics of the brain at global and microscopic scales: Neural networks and the EEG. *Behavioral and Brain Sciences*, 19:285–320, 1996.

M. P. Young and S. Yamane. Sparse population coding of faces in inferotemporal cortex. *Science*, 256:1327–1331, 1992.

M. A. Zaks, E. Park, M. G. Rosenblum, and J. Kurths. Alternating locking ratios in imperfect phase synchronization. *Physical Review Letters*, 82:42284231, 1999.

J. Zhang and M. Small. Complex network from pseudoperiodic time series: Topology versus dynamics. *Physical Review Letters*, 96:238701, 2006.

Z. Zhang, X. Luo, and M. Small. Detecting chaos in pseudoperiodic time series without embedding. *Physical Review E*, 73:016216, 2006.

Z. Zheng and G. Hu. Generalized synchronization versus phase synchronization. *Physical Review E*, 62:78827885, 2000.

Curriculum Vitae

Cristian Carmeli received his degree (Laurea cum laude) in Biomedical Engineering in 2001 from the University of Genoa, Italy. In September 2001 he won the master thesis award "Italian Society for Bioengineering". He joined the Laboratory of Nonlinear Systems (LANOS) at the Swiss Federal Institute of Technology of Lausanne (EPFL) in May 2002. During his Ph.D. work, under the supervision of Prof. M. Hasler, he tightly collaborated with Dr. Oscar De Feo and Prof. Giorgio Innocenti in a project at the frontier of engineering and neuroscience. Cristian, together with Kumiko Oshima and Martin Hasler, has been awarded with the outstanding paper award at the International Workshop on Nonlinear Circuits and Signal Processing (NCSP) held in March 2006 in Honolulu, USA. Title of the paper "State Change Detection using Multivariate Synchronization Measure from Physiological Signals". Cristian's research interests are in the field of nonlinear dynamics, time series analysis and systems biology.